DIRECTIONAL RECRYSTALLISATION IN MECHNICALLY ALLOYED ODS NICKEL BASE SUPERALLOYS

By

Murakami Kouichi

Darwin College

Department of Materials Science and Metallurgy

A dissertation submitted for the Thesis

in Natural Science

at the University of Cambridge

September 1993

... dixitque Deus

fiat lux

et facta

est lux

PREFACE

This dissertation is submitted for the Thesis in Natural Sciences at the University of Cambridge. The work was carried out under the supervision of Dr H. K. D. H. Bhadeshia at the Department of Materials Science and Metallurgy, Cambridge. Except where acknowledgement and reference to previous work is made, this work is, to the best of my knowledge, original and carried out without collaboration. Neither this, nor any substantial similar dissertation has been submitted for any degree, diploma or qualification at any other university.

Murakami Kouichi
September 1993

ACKNOWLEDGEMENTS

I would like to thank Professor C. J. Humphreys for the provision of laboratory facilities in the Department of Materials Science and Metallurgy at the University of Cambridge. I would like to express my gratitude to my supervisor, Dr Harshad K. D. H. Bhadeshia, for his constant encouragement. Thanks are also extended to the group leader Dr Harada H. of the Research and Development Corporation of Japan (JRDC).

I am grateful to all the members of the PT group for their advise, help ***or*** entertainment. Special thanks to C. T. Chou for useful discussion, more than discussion.
My heartfelt thanks to my family Mari and Moe, they have always encouraged me and sometimes comfortably disturbed me. I wholeheartedly thank all my parents, especially, my mother-in-law who rescued me from dying of dreadful hay fever.

Finally, I would like to thank my research sponsors JRDC, and Ishikawajima-Harima-Heavy-Industries Co., Ltd. (IHI), for their financial support, plenty of technical advise, facilities, scolding and encouragement.

CONTENTS

Chapter 1: INTRODUCTION

Chapter 2: LITERATURE SURVEY

Chapter 3: EXPERIMENTAL TECHNIQUES

Chapter 4: NONUNIFORM RECRYSTALLISATION IN MA6000

Chapter 5: GRAIN BOUNDARY TOPOLOGY IN MECHANICALLY ALLOYED MA6000.

Chapter 6: CHANGES IN PRECIPITATES AND DISPERSED PARTICLES DURING HEAT TREATMENT

CHAPTER 1

INTRODUCTION

1.1 Aim

The major aim of this research is to obtain a metallurgical model for the process of directional recrystallisation in mechanically alloyed oxide dispersion strengthened (ODS) nickel base superalloys. The directionally recrystallised ODS nickel base superalloys have superb high temperature strength, with the highly elongated directional grain structure imparting excellent properties along the major stress axes. It is, however, difficult to control the grain shape, orientations and other characteristics in some important alloys, because little is known about the mechanism of directional recrystallisation. This basic research is intended to facilitate methods of controlling the directions and crystallographic orientations of the grains. Then new applications will be opened up. The modeling will involve the development and testing of the theoretical concepts necessary to deal with the relationship between process parameters and microstructural changes during directional recrystallisation. Detailed and extensive experiments will be conducted to test the model.

1.2 Background

Nickel base superalloys were launched with the opening of the era of the jet engine powered aircraft. Since then, stronger materials have been required in order to improve the jet engine ability and efficiency. In general, the jet engine turbine blades are essentially strengthened with γ' whose strength has a positive temperature dependence. On the other hand, the combustion gas temperatures in the most modern gas turbines can be in excess of 1300 °C, and the maximum temperatures at the blade surface can be greater than 1000 °C even though they are cooled by flowing air. At such temperatures γ' enhancement rapidly becomes ineffective due to its coarsening, so that more stable strengthening mechanisms have been required. It is known that fine oxide dispersions (particle size $\approx$ 20 nm) are very stable and give impressive creep properties. The two strengthening factors of γ' and fine oxides were thus combined; γ' is particularly strong at medium temperatures (> 800 °C) whereas oxides impart strength at even higher temperatures.

However, the powder metallurgical method used in the manufacture of oxide dispersion strengthened (ODS) alloys can offer more exciting possibilities. This is because materials with compositions which are far from equilibrium can be produced by mechanical alloying or using rapid solidification technology. Mechanical alloying is a process in which appropriate mixtures of elemental or master alloy powders, and oxide powder(s) are stirred together in a ball mill. The powders are frequently forced into intimate metallurgical contact until a true alloy of the required composition is produced. The resultant powder is then consolidated by processes such as hot-extrusion and hot isostatic pressing (HIP), and then, occasionally given subsequent hot-rolling or forging treatments. After consolidation, the alloy undergoes primary recrystallisation to an incredibly fine-grained (sub-micron) microstructure. It is found that further heat-treatment can lead to recrystallisation which in turn leads to the formation of extremely anisotropic grains structures which are eminently suited for elevated temperature applications. The directional microstructure is quite close to that obtained by directional solidification, with the elongated columnar grains aligned along a particular sample axis. In some cases, directional recrystallisation is found during isothermal annealing, but in other cases only by annealing in a temperature gradient gives the required anisotropic grains. The latter process is most effective when the annealing does not involve a static temperature gradient, but instead, when a hot zone is traversed along the sample, giving extremely anisotropic grain structures, with grains sometimes extending over large distances ($\approx$ 1 m).

There are already industrial applications of mechanically alloyed ODS nickel base superalloys, especially in the aerospace industry. The use of the alloy is, however, restricted by the lack of a basic understanding of the factors which determine the directional grain microstructure, and in particular, how those factors could be utilised to control the development of the microstructure.

The goal of this research is to develop methods of controlling directional recrystallisation in

ODS alloys, using new metallurgical theory and experiments. There are a number of parameters needed to complete a model; we select three major objectives to this research. They are essential to develop a detailed model for the directional recrystallisation process as a function of processing parameters;

- stored energy
- particle dispersions
- geometry of grain structure

These parameters are discussed briefly in following sections.

1.3 Stored energy in ODS superalloys

It is in many cases necessary to anneal ODS superalloys using a mobile temperature gradient (called zone annealing) in order to induce directional recrystallisation. Any point in the sample thus undergoes a transient rise in temperature, during which recrystallisation can occur. This pulse of temperature also ensures that recrystallisation occurs in a gradient of temperature, since the sample outside of the heat source is relatively cold, and sometimes forced to be cooled. The heat-treatment during zone annealing is therefore anisothermal, and there are many parameters that can be varied during zone annealing, such as the peak temperature, the sample velocity and the temperature gradient.

There is little work on recrystallisation during non-isothermal heat treatment, and it is currently impossible to predict the optimum annealing conditions necessary for directional recrystallisation. A model is needed to estimate the effectiveness of the continuous heating and cooling thermal cycle [1,2]. Existing models, however, do not incorporate the effects of recovery (in particular, normal grain growth before recrystallisation) during the heating stage. ODS nickel base superalloys usually undergo primary recrystallisation perhaps during heating before extrusion into an ultra fine grain structure (grain size $\approx$ 0.2 μm). The directional recrystallisation that occurs on annealing is therefore a secondary recrystallisation process driven by the grain boundary energy. The driving force for secondary recrystallisation in the alloys is the grain boundary energy due to their fine grain structure. It can be altered by pre-annealing at a low temperature where recrystallisation is not possible but normal grain growth can occur. The pre-annealed samples would then be isothermally / anisothermally annealed at higher temperatures to study the influence of stored energy on secondary recrystallisation. It is intended that these concepts are incorporated into a theoretical model for the effect of stored energy on grain boundary velocity during recrystallisation. It has already been demonstrated that grain boundary velocity has a major influence on the microstructure that develops during zone annealing. If the maximum boundary velocity possible for a specified peak temperature is greater than the sample velocity, then directional recrystallisation is predicted and found to occur experimentally. On the other hand, if the sample velocity is larger than the boundary velocity, then equiaxial recrystallisation is predicted and found. The stored energy measurements and pre-annealing experiments are particularly relevant in finding new ways of controlling the directional recrystallisation process. The stored energies can be measured with differential scanning calorimetry (DSC) which specially designed to measure reactions at temperatures.

The results and discussion on the stored energy and its effects on recrystallisation phenomena are presented in Chapter 4 and Chapter 5.

1.4 Particle Dispersions in ODS Superalloys

There are two broad classes of materials which undergo directional recrystallisation, those which only recrystallise into an elongated microstructure when annealed in a temperature gradient, and those which directionally recrystallise even when annealed isothermally. It is still impossible to predict whether an alloy should belong to one or the other class, except by trial and error. It is therefore impossible to design the recrystallisation behavior. The ability of an alloy to undergo directional recrystallisation during isothermal heat-treatment must in many cases depend on the presence of an anisotropic distribution of grain boundary pinning particles. Such a distribution could be an artifact of the manufacturing process; particles may tend to align along the extrusion direction, although this is not always found to be the case. The model should take into account the tendency for particle alignment during extrusion as a function of particle size distribution, particle shape, particle yield strength and interfacial properties.

Furthermore, recent works have reported that oxide particles in ODS superalloys are not as thermally stable as was originally believed [3,4], and some other fine particles (such as carbides and nitrides) still exist at typical recrystallisation temperatures [4].

The behaviour and influence of the particles and their interaction with the recrystallisation phenomenon is discussed in Chapter 4 and Chapter 6.

1.5 Geometry of Grain Structure in ODS Superalloys

The characteristics of the primary grain structure, such as grain size, grain size distributions and texture, may influence the recrystallisation behaviour. One of the important geometric factors is the grain size distribution. Recrystallisation in mechanically alloyed metals seems to occur at excessively high temperatures (in excess of $0.8T_m$) and the reason for this is still unknown. It has been argued that it is the decrease in pinning force due to coarsening or dissolution of oxides that triggers recrystallisation. Solute drag mechanisms have been proposed, but are not convincing and there is no direct evidence. In fact, it is demonstrated that particle coarsening does not correlate with the recrystallisation onset in Chapter 5.

An important factor is the metallographic texture. In general, strong textures develop during recrystallisation in ODS alloys, and it is well established that they are related to the texture that exists before recrystallisation [5]. The control of texture is important for practical applications because the <100> fibre texture along stress axis gives an optimum creep life. Unfortunately the <110> fibre texture tends to appear in directionally recrystallised ODS nickel base superalloys [6].

References

1. Baloch M. M. Bhadeshia H. K. D. H.: *Mater. Sci. Technol.*, (1990), **6**, p. 1236.
2. Mino K., Harada H., Bhadeshia H. K. D. H. and Yamazaki M.: *Mater. Sci. Forum*, (1992), **88-90**, p. 1236.
3. Schaffer G. B., Loretto M. H., Smallman R. E. and Brooks J. W.: *Acta Metall.*, (1989), **37**, p. 2551
4. Hotzler R. K. and Glasgow T. K.: *Metall. Trans.*, (1982), **13A**, p. 1665

5 Versnyder F. L. and Shank M. E.: *Mat. Sci. Eng.*, (1970), **6**, p. 213.

6 Gessinger G. H.: *Powder Metallurgy of Superalloys*, Butterworths, Cambridge, (1984), p. 219.

CHAPTER 2

LITERATURE SURVEY

2.1 Superalloys

2.1.1 Introduction

Nickel base superalloys are well established in the manufacture of heat resistant components used in high temperature combustion devices, such as jet engines or gas turbine blades and discs. The alloys have to be resistant to creep, low and high frequency thermal fatigue and also corrosion.

The development of γ' nickel base superalloys is illustrated in Fig. 2.1 [1]. The first research on the alloy was in the 1940s, when it was found that a Ni-Cr alloy with a Ti addition was remarkably strengthened by the formation of Ni_3Ti (γ') precipitates. Since then, in order to enhance mechanical properties at ever increasing temperatures, a huge amount of development work has been done on the alloys. Oxide dispersion strengthened (ODS) nickel base superalloys represent one of the 'spin-offs', which is the subject of this thesis.

2.1.2 Alloy Design

It is well known that fine and uniformly dispersed precipitates can enhance the mechanical properties of alloys. The γ' phase is one of the most important factors in superalloy design. It is an intermetalic compound which has good ductility whereas almost all other intermetallic compounds are brittle. The critical resolved shear stress of γ' has a positive temperature dependence up to about 750 °C, as shown in Fig. 2.2 [2]. This is the main reason why superalloys have good high temperature properties.

Since *Nimonic 100,* the alloy strengthened with the Ni_3Al γ', the alloys have been continuously enhanced using other mechanisms. Hot forgeability, however, decreased with increases in strength so that the main fabrication method shifted to casting using advanced vacuum casting technology. Increases in durable temperatures were brought about with directional solidification, single crystal solidification and directional recrystallisation techniques. New compositions suitable for the modern fabrication have been developed. *MA6000*, made using a mechanical alloying technique (detailed later), and having an extremely elongated grain structure, is a standard alloy which is directionally recrystallised.

Nickel base superalloys usually consist of a large number of elements such as Al, Co, Cr, Mo, W, Ti, CB, Ta, Hf, and in polycrystalline alloys, the grain boundary strengthening elements C, B, Zr. Alloy design is therefore very complicated, and has been helped using methods such as PHACOMP [3], d-electron design methods [4], and the cluster-variation technique [5,6].

The phase γ' is important in enhancing elevated temperature strength, but it coarsens rapidly above 1000 °C. Coarsened γ' cannot be relied on for applications where the temperature exceeds 1000 °C. Unfortunately almost all precipitates in alloys coarsen rapidly above 1000 °C. If thermally stable fine particles can be dispersed in the matrix, then strong alloys become possible. Oxide dispersion strengthened (ODS) alloys were born from this idea. The origin of ODS alloys can be traced to the 1910s' in tungsten alloys. Table 2.1 presents the major stages in the development of ODS alloys [7]. It might be assumed that nickel base superalloys enhanced by oxide particles would have better high temperature properties. However, they cannot be produced by casting. It is impossible to add fine oxide particles to the melt of superalloys containing high chemical activity elements such as Ti, Ta, Al, because these elements can easily react with the oxide particles. Furthermore, oxide particles are badly wet by the molten alloy, making it difficult to mix the oxide and the melt.

Table 2.1 Major stages in the development of ODS alloy processing [7]

Year	Alloy	Processing
1910	Ductile Tungsten	Conventional powder metallurgy (press+sinter+draw)
1930	Cu, Ag and Be alloys	Internal oxidation
1946	SAP	Milling of Al powder with surface oxide formed *in situ.*
1958	TD-Ni	Fine powder metallurgy
1970	IN853	Mechanical alloying

Benjamin solved this difficulty by his unique idea named mechanical alloying, a kind of powder metallurgy [8,9,10,11]. After Benjamin, Grant developed mechanical grinding which is similar to mechanical alloying but in principle is completely different [12]. Mechanical alloying alone is the method used to make commercial ODS nickel base superalloys. Table 2.2 shows examples of ODS nickel base superalloys [13]. *MA6000* is a representative ODS nickel base superalloy popular amongst researches. Details of the mechanical alloying conditions and *MA6000* are mentioned later.

C. T. Sims has schematically illustrated various microstructures in the development of the nickel base superalloys (Fig. 2.3) in which the useful phases are shown on the upper side and harmful phases are on the lower side [14].

2.1.3 Control of Crystal Growth

The mechanical properties of metals can be strongly affected by grain boundaries. In the present context the grain boundaries are generally stronger than the grain interiors at lower temperatures, but for $T > 0.8T_{melt}$, the reverse is true. This is because creep due to grain boundary sliding and diffusion creep become dominant at high temperatures, and the grain boundaries work as crack initiation and propagation paths. Coarse grained materials are therefore preferred for stressed heat resistant devices. The yield stress of nickel base superalloys as a function of various microstructures and temperature is shown schematically in Fig. 2.4 [15]. At lower temperatures, structure A with the fine and deformed grains achieves about 2000 MPa yield stress, but this rapidly decreases with increasing temperature. On the other hand, structure C, with coarse and elongated grains, can keep more than 200 MPa yield stress above 1000 ° C maximum. In ODS alloys, the same tendency is obtained as shown in Fig. 2.5 and Fig. 2.6 [9,16]. Fig. 2.5 shows 10^2 and 10^3 hours creep rupture stress as a function of average grain diameter in a TD-NiCr, a sort of ODS superalloy produced by coprecipitation method, and Fig. 2.6 shows 10^2 hours creep rupture life as a function of grain aspect ratio [9]. The coarsening and elongation effects on creep strength are evident. Improvement in the creep properties of coarse grained materials may be obtained if the grains have fewer boundaries which are normal to the stress axis; thus the grain shape should be elongated along the stress direction as mentioned above.

Table 2.2 Various ODS high temperature alloys (wt%) [13]

Alloy	Fe	Ni	Co	C	Cr	Mo	W	Ti	Al	B	Zr	Others
MA6000	-	bal.	-	0.05	15.0	2.0	4.0	2.5	4.5	0.01	0.15	2.0Ta, $1.1Y_2O_3$
MA754	1.0	bal.	-	0.05	20.0	-	-	0.5	0.3	-	-	$0.6Y_2O_3$
MA956	bal.	-	-	-	20.0	-	-	0.5	4.5	-	-	$0.5 Y_2O_3$
TD-Ni	-	bal.	-	-	-	-	-	-	-	-	-	$2.0 ThO_2$
TD-NiCr	-	bal.	-	-	20.0	-	-	-	-	-	-	$2.0 ThO_2$
TMO-2	-	bal.	9.7	0.05	5.9	2.0	12.4	0.8	4.2	0.01	0.05	5.4 Ta, $1.1Y_2O_3$

Ideally, there should be no boundaries boundaries.

Two general techniques exist for producing such materials. One method, known as directional solidification, involves controlling the heat flow. Single crystals are also produced using the quite similar procedure of directional solidification [17,18]. Fig. 2.7 shows various precision casting methods and an example of a furnace for directional solidification designed by Rolls-Royce Ltd. [19]. Molten alloy in a mold is moved into the cooled assembly, and solidified along one direction. In the directional solidification of nickel base superalloys, <001> dendrites grow along the temperature gradients. Grains initiated at the first stage are in random orientation, but those oriented along <001> grow rapidly as shown as Fig. 2.8. A single crystal is produced by using a specific mold which has a selector to permit the passage of only one grain of all of the <001> orientated grains [17].

The relationship between crystal orientation and creep rupture strength is illustrated in Fig. 2.9 [20]. The strength decreases with increasing identification number; 1 is the strongest. The <111> orientation is the best, followed by the <001> orientation, and the worst being <011>. At 760 ° C, the <111> orientation rupture life is more than a thousand times that of the <011>. The Young's modulus in the <001> orientation is the smaller; this is beneficial to thermal fatigue properties. The <001> orientation is fortunately the preferred orientation for the solidification. Unfortunately, recrystallised *MA6000*, the main material for the present research, there is an the <011> texture (detailed later).

The other method involves controlled recrystallisation (usually after deformation). In its best known form, this type of process involves straining the material to produce a particular dislocation density, and then heating above the recrystallisation temperature under conditions which encourage grain growth rather than nucleation. This produces elongated grains [21]. The heating is usually performed in a moving thermal gradient furnace, as in a directional solidification furnace but the temperature gradient is larger. A schematic drawing of the furnace for the directional recrystallisation is shown in Fig. 2.10 [22].

There is another type of recrystallisation process which is known as secondary recrystallisation. Certain existing grains grow at the expense of other somewhat finer grains. This is basically as same as primary recrystallisation but the initial material has a fine recrystallised grain structure and a dispersed fine second phase [23,24,25].

Oxide dispersion strengthened nickel base superalloys involve large amounts of γ', dispersed fine oxide particles, and a highly controlled structure and can be made by mechanical alloying. Typical production procedures of ODS nickel base superalloys are illustrated in Fig. 2.11 [26]; each step is discussed further in later sections.

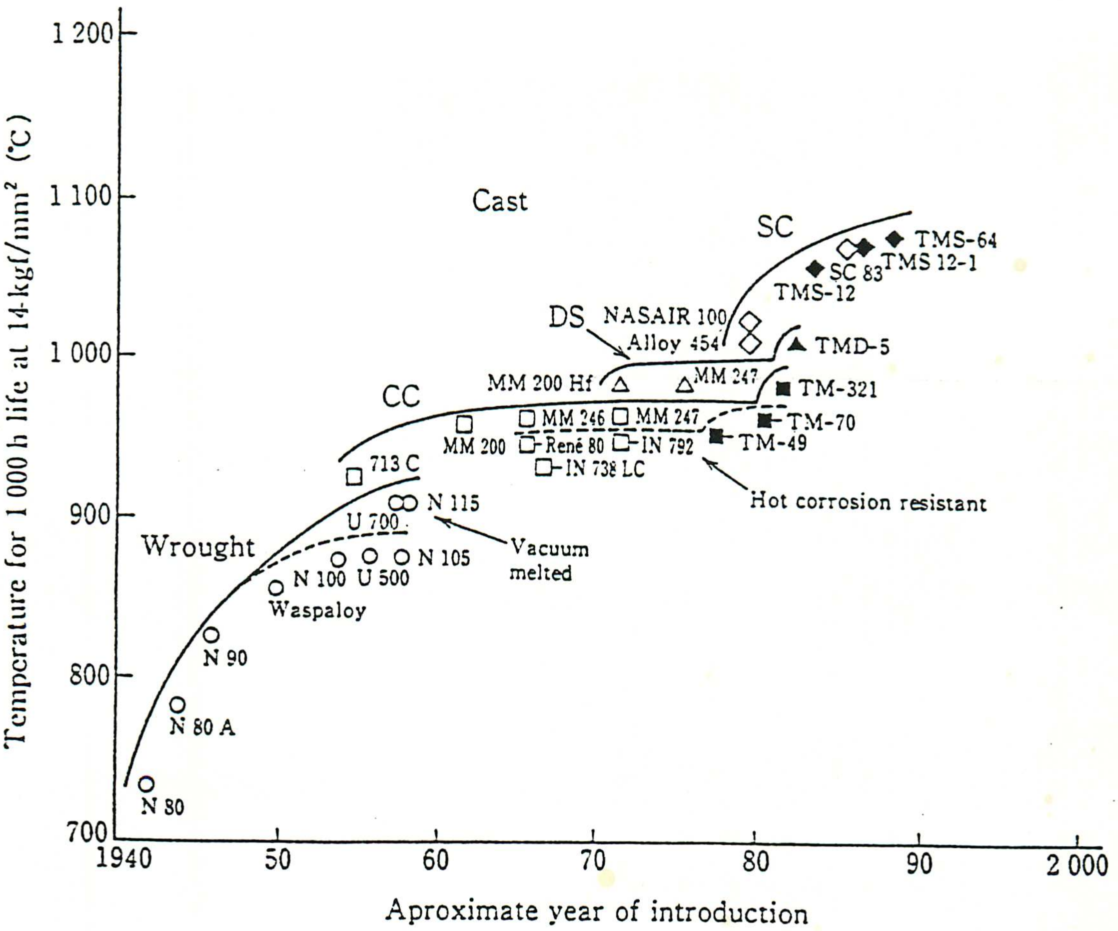

Fig. 2.1 Trends in the development of nickel base superalloys and assorted processes development [1].

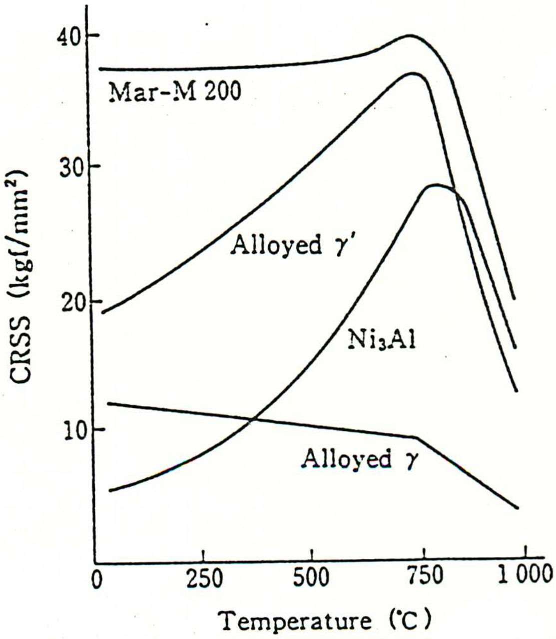

Fig. 2.2 Temperature dependence of critical shear stress of single crystals [2].

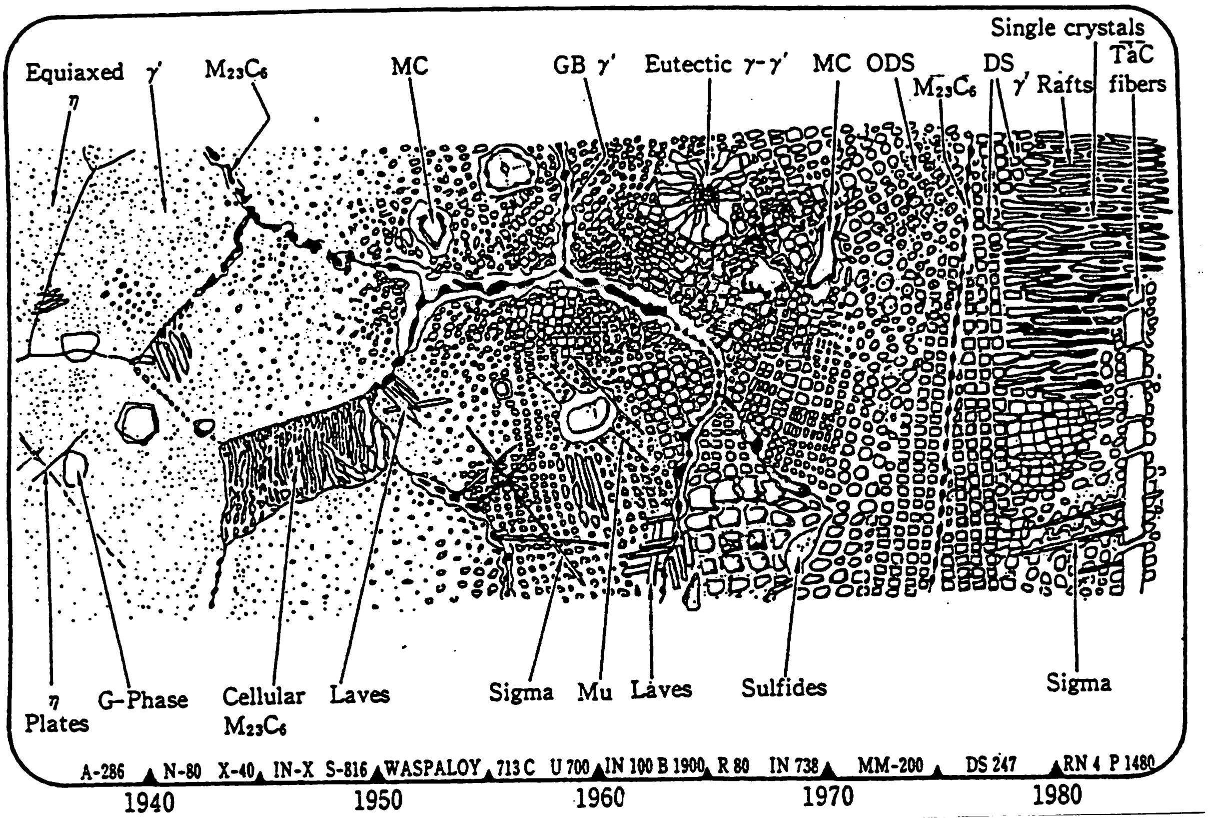

Fig. 2.3 Illustration of various phases and structures in superalloys as a history. The phases in the lower half of the diagram tend to be detrimental [14].

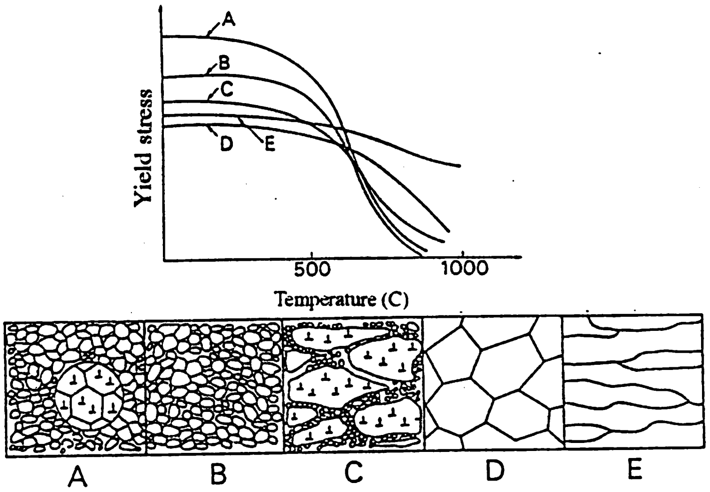

Fig. 2.4 Relationships among structures and yield stresses at various temperatures [15].

A: Fine grains with deformation

B: Fine grains

C: Necklace

D: Coarse grains

E: Coarse and elongated grain

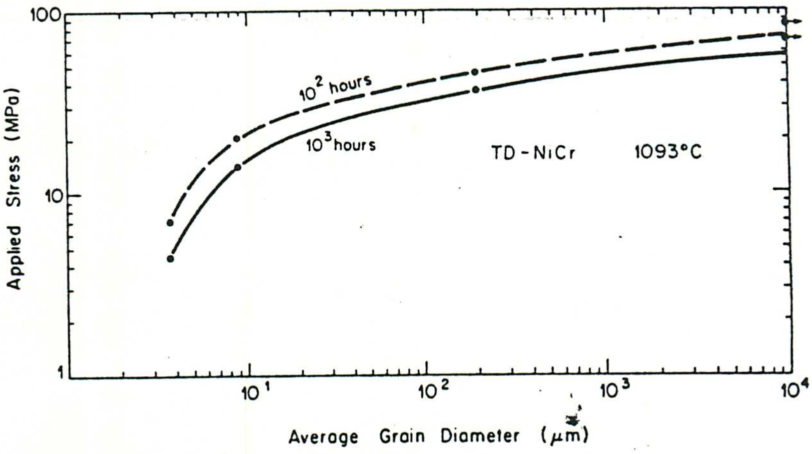

Fig. 2.5 The effects of grain size on 100 hours and 1000 hours creep rupture strengths of *TD-NiCr* [9].

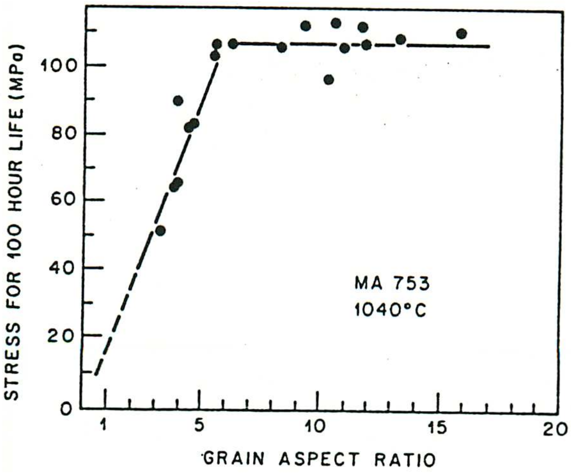

Fig. 2.6 100 hour creep lives as a function of grain aspect ratio in *MA753* [16].

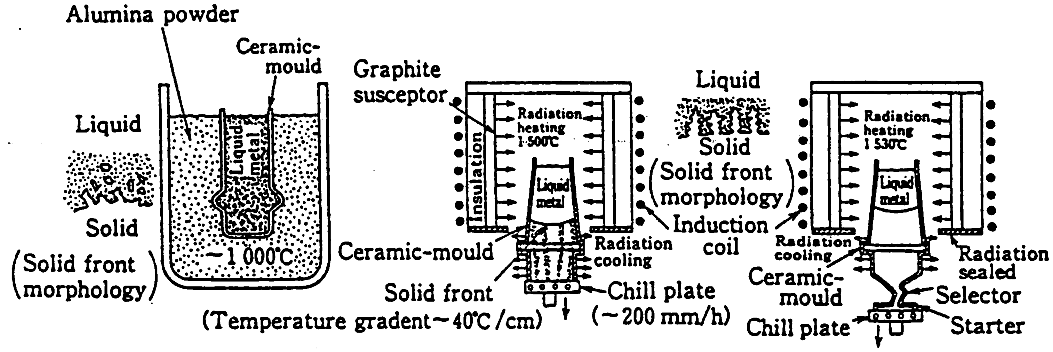

(a) Polycrystal casting

(b) Columner grain casting

(c) Single crystal casling

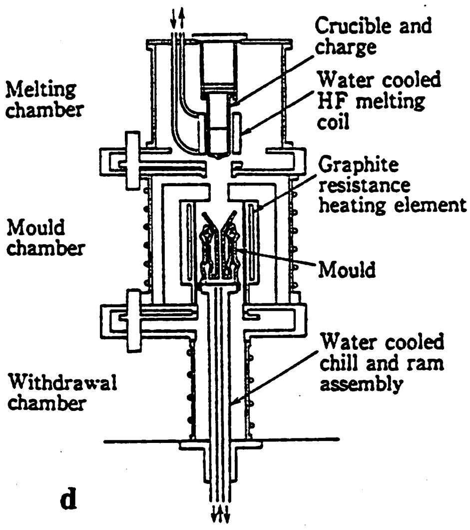

Fig. 2.7 Various precision casting methods [19].

a: Polycrystal

b: Directional solidification (DS)

c: Single crystal (SC)

d: Schematic drawing of a DS/SC furnace in Rolls- Royce Ltd.

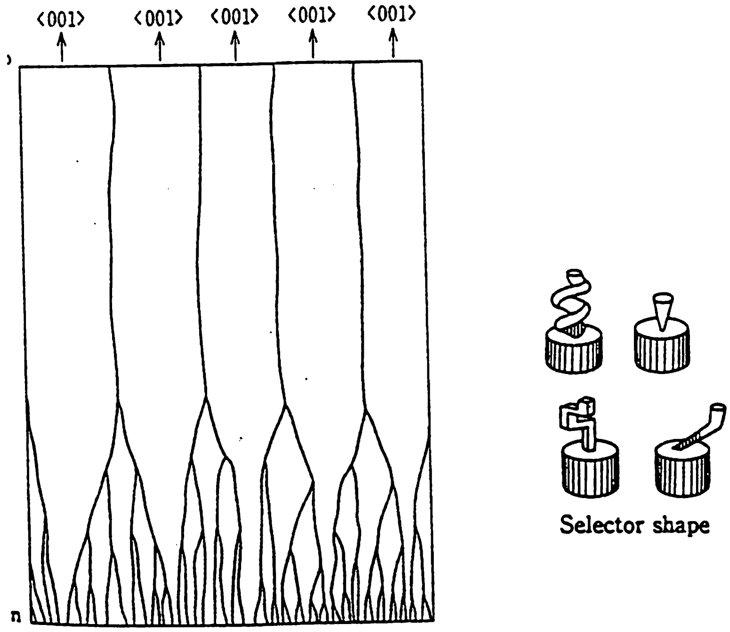

Fig. 2.8 Schematic drawing of columnar grain growth during directional solidification and various selectors for single crystal production [17].

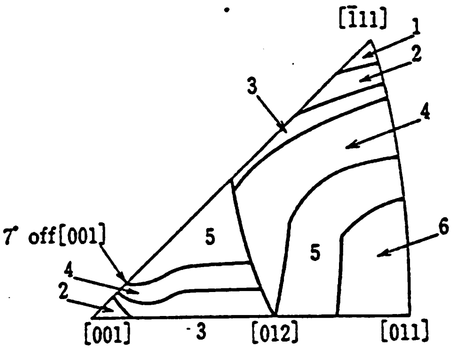

Fig. 2.9 Crystal orientation dependence on creep strength. Orientation (1) in the figure is the strongest and orientation (6) is the weakest [20].

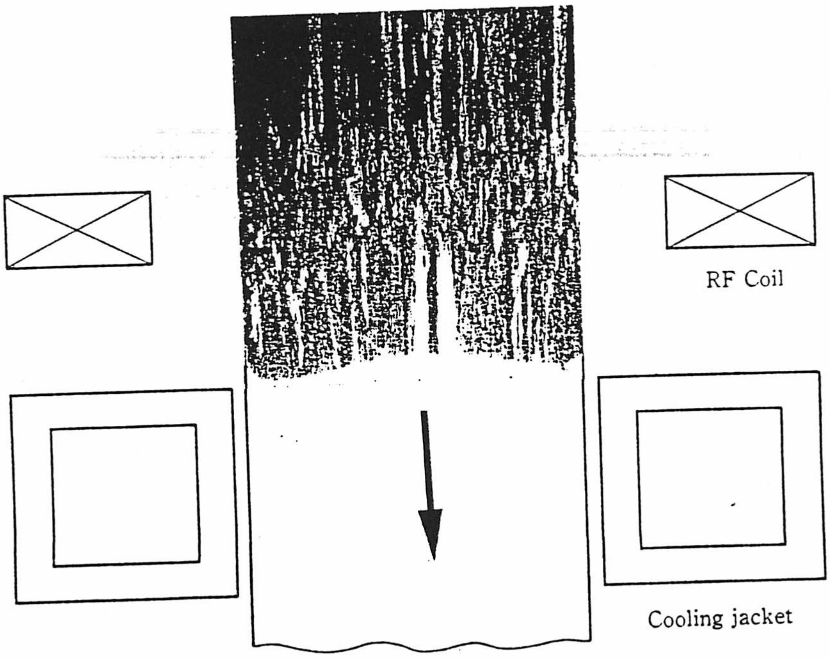

Fig. 2.10 Schematic drawing of a directional recrystallisation furnace and a typical recrystallised structure [22].

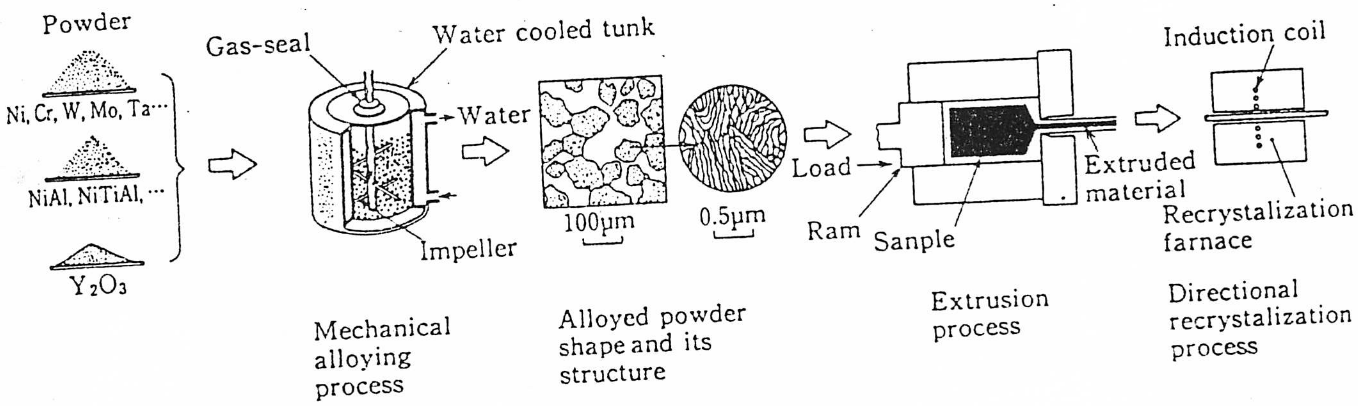

Fig. 2.11 Typical procedure of mechanically alloyed ODS superalloys [26].

2.2 Mechanical Alloying

2.2.1 Mechanical Alloying

In order to disperse fine oxide particles in alloys which contain many active elements, Benjamin hit on the idea of mechanical alloying [8,9,10,11]. This is usually done in a high energy ball mill or a machine called an atritor whose structure is shown in Fig. 2.12. Metal powders of the required composition, oxide powder(s) and usually steel or Ni balls are set together into the machine [27]. Then the powders and balls are strongly stirred with a rotating mill or an agitator.

Alloying metal powders are classified into two kinds, pure metals and master alloy. Elements like pure Ni or Cr, which have high ductility, work as binders and need to be more than 15 wt % [10]. On the other hand, high chemical activity elements such as Ti, B are to be alloyed others with such as Ni to reduce potency and avoid oxidation during the mechanical alloying process. The size of oxide particles is very important for mechanical properties at elevated temperatures. Benjamin reported that 15 -30 nm diameter Y_2O_3 is rather suitable for ODS superalloys containing 1-2 wt % oxide [28]. As shown in Fig. 2.13, metal powders and oxide particles are repeatedly pressed, milled and joined among the balls [10]. It is said that each of the elements is worked into a layer at the early stages. The thickness of the layers becomes atomic as the alloying progress and oxide particles are uniformly dispersed. However, some reports showed that alloying is not perfectly completed without diffusion at high temperatures [29,30].

Another method to disperse oxide in superalloys using a metal alloy powder of the required composition (powder size less than 50 μm) and oxide powder(s) has been developed by Grant [12]. This method is called mechanical grinding. The difference relative to mechanical alloying is shown in Fig. 2.14 [22]. Mechanical grinding is still experimental, but it has cost advantages and a greater reproducibility because of the use of only one powder.

2.2.2 Consolidation

The consolidation of the mechanically alloyed powder is quite difficult. They are impossible to sinter for several reasons [31,32]:

(1) Their large individual powder diameters of 60 - 70 μm virtually reduce to zero the capillary forces which are responsible for densification.

(2) The high hardness values of milled powder do not permit cold compaction.

(3) At sintering temperatures, recrystallisation and grain growth would take place, thereby eliminating any chance of obtaining the recrystallised coarse and elongated grains in large diameter compacts.

The principal objective in the consolidation of mechanically alloyed powders is to obtain a fully dense compact which can be further worked [33].

The most common commercial procedure is hot extrusion. The powder is canned under vacuum into mild steel, then hot extruded at more than 1000 ° C. The conditions during extrusion are quite important, because of their affects on the secondary recrystallised microstructures formed during subsequent annealing. For example, the creep rupture life as a function of the extrusion temperature and ratio is illustrated in Fig. 2.15 [33]. The most preferred domain for optimum creep life is shown as a hatched area in the figure. After solidification, the microstructure is very fine primary recrystallised grains whose mean diameter is usually less than 0.5 μm. A typical example just after solidification is shown in Fig. 2.16 [31]. Hot isostatic pressing (HIP) is also a general technique for consolidation, but does not involve deformation so that the primary recrystallised grain size tends to larger than that obtained by hot-extrusion (Fig. 2.17) [34, 35].

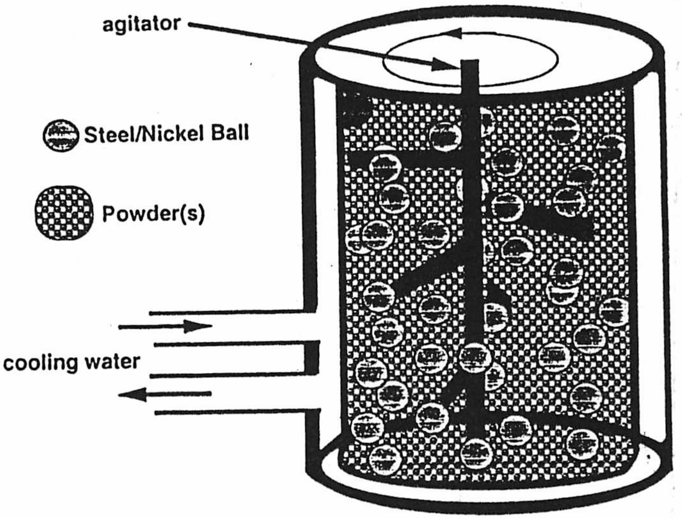

Fig. 2.12 Schematic drawing of an attritor machine [27].

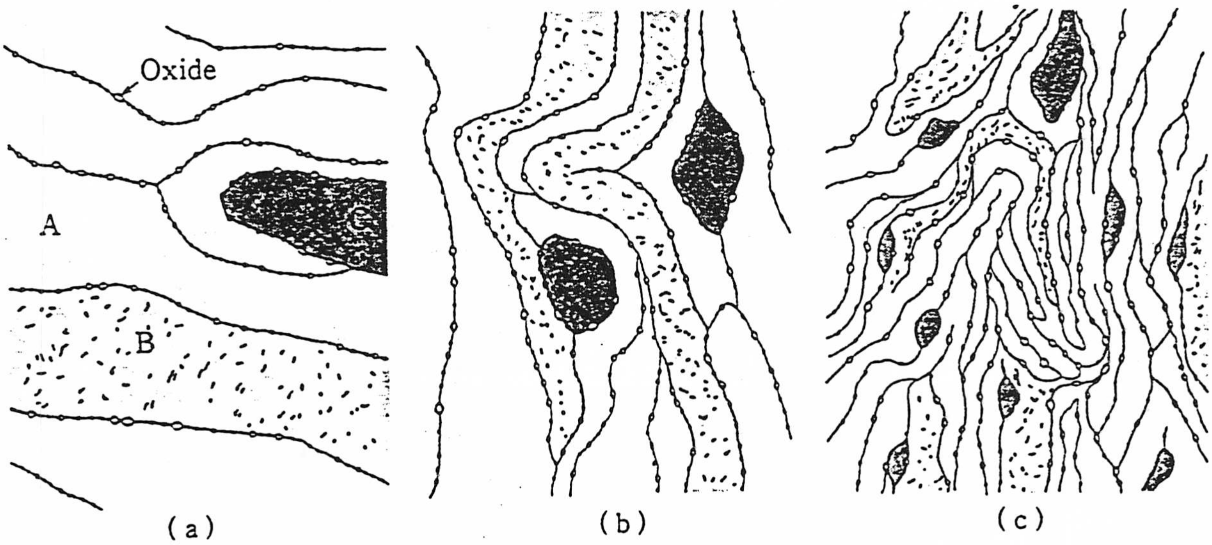

Fig. 2.13 Various microstructural stages during mechanical alloying [10].

a: early stage

b: middle stage

c: latter stage

A and B in the figure are metallic powders.

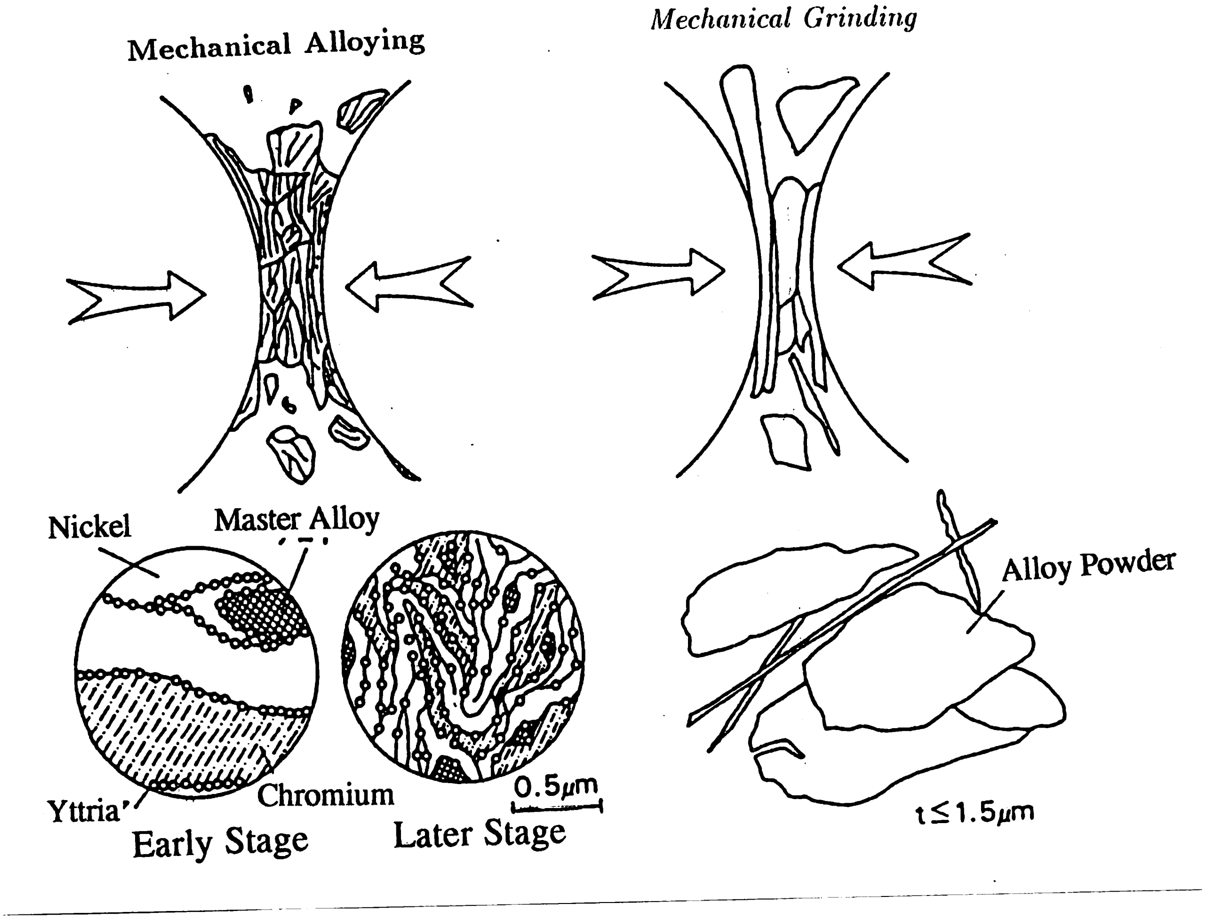

Fig. 2.14 The differences between 'mechanical alloying' and 'mechanical grinding' [22].

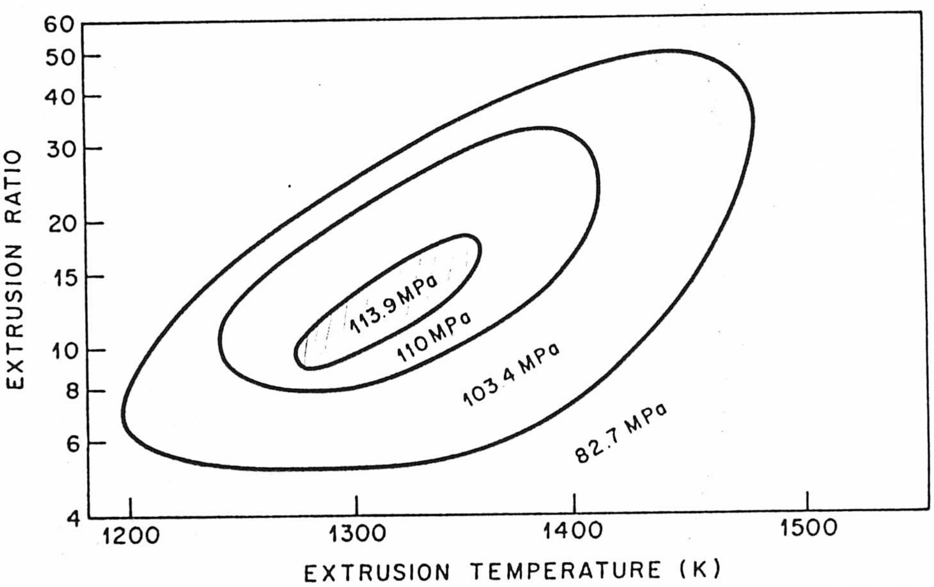

Fig. 2.15 Recrystallisation response of *MA753* as a function of extrusion conditions. The 1000 hours creep rupture strengths at 1311 K are indicated [33].

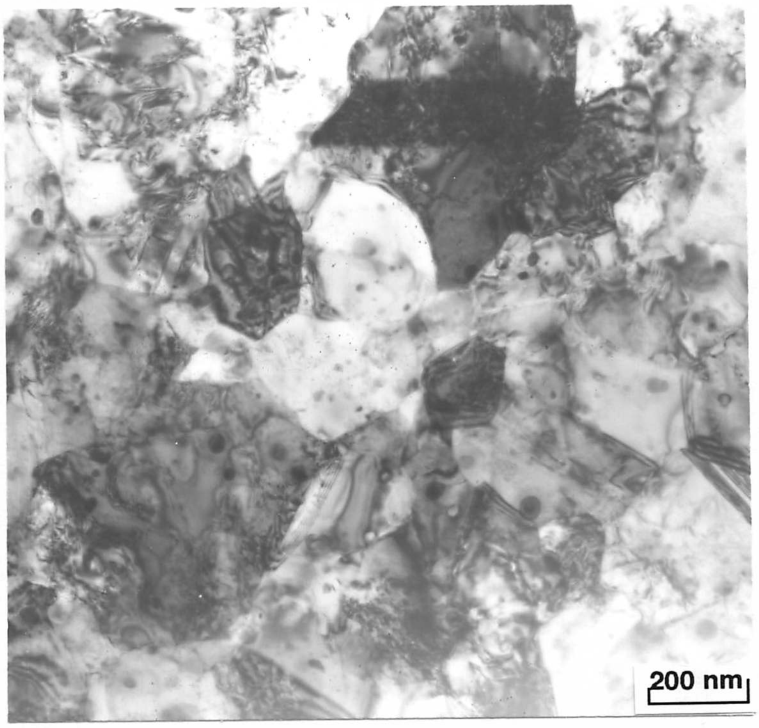

Fig. 2.16 TEM metallographic data of as-extruded *MA6000.* The primary recrystallised grain structure [31].

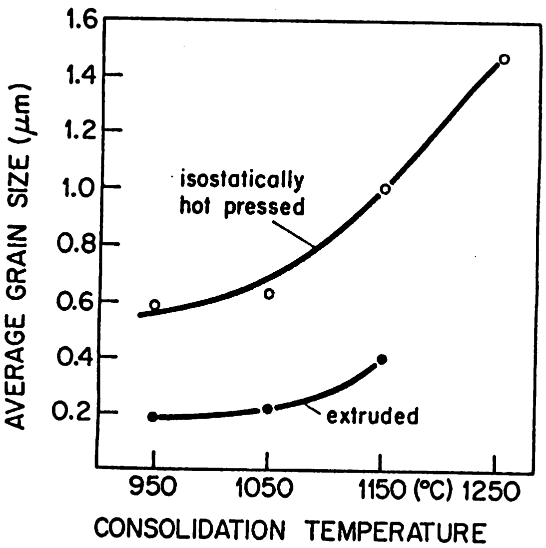

Fig. 2.17 Comparison of grain sizes in *MA738* obtained from HIP and hot-extrusion, as a function of consolidation temperature [34].

2.3 Directional Recrystallisation

2.3.1 Introduction

As shown in Figs. 2.5 and 2.6, the creep rupture life can be significantly improved by coarsening and elongating the grain structure. The larger aspect ratio also brings significantly longer creep rupture life, corresponding to changes in rupture morphology from intergranular to transgranular (Fig. 2.18) [36]. In order to obtain the elongated large grain structure, the consolidated alloy is annealed at higher temperature to induce secondary recrystallisation. Some extruded alloys form this structure by simple isothermal annealing, but others do not. The mechanism is not known, and the grain aspect ratios of isothermally annealed alloys show considerable scatter. Allen applied the zone annealing method to ODS alloys and succeeded in obtaining the large aspect ratio grain structure [37]. Materials having the ability for recrystallisation are passed through a high-frequency furnace and heated to a recrystallisation temperature.

As long as the furnace velocity is less than the grain boundary velocity, and if nucleation ahead of the recrystallisation front can be avoided (by the use of a large temperature gradient), then a columnar grain structure is obtained.

The furnace travel velocities and temperature gradients are relative to material parameters such as stored energy, boundary mobility, and texture. It is possible to obtain an elongated grain structure by using primary recrystallisation [22,38]. However, the travel velocity should be smaller by one or two orders than that used during secondary recrystallisation. A cooling jacket can be used to introduce a high temperature gradient. The high-frequency furnace can induce large temperature gradients, making it difficult to uniformly heat complicated shapes. Radiant heating furnaces have been applied recently [22]. The parameters used in the calculations presented below are listed in Table 2.3.

Table 2.3 Parameters used for the calculations presented in section 2.3

k, n	Material constants determined by experiments
M	Grain boundary mobility
N_V	Number of particles per unit volume
Q	Activation energy for the atom transfer across a boundary
R	Gas constant
R_0	Mean grain radius
R_C	Critical grain radius for grain growth in particle free matrix
R_g	Radius of growing grain
r	Mean particle radius
r_u	Critical particle radius which can pin grain boundary migration
s	Pinning force due to one particle
V_M	Molar volume
V_V	Volume fraction of particle
v	Grain boundary velocity
X	Recrystallised volume fraction
ΔG_P	Pinning force due to particles on grain boundary migration
ΔG_S	Stored energy for grain growth
δ	Atomic distance
σ	Grain boundary energy per unit area
υ	Atomic jump frequency

2.3.2 Secondary Recrystallisation Theories

The time dependence of the progress of secondary recrystallisation can be described as that of primary recrystallisation by the well known Avrami relation [39,40]:

$$X = 1 - \exp(-k\,t^n) \tag{2.1}$$

where X is fraction of secondary recrystallised region, t is annealing time and k and n are determined by experiment. Secondary recrystallisation is also called discontinuous grain growth, and represents a special case of grain coarsening. The free energy

ΔG which is responsible for the grain coarsening process originates from the presence of grain boundaries present in the matrix and gradually decreases during coarsening. Hence the relation holds:

$$\Delta G_S = V_M C_0 \sigma / R_0 \qquad (2.2)$$

where V_M is molar volume, R_0 is mean grain diameter, σ is the grain boundary energy per unit area and C_0 is a geometric factor between 1 and 3 [41]. This relation holds for the mean grain diameter. The growth behaviour of an individual grain is much more involved. It will be governed by the individual processes which occur in the matrix during annealing such as the straightening of a curved boundary, and shifting of the position of a grain boundary junction into an equilibrium position with respect to the stresses from the adjoining grain boundaries.

Feltham has described the grain growth behaviour of individual grains in more detail [42]. Large grains with more than six sides in a micrograph tend to grow at the expense of smaller grains. A distribution of grain size normally exists as shown as Fig. 2.19, described as a 'log normal' distribution [43]. As outlined as Fig. 2.20a, only large grains continue to exist during continuous grain coarsening [44]. The majority of smaller grains disappear in spite of the fact that the mean grain diameter grows as the square root of the isothermal annealing time. Secondary recrystallisation requires that the grain growth be strongly impeded, with the exception of a few grains which act as the nuclei for the secondary recrystallisation. Then the initial rate of grain growth is independent of time, and the motion of grain boundaries of those growing grains is directed towards the centre of curvature. During the process of secondary recrystallisation the distribution of grain size becomes very inhomogeneous, as shown in Fig. 2.20b [44].

Influence of Small Particles

In Fig. 2.21 is a schematic drawing of the interaction of a grain boundary and small particles [45]. Zener has first outlined how particles impede grain growth [46]. The theory has been modified and developed to involve the real shape of the pinned grain boundary by particles, variation in grain boundary energy or variation in particle shape [47,48,49,50,51,52,53, 54,55,56,57,58]. These modifications give results close to Zener's first estimates. On the Zener theory, a particle at a grain boundary decreases the area of the boundary by the cross section of the particle. The motion of a boundary through a matrix with spherical particles of a mean diameter r is exposed to a drag which decreases the free energy of grain boundary motion by ΔG_P. Fig. 2.22 shows a spherical particle of radius r intersected by a grain boundary [59]. The grain boundary energy σ is thus saved in the area πr^2, the reduction of s being given by;

$$s = \sigma \pi r^2 \tag{2.1}$$

The volume fraction of particles of uniform size r is given by;

$$V_V = N_V 4 \pi r^3 / 3 \tag{2.2}$$

where N_V is the number of particles per unit volume. It follows that ΔG_P is;

$$\Delta G_P = \sigma N_v = 3\sigma V_V / 4r \tag{2.3}$$

Secondary recrystallisation requires some kind of a restraint on uniform grain coarsening. Small particles of submicron size are inhibitors to normal grain coarsening, allowing secondary recrystallisation to occur.

There are two well established secondary recrystallisation theories involving the effects of fine particles. Hillert showed that the effective driving force ΔG_S for grain coarsening is [60];

$$\Delta G_S = k\sigma(1 / R_g - 1 / R_C - 3V_V / 4r) \tag{2.4}$$

Grains of diameter greater than R_C are able to grow in the absence of particles. R_C is close to the average grain size. R_g is the similar to R_C but allows for the presence of particles. Grain coarsening requires $\Delta G_S > 0$, therefore ;

$$R_g > 1/(1/R_c - 3V_V/4r) \qquad (2.5)$$

Thus, the grains larger than $1/(1/R_c - 3V_V/4r)$ alone can grow in particle dispersed materials according to the theory.

In Gladman's theory, secondary recrystallisation is triggered by a reduction of ΔG_P [47]. Reduction of ΔG_P is usually caused by the dissolution or coarsening of particles. If r_u is the maximum radius of the particles which can pin boundary migration, it is given by;

$$r_u = \frac{6R_0V_V}{\pi\left(\frac{3}{2} - \frac{2}{H}\right)} \qquad (2.6)$$

where $H = R_g / R_0$, the ratio of growing grain size and average grain size. This equation indicates that with the progress of recrystallisation, r_u increases, so that a growing grain can grow more easily. This leads the selective growth and thus a coarse grain structure is obtained.

Coarse structures for Si-3 wt % steel [61], Mo single crystals [62] and W filaments [63] are certainly produced using this phenomenon. The difficulty is that the oxide particles in ODS superalloys are thermally stable (at 1000 - 1400 °C), so that coarsening or dissolution cannot trigger recrystallisation [64]. Recent work on particles in ODS superalloys have revealed that the oxides (namely ThO_2 in a TD-NiCr alloy [65], Y_2O_3 *MA6000* [66,67]) are not so stable and that there are other kinds of relatively stable particles such as TiC, Ti(C,N) TiN[67], TaC [68]. Structural changes in Y_2O_3 have also been reported [67]. These issues are discussed in Chapter 6 and 7.

The most modern ODS superalloys can have γ' dissolution temperatures as high as 1250 °C which are very close to (and sometimes in excess of) the recrystallisation temperatures [69]. It is well established that γ' dissolution does not correlate with the onset of recrystallisation. However, there may be other γ' effects. For example, the lack of high aspect ratio grain structures has been attributed γ' dissolution induced nucleation at the recrystallisation front during zone annealing [70].

Solute Drag

It is well known that solute atoms can retard grain boundary migration. Early theoretical work on the grain boundary dragging effects of solutes considered high purity metals [71,72,73,74]. These theories predict that under certain conditions a moving grain boundary can tear itself free from the accompanying solute cloud. It has been proposed that this is why ODS alloys recrystallise at abnormally high temperatures (Fig. 2.23) [75]. Primary recrystallisation during zone annealing in Ni-X binary alloys has been studied systematically [38]. Fig. 2.24 shows the effect of Cu on the recrystallisation structure [38]: An increase in Cu leads to more equiaxed grain structures. This phenomenon has been attributed to solute drag. However, the evidence on boron effects indicates an encouragement of recrystallisation rather than a retardation. Boronised *MA6000* has recrystallisation temperatures 20 - 40 K lower than that of obtained without boron (Fig.2.25) [30]. The solute drag mechanism is at the moment speculative and cannot explain the fact that recrystallisation can occur at relatively low temperatures in ordinary superalloys [89].

Local Inhomogeneities

The onset of recrystallisation may be due to local inhomogeneities in particle or solute content. Fig. 2.26 shows a particle free zone where recrystallisation has started. Fig. 2.27 shows high Cr content grains in an as-extruded sample of *MA6000* [30].

Particle alignment is a heterogeneity which has a strong effect on recrystallisation behaviour. Nes *et al.* introduced a modified model of Zener's pinning mechanism involving an inhomogeneous particle distribution [45]. The model showed the particle alignment induces elongated grain structure (Figs. 2.28, 29). In Fig. 2.28, a planar boundary intersects the particle aligned layers (hatched area) at an angle α within the equidistant parallel layers of thickness d and spacing l is the distance between layers. If there is enough driving force for boundary migration, the boundary becomes a jagged shape, and macroscopic shape is achieved Fig. 2.29.

There some interesting reports on zone annealing perpendicular to the extrusion direction (*i.e.* cross-annealing). One report shows there are highly elongated grain structure along the travel direction [76] but the other shows grains which are elongated along extrusion direction [77]. In the former case, equiaxed grain structures should be obtained by only isothermal annealing, however, in the latter case elongated grain structure should be obtained. Particle alignment is discussed in Chapter 4.

Boundary Mobility

The rapid progress of material through the zone annealing furnace gives better productivity. However, the speed should be slower than the migration velocity of secondary recrystallisation grains. Fig. 2.30 shows metallographic data of the effect of the specimen travel speed on recrystallised structures. Figs. 2.30 a-f are for *MA6000* [66] and Figs. 2.30 g-i are for a Ni-Cu alloy which undergoes primary recrystallisation [38]. In both cases, there is a critical velocity in which grain structures changes from equiaxed to elongated.

Baloch *et al.* showed that boundary mobility can be deduced using the transition velocity from elongated to an equiaxed grain structure (*MA6000*) [76]. The grain boundary velocity v during recrystallisation at a temperature T is given by [78]:

$$v = M\,[1 - \exp(-\Delta G / RT)] \qquad (2.7)$$

where M is the boundary mobility, ΔG is the effective driving force for recrystallisation and R is the universal gas constant. The Boundary mobility M is theoretically given by [78]:

$$M = \delta \upsilon \exp(-Q / RT) \qquad (2.8)$$

where δ and υ are the distance and atomic jump frequency across the boundary respectively, and Q is an activation energy for the atom transfer across the boundary. Then v is given by

$$v = \delta \upsilon \exp(-Q / RT)\,[1 - \exp(-\Delta G / RT)] \qquad (2.9)$$

Temperature Gradient

The temperature gradient is also important in order to obtain a highly elongated structure. Fig. 2.31 shows the effect of temperature gradient on the secondary recrystallisation structures of *TMO-2* (Fig. 2.31-a,b,c) [79] and primary recrystallisation of the Ni-Cu alloy (d,e) [38]. The greater temperature gradients induce more elongated grain structures. A large temperature gradient helps retard uniform grain coarsening (Fig. 2.32) [80]. In order to synthesise thermal effects such as traveling speed and temperature gradient, the concept of kinetic strength has been introduced. This was originally proposed by Holloman and Jaffe, who suggested that for an isothermal heat treatment (at temperature T for time period t), the kinetic effect should be related to the $t \exp(-Q/RT)$, where Q is an effective activation energy [81]. If temperature is a function of time, then the anisothermal annealing effect B can be as follows:

$$B = \int t \exp(-Q/RT)\, dt \qquad (2.10)$$

Baloch *et al.* have applied the concept of kinetic strength to zone annealing, and showed that a minimum kinetic strength is needed to complete recrystallisation [78]. Mino *et al.* showed that the kinetic strength can describe the dependence of recrystallisation temperature on heating rate in *MA956,* which is an iron base ODS alloy [82].

Texture

Strong crystallographic textures develop during the recrystallisation of ODS alloys, as shown in Table 2.4 [83]. Texture can be very complicated [83,84]. For example, Chou *et al.* show the relationship between the as-deformed and recrystallised textures in ODS steels *MA956* and *MA957* [85]. On the other hand, in *MA6000,* in spite of the absence of strong texture in the as-received (as primary recrystallised) condition, a strong [110] fiber texture develops during secondary recrystallisation [86]. It is also reported that for *MA6000,* in spite of the absence of textures as measured using X-ray diffraction, 10 - 25 % of the grains have [110] within 10° of the extrusion direction [87].

Table 2.4 Crystallographic texture in recrystallised coarse grained ODS alloys [83]

Alloy	Heat treatment	Experimental	Texture
MA 6000	Zone annealed	TEM, SAD, Laue	[110]
MA 6000	Zone annealed	Diffractometer	(031)[013]
MA 754	Isothermally annealed at 1200 °C	TEM SAD	[100]
MA 754	Not reported	Not reported	(011)[100]
MA 956 (sheet)	Isothermally annealed at 1200 °C	Laue	(125)
MA 956 (bar)	Not reported	Not reported	(332)[113]

2.3.3 Effect of Pre-Working

Isothermal Forging

In practical procedures such as turbine blade production, there are one or more procedures before the annealing heat treatment, in order to produce the shape of the blade. Blades should have a hollow structure to circulate cooling air and the wall thickness must be very thin. It is impossible to fabricate this shape after directional recrystallisation (machining alone can do but is very expensive) therefore hot forging is necessary before recrystallisation.

Nickel base superalloys involving a large amount of γ' are impossible to forge at high speed. Isothermal (materials and also dies are heated to the relevant temperature) hot forging at low speed is necessary, the forging time being about 30 min. Researches on the effect of hot forging on subsequent recrystallisation report that the higher temperature, the lower speed and the larger deformation yield a decreasing ability for recrystallisation. A good condition for forging is a bad condition for recrystallisation [88].

The total amount of deformation due to forging also strongly affects recrystallisation behaviour. There is perhaps an optimum amount and quality of stored energy for the recrystallisation to give an elongated grain structure. If extra dislocations are introduced into the primary recrystallised grains, stored energy becomes allowable for uniform grain growth. Fig. 2.33 shows TEM micrographs after hot deformation of an as-extruded alloy *TMO-2* [88]. The more heavily deformed area has the larger grain structure. The optical microstructure of tensile test specimen shown in the figure are the structures of deformed and subsequently annealed (at 1300 ° C) sample. The deformed area has no ability for recrystallisation and the non-deformed area alone recrystallised. Fig. 2.34 quantitatively illustrates this grain growth during the hot deformation of *MA6000* [90].

Pre-annealing

There is decreasing tendency for recrystallisation in samples which are heated without forging. Fig. 2.35 shows the effect of pre-annealing on subsequent recrystallisation [91]. The higher temperature and the longer time pre-annealing reduces the ability for recrystallisation. Fig. 2.36 illustrates the effect of pre-annealing on the recrystallised grain size [92]. As increasing holding time leads to an increase in grain size following by a sudden decrease. This may be explained in terms of primary grain coarsening. The present research shows that the effect of pre-annealing is not so simple (Chapter 5). Fig. 2.37 shows the effect of heating rate on recrystallised grain size [93].

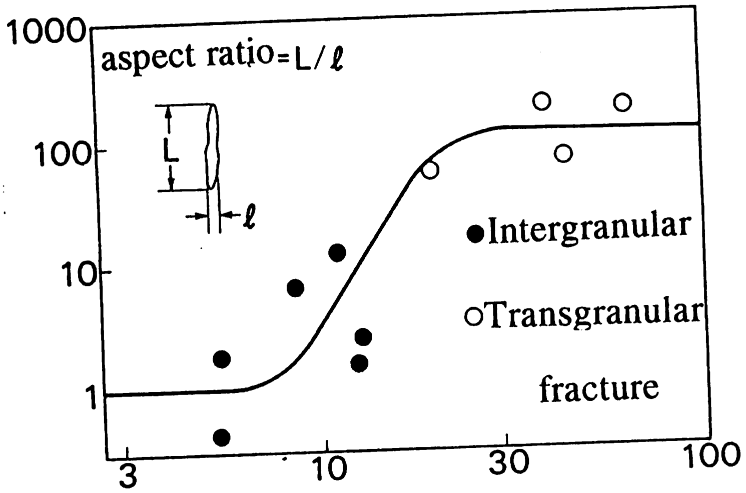

Fig. 2.18 Creep rupture lives at 1311 K as a function of grain aspect ratio in *MA6000* [36].

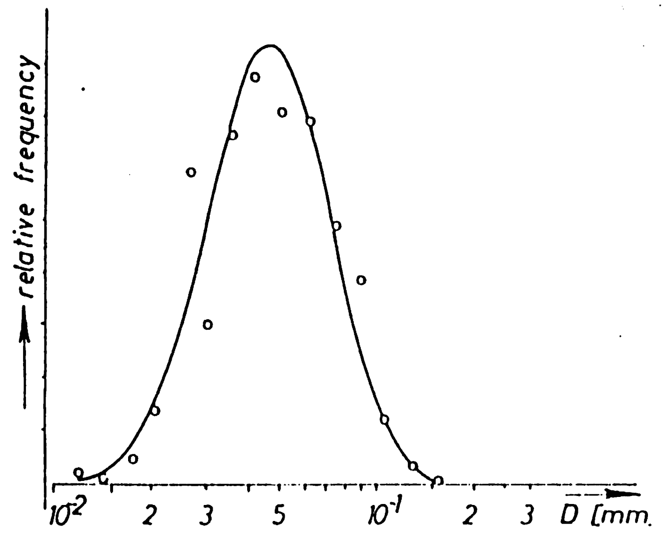

Fig. 2.19 Distribution of grain sizes in a primary recrystallised Fe -3 % Si steel [43].

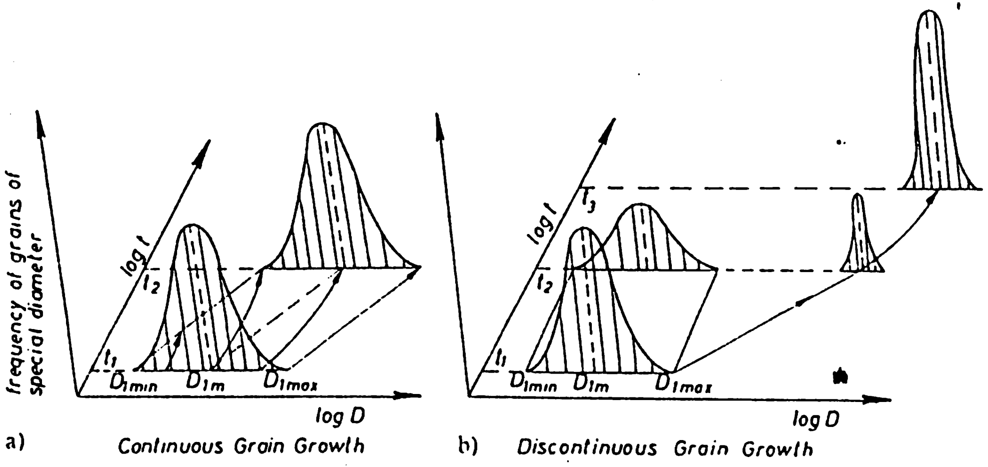

Fig. 2.20 Schematics of continuous and discontinuous grain growth [44]. *t* stands for annealing time and *D* stands for grain diameter.

a: Continuous grain growth

b: Discontinuous grain growth

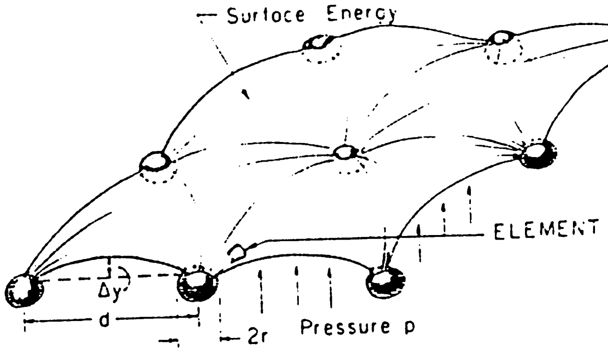

Fig. 2.21 Schematic drawing of the interaction between a grain boundary and small particles [45].

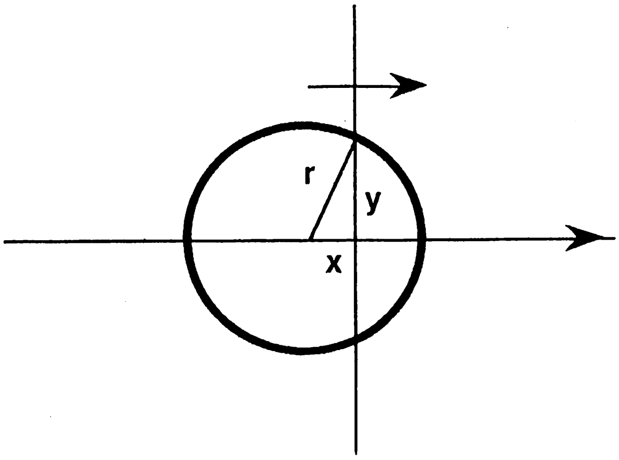

Fig. 2.22 Interaction between a grain boundary and a spherical particle [46].

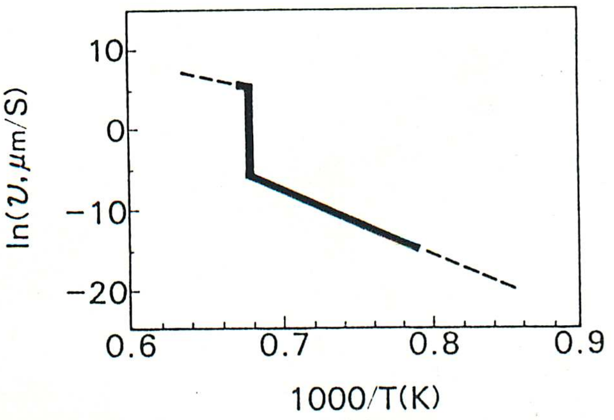

Fig. 2.23 The grain boundary migration rate v as a function of temperature in *MA6000* [64].

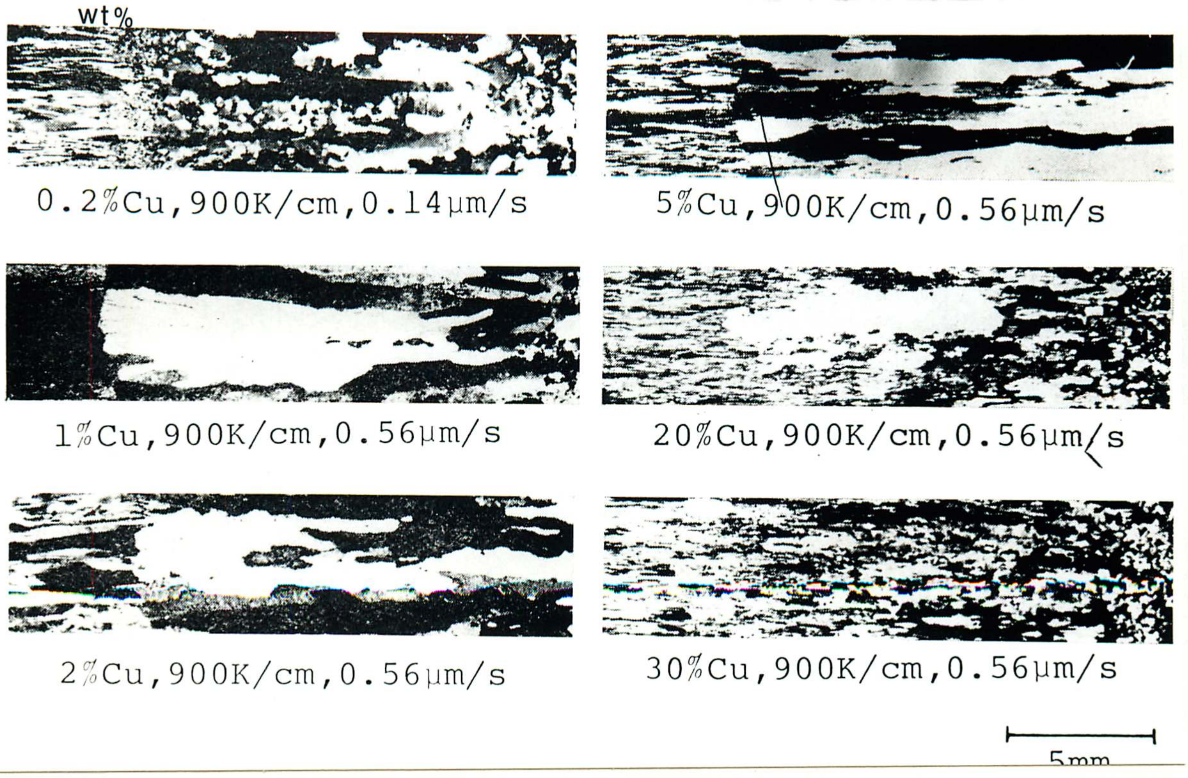

0.2%Cu,900K/cm,0.14μm/s

5%Cu,900K/cm,0.56μm/s

1%Cu,900K/cm,0.56μm/s

20%Cu,900K/cm,0.56μm/s

2%Cu,900K/cm,0.56μm/s

30%Cu,900K/cm,0.56μm/s

Fig. 2.24 The effects of the amount of Cu on recrystallisation in Ni-Cu alloys [65].

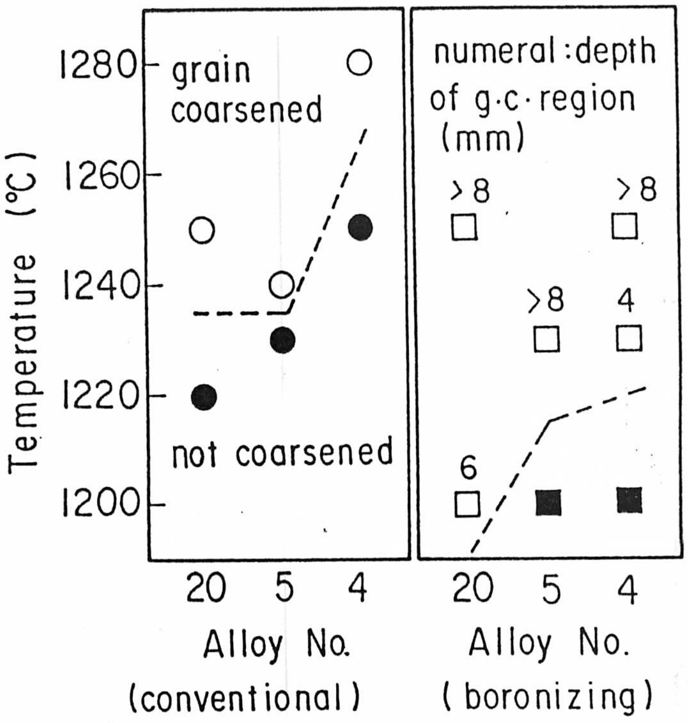

Fig. 2.25 The effects of boronising on abnormal grain growth temperature [30].

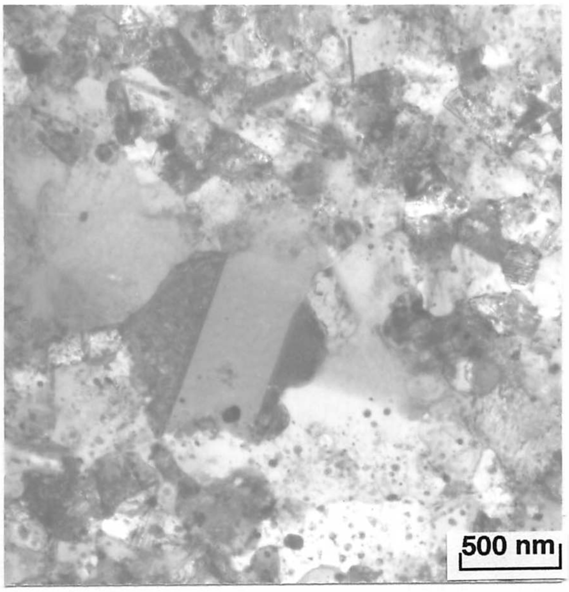

Fig. 2.26 The early stage of recrystallisation in *MA6000*. Annealed and strained (16 %) at 1453 K [30].

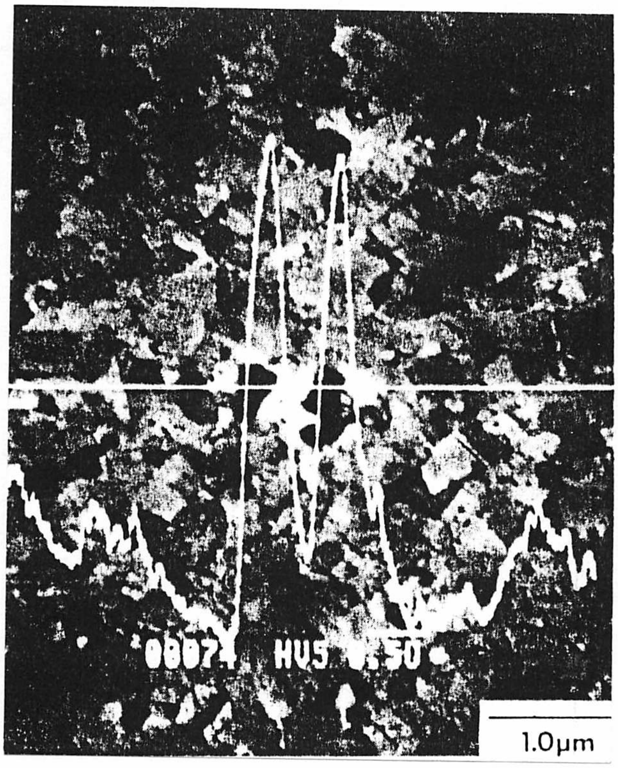

Fig. 2.27 High Cr content grains in the as-extruded *MA6000*. White line in the figure is Cr line analysis [30].

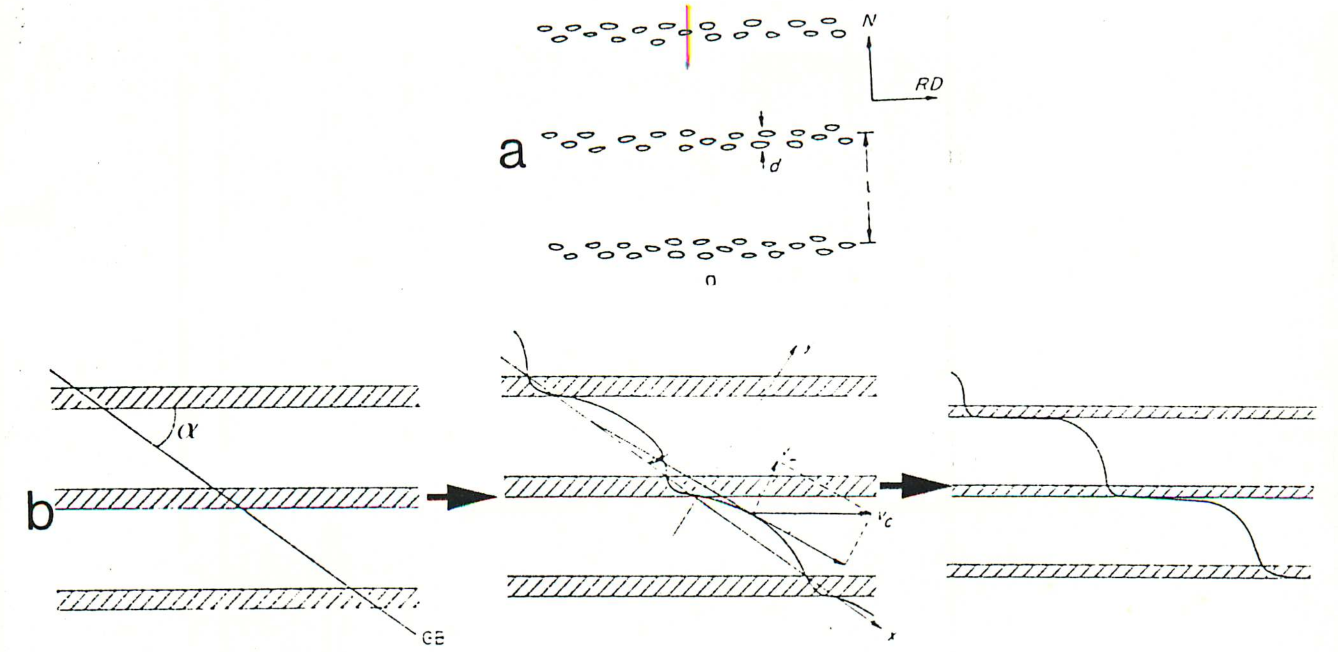

Fig. 2.28 a: Alternative geometries of a boundary moving at an angle α with respect to the particle layers [45].
b: Particle layers.

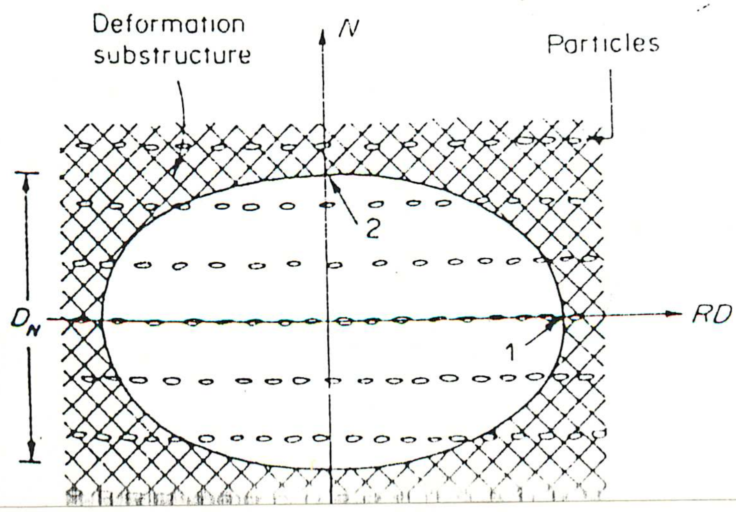

Fig. 2.29 Schematic diagram of a short transverse-longitudinal section of a recrystallised grain in a particle layered matrix [45].

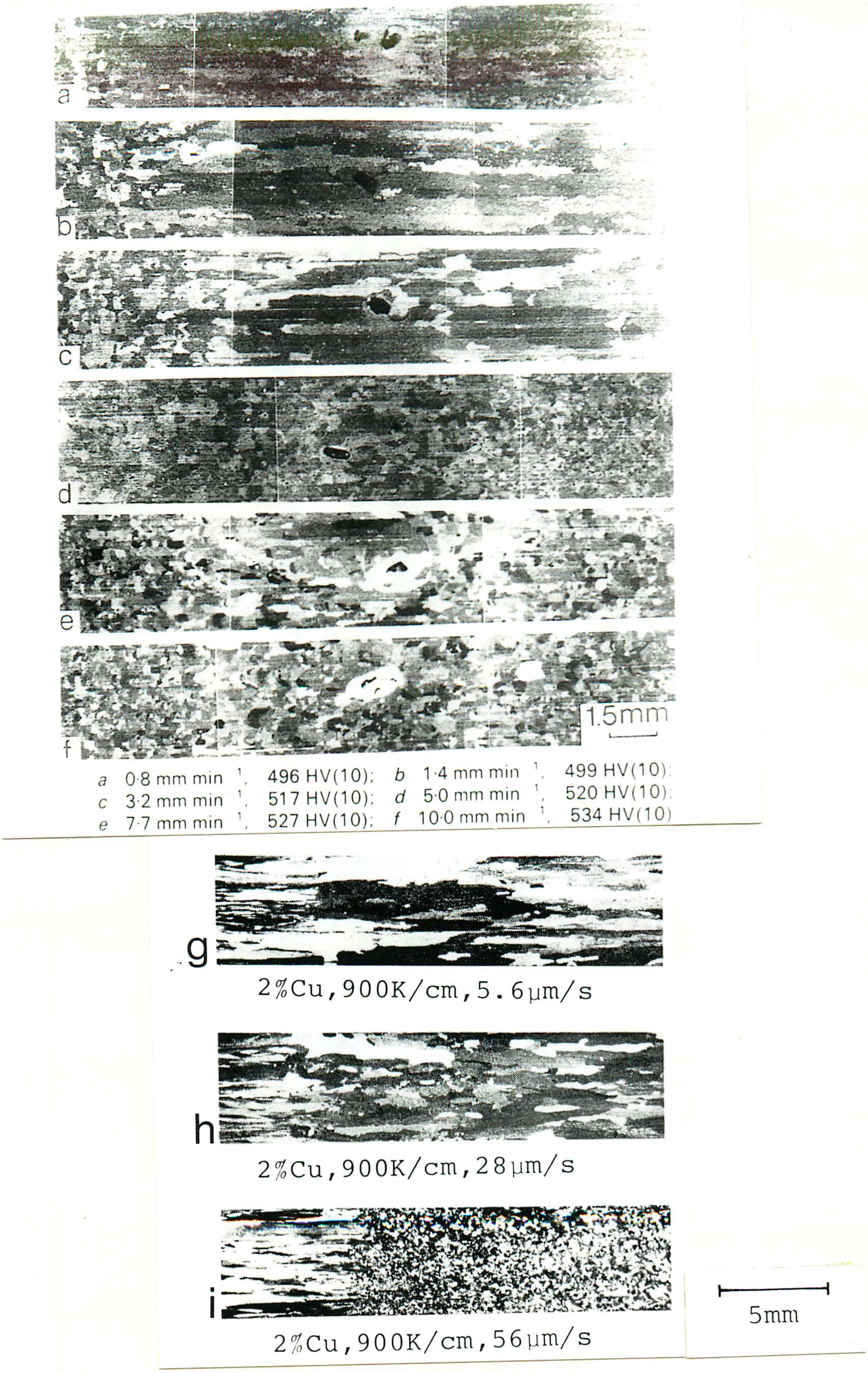

a 0·8 mm min^{-1}, 496 HV(10); *b* 1·4 mm min^{-1}, 499 HV(10);
c 3·2 mm min^{-1}, 517 HV(10); *d* 5·0 mm min^{-1}, 520 HV(10);
e 7·7 mm min^{-1}, 527 HV(10); *f* 10·0 mm min^{-1}, 534 HV(10)

2%Cu,900K/cm,5.6μm/s

2%Cu,900K/cm,28μm/s

2%Cu,900K/cm,56μm/s

Fig. 2.30 The effects of specimen traveling speed on microstructures obtained after zone annealing.
a~f: Secondary recrystallisation in *MA6000* [66].
g~i: Primary recrystallisation in a Ni - 2 wt % Cu alloy [38].

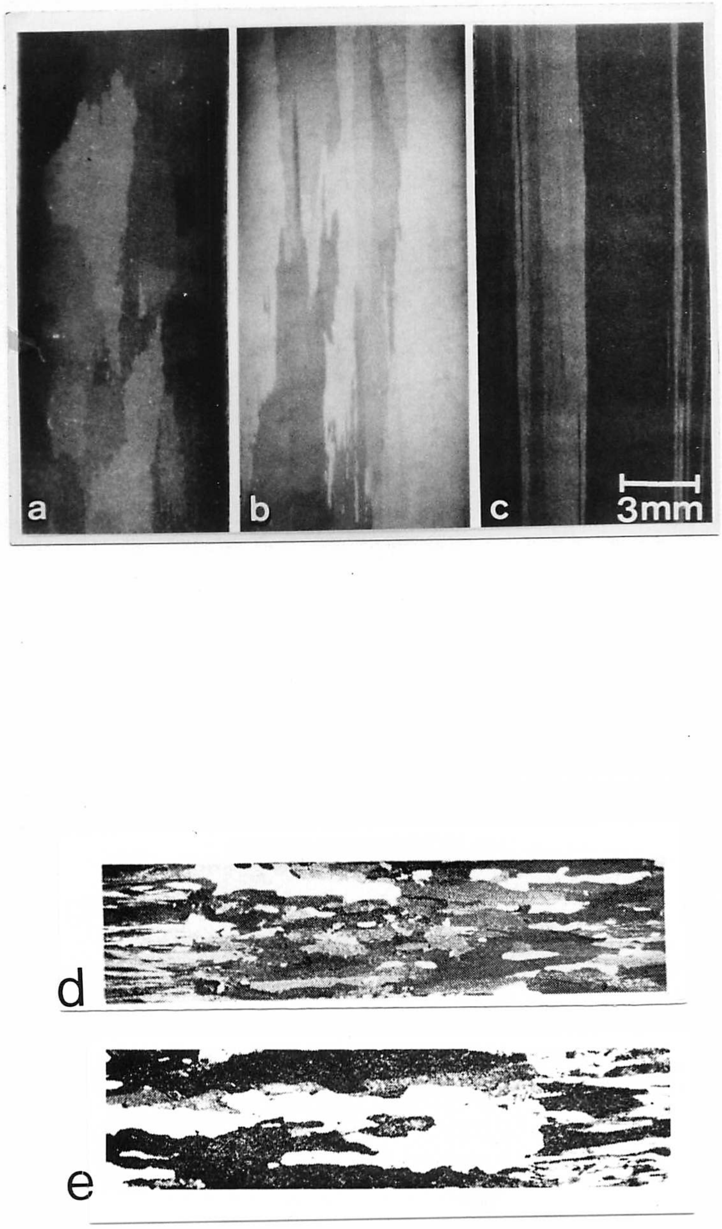

Fig. 2.31 The effects of temperature gradient on microstructures obtained after zone annealing.

a~c: Secondary recrystallisation in *TMO-2* [79].

d~e: Primary recrystallisation in a Ni - 2 wt % Cu alloy [38].

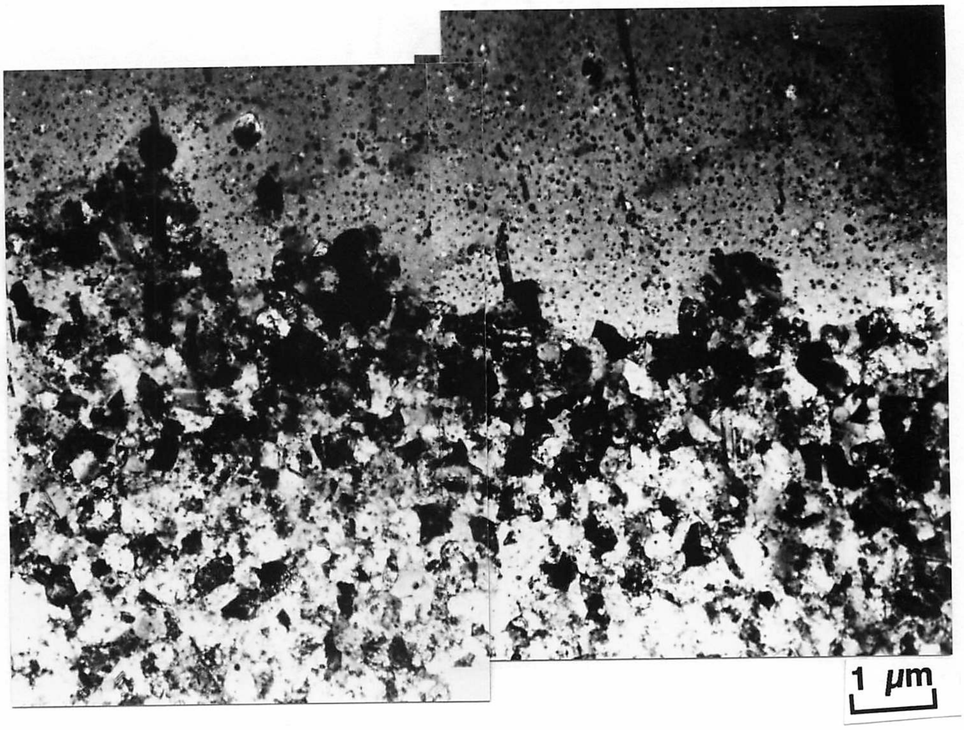

Fig. 2.32 TEM micrograph for the recrystallised / unrecrystallised interface in interrupted zone annealing *TMO-2* [80].

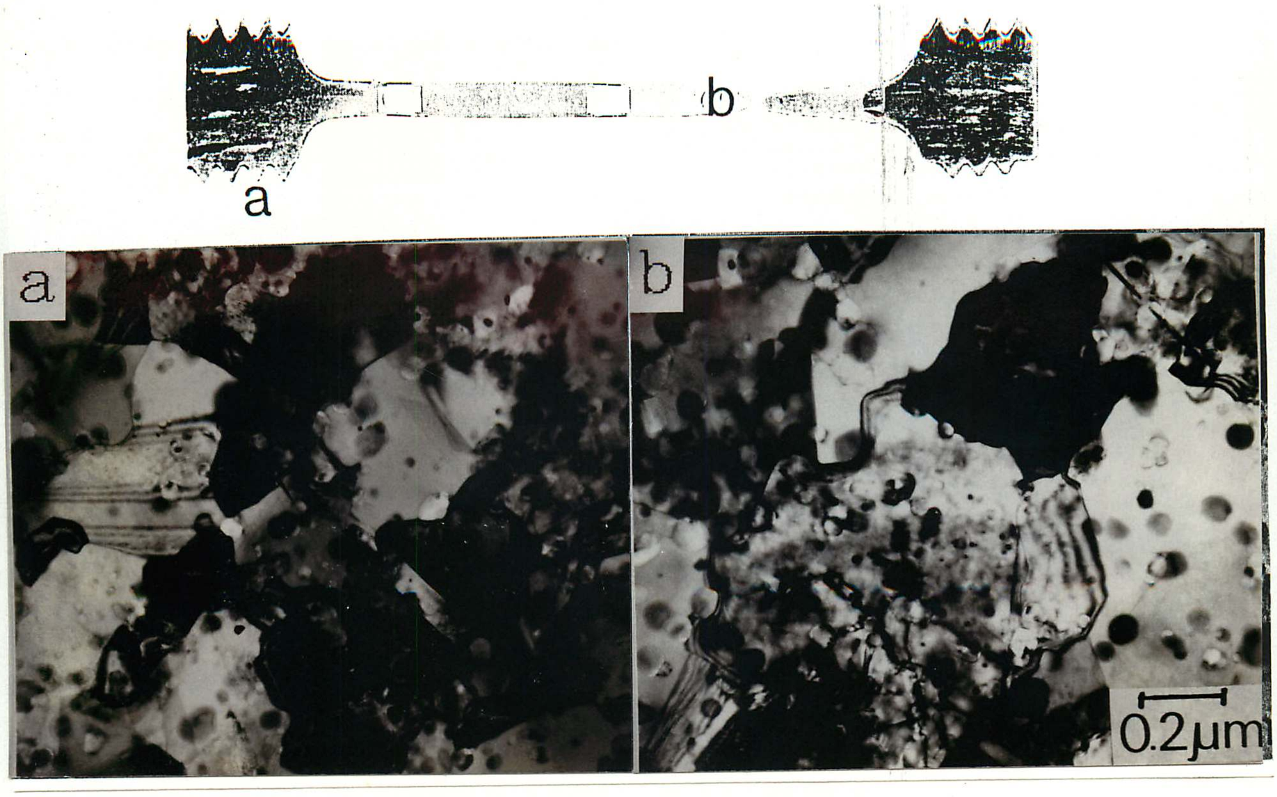

Fig. 2.33 The effects of hot deformation strain rate on microstructures in *TMO-2* [89].

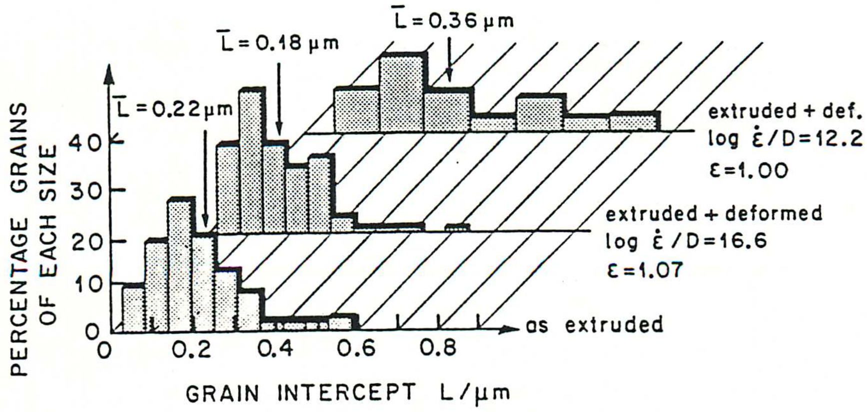

Fig. 2.34 Grain size distributions as a function of deformation condition in *MA6000* [90].

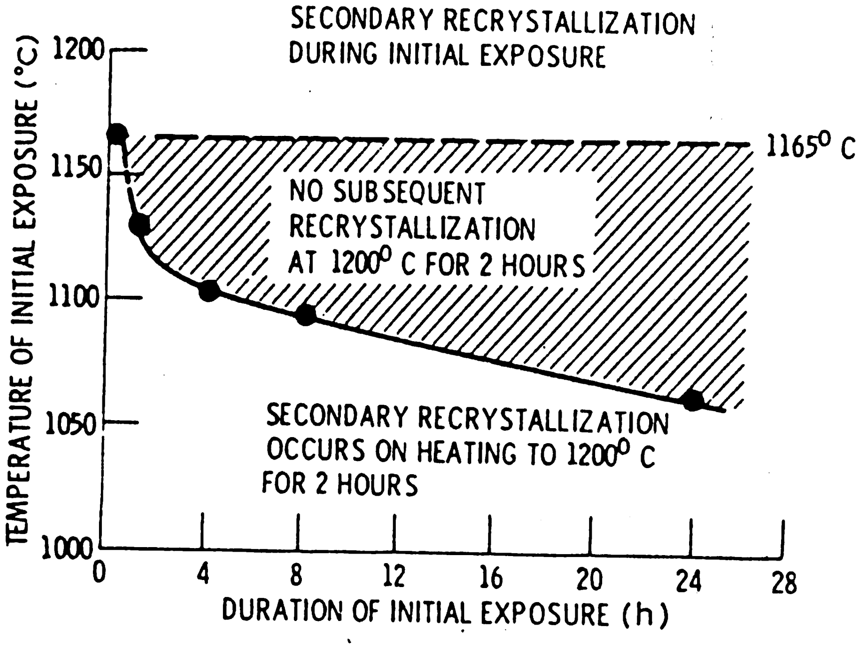

Fig. 2.35 The effects of initial exposure time and temperatures on the relationship of secondary recrystallisation capability in *MA6000* [91].

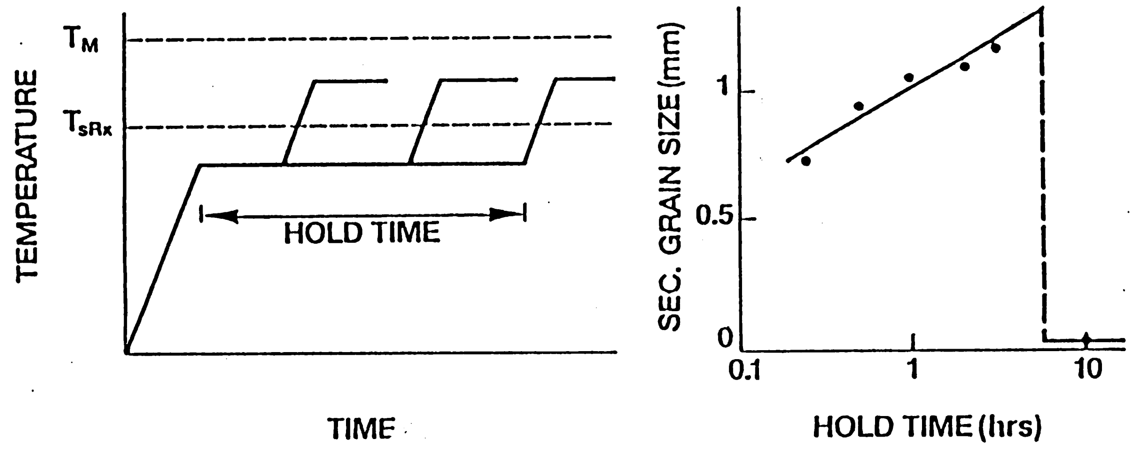

Fig. 2.36 Grain sizes (longitudinal) as a function of the holding time at 1373 K in *MA6000*. The final annealing temperature is 1523 K [92].

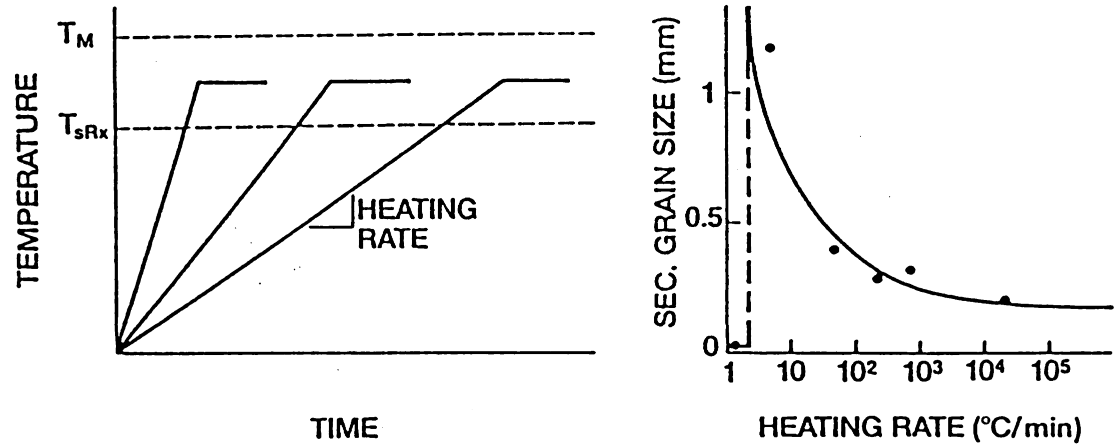

Fig. 2.37 Grain sizes (longitudinal) as a function of the heating rate in *MA6000*. The final annealing temperature is 1523 K [93].

2.4 *MA6000*

2.4.1 Introduction

MA6000 is an representative ODS nickel base superalloy. Its chemical composition is shown in Table 2.5. Several physical characteristics are shown in Table 2.6 [94]. *MA6000* has been specially designed for high temperature use in applications of turbine blades. However, the mechanical properties at elevated temperatures are not found to be adequate. Creep strength beyond 1000 °C is excellent, but at lower temperatures it is less than those of modern single crystals. This is because that total amount of fine γ' is not so large. If the amount of fine γ' could be increased, the creep strength could in principle be improved. However, an increase γ' phase fraction raises the γ' dissolution temperature, so that the production of elongated grain becomes difficult.

2.4.2 Microstructure

After directional recrystallisation, a very elongated recrystallised grain structure is obtained. The mean size of γ' after recrystallisation is about 200 - 300 nm. Before recrystallisation annealing there are several tens of nm sized particles dispersed in the matrix. Not only Y_2O_3 oxide added at the stage of mechanical alloying, but also Y_3Al_5O, $YAlO_3$ hexagonal, $Y_4Al_2O_9$, $YAlO_3$ pervoskite, and several kinds of carbides such as $M_{23}C_6$, Ti(C,N) are found [66,67,94]. However, after directional recrystallisation oxides composition or morphology changing : there are not $Y_4Al_2O_9$ and almost all oxide particles have crystallographic orientation relationships except $YAlO_3$. Fig. 2.38 illustrates the distribution in the particles (kinds of oxide particles are not distinguished) of as-extruded and after zone annealing [67]. It is shown that larger particles are increased after zone annealing. Fig. 2.39 illustrates the relationships between particle size distributions and subsequent annealing after zone annealing [67].

Table 2.5 Chemical composition of *MA6000* as used in this research (wt %)

C	Cr	Al	Ti	Ta	Mo	W	Zr
0.058	14.96	4.44	2.28	1.97	1.96	3.91	0.13
Si	Mn	P	S	Fe	V	Y_2O_3	Ni
0.08	0.01	0.006	0.001	1.49	0.01	1.08	bal.

Table 2.6 Several physical characteristics of *MA6000*

γ' (vol. %)	Density (kg m^{-3})	Solvus (K)	Solidus (K)
52	8.11	1438	1596

These figures show that oxides in superalloys are not so thermally stable and it can be coarsening and changing in composition at least higher than 1100 ° C.

2.4.3 High Temperature Properties

Creep

Fig. 2.40 shows 10^3 hours rupture strength in *MA6000* compared with other modern important casting nickel base superalloys [95]. *MA6000* has superior creep strength, but not at temperatures lower than others 880 ° C. More data on the creep strength of *MA6000* are shown in Fig. 2.41. in which the applied stress is illustrated as a function of creep rupture time and temperature [96].

Fatigue

Fig. 2.42 shows the low cycle fatigue properties [97]. *MA6000* is rather stronger than the best directionally solidified super alloys. The yield stress of *MA6000* at 760 °C is comparable to the directionally solidified *MarM200. MA6000* has a longer fatigue life at the same plastic strain. Fig. 2.43 illustrates the dependence of fatigue crack growth rate on the direction of the material [98]. The growth rate normal to the grain elongated direction is higher than that of parallel. Fig. 2.44 shows thermal fatigue life (number of cycles to the first crack initiation) in a flowing bed test. *MA6000* ranks with other modern single crystal or directionally solidified super alloys [95].

High temperature corrosion resistance

Fig. 2.44 shows also that *MA6000* has high corrosion resistance and oxidation resistance. Fig. 2.45 illustrates sulphidation resistance for several superalloys in a burner rig test according to military code [95].

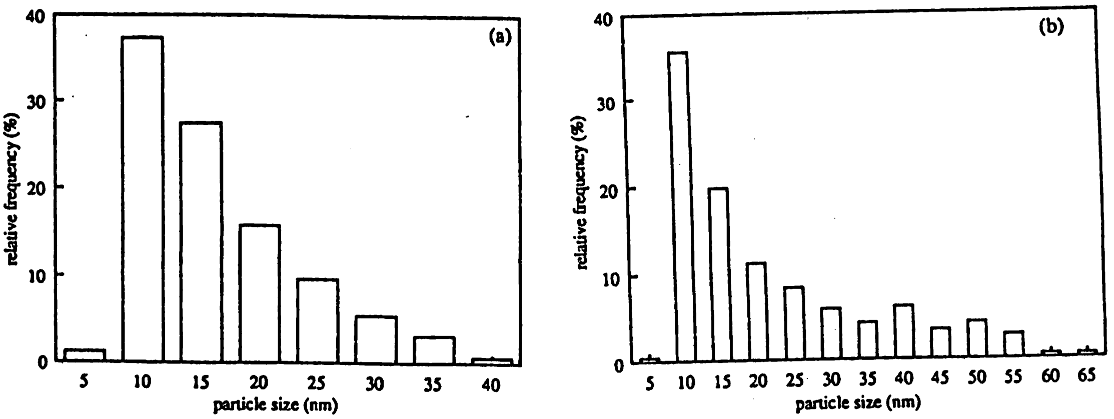

Fig. 2.38 Particle size distributions before (a) and after (b) zone annealing. There are fewer small particles and approximately 400 particles per material were used for counting [67].

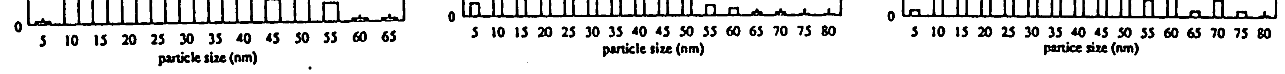

Fig. 2.39 Particle size distributions illustrating oxide coarsening at 1373 K. Approximately 400 particles per material were used for counting [67].

a: as-zone annealed.

b: annealed at 1373 K for 3000 h.

c: annealed at 1373 K for 10000 h.

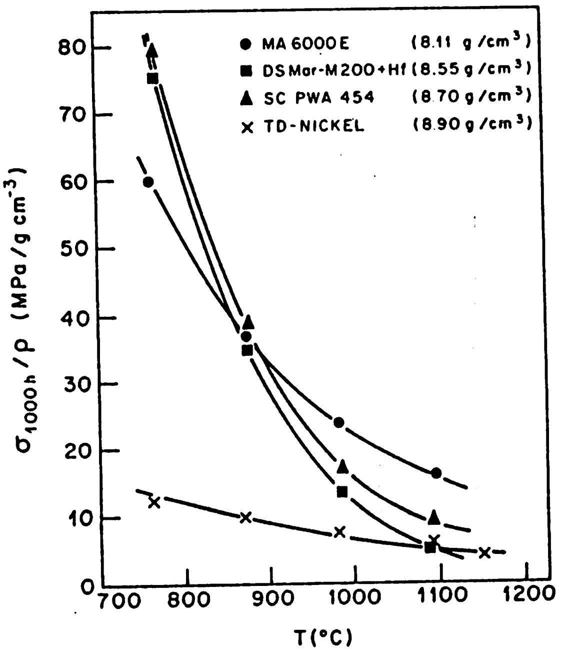

Fig. 2.40 Comparison of the 1000 h specific rupture strengths in *MA6000*, with those of several the most modern alloys [95].

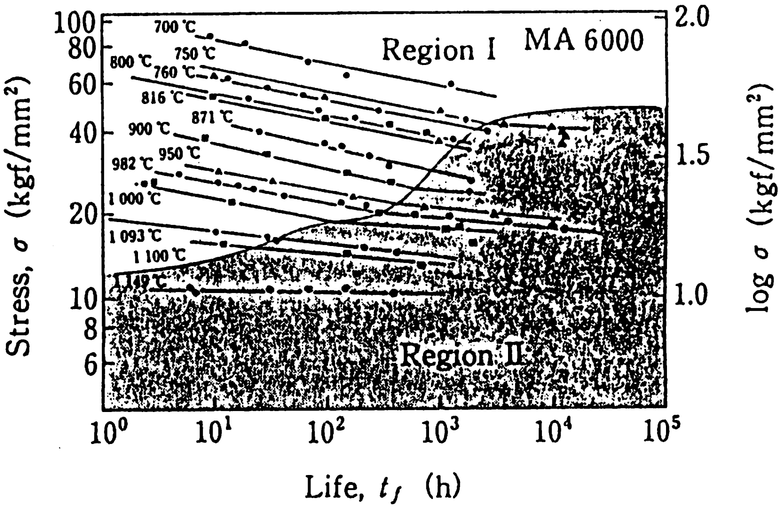

Fig. 2.41 Creep rupture strengths at various temperatures in *MA6000*. Two different line gradients are revealed [96].

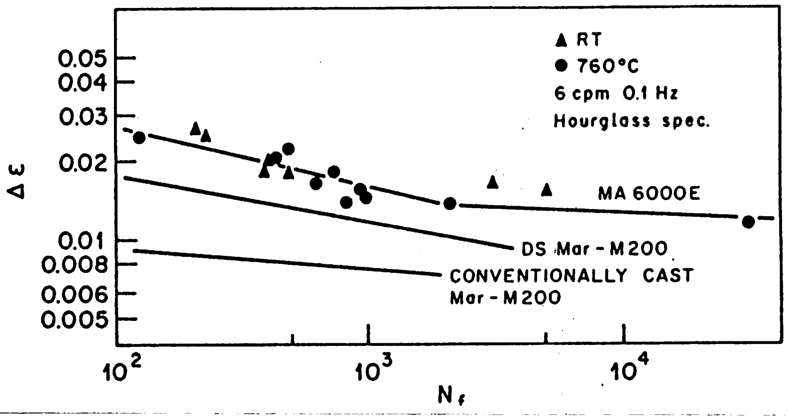

Fig. 2.42 Low cycle fatigue behaviours of *MA6000* compared with those of several the most modern cast alloys [97].

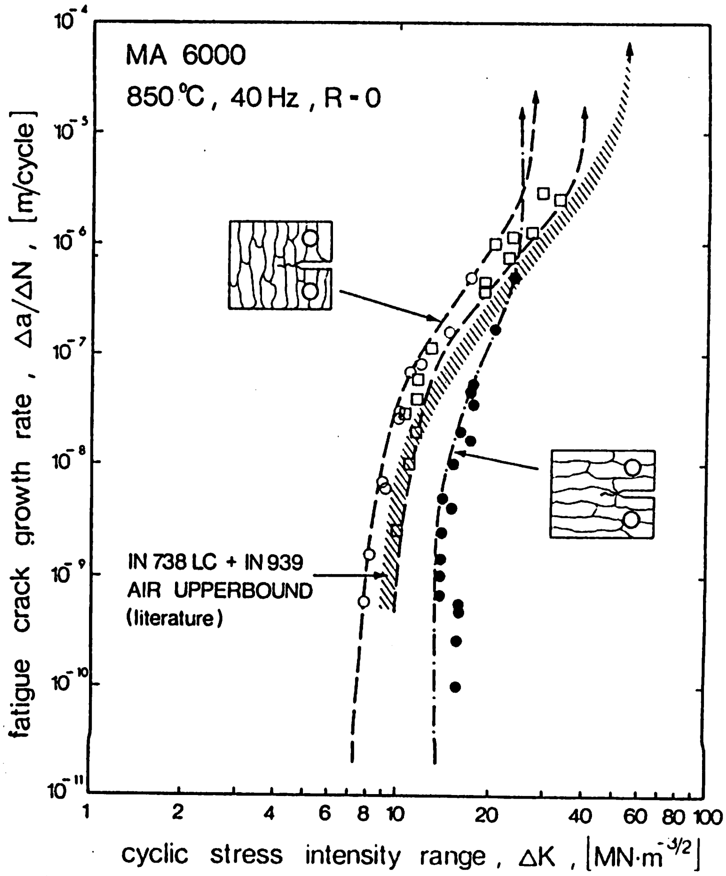

Fig. 2.43 Dependence of structural directions on cyclic crack propagation rates as a function of the cyclic stress intensity factor in *MA6000* [98].

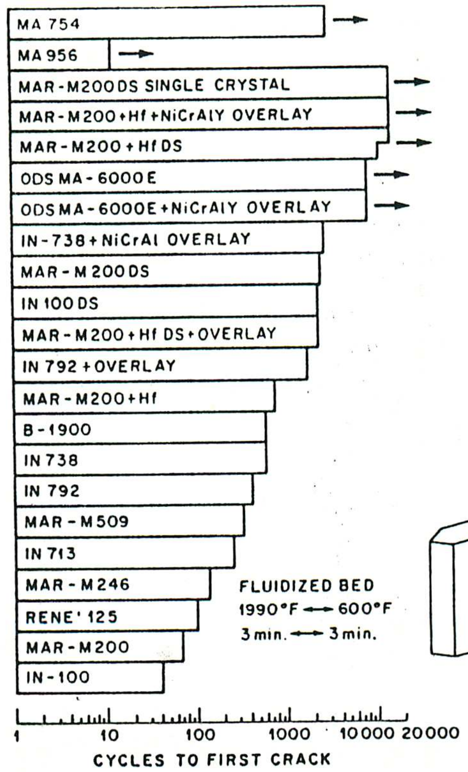

Fig. 2.44 Fluidised-bed thermal fatigue results for conventional superalloys and ODS superalloys (hatched) [95]. Arrows indicate that the lives are greater than the test cycles.

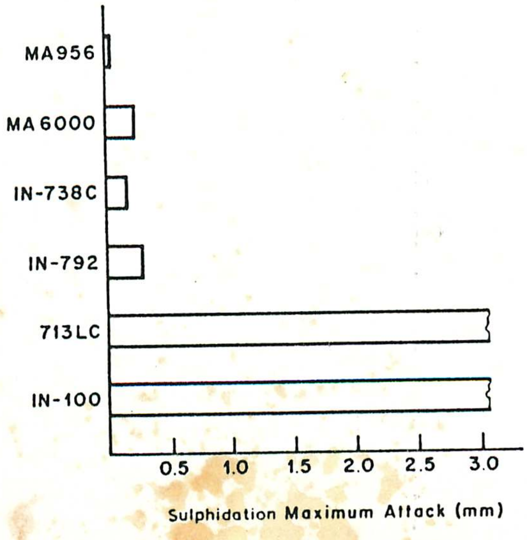

Fig. 2.45 Comparison of the corrosion resistance of *MA6000* with those of other superalloys. Testing conditions;
in 30.1 ratio of air and fuel (JP-5) with 5 wt% sea water at 1186 K for 312 h followed by 2 min air blast [95].

References

1. Gessinger G. H.: *Powder Metallurgy of Superalloys*, Butterworths Cambridge (1984) p. 8.
2. Kear B. H., Copplly S. M. and Versnyder F.L.: *Proceedings of International Conference on the Strength of Metals and Alloys*, (1968), **9**, p. 672.
3. Barrows R. G. and Newkirk J. B.: *Metall. Trans.*, (1972), **3**, p. 2899.
4. Yukawa N., Morinaga M., Murata Y. and Ezaki H.: *Superalloys 1988, Proceedings of International Symposium on Superalloys*, ed. by Dahl D.N. *et al.*, ASM, (1988), p. 225.
5. Sanchez J. M.: *Acta Metall.*, (1984), **32**, p. 1519.
6. Enomoto E., Harada H.: *Metall. Trans.*, (1989), **20A**, p. 649.
7. Harada H. : private communication, April (1992).
8. Benjamin J. S.: *Metall. Trans.*, (1970), **1**, p. 2943.
9. Benjamin J. S. and Bomford M. J.: *Metall. Trans.*, (1974), **5**, p. 615.
10. Benjamin J. S. and Volin T. E.: *Scientific American*, (1976), **234**, p. 40.
11. Benjamin J. S.: *Metall. Trans.*, (1970), **1**, p. 2943.
12. Smith C. S. and Grant N. J.: *Materials Science and Engineering*, (1987), **89**, p. 129.
13. *Handbook for High Performance Crystal Controlled Alloys Techniques,* Nihon Kikaku Kyoukai, ed. by M. Yamazaki, Japan, (1990), p. 167.
14. Sims C.T.: *Superalloys 1984, Proceeding of 5th International Symposium on Superalloys*, ed. by Gell M. *et al.*, ASM (1984), p. 399.
15. Gessinger G. H.: *Powder Metallurgy of Superalloys*, Butterworths, Cambridge, (1984), p. 328.
16. Kane R. D. and Ebert L. J. : *Metall Trans.*, (1971), **5**, p. 133.
17. Mclean M.: *Directionally Solidified Materials for High Temperature Service*, (1983), The Metal Society, p. 114.
18. Piercey B. J.: *Single Crystal Metallic Part U.S. Patent* No. 3 494 709 (1970).
19. Gell M., Duhl D. N., and Giamei A. F.: *Proceedings of the 4th International Symposium on Superalloys*, ed. by Tien J.K. *et al.*, ASM, (1980), p. 205.
20. Versnyder F. L. and Shank M. E.: *Materials Science and Engineering*, (1970), **6**, p. 213.
21. *The Art and Science of Growing Crystals*, ed. by Gilman J.J. *et al.*, John Wiley

Publishing Co., (1964), p. 415.

22. Mino K.: *Iron and Steel Japan,* (1989), **75**, p. 1580.
23. Kaiser H. F. and Taylor H. F.: *Tans. AIME,* (1939), **180**, p. 163.
24. Dunn C. G. and Walter J. L.: *Trans. AIME,* (1961), **221**, p. 221.
25. Philip T. V. and Lenhart P. E.: *Trans. A IME,* (1961), **221**, p. 439.
26. *Handbook for High Performance Crystal Controlled Alloys Techniques,* Nihon Kikaku Kyoukai, ed. by M. Yamazaki, Japan, (1990), p. 449.
27. *Handbook for High Performance Crystal Controlled Alloys Techniques,* Nihon Kikaku Kyoukai, ed. by M. Yamazaki, Japan, (1990), p. 171.
28. Cairns R. L., Curwick L. R. and Benjamin J. S.: *Metall. Trans.*, (1975), **6A**, p. 179.
29. Mino K. and Asakawa K.: *Trans. ISIJ,* (1987), **27**, p. 823.
30. Nakagawa Y.G., Terashima H. and Mino K.: *Proceeding of the 6th International Symposium on Superalloys,* (1988), ed. by Duhl D.N., p. 81.
31. Morse J. P. and Benjamin J. S.: *Materials Processing American Society for Metals*, Metals Park, Ohio, (1976), p. 165.
32. Gessinger G. H.: *Powder Metallurgy of Superalloys*, Butterworths, Cambridge, (1984), p. 328.
33. Redden T. K. and Barker J. F.: *Met. Prog.*, (1965), **87**, p. 107.
34. Singer R. F. Gessinger G. H. : P/M 82 Europe, Int. Powder Metallurgy Conf., (1982), p. 315.
35. Gessinger G.: H.: *Powder Metallurgy of Superalloys*, Butterworths Cambridge, (1984), p. 240.
36. Artz E. and Singer R. F.: *Superalloys*, ed. by Gell M., TMS-AIME, (1984), p. 369.
37. Allen R. E.: *Proceeding of 2nd International Conference of Superalloys*, Metals and Ceramic Information Center, (1972), p.X1.
38. Hamanaka H. and Miura I.: *Iron and Steel Japan,* (1984), **70**, p. 1857.
39. Avrami M. and Chem J.: *Physics,* (1939) **7**, p. 1103.
40. Avrami M. and Chem J.: *Physics,* (1940) **7**, p. 212.
41. *Recrystallization of Metallic Materials,* (1978), ed. by Hassner F., K. Hasselkus, Stuttgart, p. 12.
42. Feltham P.: *Acta Metall,* (1957), **5**, p. 97.

43. *Recrystallization of Metallic Materials*, (1978), ed. by Hassner F., p. 98.

44. *Recrystallization of Metallic Materials*, (1978), ed. by Hassner F., p. 99.

45. Nes E., Ryum N. and Hunderi O. : *Acta Metall*, (1985), **33**, p. 11.

46. Zenner C.: *Trans. AIME*, (1948), **175**, p. 5.

47. Gladman. T.: *Proc. Roy. Soc.*, (1966), **A294**, p. 298.

48. Ashby M.F., Harper J. and Lewis J.: *Trans. Met. Soc.* AIME, (1969), **245**, p.413.

49. Nes E.: *Metal Sci.*, (1979), **13**, 211.

50. Ryum N., Hunderi O. and Nes E.: *Scripta Metall*, (1983), **17** p. 1281.

51. Ashby M. F., and Centamore: *Acta Metall*, (1968), **16**, p. 1081.

52. Haessner F., Hornborgen E. and Mukerjee N. Z.: *Metallk*, (1966), **57**, p. 171.

53. Fullman R. L.: *Metal Interfaces*, (1952), American Society of Metals, Metals Park, Ohio, p. 179.

54. McLean D.: *Grain Boundaries in Metals*, (1957), Claredon Press, Oxford.

55. Hellman P. and Hillert M.: *Scand. J. Metall*, (1975), **4**, p. 211.

56. Hazzledine P. M., Hirsch P. B., and Louat N.: *Recrystallisation and Grain Growth of Multi-Phase and Particle Containing Materials.*, ed. by Hanson N. *et al.*, (1980), RisØ National Lab., Roskilde, Denmark. p. 159.

57. Louat N.: *Acta Metall.*, (1982), **30**, p. 1291.

58. Louat N.: *Phil. Mag.*, (1983), **47**, p. 903.

59. *Recrystallization of Metallic Materials*, (1978), ed. by Hassner F., Hasselkus, Stuttgart, p. 15.

60. Hillert M.: *Acta Metall.*, (1965), **13**, p. 227.

61. Littmann M. F. and Heck J. E.: *U. S. Patent, 2559340,* (1952).

62. Fujii K. and Hiraoka H.: *Iron and Steel Japan*, (1985), **71**, p. 1408.

63. Walter J. L.: *Trans.Met. Soc.* AIME, (1967), **239**, p. 272.

64. Alexander G. B., *et al.*: *U. S. Patent 2972908*, (1961).

65. Seltzer M. S. and Wilcox B. A.: *Metall. Trans.*, (1972), **3**, p. 2357.

66. Schaffer G. B., Loretto M. H., Smallman R. E. and Brooks J. W.: *Acta Metall.*, (1989), **37**, p. 2551.

67. Hotzler R. K. and Glasgow T. K.: *Metall. Trans.*, (1982), **13A**, p. 1665.

68. Mino K., Nakagawa Y. G., and Ohtomo: : *Metall. Trans.*, (1987), **18A**, p. 777.

69. Mino K.: *Proceeding of Plansee Seminar 1993*, Austria, Tyrol, (1993), in press.
70. Mino K. private communication. May, 1993.
71. Lucke K. and Detert K.: *Acta Metall.*, (1957), **5**, p. 628.
72. Cahn J. W.: *Acta Metall.*, (1962), **10**, p. 789.
73. Hillert M. and Sundman B.: *Acta. Metall.*, (1976), **24**, p. 731.
74. Hillert M.: *Met. Science*, (1979), March-April, p. 118.
75. Jongenburger C. P. and Singer R. F.: *Advanced Materials and Processing Techniques, for Structural Applications*, ed. by Khan T. and Lasaimoniet A., (1988), p. 339 .
76. Baloch M. M. Bhadeshia H. K. D. H.: *Mat. Sci. and Tech.*, (1990), **6**, p. 1236.
77. Hanada H. *et al.*: *Japan Institute of Metals Annual Meeting,* Spring (1992).
78. Christian J. W.: *Theory of Transformation in Metalls and Alloys, part 1, 2nd edition,* Pergamon Press, Oxford, (1975), p. 479.
79. *Handbook for High Performance Crystal Controlled Alloys Techniques,* Nihon Kikaku Kyoukai, ed. by M. Yamazaki, Japan, (1990), p. 493.
80. *Handbook for High Performance Crystal Controlled Alloys Techniques,* Nihon Kikaku Kyoukai, ed. by M. Yamazaki, Japan, (1990), p. 551.
81. Holloman J. H. and Jaffe L. D.: *Trans. AIME*, (1945), **162**, p. 223.
82. Mino K., Harada H. and Bhadeshia H. K. D. H.: *International Conference on Mechanical Alloying, Japanese Powder Metallurgy Foundation*, 6-10 May, (1991).
83. Gessinger G. H.: *Powder Metallurgy of Superalloys*, Butterworths, Cambridge, (1984) p. 219.
84. Chou T. S. and Bhadeshia H. K. D. H.: *Metall. Trans.*, (1993), **24 A**, p. 773 .
85. *Recrystallization of Metallic Materials*, (1978), ed. by Hassner F., p. 105.
86. Marsh J. M. and Martin J. W.: *Mat. Sci. and Tech.*, (1991), **7**, p. 193.
87. *Handbook for High Performance Crystal Controlled Alloys Techniques,* Nihon Kikaku Kyoukai, ed. by M. Yamazaki, Japan, (1990), p. 439.
88. *Handbook for High Performance Crystal Controlled Alloys Techniques,* Nihon Kikaku Kyoukai, ed. by M. Yamazaki, Japan, (1990), p. 509.
89. Dahlen M., *Thermomechanical proceeding of powder metallurgy superalloys*, Doctoral Thesis, Dept. of Engineering Metals, Charmels University of Technology, Gothenburg, Sweden, 1980

90. Singer R. F. and Gessinger G. H.: *Metall. Trans.*, 1982), **13A,** p. 1463.

91. Jongenburger C. P. and Singer R. F.: *Advanced Materials and Processing Techniques, for Structural Applications*, ed. by Khan T. and Lasaimoniet A., (1989), p. 339.

92. *Handbook for High Performance Crystal Controlled Alloys Techniques,* Nihon Kikaku Kyoukai, ed. by M. Yamazaki, Japan, (1990), p. 171.

93. *Handbook for High Performance Crystal Controlled Alloys Techniques,* Nihon Kikaku Kyoukai, ed. by M. Yamazaki, Japan, (1990), p. 468.

94. *Inco Catalogue*, Inconel Alloy MA6000.

95. Benn R. C., Curwick L. R. and Hack G. A. J.: *INCO Technical Paper*, (1980), p. 1078.

96. Kim Y. G., and Merric H. F.: *NASA CR-159493*, May, (1979).

97. Gessinger G. H.: *Powder Metallurgy of Superalloys*, Butterworths, Cambridge, (1984) p. 267.

CHAPTER 3

EXPERIMENTAL TECHNIQUES

3.1 Alloy

The alloy (Table 3.1) was prepared at INCO ALLOYS Hereford by the mechanical alloying technique. This involves the ball milling of a mixture of nickel powder (particle size 4 - 7 μm) and powdered chromium, molybdenum, tungsten, tantalum, and master nickel base alloy powders containing the reactive elements aluminum, titanium, zirconium (particle size - 150 μm). The yttrium oxide is introduced into the mixture in the form of 1 μm aggregates, each consisting of numerous individual particles of size 20 - 40 nm with an average size of 25 nm.

The mechanically alloyed powder is then extruded using a mild steel canning material into 48 mm diameter bar, followed by hot-rolling (1040 °C) into 23 mm square bar. The normal commercial practice at this stage is to induce primary recrystallisation into an anisotropic grain microstructure, but for the present purpose, the alloy was supplied without having been given any heat treatment after hot - rolling.

Table 3.1 Chemical composition (wt %)

C	Si	Mn	P	S	Al	Co	Cr	Fe	Mo
0.058	0.080	0.010	0.006	0.001	4.440	0.220	14.96	1.490	1.960
N	Nb	Ni	O	Ta	Ti	V	W	Zr	Y_2O_3
0.200	0.05	bal.	0.670	1.970	2.280	0.010	3.190	0.130	1.080

3.2 Heat - Treatments

In order to understand the recrystallisation behaviour, various heat treatments were carried out. The three typical types of heat treatments are:

(1) Continuous heating: Heating from room temperature to various temperatures at a variety of heating rates, (2.5 - 40 K min^{-1}, Fig. 3.1 A).

(2) Isothermal annealing: Heating from room temperature to various temperatures at a constant heating rate (10 K min^{-1}), and keeping at the temperatures (Fig. 3.2 B).

(3) Pre-annealing: Heating from room temperatures up to various temperature at a constant heating rate (10 K min^{-1}) and annealing at that temperature which is below the recrystallisation temperature. This was followed by heating at a constant rate (10 K min^{-1}) up to 1300 ° C (Fig. 3.3 C).

Some variations in these heat treatments such as controlled cooling, were also used some experiments.

Almost all the heat treatments were performed using either a computer controlled resistance furnace or a differential scanning calorimeter (DSC) furnace. DSC is discussed later. The samples heat treated in the resistance furnace were settled in quartz tubes with argon gas; those treated in the DSC furnace were protected by He at a flow rate of 50 mm min^{-1}. Helium is preferred because it gives a fast cooling rate compared with Ar. The specimens were 5 mm square by 10 mm in length for the resistance furnace heat treatments, and 5 mm square by 3 mm in length for the DSC furnace. They were cut from the as-received bar (as extruded followed by hot rolling), which was 23 mm square and 1m in length.

3.3 Optical Microscopy

Metallographic samples were all cut on a plane parallel to the extrusion direction. They were hot mounted using an automatic press, and then mechanically ground down to the 1200 grade silicon carbide paper before mechanical polishing using 1μm diamond paste. The etchant was a mixture of 2g $CuCl_2$ in 40 ml HCl and 80 ml ethanol.

3.4 Transmission Electron Microscopy and Scanning Electron Microscopy.

Transmission electron microscopy (Phillips 400 T, 120 kV) was carried out on thin foils and carbon extraction replicas. The thin foils were cut in various directions from the heat treated samples. They were subsequently ground down to 0.05 mm by ablation on 1200 grit SiC coated paper and then electropolished using twin jet electropolisher below - 50 ° C. The polishing solution consisted of 5 % perchloric acid, 25 % glycerol and 70 % ethanol mixture. The voltage used was about 55 V.

Carbon extraction replicas are taken from optical microscopy specimens. Evaporated carbon films are peeled off from specimens in a 5 % hydrochloride and 95 % ethanol mixture using 1.5 V direct current electric dissolution. The carbon films were then scooped up on copper mesh and prepared for TEM observations.

Scanning electron microscope (CAMSCAN) was carried out same specimens as metallographic specimens at accelerate voltage 20 kV.

3.5 Composition Analysis

An energy dispersion X-ray analyser (EDX: Link system) with the TEM was carried out to identify chemical compositions of the heavy elements present in the fine particles. An electron probe micro analyser (EPMA: JEOL 6400) was also used for composition analysis.

X-ray identification of extracted residues was carried out using an X-ray diffraction analyser (RIGAKU GFX-RAD3C).

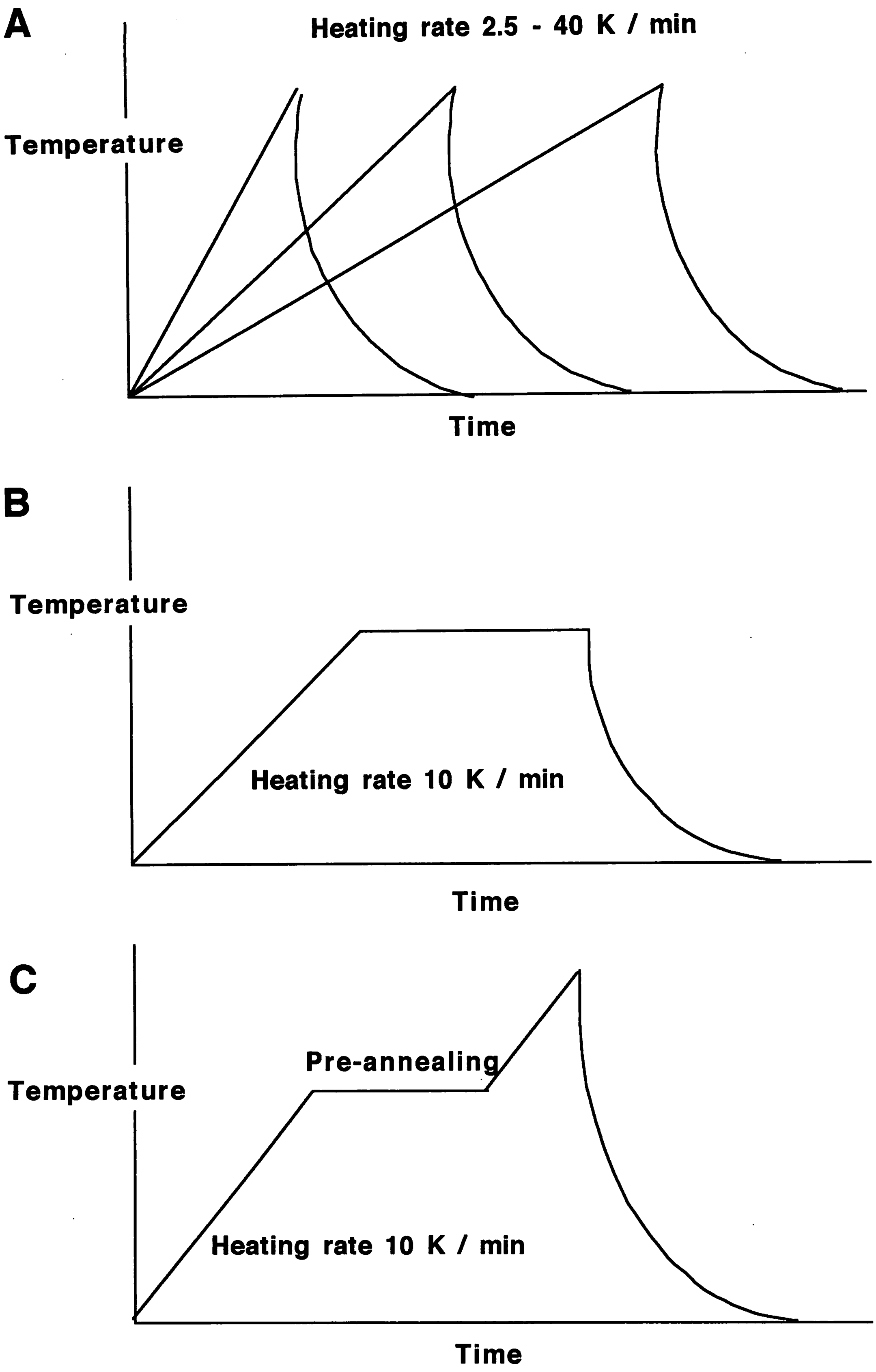

Fig. 3.1 Heat patterns;
A: Continuous heating at various heating rates
B: Isothermal annealing
C: Pre-annealing and subsequent annealing

3.6 Differential Scanning Calorimetry

Differential Scanning Calorimetry (DSC) was carried out using a Netzsch DSC404/3/413/D machine which is specially designed for operation at high temperatures. The equipment is a heat flux DSC with computer control and data acquisition (Fig. 3.2). It has a Pt/Rh furnace which has very low temperature gradient characteristics. The sample and reference are placed in thermally balanced Pt or aluminum crucibles. Any event leading to differences in heat evolution, or heat capacity between the sample and reference causes a signal, which can be interpreted to reveal thermodynamic data associated with the event. Experiments were carried out during continuous heating (1 - 99.9 K min^{-1}). A reference of mass comparable to the sample was used, made of either pure nickel or of the same alloy as the sample, but in an already recrystallised condition. This led to a very significant improvement in accuracy, consistent with earlier research [1].

Crucibles

Two kinds of crucible materials, pure platinum (Pt) and alumina (Al_2O_3), are available for the DSC. In general, Pt has a better thermal conductivity than alumina and hence a better sensitivity with respect to measurements. The platinum crucible is thus suitable for almost all measurements, but it has some defects as follows:

(1) The platinum crucible may react with some highly active materials such as liquid metals. ODS superalloy or steel recrystallisation temperatures are very close to their melting temperatures, so that partial melting may take place during measurement.

(2) The platinum crucible sometimes bonded to the sample-reference stage (which is a platinum alloy, Fig. 3.2) by diffusion at high temperatures (more than 1200 °C).

(3) The platinum crucible is very expensive. To obtain good heat flow, a crucibles must have plane bottom. Unfortunately, the platinum crucible is easily deformed during handling. A new crucible is normally necessary for every 10 experiments. The alumina crucible is stronger and cheeper. Normally it can be used for more than 50 experiments.

For these reasons, the alumina crucibles were mainly used in the present work to obtain data under stable conditions and to avoid fatal machine damage.

The Effects of Sample Size and Heating Rate

If the size of a sample or its thermal capacity is very large, then that uniform heating becomes difficult. Smaller samples lead to smaller temperature gradients, but the signal to noise ratio deteriorates. Fig. 3.3 shows the measured melting temperatures of pure gold (99.99wt%) as a function of sample weight. The thin line in the figure represents literature data [2]. The measured melting points are nearly constant in the weight range of 0.7 mg - 350 mg and slightly lower than the literature data, but the differences are very small, within 2.5 ° C. Latent heats as a function of sample weight are illustrated in Fig. 3.4, they are almost constant and consistent with literature data [2]. It can be said that the effect of sample mass on measurements is negligible, at least for simple reactions. Recalibration was carried out for temperature and sensitivity after every 100 measurements. The data shown in Figs. 3.3 and 3.4 were taken after 98 measurements since the previous calibration.

Further data with respect to sample weight are shown in Fig. 3.5. They illustrate some reactions in *MA6000* such as gamma prime dissolution recrystallisation start and finish, as a function of sample weight at the heating rates 10 and 20 K min^{-1}. The secondary recrystallised grain size in *MA6000* is very large, typically 200 μm in width and 2 - 3 mm in length, so that some size effects might be expected on recrystallisation. The smallest sample size measured was about 1 mm cube (35 mg) and the largest one was about 4 mm square and 3 mm in height (450 mg). Every sample was located in a crucible with the extrusion direction parallel to the vertical axis except for one sample (Fig. 3.6), whose data are marked with an asterisk. All reaction temperatures were found to be reasonably constant for the weight range considered. The sample direction within the crucibles did not appear to have any effect on the measurements. Fig. 3.7 shows original DSC peaks due to the recrystallisation of a small specimen (35 mg) and a large specimen (210 mg). The enthalpy change due to recrystallisation is very small (less than 1 J g^{-1}), and the signal/noise ratio (S/N ratio) for the small specimen is low by comparison with the larger one, often making the determination of reaction temperatures difficult. For these reasons, it is better to use larger specimens; those used in the present work were typically 200 - 300 mg.

The effects of heating rate on pure metal melting temperatures of gold, nickel and cobalt are shown in Figs. 3.8, 3.9 and 3.10 respectively. Fig. 3.11 illustrates the latent heats of fusion for pure gold as a function of heating rate. Every specimen weight was typically 200 mg, which was to be close to those of *MA6000* experiments. As expected, the measured melting temperatures increase with heating rate, the melting temperature differences between the slowest heating and the fastest heating is 4 K for gold, 8 K for nickel, 10 K for cobalt. Latent heats of pure gold were also almost constant within the range of heating rate 2.5 - 40 K min^{-1}.

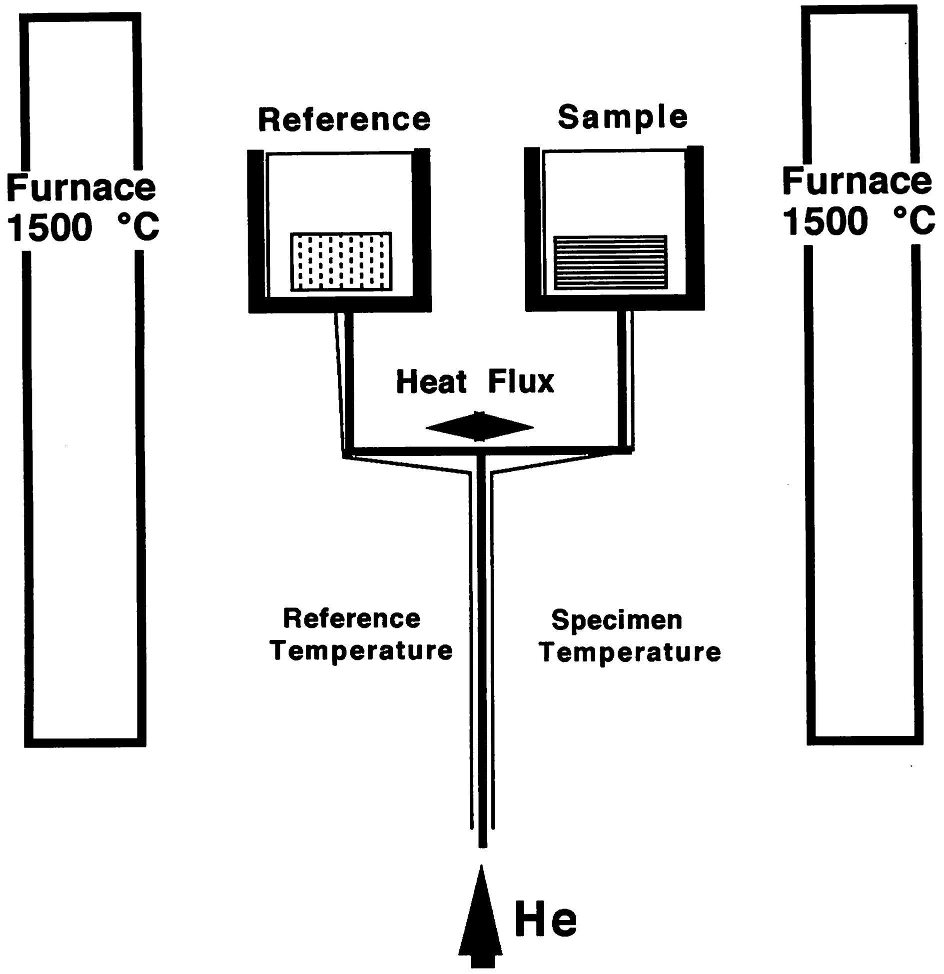

Fig. 3.2 Schematic drawing of a differential scanning calorimeter.

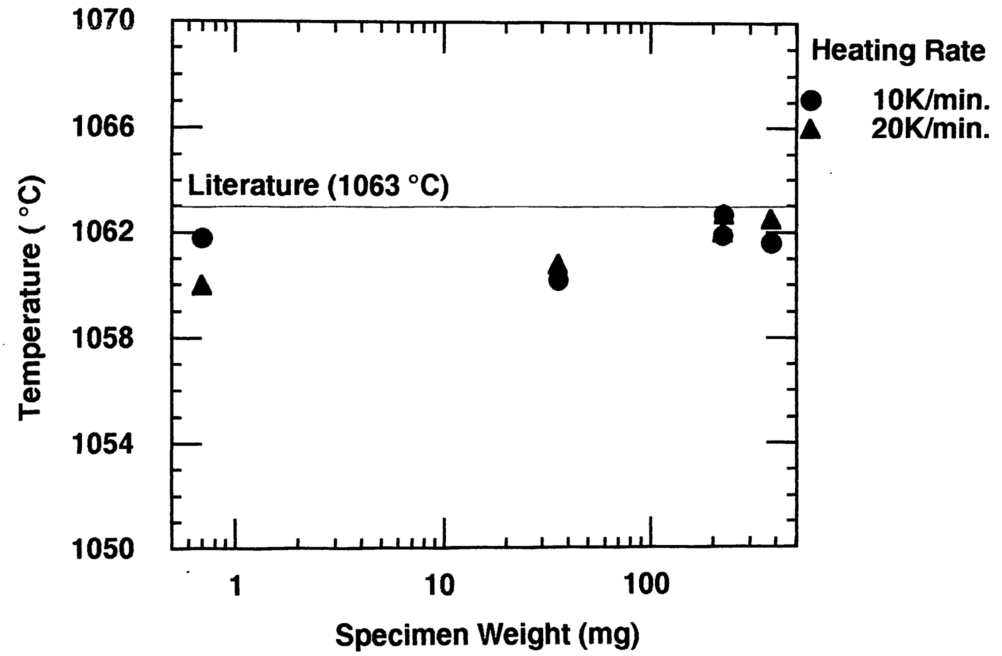

Fig. 3.3 Pure gold melting points measured by DSC as a function of specimen weight. Measurements were done after 98 experiments since the previous calibration.

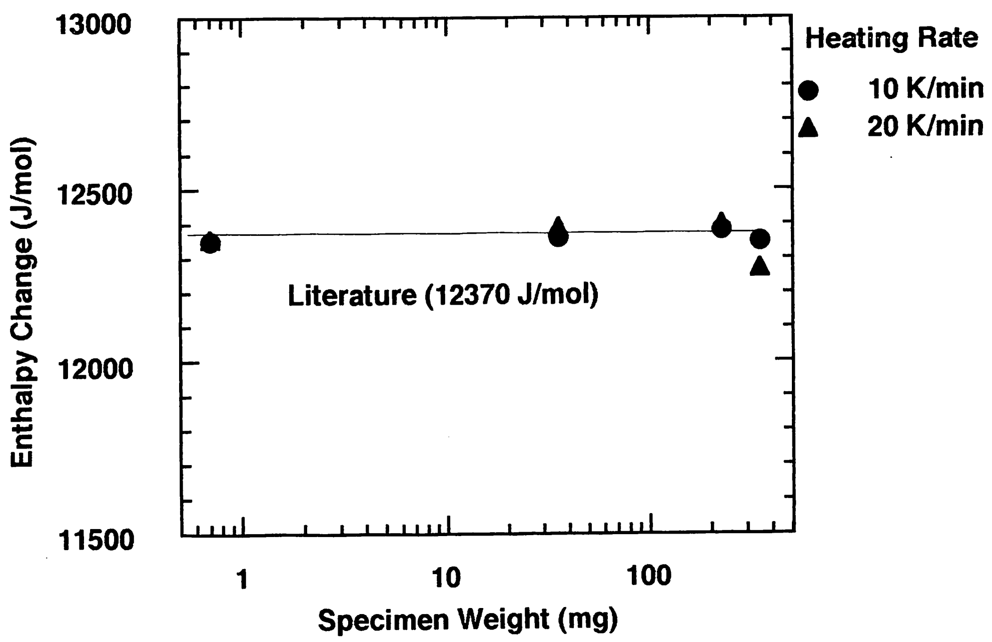

Fig. 3.4 Latent heat of fusion of gold measured by DSC as a function of sample weight.

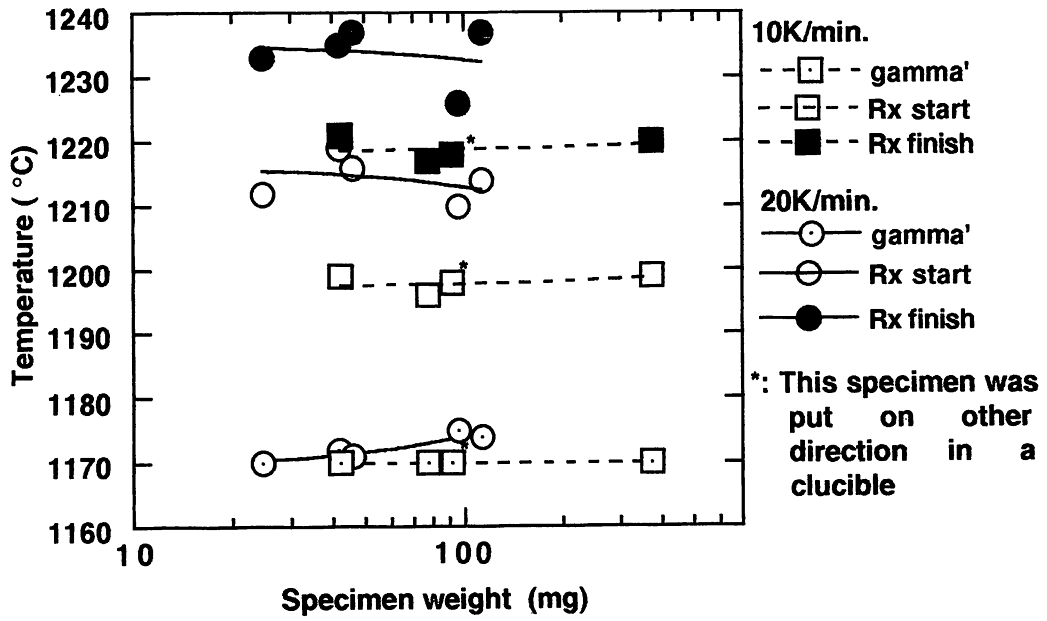

Fig. 3.5 Various reaction temperatures of *MA6000* as a function of specimen weight and heating rate. Rx stands for recrystallisation.

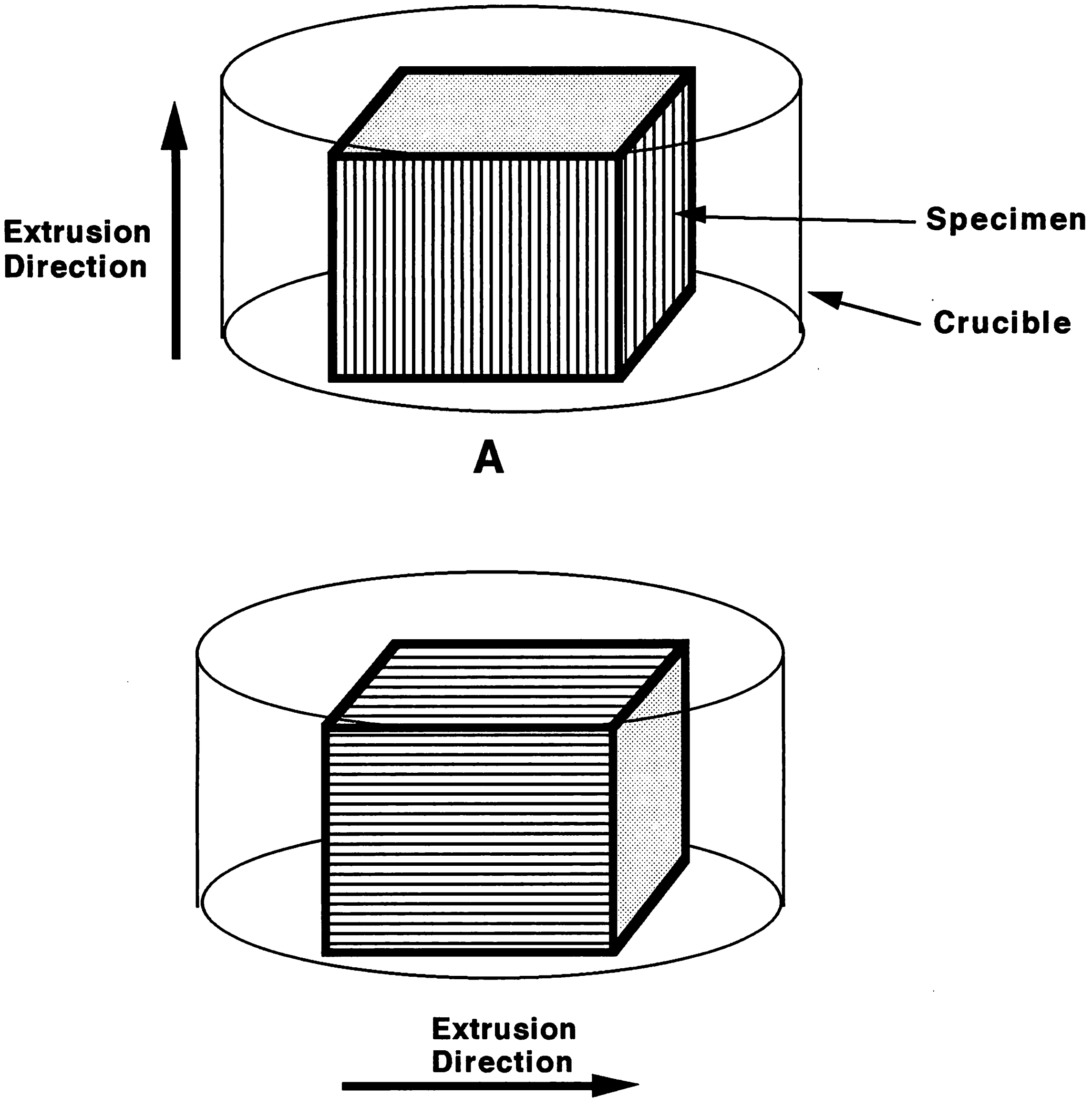

Fig. 3.6 Schematic drawing of sample locations in DSC crucibles.

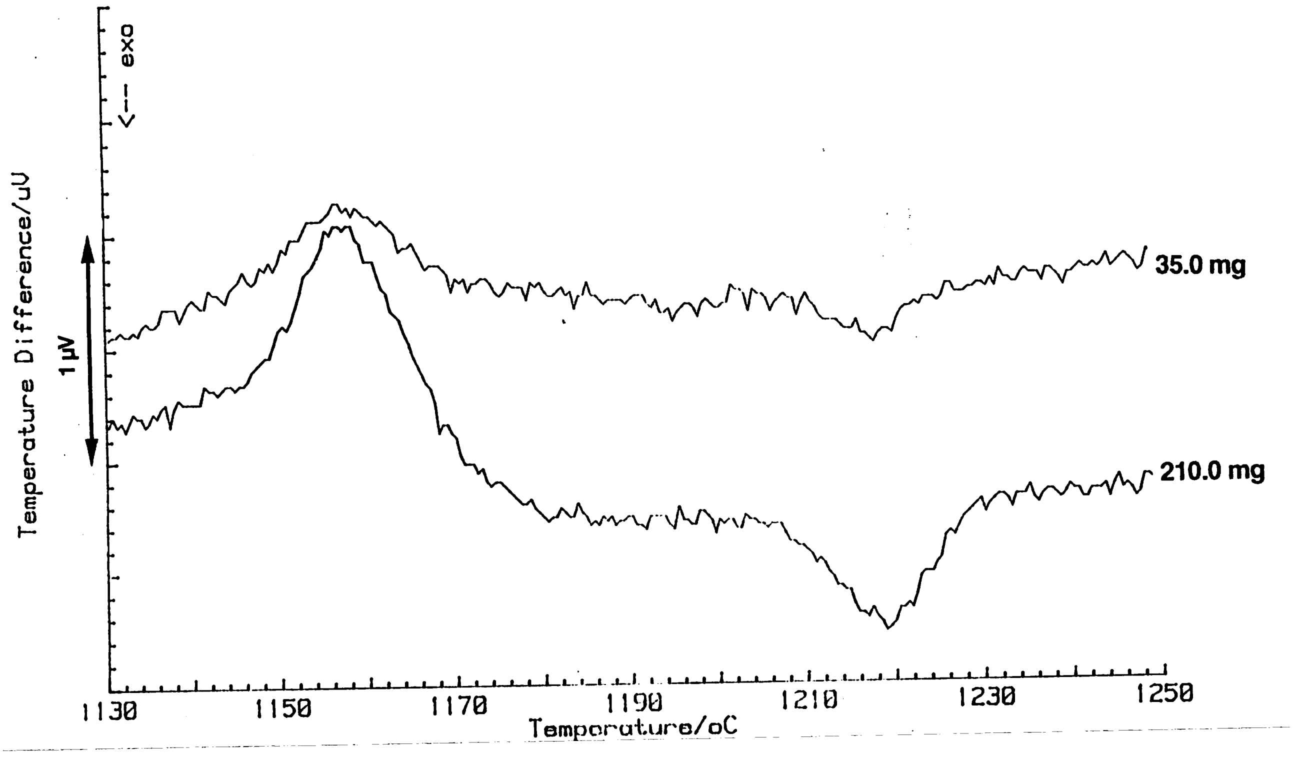

Fig. 3.7 Original DSC peaks due to the recrystallisation of a small specimen (35.0 mg) and a large specimen (210.0 mg).

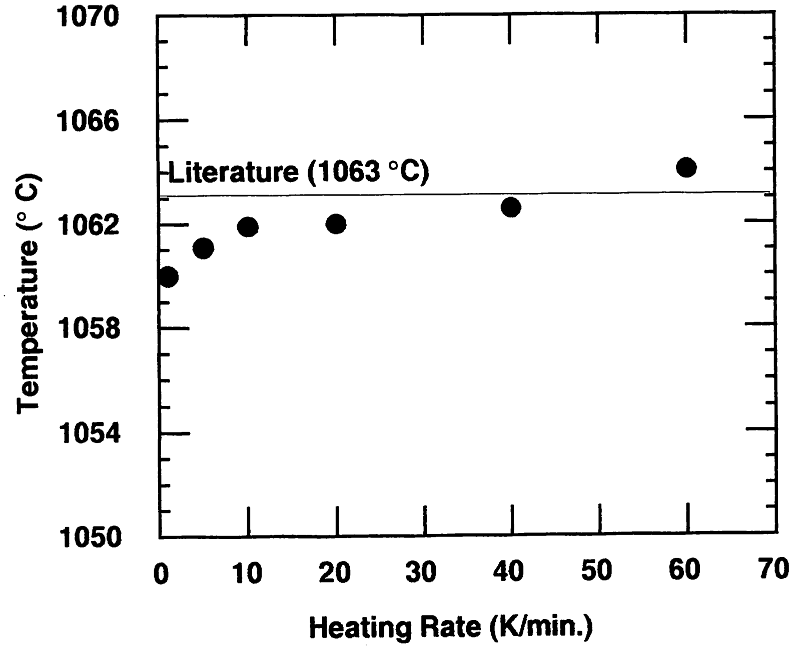

Fig. 3.8 Pure gold melting temperatures measured by DSC as a function of heating rate. The sample weight was 201.0 mg.

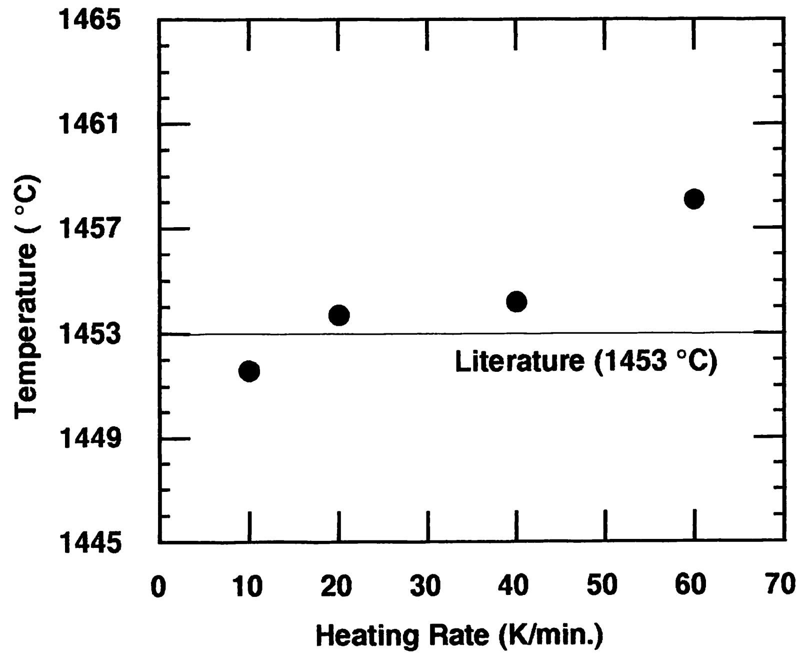

Fig. 3.9 Pure nickel melting temperatures measured by DSC as a function of specimen weight. The typical sample weight was 200 mg.

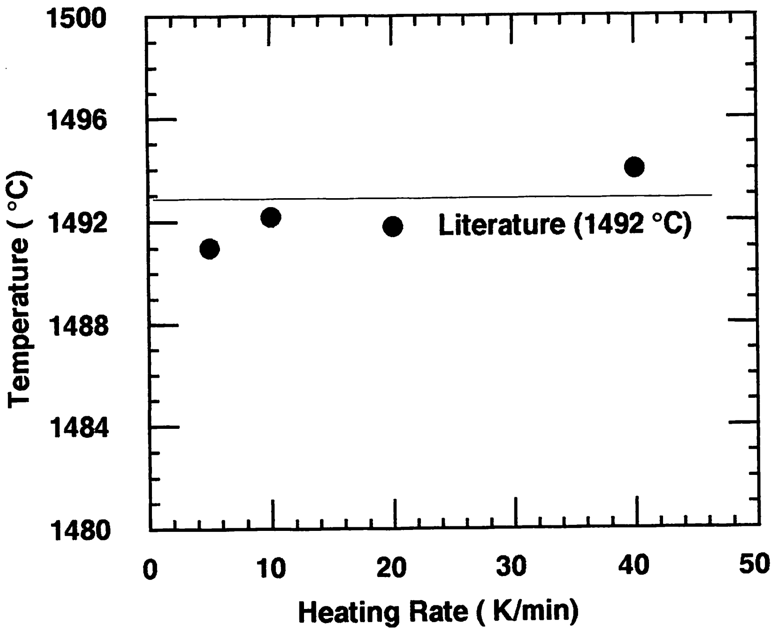

Fig. 3.10 Pure cobalt melting temperatures measured by DSC as a function of specimen weight. The typical sample weight was 200 mg.

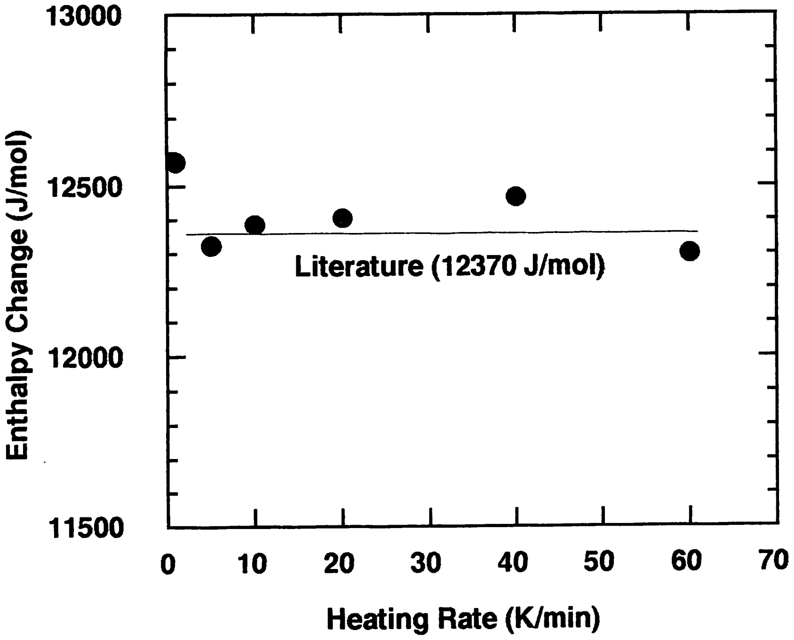

Fig. 3.11 Latent heats of gold measured by DSC as a function of heting rate. The sample weight was 201.0 mg.

References

1. Mino K., Harada H., Bhadeshia H. K. D. H. and Yamazaki M.: *Mater. Sci. Forum*, (1992), **88 - 90**, p. 1236.
2. *Handbook of Chemistry and Physics*, 57 ed., Weast R. C., ed., CRC Press, Cleveland, OH, USA, (1977).

CHAPTER 4

NONUNIFORM RECRYSTALLISATION IN MA6000

4.1 Introduction

Both the mechanical alloying process and the subsequent hot-deformation process can lead to inhomogeneities, especially since the strength levels involved even at high-temperatures are large. It is common knowledge that such materials tend to show batch-to-batch variations, and variations within single extruded samples. The purpose of the present work was to examine the secondary recrystallisation behaviour across the cross section of extruded bar, in order to understand better the factors responsible for variations in grain structure across the cross section. It is unlikely that such variations can be eliminated completely, given the difficulties in processing. Nevertheless a better understanding of the inhomogeneities that might exist can perhaps suggest heat treatment procedures which give uniform microstructures in spite of the heterogeneities.

4.2 Experimental Procedure

Metallographic samples ($10 \times 23 \times 23$ mm) were prepared on a plane normal to the extrusion direction. They were etched using a mixture of 2 g $CuCl_2$ in 40 ml HCl and 80 ml ethanol.

The heat treatments were carried out in a differential scanning calorimeter (DSC) which has a computer controlled furnace, using $5 \times 5 \times 2$ mm samples taken from specific positions within the cross-section of the extruded bar. One of the long edges of the sample was parallel to the extrusion (and rolling) direction. The sample and reference were placed in thermally balanced Al_2O_3 crucibles.

Calorimetric measurements were carried out during continuous heating (2.5 - 40 K min^{-1}). In all cases, the experiments were carried out using a helium atmosphere in the DSC chamber, the helium flow rate being 50 K min^{-1}.

"Isothermal annealing" experiments were also carried out in the DSC, involving the heating of samples to the chosen isothermal temperature at a rate of 20 K min^{-1}, and then holding at the annealing temperature for a variety of time periods. The samples were prepared as illustrated in Fig. 4.1, from the surface, intermediate and core regions of the extruded bar.

4.3 Experimental Results

4.3.1 Gamma Prime Solution and Carbide Solution

It is now well established that the onset of recrystallisation in mechanically alloyed ODS superalloys does not correlate with the dissolution of γ' precipitates during heating. Nevertheless, recrystallisation always occurs at some temperature beyond that at which the γ' has dissolved. It was therefore intended to conduct the isothermal annealing experiments at temperatures above the γ' solution temperature, which was determined experimentally using differential scanning calorimetry.

The γ' solution is endothermic during heating whereas recrystallisation is exothermic. Hence, by ensuring that the reference has a slightly smaller mass than the sample, it is possible to ensure that the two peaks due to γ' solution and recrystallisation point in opposite directions. Using an already recrystallised specimen for the reference gives better resolution of peaks for the small enthalpy change of secondary recrystallisation [1]. However, recrystallised specimens also contain γ' (which precipitates during cooling) whose dissolution temperatures might differ slightly from the unrecrystallised specimens. It has been reported that for the mechanically alloyed superalloy, the γ' dissolution temperature observed in the first scan of a DSC experiment is different from that found for the second scan, probably because of γ' size differences [2]. Therefore, γ' dissolution cannot be determined accurately by the experiments using recrystallised alloys for references. In the present work, the recrystallisation behaviour was followed in the DSC experiments using a recrystallised reference, but γ' dissolution was measured without any reference.

Figs. 4.2 and 4.3 show typical experimental results, which indicate that most of the γ' dissolves by about 1180 °C at any of the heating rates in the range 2.5 - 40 K min^{-1}. The recrystallisation and solution processes are seen to be well separated in terms of temperature. Fig. 4.4 illustrates further data. As expected, the solution kinetics are elevated to higher temperatures as the heating rate is increased. More significantly, there is no dependence of γ' solution kinetics on sample position within the extruded bar. This indicates that any inhomogeneous recrystallisation behaviour cannot be attributed to variations in chemistry or γ' morphology with position. As already pointed out, isothermal annealing was achieved by heating samples to the chosen temperature at a rate of 10 K min^{-1}, so that the γ' should be dissolved by 1180 °C. All isothermal annealing experiments were therefore carried out above 1180 °C.

The endothermic peaks around 1100 °C are due to $M_{23}C_6$ dissolution. $M_{23}C_6$ carbides completely dissolve before recrystallisation begins, so that carbide dissolution also does not correlate with the recrystallisation onset. Fine (10 - 200 nm) Ti(C,N) can also be seen at any stage of heating (Chapter 6) [3]. They coarsen during heat treatment, but can be shown not to be responsible for triggering recrystallisation either. For example, isothermal annealing at 1160 °C for 3000 min causes a considerable coarsening of both the oxides and carbides, but recrystallisation still does not occur. In fact, there are no large differences of particle size before and after continuous heating recrystallisation experiments. Details of particle changes are mentioned in Chapter 6.

4.3.2 Recrystallisation during Isothermal Annealing

As pointed earlier, during solid-state processing, directional grain structures are usually produced by annealing extruded bars in a temperature gradient or by zone annealing. Without this procedure, recrystallisation occurs into an equiaxed grain structure; an exception to this is the case where the alloy contains dispersions of particles aligned along the extrusion direction, in which case anisotropic grains are obtained even during isothermal recrystallisation [4,5]. Thus, the isothermal annealing experiments reported below constitute a critical test for the presence or absence of aligned particle dispersions.

The metallographic data following annealing at temperatures in the range 1180 -1240 ° C for 60 min are presented in Figs. 4.5 - 4.7 and for 1440 min in Figs. 4.8 - 4.10. The complete set of results are summarised in Table 4.1. Samples taken from the surface of the extruded bar (*i.e.* from a depth not exceeding 1.2 mm) recrystallise most easily, giving extremely anisotropic grains elongated along the extrusion direction. The length-to-width ratio (the aspect ratio) as observed on random sections containing the extrusion direction was measured to be about 15. The lowest temperature at which recrystallisation began was found to be about 1180 °C.

Similar though somewhat retarded recrystallisation behaviour was observed in the intermediate regions, where recrystallisation occurred during annealing at temperatures below about 1200 ° C, the aspect ratio of the anisotropic recrystallised grains was once again measured to be greater than 15.

Recrystallisation was most sluggish in the core regions (depth than 8 mm below the surface). Complete recrystallisation could only be obtained during annealing at 1240 ° C, and the resulting grain structure tended to be more equiaxed with a much smaller aspect ratio of about 4.5.

The development of anisotropic grains during isothermal annealing is attributed to the alignment of oxide particles along the extrusion direction. The alignment is expected to be strongest along the surface regions where the deformation imparted during extrusion is also expected to be most intense.

Table 4.1 Summary of Metallographic Data Following Isothermal Annealing

Time (min)	60			480			1440		
Temperature (°C)	Surface	Inter-mediate	Core	Surface	Inter-mediate	Core	Surface	Inter-mediate	Core
1180	Δ	Δ	×	○	Δ	×	○	Δ	×
1200	○	Δ	×	○	Δ	×	○	Δ	×
1240	○	○	Δ	○	○	○	○	○	○

○-Complete recrystallisation; Δ-partial recrystallisation; ×-no recrystallisation

4.3.3 Stored Energy

If the degree of deformation is expected to be larger at the surface regions of the extruded bar, then it is possible that the stored energy in those regions might also be larger. However, it is also possible that the stored energy reaches saturation, in which case it may not vary with position. Fig. 4.11 shows measurements of the stored energy as a function of the sample position and the heating rate in the DSC. It is evident that there are no significant variations either with position in the extruded bar, or with the heating rate. Since almost all of the stored energy in as-extruded *MA6000* is in the form of grain boundaries, the results indicate that there are no significant differences in the primary grain structure across the cross-section of the bars. It is explained in Chapter 5 that direct measurements of the primary grain sizes and those calculated using stored energy data show good agreement.

Fig. 4.12 illustrates typical DSC curves (10 K min^{-1}), showing the exothermic recrystallisation peaks for both the intermediate samples and core samples. Although the peak areas are similar, there are clear differences in detail. The intermediate sample begins and completes recrystallisation at lower temperatures relative to the core sample. This is consistent with the metallographic data reported earlier from isothermal annealing experiments, that recrystallisation is earlier for the intermediate samples.

Further experiments involving continuous heating (Fig. 4.13) revealed the same result, that the surface regions always recrystallised more readily relative to the core regions. The core regions were also found to be much more sensitive to the heating rate. The grain microstructures are illustrated in Figs. 4.14 and 4.15; they were found to be anisotropic, although the aspect ratios could not be measured because of the small size of the samples used in the DSC experiments. However, the core grains were always much coarser (Fig. 4.16), their size decreasing as the heating rate increased. This can be expected because recrystallisation is delayed to high temperatures as the heating rate increases, so that nucleation rate might also be larger. On the other hand, the grain width for the intermediate regions was wholly insensitive to the heating rate, perhaps because the aligned oxide particles prevent growth beyond some limiting size determined by the spacing between the bands of particles.

An explanation for these results relies on the earlier hypothesis that the oxide particles are more aligned near the surface regions. For randomly dispersed particles, the grain boundary velocity v_R is expected to be isotropic. For aligned particles, it should be easier for grain boundary motion to occur parallel to the extrusion direction (velocity v_X) and more difficult for the motion normal to the the extrusion direction $v_{Y,Z}$, with $v_{Y,Z} < v_R < v_X$. Since growth along the extrusion direction is less impeded, recrystallisation can initiate more readily, thereby explaining the faster kinetics at the surface regions.

Fig. 4.17 illustrates some direct evidence for the presence of a higher degree of particle alignment along the extrusion direction in regions close to the surface of the bar. Recrystallised grain boundaries are parallel to the alignment of particles. Further detailed evidence of particle alignment is illustrated in Fig. 4.18, in which the high and low particle density interface corresponds to a recrystallisation grain boundary. In fact, as detailed in Chapter 6, there are thick slabs containing a large number density of particles, parallel to the extrusion direction. There are separated by depleted slabs. It is the depleted regions which rapidly recrystallise, and the new grains are prevented from growing into particle rich regions by pinning. The particle-rich regions recrystallise later in the annealing process.

Suppose we consider three dimensional growth. The equation assumes that the growth velocity is independent of position, *i.e.*, there is a constant growth velocity along Y, Z. Therefore, recrystallisation becomes more difficult in an anisotropic material, since $v_Y, v_Z < v_X$. However, in reality, there are bands of particles parallel to the extrusion direction. Therefore, growth along Y and Z will initially be very rapid and will stop when a boundary reaches a particle band (Fig. 4.19). Then the growth becomes one-dimensional along X, in which recrystallisation is easier in an anisotropic material.

Both banding and easy recrystallisation are observed in experiments in *MA6000*, confirming that the problem can be treated essentially as one-dimensional growth along the extrusion direction. (Note that as $v_Y, v_Z < v_X$, the one dimensional growth representation becomes better).

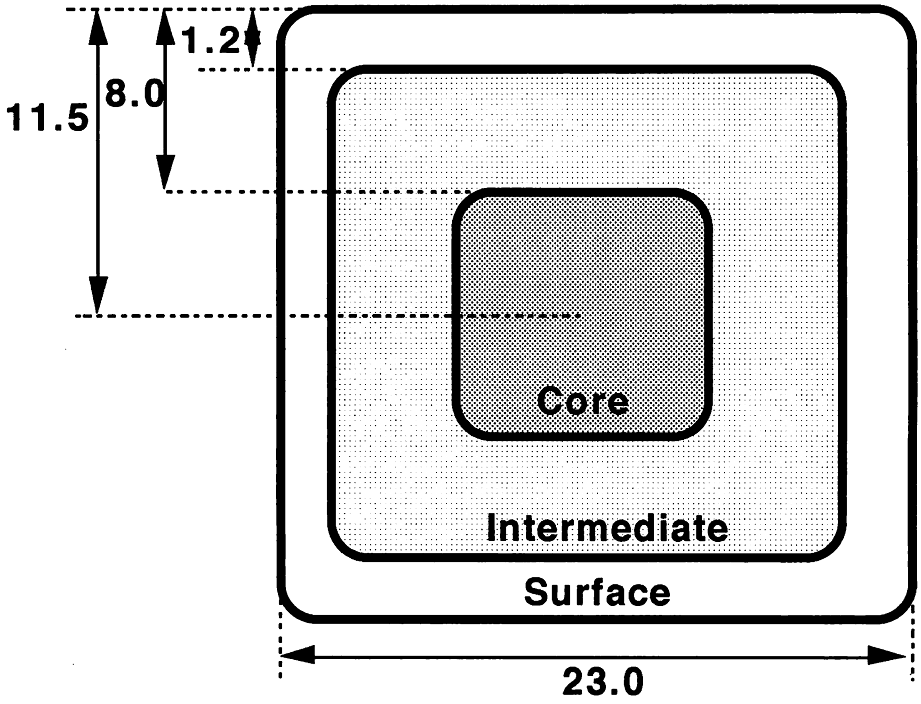

Fig. 4.1 Illustration of the surface, intermediate and core samples extracted from as received *MA6000* bar. The extrusion direction is normal to the plane of the diagram.

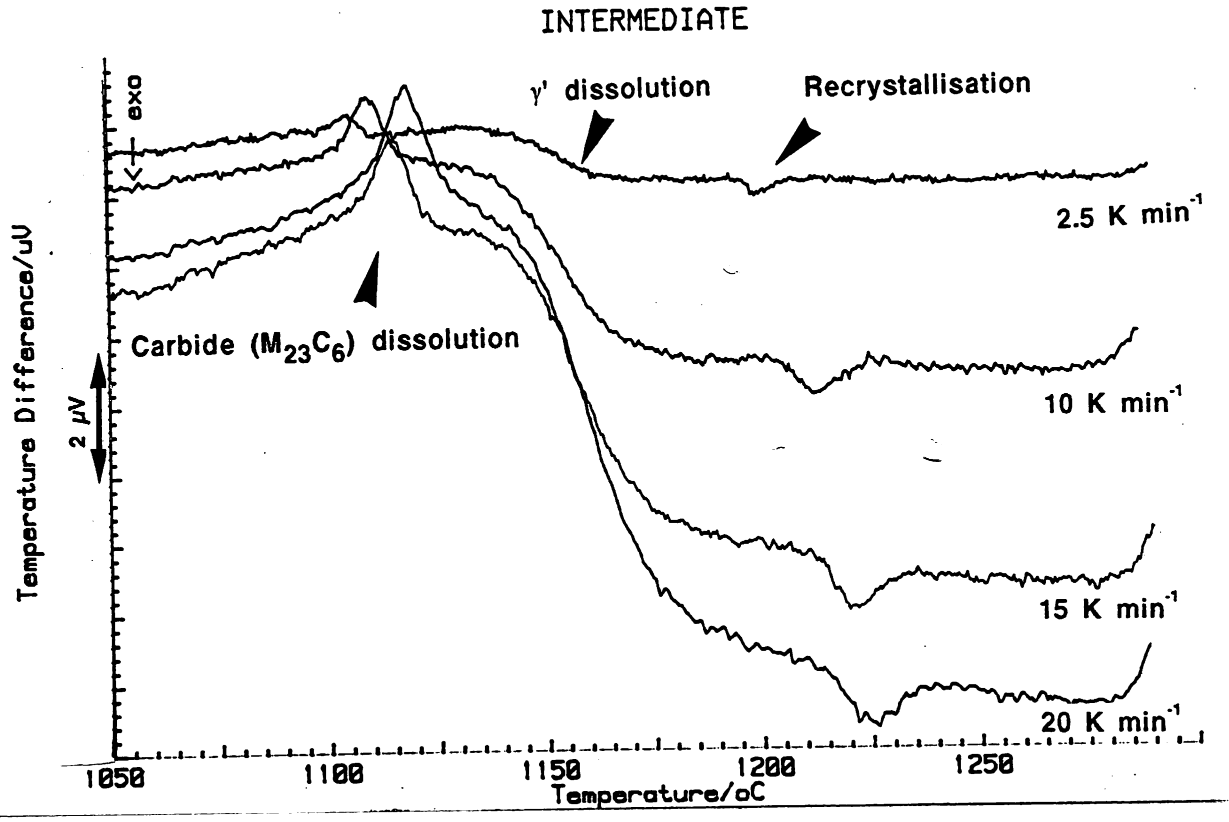

Fig. 4.2 Typical differential calorimetric data showing carbide dissolution, γ' dissolution and recrystallisation peaks at various heating rates. The samples are from the intermediate region.

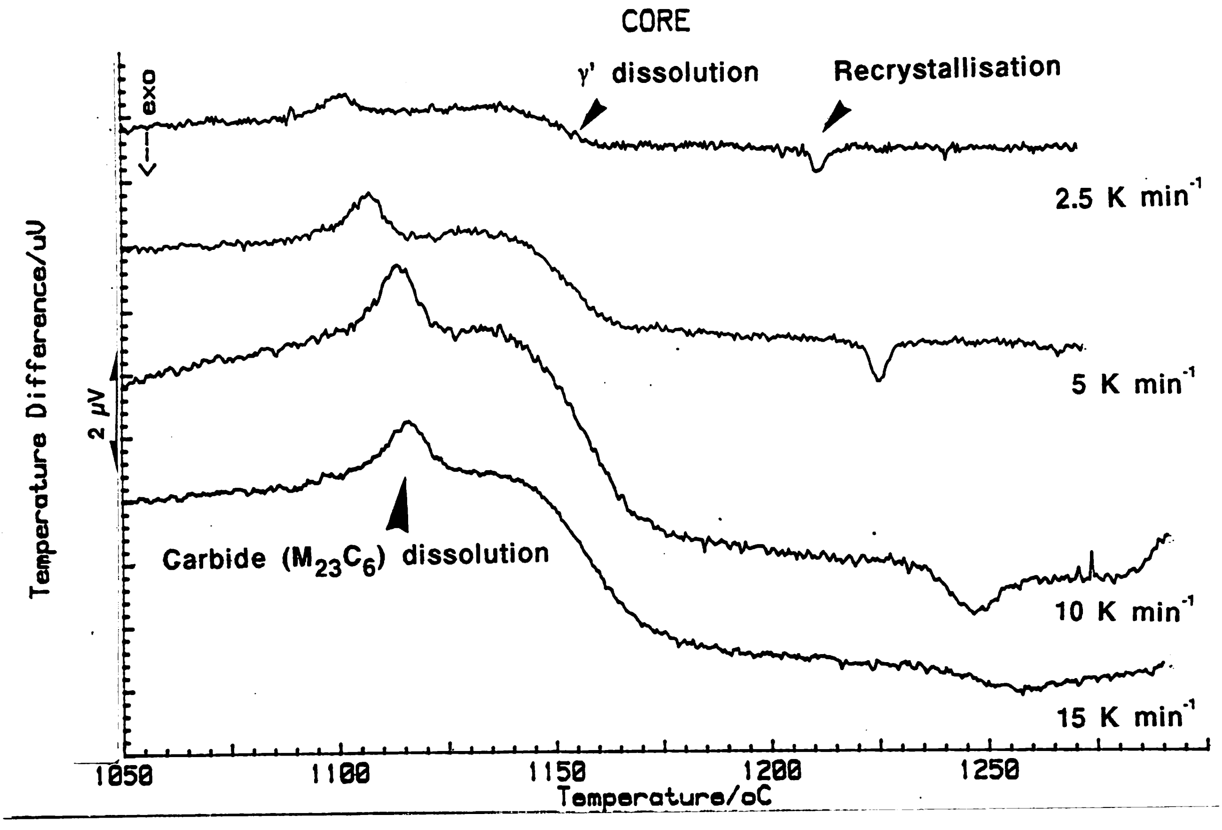

Fig. 4.3 Typical differential calorimetric data showing carbide dissolution, γ' dissolution and recrystallisation peaks at various heating rates. The samples are from the core region.

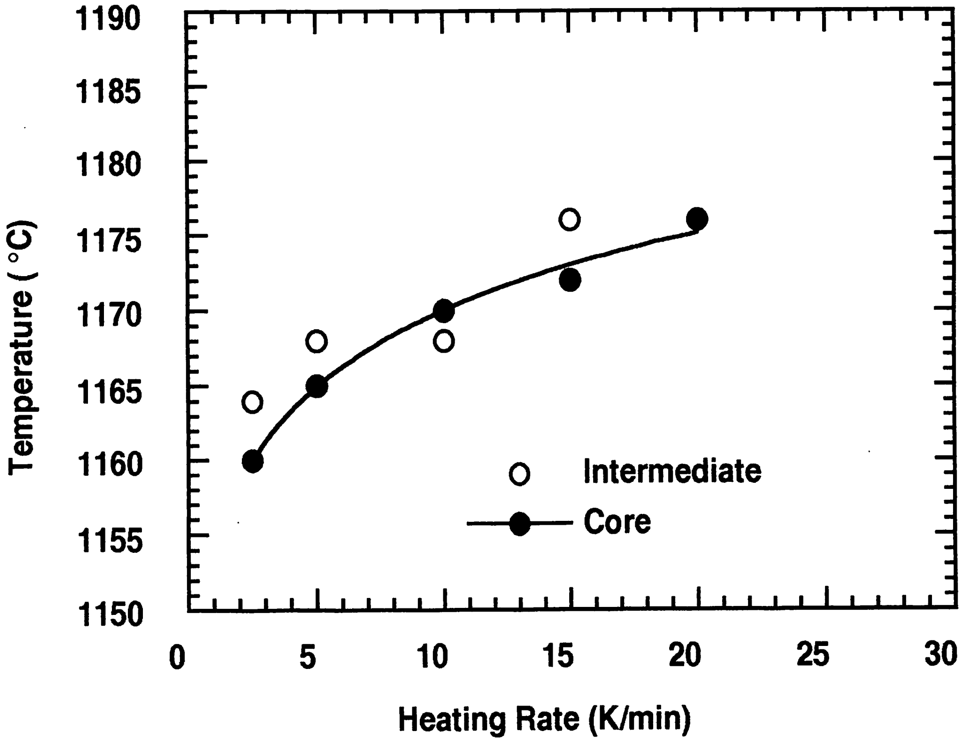

Fig. 4.4 Differential scanning calorimetry data showing the γ' dissolution finish temperatures as a function of heating rate for both the intermediate and the core specimens.

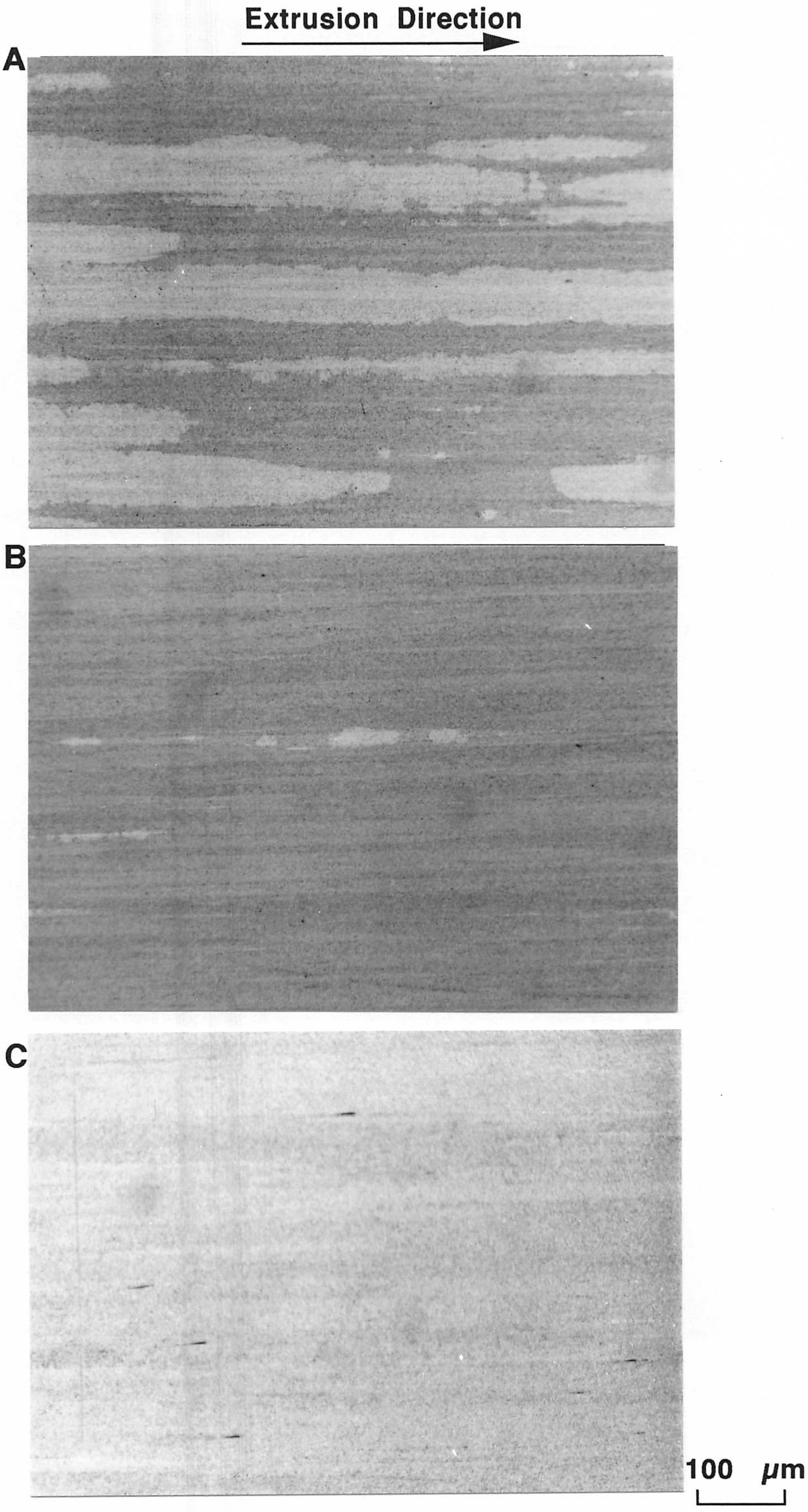

Fig. 4.5 Metallographic data from isothermal annealing experiments carried out at 1180 °C for a time period of 60 min.
A: Surface B: Intermediate C: Core

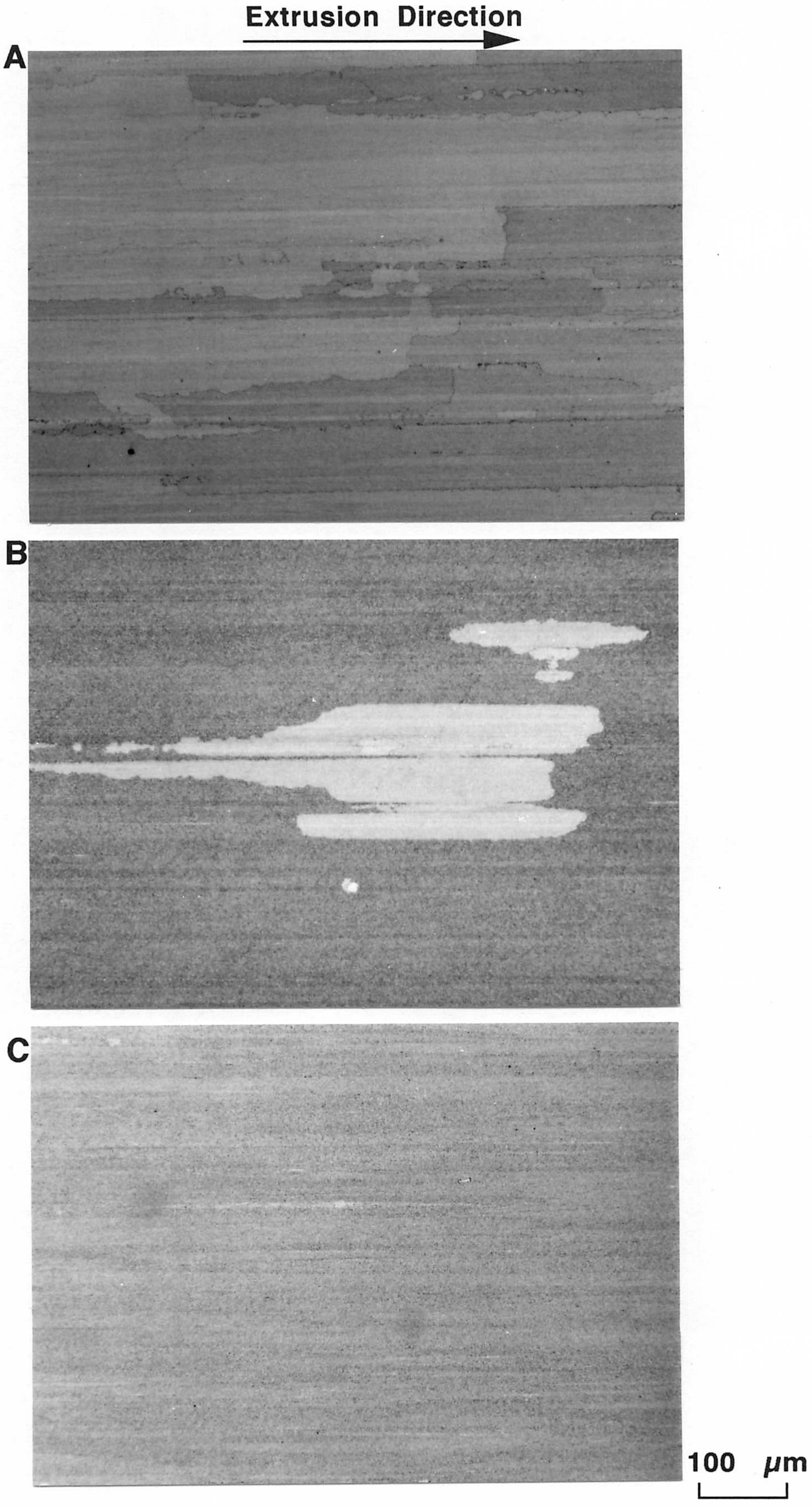

Fig. 4.6 Metallographic data from isothermal annealing experiments carried out at 1200 °C for a time period of 60 min.
A: Surface B: Intermediate C: Core

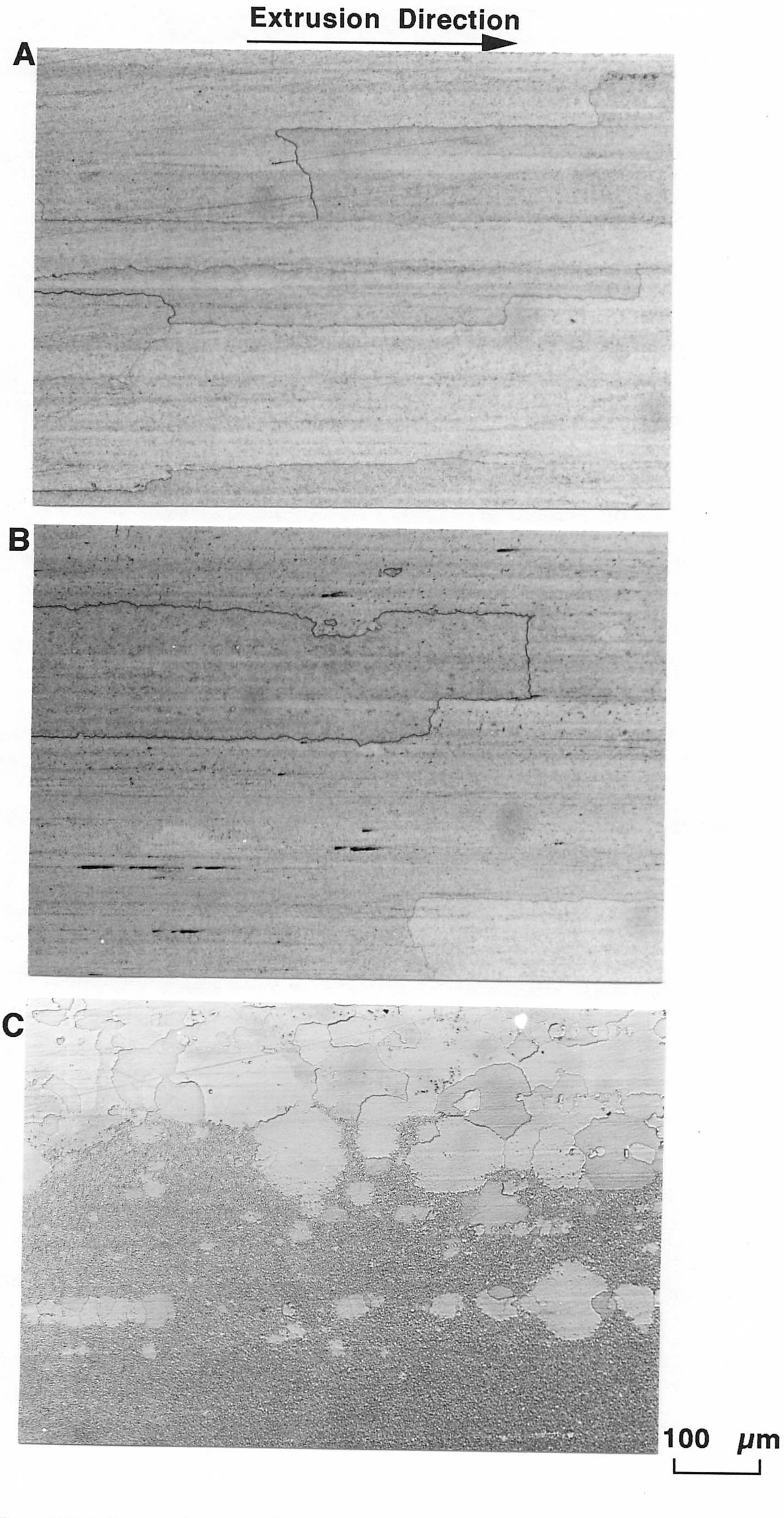

Fig. 4.7 Metallographic data from isothermal annealing experiments carried out at 1240 °C for a time period of 60 min.
A: Surface B: Intermediate C: Core

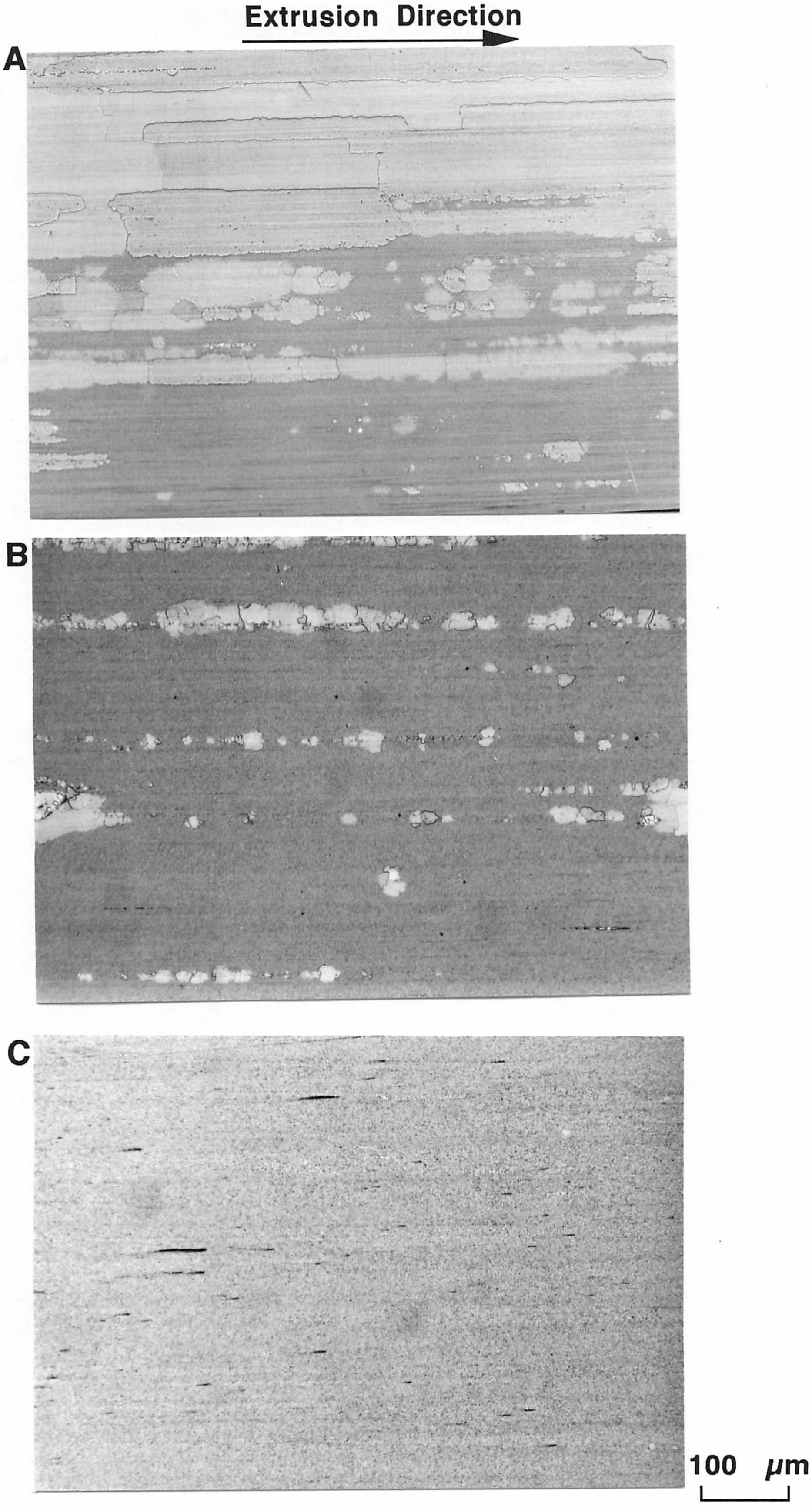

Fig. 4.8 Metallographic data from isothermal annealing experiments carried out at 1180 °C for a time period of 1440 min.
A: Surface B: Intermediate C: Core

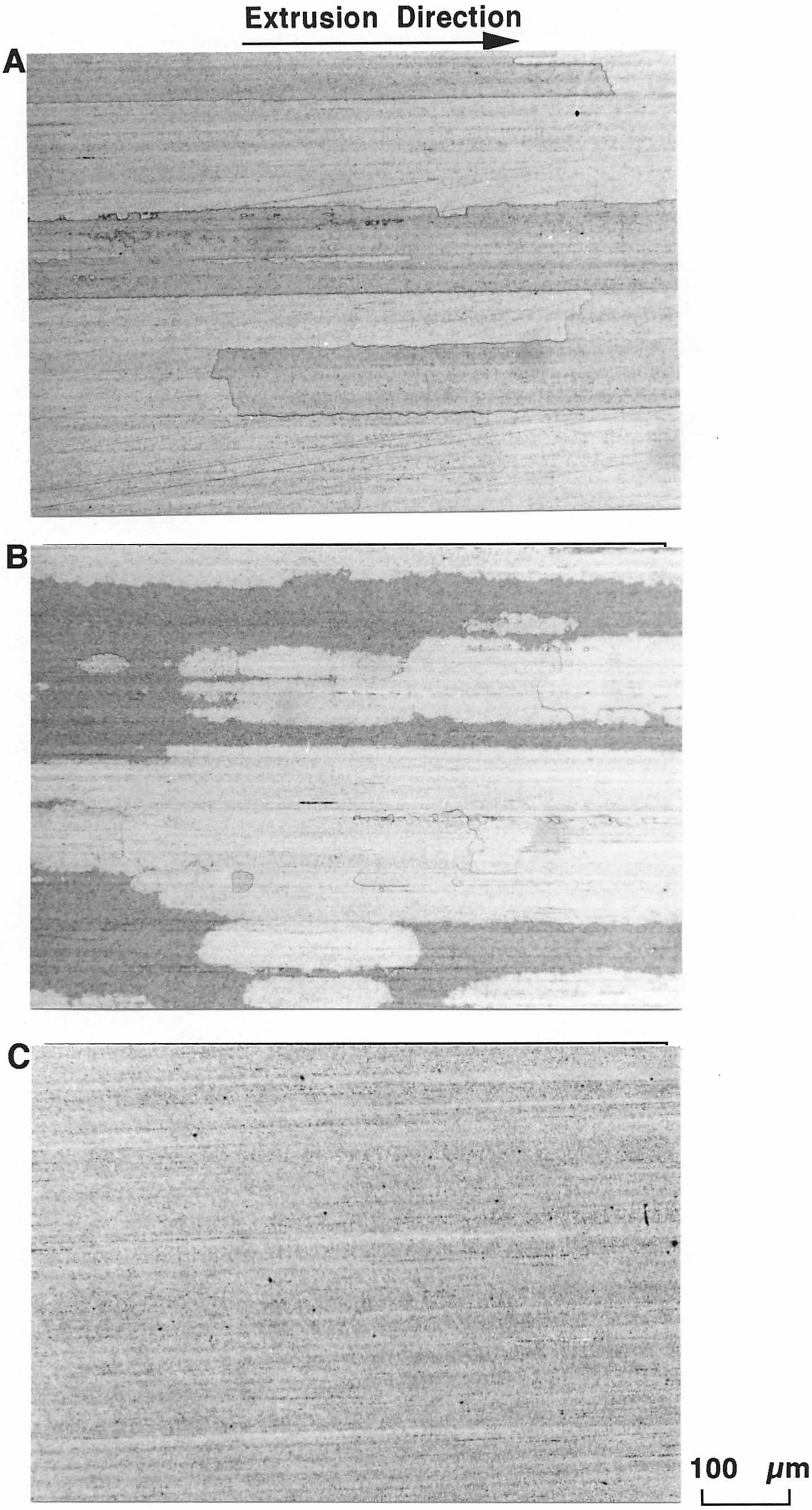

Fig. 4.9 Metallographic data from isothermal annealing experiments carried out at 1200 °C for a time period of 1440 min.
A: Surface B: Intermediate C: Core

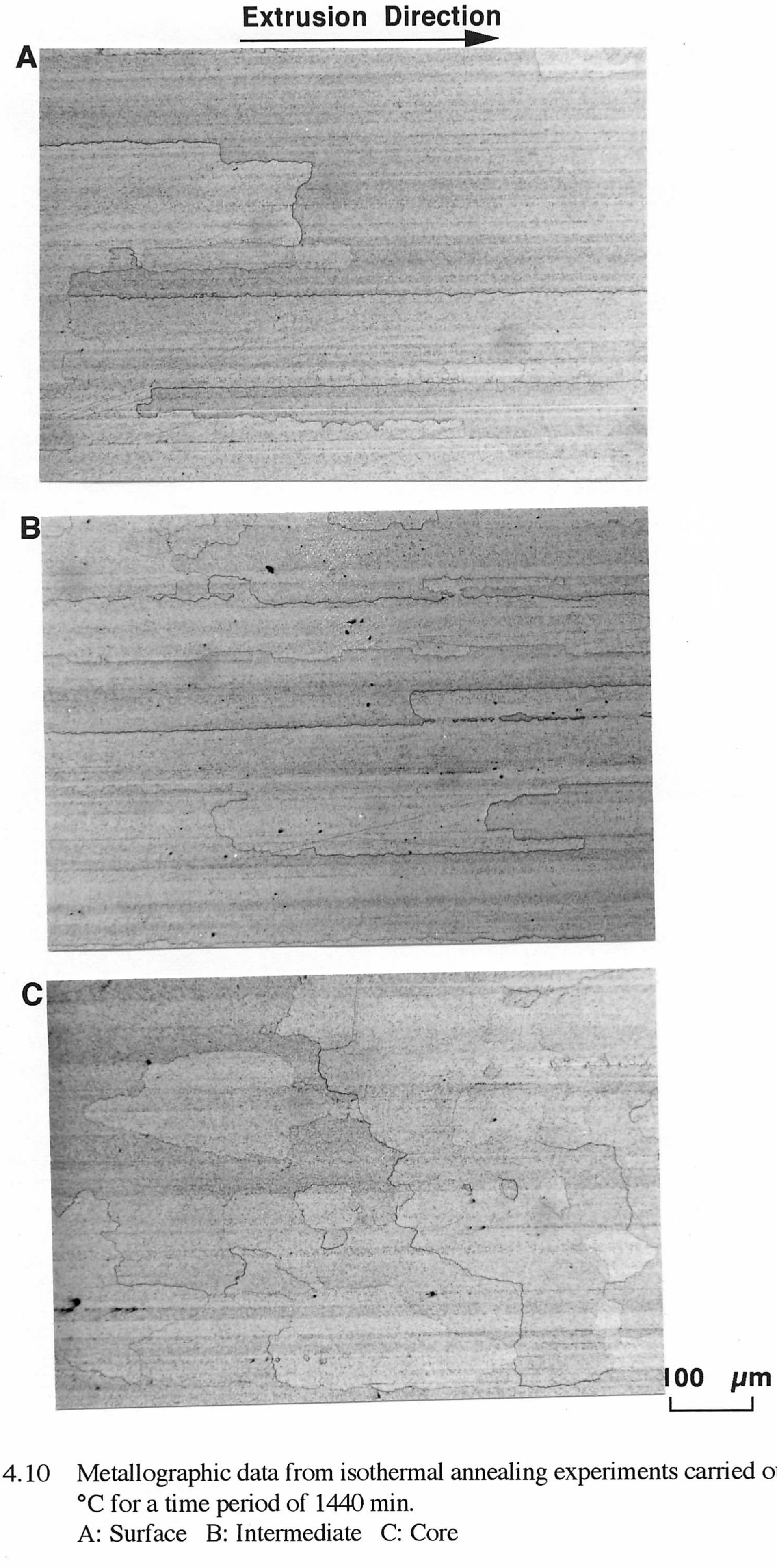

Fig. 4.10 Metallographic data from isothermal annealing experiments carried out at 1240 °C for a time period of 1440 min.
A: Surface B: Intermediate C: Core

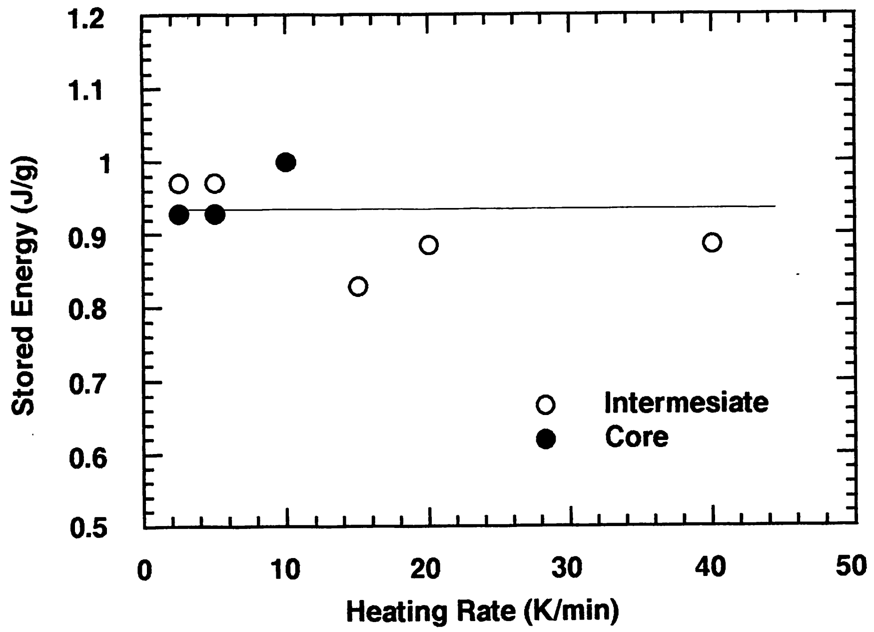

Fig. 4.11 Variation in stored energy as a function of heating rate and sample position in the extruded bar.

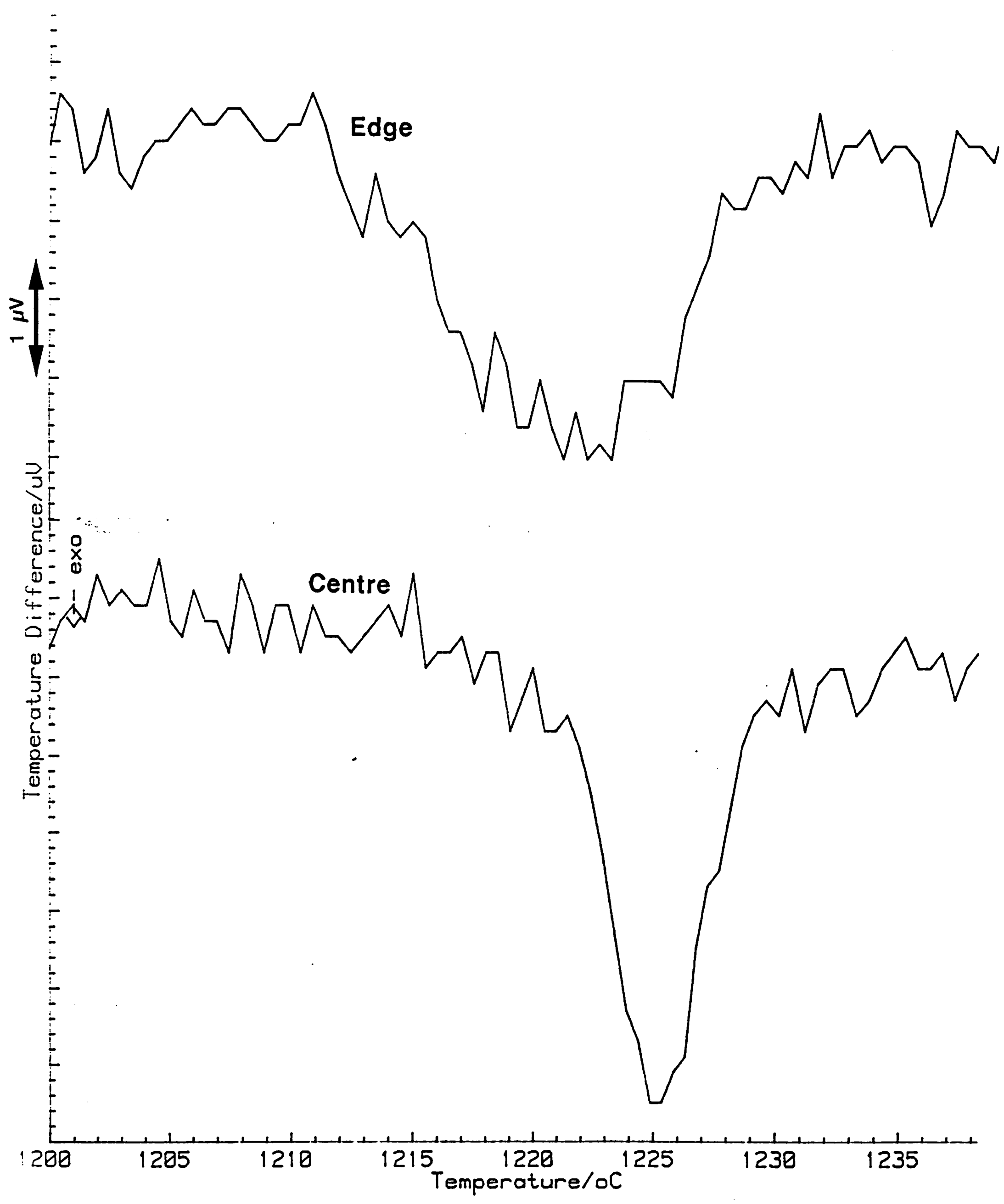

Fig. 4.12 Typical DSC recrystallisation peaks from the intermediate and core specimens (10 K min^{-1})

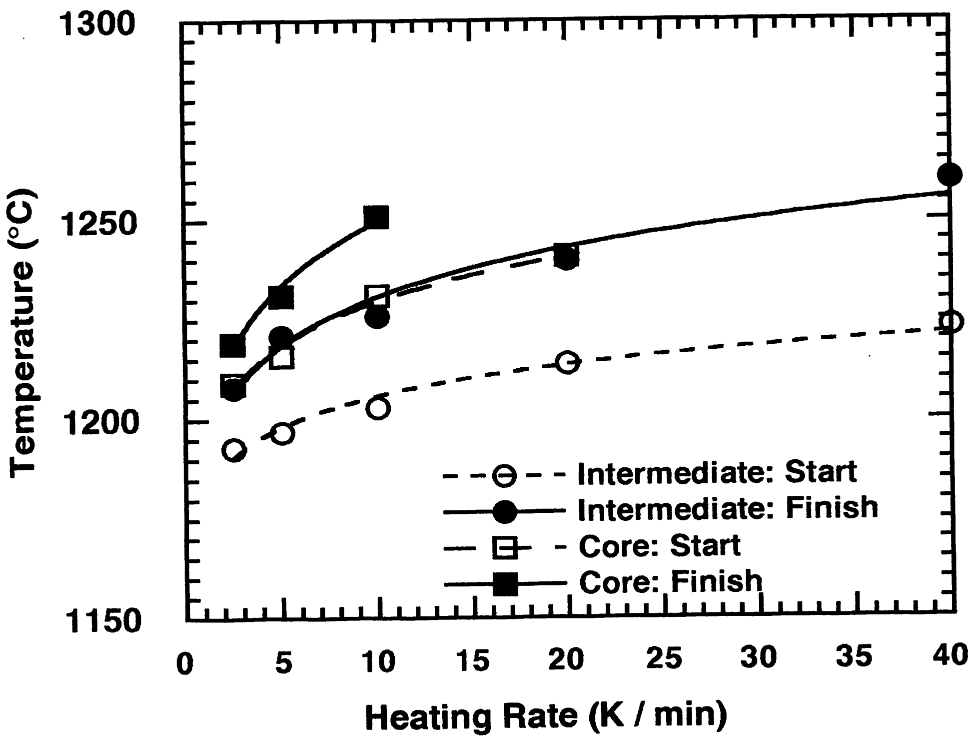

Fig. 4.13 Recrystallisation start and finish temperatures as a function of heating rate and sample position in the extruded bar.

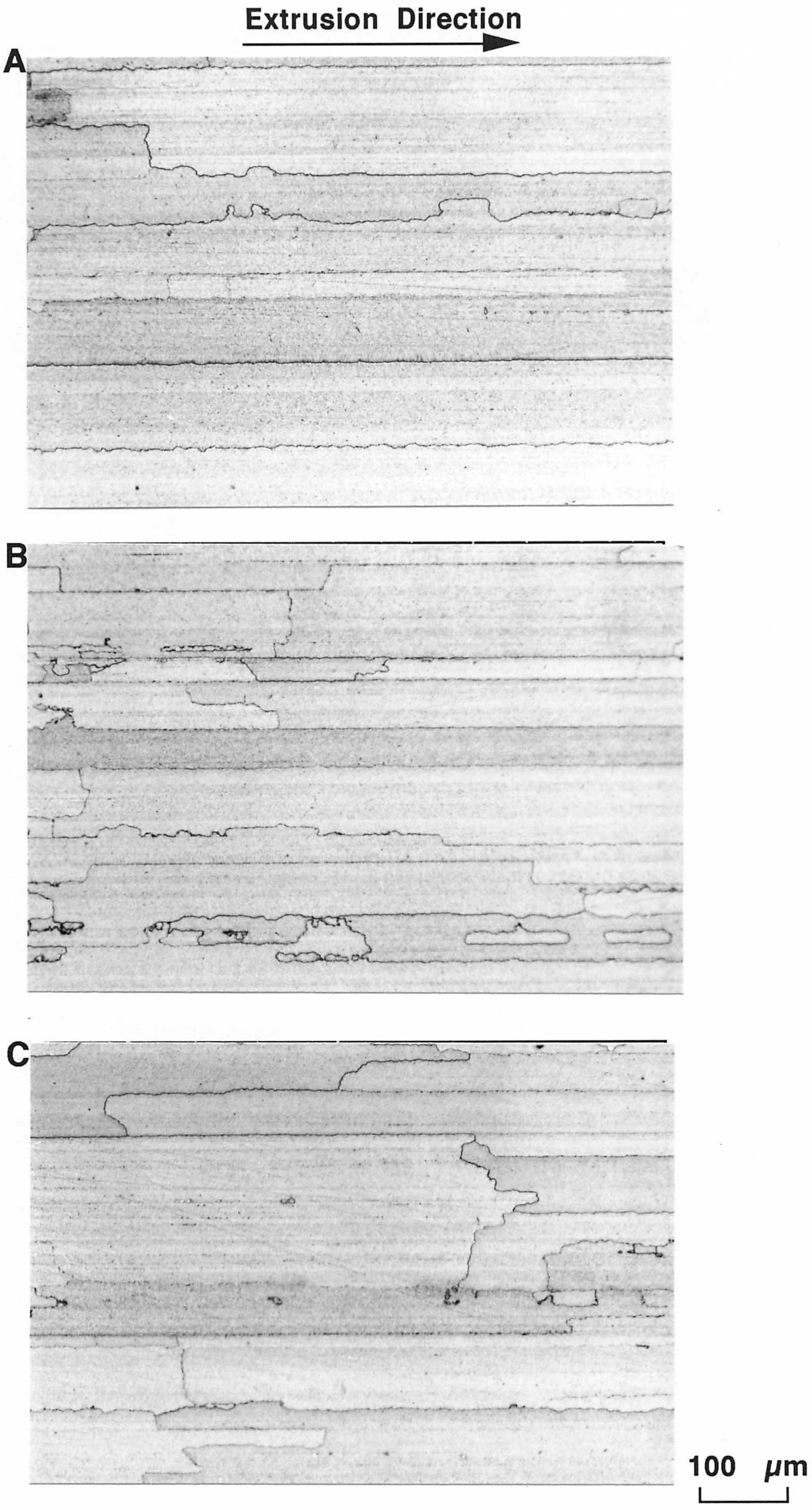

Fig. 4.14 Metallographic data of the intermediate region from continuous heating experiments. The heating rates were:
A: 2.5 K min^{-1} B: 10 K min^{-1} C: 40 K min^{-1}

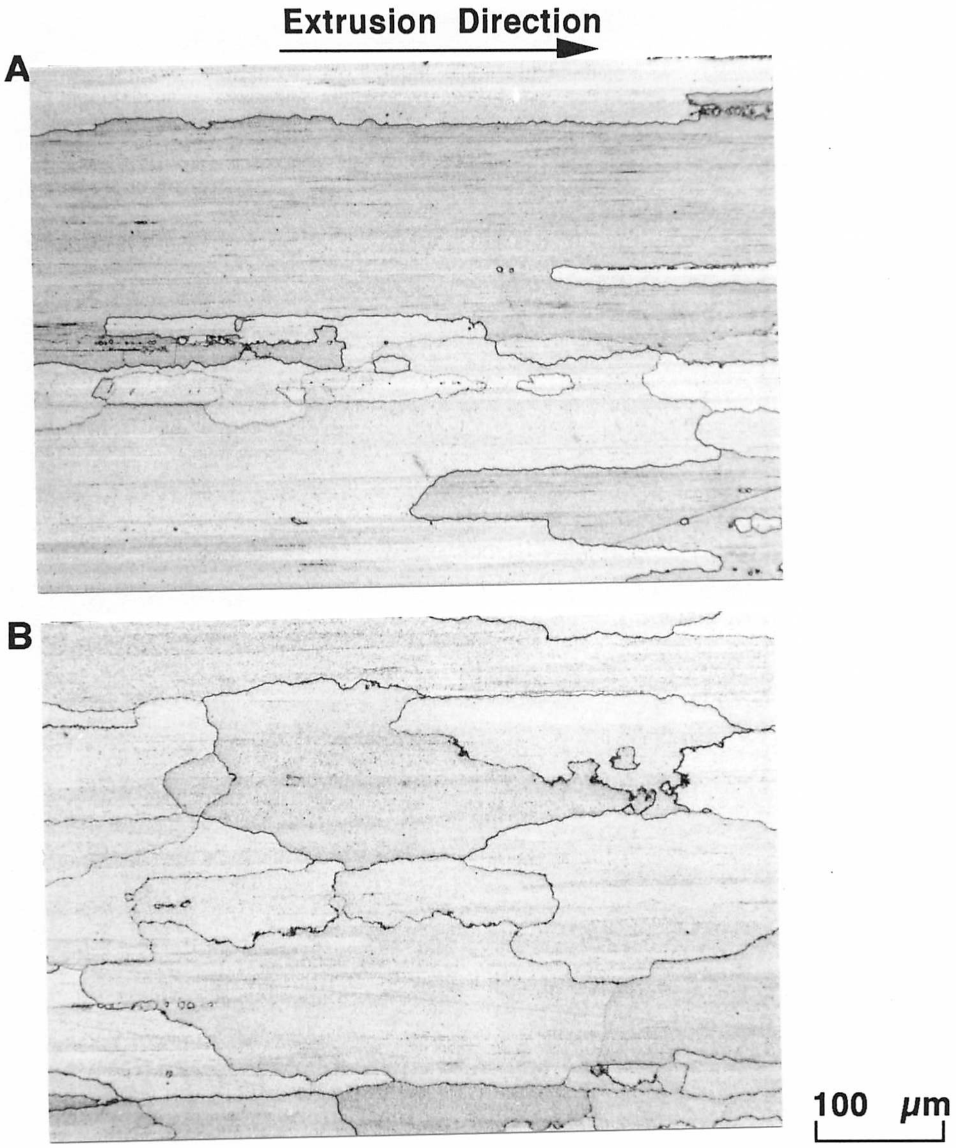

Fig. 4.15 Metallographic data of the core region from continuous heating experiments. The heating rates were:
A: 2.5 K min^{-1} B: 10 K min^{-1}

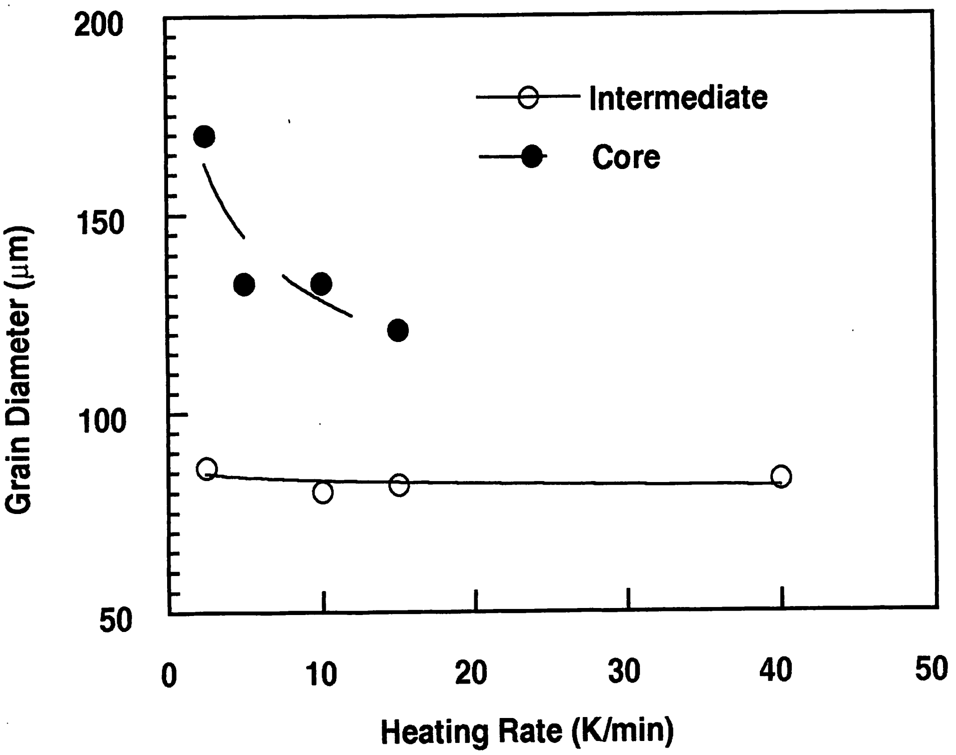

Fig. 4.16 Plot of recrystallised grain width as a function of the heating rate and sample position in the extruded bar.

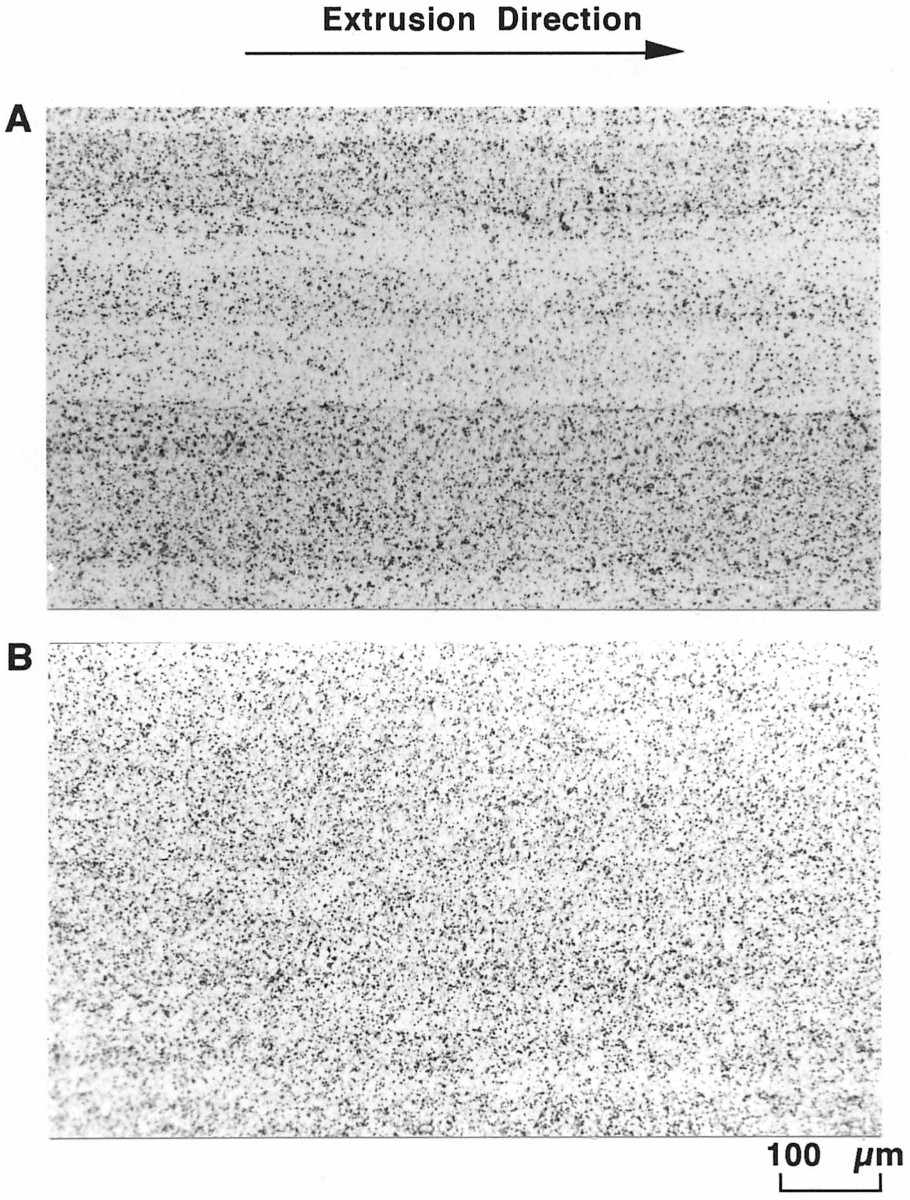

Fig. 4.17 Optical micrographs from (A) intermediate and (B) core regions of the extruded bar, illustrating the large degree of particle alignment associated with the intermediate regions.

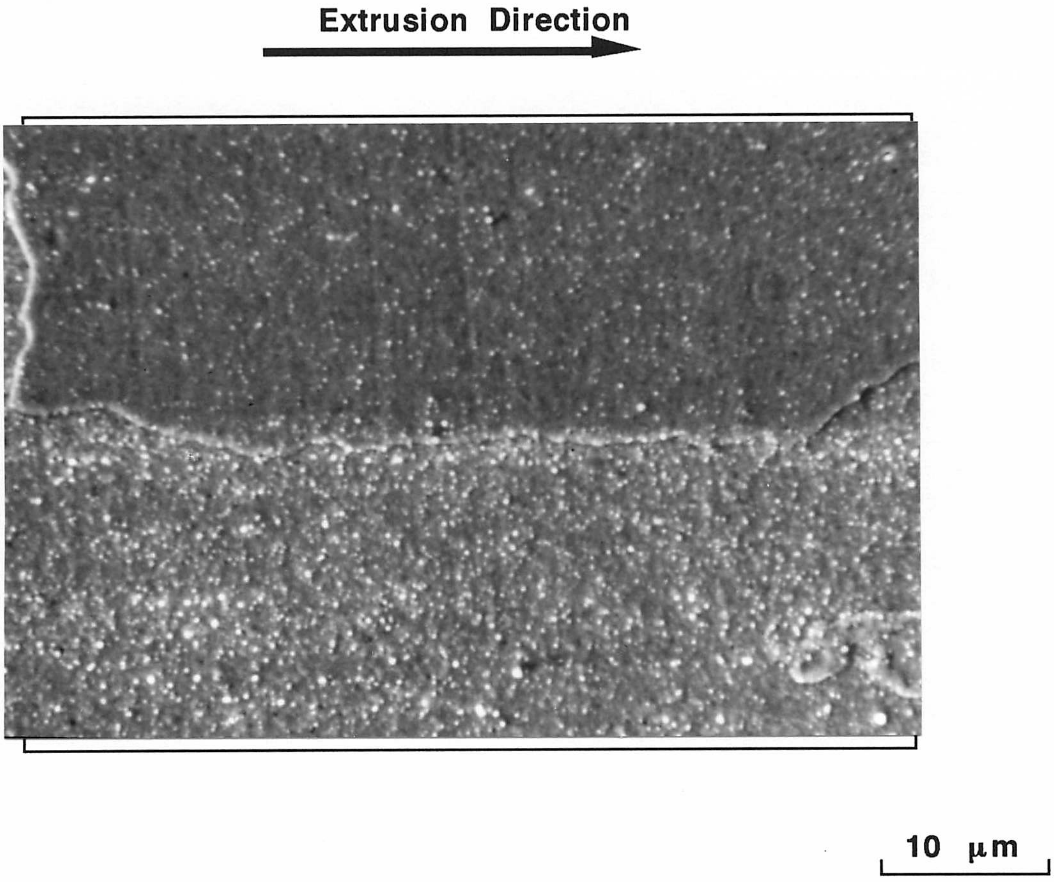

Fig. 4.18 SEM structures illustrating high and low particle density regions. A recrystallised grain-boundary corresponds to the interface between high and low particle density regions in the SEM structure. Intermediate region, continuously heated up to 1230 °C and water quenched, fully recrystallised.

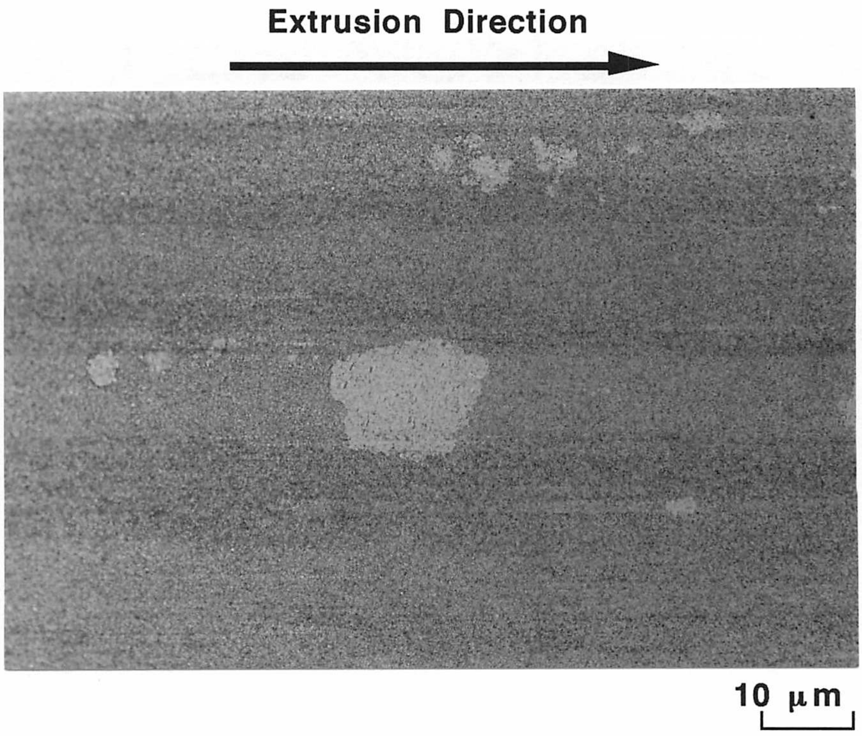

Fig. 4.19 Early stages of recrystallisation for the intermediate specimen isothermally annealed at 1180 °C for a time period of 60 min, illustrating recrystallisation fronts stop at particle bands (arrows A, B), and grains smaller than the particle band width (arrows C, D) are isotropic.

4.4 Model

The complexity of recrystallisation in ODS materials has been emphasized in an excellent review by Humphreys [6,7]. The kinetics depend on particle size and dispersion geometry and can be accelerated or retarded depending on the detailed state of the dispersion and the extent of deformation. It is also well established that particles can exert pinning forces on moving grain boundaries [8-11]. The work presented subsequently is necessarily an oversimplification of these complex phenomena, but it is believed to be capable of fairly representing the experimental observations.

Two interesting qualitative conclusions emerge from the preceding study: recrystallisation is easier in the surface regions and is also less sensitive to the heating rate. Both of these effects were attributed to the relatively larger degree of particle alignment in the surface regions. In this section, we develop a quantitative model which provides further justification for this interpretation of the experimental data.

If it is assumed that the oxide particles all have an identical radius r, then the number of particles per unit volume is given by:

$$N_V = 3V_v \,/\, (4\pi r^3) \tag{4.1}$$

where V_v is the volume fraction of oxide particles. The particle spacing along the orthogonal directions d_x (the extrusion direction), d_Y and d_Z is therefore given by

$$d_X = (A^2 \,/\, N_V)^{1/3} \tag{4.2}$$

$$d_Y = d_Z = d_X \,/\, A \tag{4.3}$$

where A represents the anisotropy of the oxide particle dispersion. A value of unity gives an isotropic dispersion, whereas small values ($0 < A \leq 1$) tend to make the particles align along the extrusion direction . It is assumed that the particle spacing is uniform in the directions normal to the extrusion direction. It also follows that the number of particles per unit area is given by:

$$N_X = (d_Y d_Z)^{-1} \tag{4.4}$$

$$N_Y = N_Z = (d_X d_Z)^{-1} \tag{4.5}$$

where N_X is the number density of particles on the plane normal to the X direction. The grain boundary velocity during recrystallisation is given by [12]:

$$v = \delta\upsilon \exp\{-Q / RT\} [1 - \exp\{-\Delta G / RT\}] \tag{4.6}$$

where δ and υ are the distance and atomic jump frequency across the boundary respectively, R is the universal gas constant, and Q is an activation energy for the transfer of atoms across the boundary. The term ΔG is the effective driving force for recrystallisation, which does not vary with temperature, but is modified by the particle pinning force :

$$\Delta G \approx \Delta G_s - (C_1 V_V V_M \sigma / r) \tag{4.7}$$

where ΔG_s is the stored energy in the material due to the grain boundaries, σ is the grain boundary energy per unit area, and $V_M \approx 7.1 \times 10^{-6}\ \mathrm{m^3 mol^{-1}}$ is the molar volume. C_1 is a constant whose magnitude depends on the details of the pinning process [8]. The equation applies to the case where the particles are uniformly dispersed. When they are not, we get:

$$\Delta G_{X,Y,Z} \approx \Delta G_s - (C_1\, r\, N_{X,Y,Z}\, V_M\, \sigma) \tag{4.8}$$

making the boundary velocity a function of the orientation relative to the extrusion direction.

It is reasonable to assume that recrystallisation begins from a number of pre-existing nuclei (grains), so that the fraction ξ of the sample that is isothermally recrystallised can be obtained using the classic Johnson-Mehl-Avrami approach [13] as:

$$\xi = 1 - \exp\{-n_V v_X v_Y v_Z t^3\} \tag{4.9}$$

where n_V is the fixed number of nuclei available per unit volume at the start of recrystallisation, and t is the heat-treatment time.

The theory presented so far deals with isothermal recrystallisation: the experiments on the other hand, involved continuous heating. This anisothermal heat-treatment can be taken into account by representing the continuous heating curve as a series of small isothermal steps at successively rising temperatures. Each step thus represents an isothermal anneal for a time period t_i, where the subscript denotes the step number. The value of fraction recrystallised, the time interval and temperature for the first step is therefore, ξ_1, t_1 and T_1, respectively. To achieve this same degree of transformation, but at the temperature T_2 requires, in general, a different time t'_1. Assuming that the reaction is isokinetic [13], the value of ξ_2 can be estimated by annealing for a time interval t'_1+t_2 at T_2. This procedure can be continued until the sample is fully recrystallised.

The calculations were carried out assuming the values listed in Table 4.2. Most of these values are crude (though reasonable) estimates, so that results from the model should only be use to assess trends rather than give exact agreement with experimental data. It has been verified that the trends are not sensitive to the chosen values of the input parameters. The activation energy Q is assumed to be that the self-diffusion of nickel [14]. C_1 is chosen in order to obtain recrystallisation at temperatures close to those observed.

Calculations using the model and the parameters listed in Table 4.2 are presented in Fig. 4.20. They confirm that recrystallisation can be expected to occur at higher temperatures as the precipitate dispersion becomes more uniform. Furthermore, the recrystallisation kinetics also should become more sensitive to the heating rate (for samples with relatively uniform dispersion), consistent with experimental observations. Trends of calculations are good agreement with experiments, however, they do not correspond absolutely to the experimental values. In particular, the calculated recrystallisation start temperatures are too low.

Table 4.2 Parameters Used in the Model for Recrystallisation in the Presence of an Anisotropic Dispersion of Particles

Q	284512 J mol^{-1}
σ	0.6 J mol^{-1}
r	2×10^{-8} m
V_V	0.01
ΔG_S	50 J mol^{-1}
δv	0.12×10^{18}m min^{-1}
n_V	$7.4\times10^{8}\text{m}^{-3}$
C_1	3.14

This calculations can be improved by modifying some values in the model. Fig. 4.21 illustrates better fitting between experiments and calculations using the same parameters in Table 4.2 except a larger activation energy Q (700000 J mol^{-1}) and a larger value for δv (0.12×10^{34}m min^{-1}), although the physical meaning of the value of Q is not clear. Recrystallisation start temperatures, however, are still far from those measurements. This is probably because the model does not consider trigger mechanisms for recrystallisation onset (appendix 2).

A computer program for the calculations discussed here is listed in appendix 1.

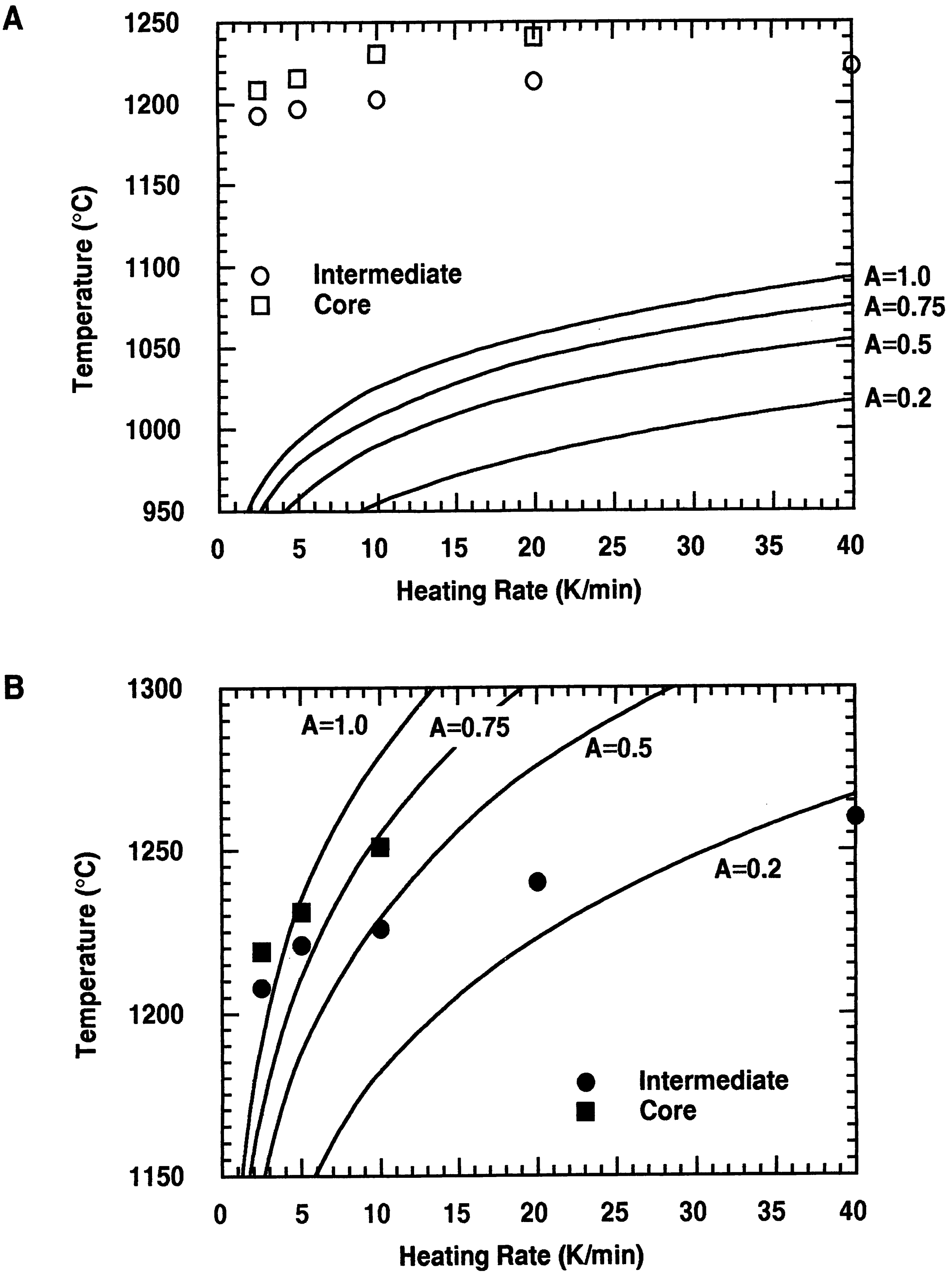

Fig. 4.20 Calculations illustrating the variation in the recrystallisation start and finish temperatures as a function of the heating rate and of the degree of anisotropy (A) in the particle dispersion.

A: Start temperatures B: Finish temperatures, Activation energy Q=284.5 kJ mol^{-1}.

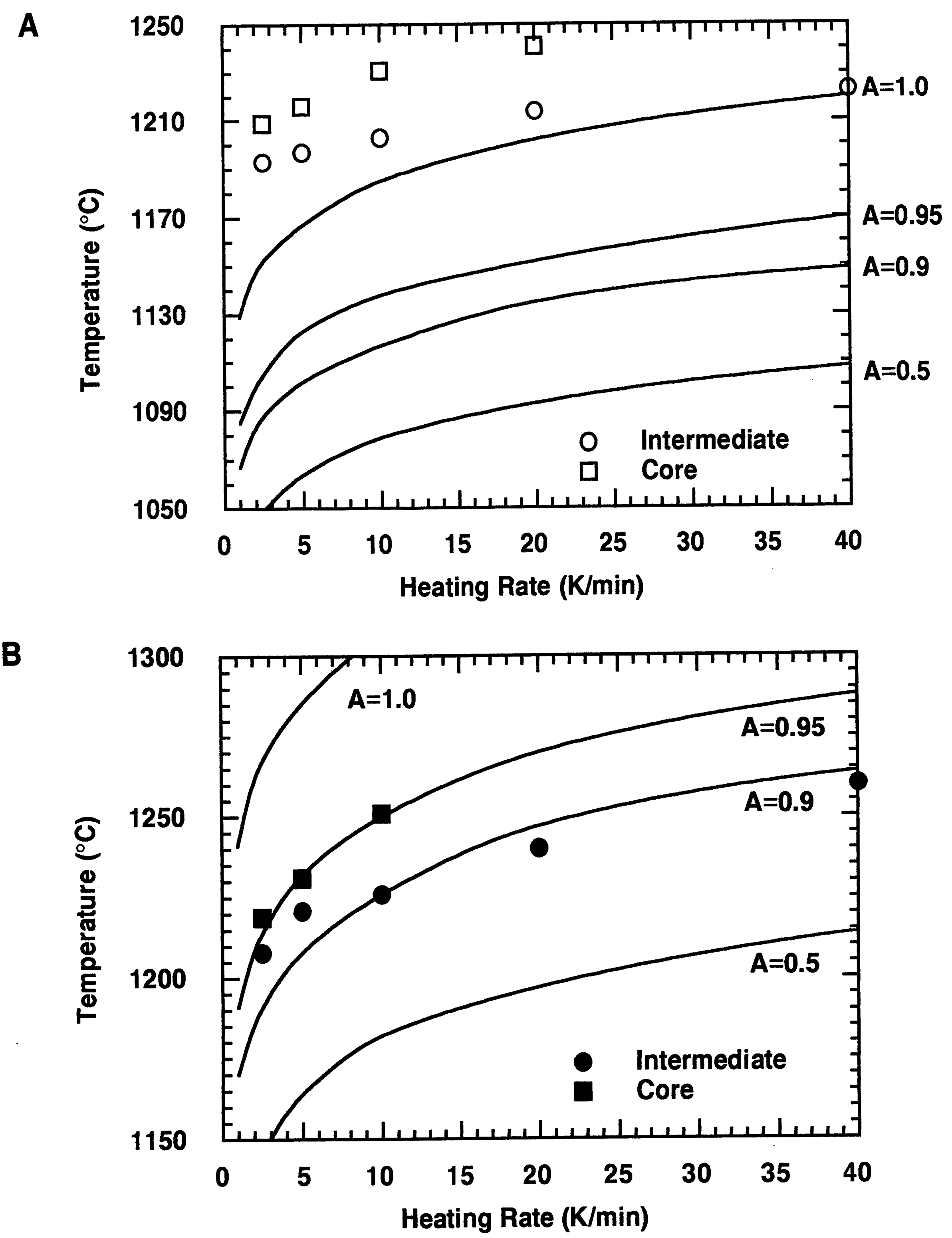

Fig. 4.21 Calculations illustrating the variation in the recrystallisation start and finish temperatures as a function of the heating rate and of the degree of anisotropy (A) in the particle dispersion.

A: Start temperatures B: Finish temperatures, Activation energy Q=700.0 kJ mol^{-1}.

4.5 Conclusions

Extruded bars of *MA6000* are found to exhibit significant variations in microstructure following secondary recrystallisation anneals. The surface regions are found to recrystallise at a more rapid rate relative to the cores of the bars. Furthermore, the recrystallised grains at the surface are more anisotropic relative to the core regions. These results can be understood if it is assumed that inhomogeneous deformation during extrusion causes a more pronounced alignment of particles at the surface regions. This interpretation has to some extent been verified using a theoretical model for recrystallisation in the presence of anisotropic dispersion of pinning particles.

References

1. Mino K., Harada H., Bhadeshia H. K. D. H. and Yamazaki M.: *Mater. Sci. Forum*, (1992), **88 - 90**, p. 1236.
2. Mino K.: Proceedings of *Plansee seminar on Refractory Metals and Hard Materials-Key to Advance Technology*, (1993), in press.
3. Hotzler R. K. and Glasgow T. K.: *Metall. Trans.*, (1982), **13A**, p. 1665
4. Baloch M.: Ph. D. Thesis, University of Cambridge, Cambridge United Kingdom, (1989).
5. Deards N. and Bhadeshia H. K. D. H.: *Mater. Sci. Forum*, (1992), **94 - 96,** p. 741.
6. Humphreys F. J.: *Met. Sci.*, (1979), **13**, p. 136
7. Humphreys F. J.: *Recrystallization '90*, T. Chandra, ed., TMS, Warrendale, PA, (1990), p. 113.
8. Zener C.: Private communication to Smith C.S.: *Trans. TMS-AIME*, (1949) **175**, p. 15.
9. Nes E., Ryum N., and Hundri O.: *Acta Metall.*, (1985), **33**, p. 11.
10. Hundri O., Nes E., and Ryum N.: *Acta Metall.*, (1989), **37**, p. 129.
11. Ashby M. F., Harper J., and Lewis J.: *Trans. TMS-AIME*, (1969), **245**, p. 413
12. Christian J. W.: *Theory of Transformations in Metals and Alloys*, Part 1, 2nd ed., Pergamon Press, Oxford (1975), p. 479.
13. Christian J. W.: *Theory of Transformations in Metals and Alloys*, Part 1, 2nd ed., Pergamon Press, Oxford (1975), p. 545.
14. *Handbook of Chemistry and Physics*, 57 ed., Weast R. C., ed., CRC Press, Cleveland, OH, USA, (1977).

CHAPTER 5

GRAIN BOUNDARY TOPOLOGY IN MECHANICALLY ALLOYED *MA6000*

5.1 Introduction

The purpose here is to investigate the role of energy stored in the primary recrystallised structure, on the shape of the grain boundaries that develop after secondary recrystallisation. The indications are that rather ragged boundaries lead to better mechanical properties, particularly creep resistance [1,2,3]. Surface tension effects normally oppose rough boundaries, but as stated earlier, *MA6000* contains a dispersion of oxide particles which at low driving forces should lead to grain boundary pinning and hence to convoluted boundaries.

5.2 Experimental

Specimens for the experiments were taken from the as-extruded and hot-rolled bar. The locations from which they were extracted were carefully selected, because the recrystallisation behavior is known to be sensitive to position in the bar [4]. Samples were therefore studied from two different locations, the intermediate region and the core region of the bar (Fig. 5.1). Recrystallisation temperatures in the core specimens are generally higher than the intermediate specimens and the grain structures there tend to be more equiaxed (Chapter 4) [4].

The stored energy was controlled by isothermal pre-annealing at relatively low temperatures (1100 - 1180 °C) where heat treatment can be conducted without recrystallisation.

The γ' solution temperature for this alloy is somewhat larger than 1160 ° C, and gross recrystallisation occurs at temperatures in excess of 1200 ° C during continuous heating at 10 K min^{-1} (the heat treatment is illustrated in Fig. 5.2). The heat treatments were carried using a differential scanning calorimeter when the pre-annealing was followed immediately by continuous heating. Otherwise, a computer controlled resistance furnace was used.

Transmission electron microscopy was carried out on thin foils or carbon extraction replicas and the microstructures were also examined using optical microscopy.

5.3 Results and Discussion

The measured effect of pre-annealing on the stored energy is illustrated in Figs. 5.3 - 5.5. As expected, the stored energy decreases with increasing time and temperature. However, the magnitude of the changes are different for the intermediate and core regions. The effects of pre-annealing up to 1160 ° C on the stored energy are not very large and are almost the same for both regions. For pre-annealing beyond 1160 ° C, the changes during pre-annealing increase with increasing temperature in the intermediate specimens. This contrasts with smaller dependence of the stored energy on the pre-annealing temperature for the core specimens. Representative TEM micrographs are shown in Figs. 5.6 and 5.7, with corresponding average grain sizes are given in Table 5.1. Except for the 1180 ° C annealed intermediate specimens, the DSC measurements correspond well with the TEM observations. This is because the early stages of recrystallisation take place during pre-annealing in the intermediate specimens (Figs. 5.8, and 5.9). These localised recrystallisation events, which obviously occurred during pre-annealing, must be expected to influence any subsequent recrystallisation at high temperatures. Optical micrographs of representative pre-annealed intermediate specimens which were then heated at 10 K min^{-1} to complete the recrystallisation process are shown in Figs. 5.10 and 5.11. It is clear that the effects of pre-annealing on the intermediate specimens are much larger than on the core specimens.

In the intermediate specimens, there are two main effects of pre-annealing. Firstly, there are noticeable changes in the grain size. There is a refinement of the microstructure, together with a lesser degree of anisotropy, as the pre-annealing is increased in excess of 1170 ° C. On the other hand, for samples pre-annealed below 1160 ° C, the fully recrystallised structures are found to be coarser; the grain widths are noticeably larger. This is because pre-annealing below 1160 ° C stimulates only a few nucleation sites but no significant grain growth occurs. These few nuclei can grow rapidly under the influence of a large stored energy. Therefore, coarse grain structures are obtained. Beyond this pre-annealing temperature, grain growth can take place anywhere, giving rather equiaxed grain structures in the fully recrystallised samples. Large grains are observed along local particle free zones and isolated larger grains are seen amongst fine grains in the intermediate specimen pre-annealed at 1160 ° C. These local inhomogeneity must be very important during the early stages of nucleation.

As mentioned earlier, after the 1180 ° C pre-annealing heat treatment, very large grains are seen to grow at the expense of the fine grains. Core specimens, however, even after the 1180 ° C anneal remained uniform in grain structure. It seems that the differences in microstructures are mainly due to inhomogeneity of particle distribution. In Chapter 4, it was shown that randomly particle dispersed structures have higher recrystallisation temperatures compared with regions where the particles are aligned. Details about the actual particle characterisation in the alloy are presented in Chapter 6. In addition to the above effects, the recrystallised grain boundaries seem to become more ragged as the stored energy is reduced by pre-annealing. Representative, high magnification comparisons of smooth and rough boundaries are presented in Figs. 5.12 and 5.13.

The increased raggedness of the grain boundaries at low stored energy is expected, since the driving force for grain boundary motion is reduced relative to any pinning force due to oxide particles. This should make the pinning effects more pronounced and hence obvious in the microstructure.

Table 5.1 Average grain size

Heat Treatment	Intermediate (μm)	Core (μm)
As-received	0.28	0.27
1160 ° C, 60 min	0.30	0.29
1180 ° C, 60 min	0.31	0.29

Further data from the calorimetric experiments on the recrystallisation temperatures are presented in Figs. 5.14 and 5.15. Representative DSC peaks due to recrystallisation are shown in Figs. 5.16 and 5.19. They reveal that recrystallisation during continuous heating becomes easier as the amount of pre-annealing is increased. This is not surprising given that the elevated temperatures involved during pre-annealing initiate recrystallisation on a microscopic scale, and hence makes further secondary recrystallisation easier during continuous heating.

Different pre-annealing data are presented in Fig. 5.14, for specimens which are pre-annealed, furnace cooled to room temperature and then heated up to 1300 °C. The recrystallisation temperatures are much higher compared with directly heated samples, while the stored energies and recrystallised structures are very similar or somewhat larger (Figs. 5.3 and 5.18). The reason for this is not clear and it cannot be attributed to carbide dissolution and precipitation. For example, as shown in Fig. 5.19, there are at least two kinds of carbide in the as-received alloy (Fig. 5.19.A); one is a Cr-rich carbide also containing Mo, Ni and W (Type 1), the other is a Ti-rich carbide also containing Ta (Type 2). The Cr rich carbides dissolve after annealing at 1160 °C for 60 min (Fig. 5.19 B). By contrast, the Ti rich carbides (Type 2) exist at every stage of heat treatment, and their compositions are almost identical for all the carbides. As illustrated in Fig. 5.19 C, there are other carbides, of irregular shape and with a composition which is the Ti-rich but with substantial quantities Cr (Type 3) in specimens annealed at 1160 °C followed by furnace cooling. These carbides perhaps precipitate during cooling, but were not found in a specimen reheated to 1210 °C before recrystallisation (Fig. 5.19 D). Type 3 carbides were identified to be $M_{23}C_6$ by X-ray diffraction of extracted particles (Fig. 5.20). There are no significant differences in the particle size distributions between the specimen once furnace cooled after pre-annealing followed by continuous heating, and the sample pre-annealed and water quenched (Fig. 5.21, pre-annealing temperature 1180 °C). Different heat treatments may give different distributions of particles, but the onset of recrystallisation was not much affected. On the other hand, the differences were found to affect final recrystallised structures.

Fig. 5.22 shows that the grain width goes through a maximum as more intense pre-annealing treatments were applied. The error bars in the diagram stand for the maximum and the minimum values of measured apparent widths. The effect of a short pre-anneal is to cause a sudden rise in grain width, because the pre-annealing induces a few recrystallisation nuclei without much change in stored energy. These few nuclei therefore grow rapidly during the high temperature treatment, giving the sudden rise in grain size. Further pre-annealing causes a reduction in grain size because it is accompanied by a decrease in stored energy which reduces the grain growth rates. This in turn allows more nuclei to develop independently, giving grain refinement and a more equiaxed grain microstructure.

5.4 Conclusions

The effect of a pre-annealing heat treatment below the temperature at which significant recrystallisation begins, is to reduce the stored energy. However, the pre-annealing process does, on a microscopic scale, initiate the recrystallisation process, and hence subsequent gross recrystallisation is accelerated.

There are two other consequences of the reduced stored energy. Firstly, the recrystallised grain boundary topology becomes relatively rough as the driving force for grain boundary motion is reduced relative to the pinning force due to oxide particles. Secondly, due to the associated reduced grain boundary velocity, recrystallisation is able to develop from many different sites during subsequent continuous heating, giving a more refined ultimate microstructure. By contrast, at large stored energies the grain growth velocity is so large that the few grains which begin their growth first are able to swamp all others, giving a coarse grain structure.

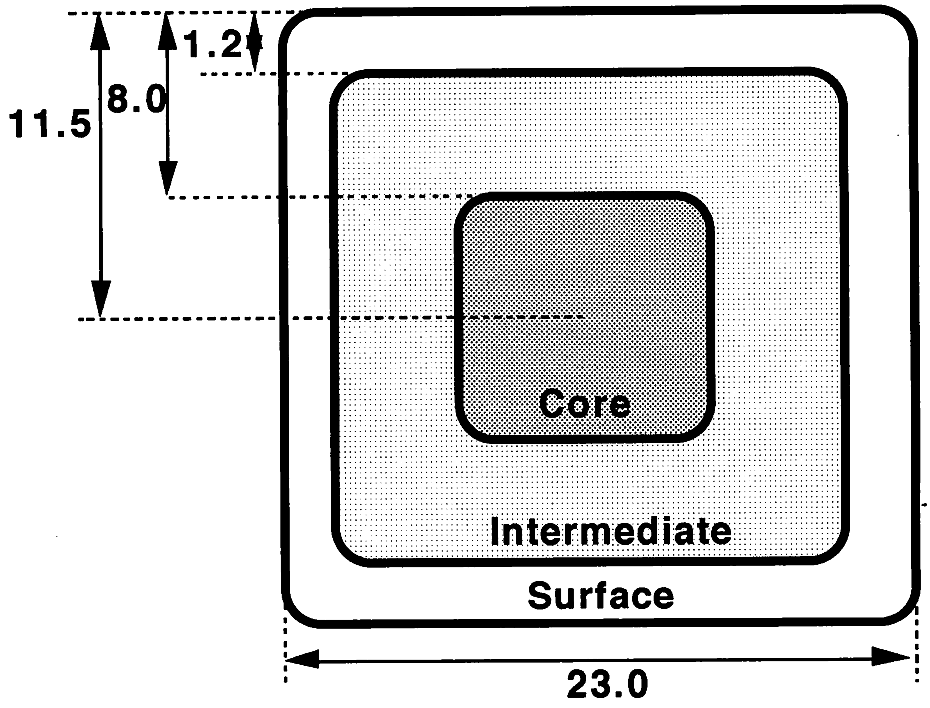

Fig. 5.1 Illustration of the surface, intermediate and core samples extracted from as received *MA6000* bar. The extrusion direction is normal to the page.

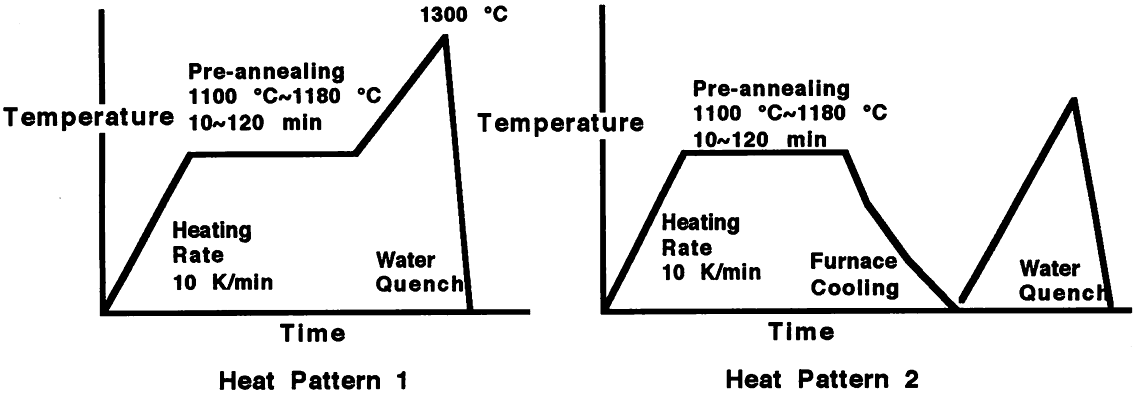

Fig. 5.2 Schematic illustration of the heat treatments used.

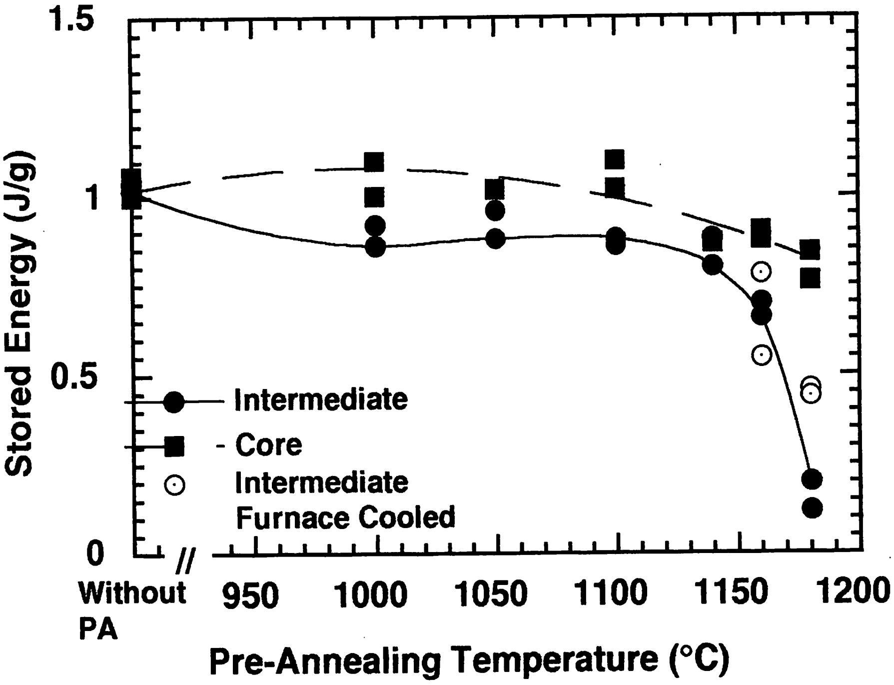

Fig. 5.3 Variation in stored energy as a function of pre-annealing temperature, for a time period of 60 min. PA stands for pre-annealing.

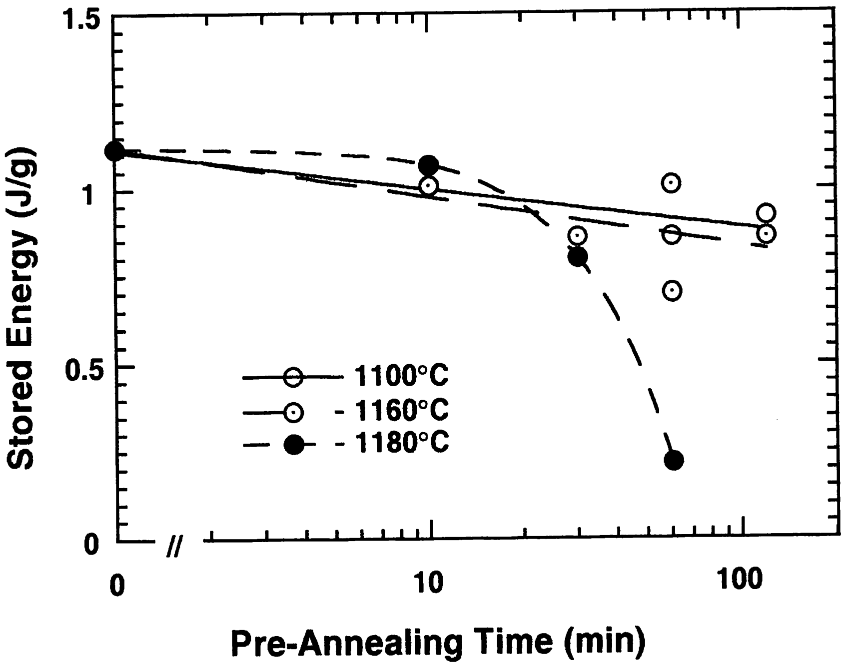

Fig. 5.4 Stored energy as a function of pre-annealing temperature and time for the intermediate specimens.

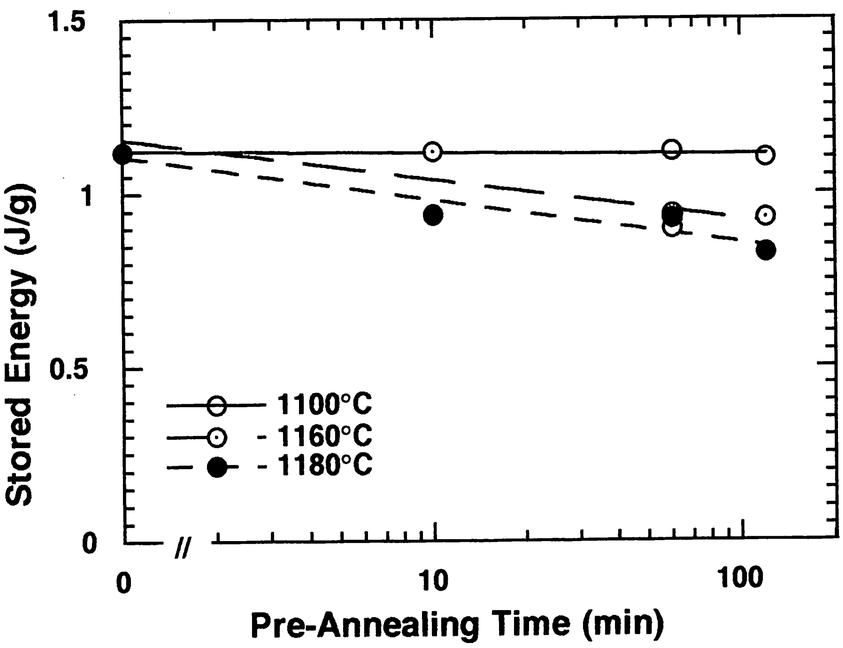

Fig. 5.5 Stored energy as a function of pre-annealing temperature and time for the core specimens.

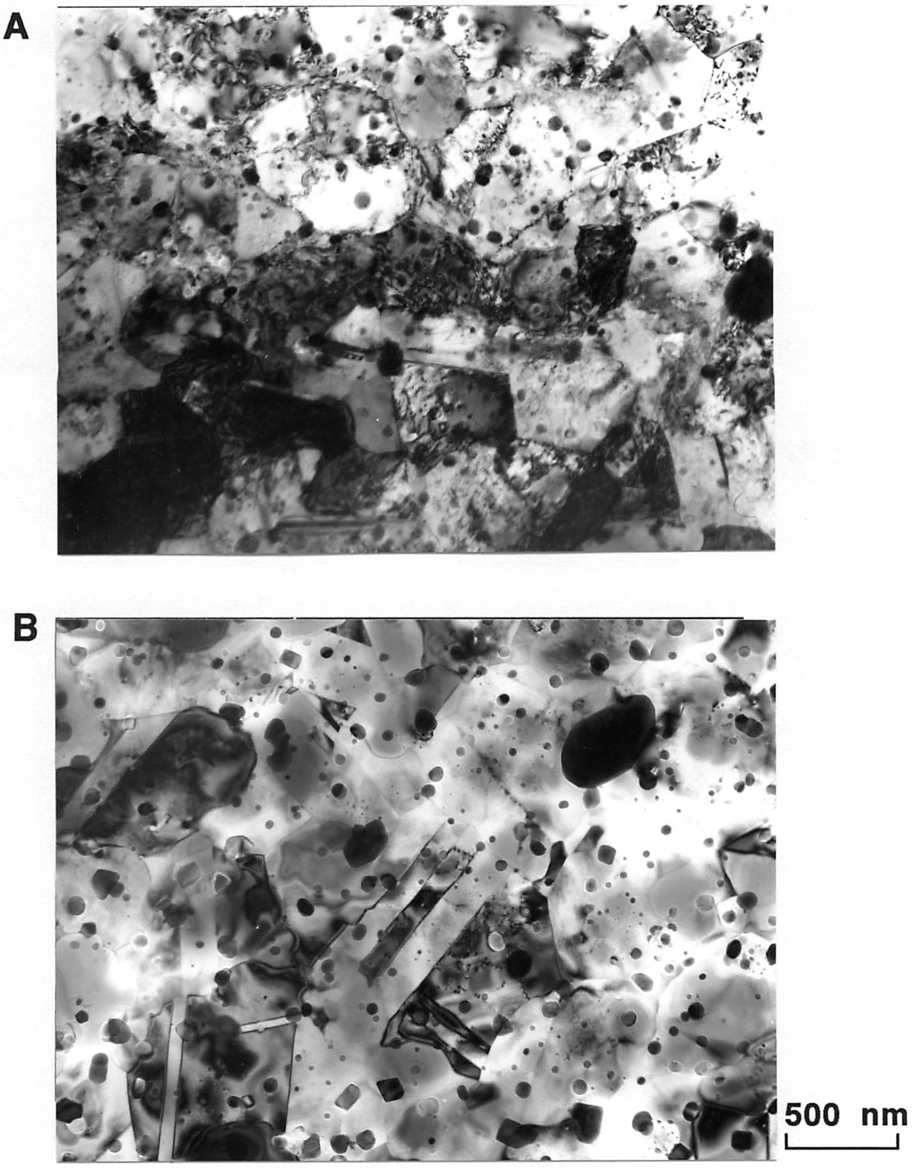

Fig. 5.6 TEM micrographs illustrating the unrecrystallised grain structures of the intermediate specimens.

A: As-received

B: Annealed at 1180 °C for 60 min and water quenched.

Extrusion direction is normal to the page.

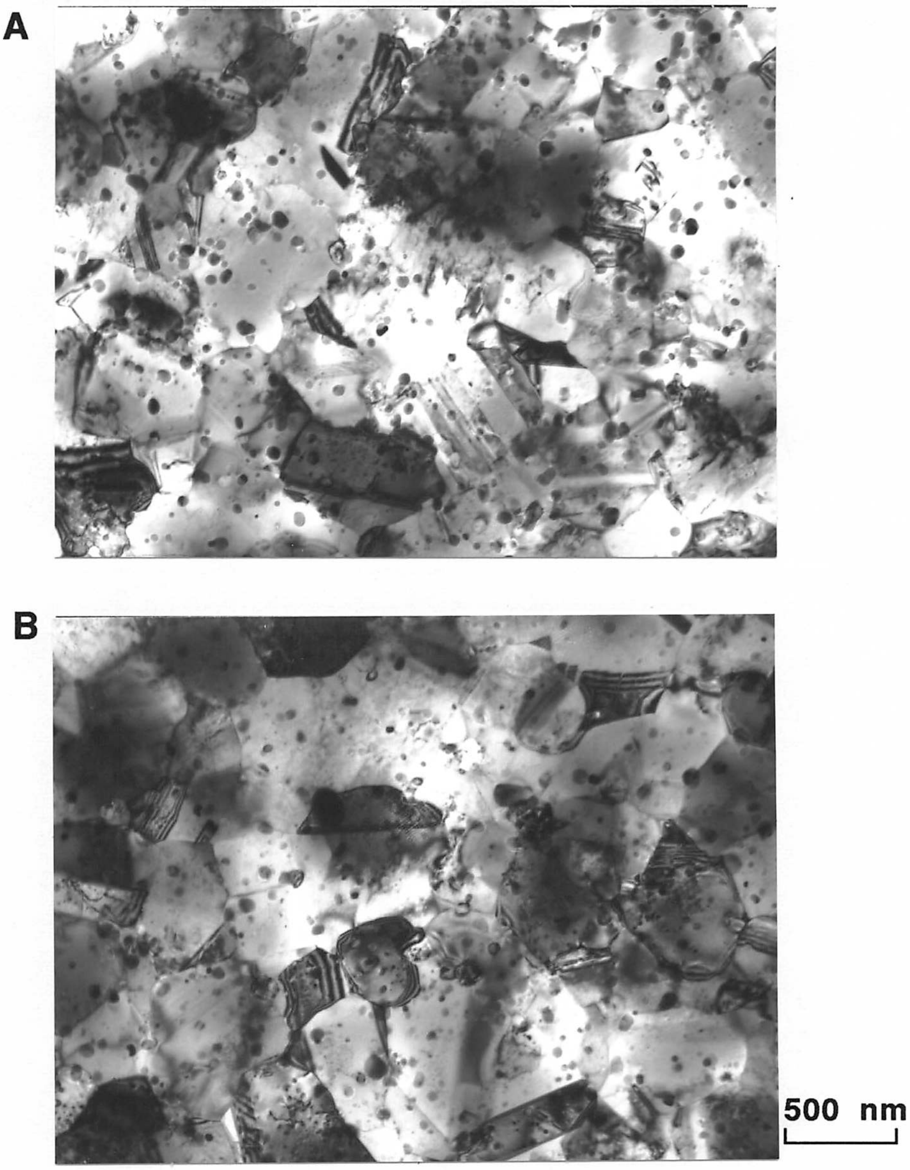

Fig. 5.7 TEM micrographs illustrating the unrecrystallised grain structures of the core specimens.

A: As-received

B: Annealed at 1180 °C for 60 min and water quenched.

Extrusion direction is normal to the page.

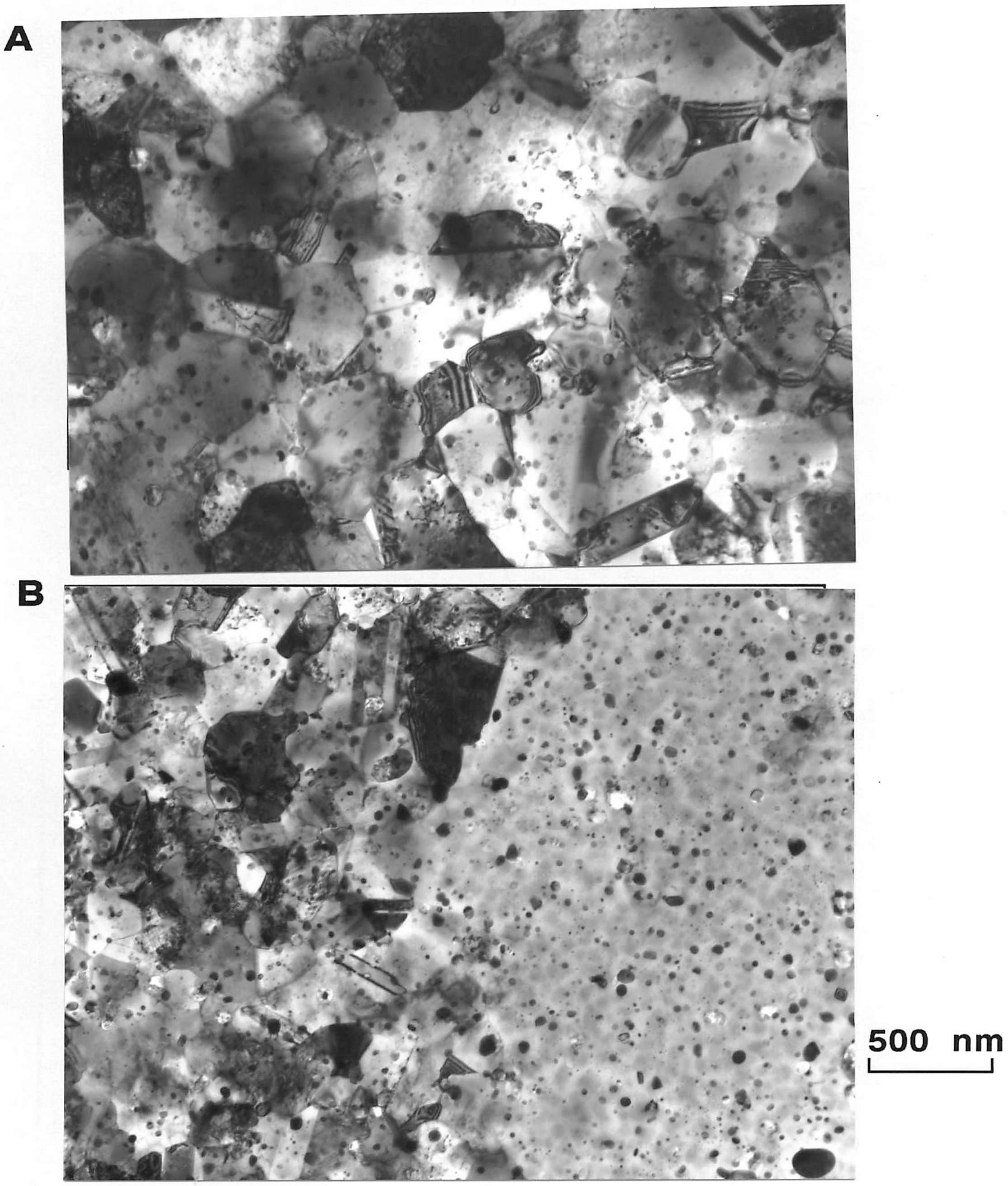

Fig. 5.8 TEM micrographs illustrating the unrecrystallised grain structures of the intermediate specimens.

A: Annealed at 1160 °C for 60 min and water quenched.

B: Annealed at 1180 °C for 60 min and water quenched.

Extrusion direction is normal to the page.

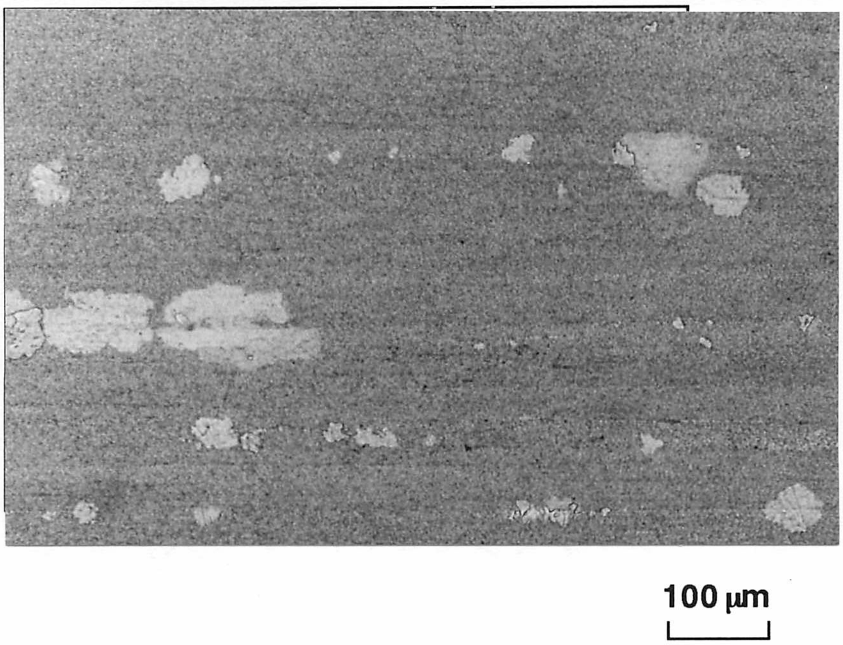

Fig. 5.9 Metallographic data illustrating the early stages of recrystallisation taking place during isothermal pre-annealing. Intermediate specimen, annealed at 1180 °C for a time period of 60 min.

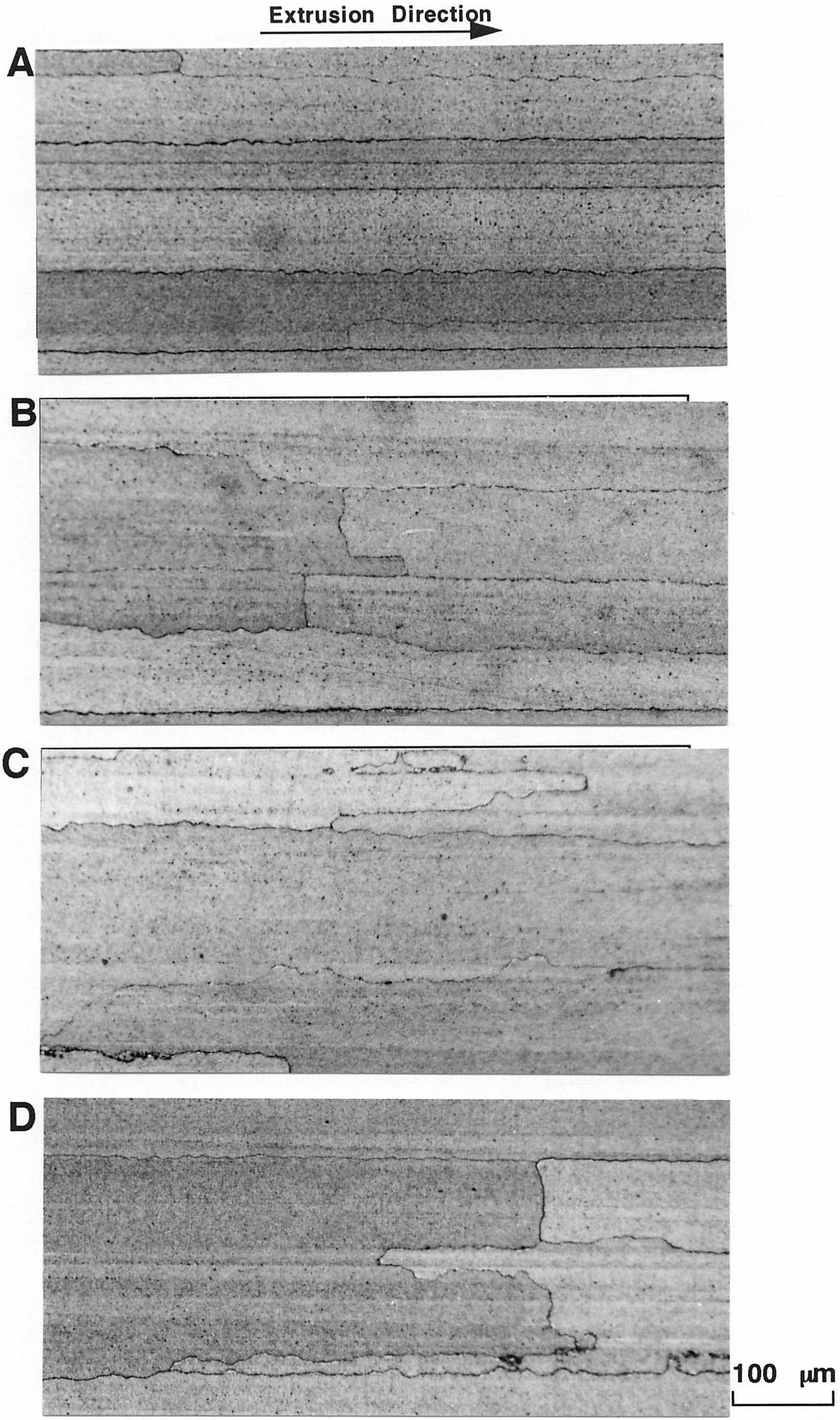

Fig. 5.10 Metallographic data from pre-annealed specimens of the intermediate specimens which were then fully recrystallised. Pre-annealed at;
A: Without pre-annealing B: 1000 °C C: 1050 °C D:1100 °C
for a time period of 60 min.

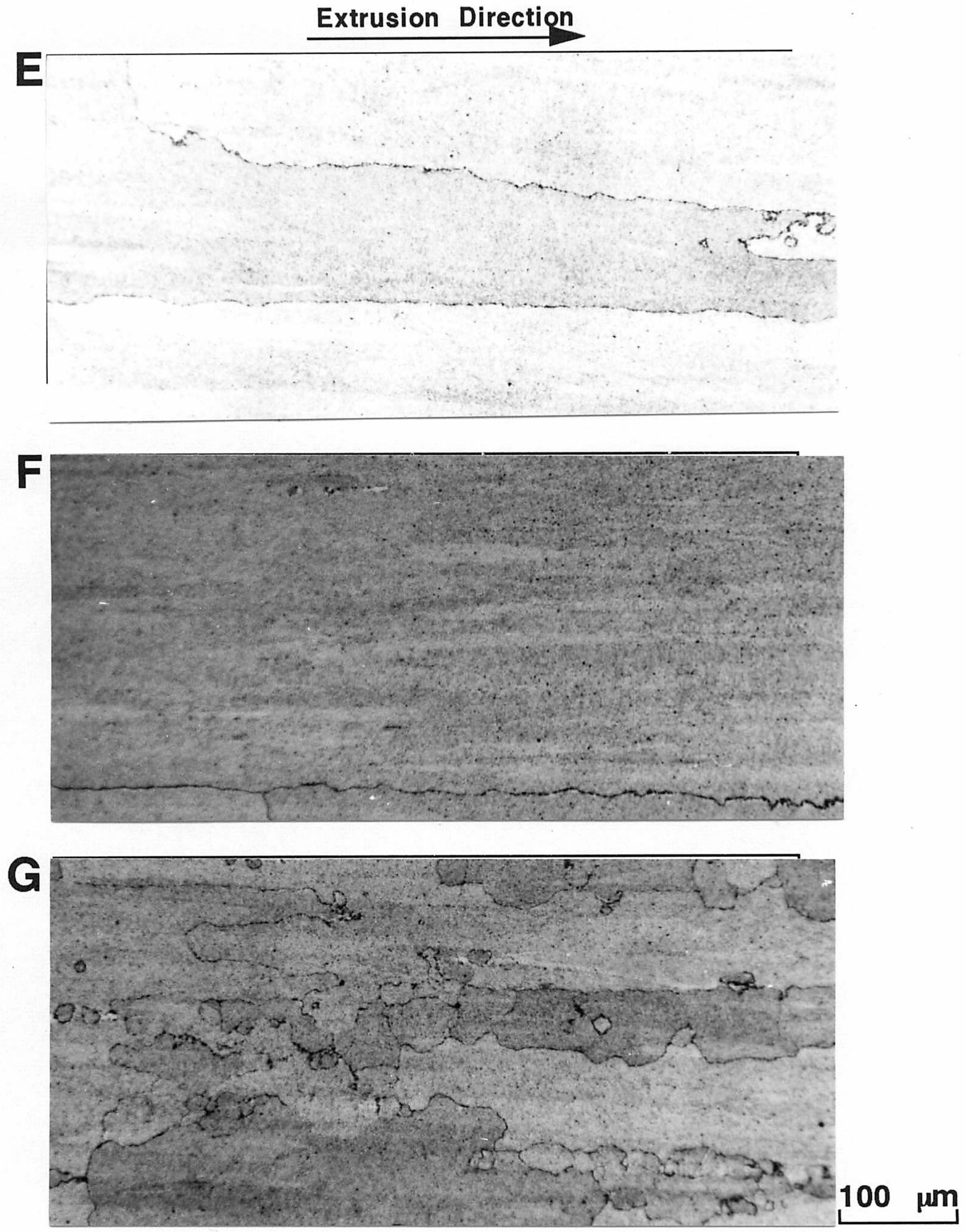

Fig. 5.10 Metallographic data from pre-annealed specimens of the intermediate specimens which were then fully recrystallised. Pre-annealed at;
A: Without pre-annealing B: 1140 °C C: 1160 °C D:1180 °C
for a time period of 60 min.

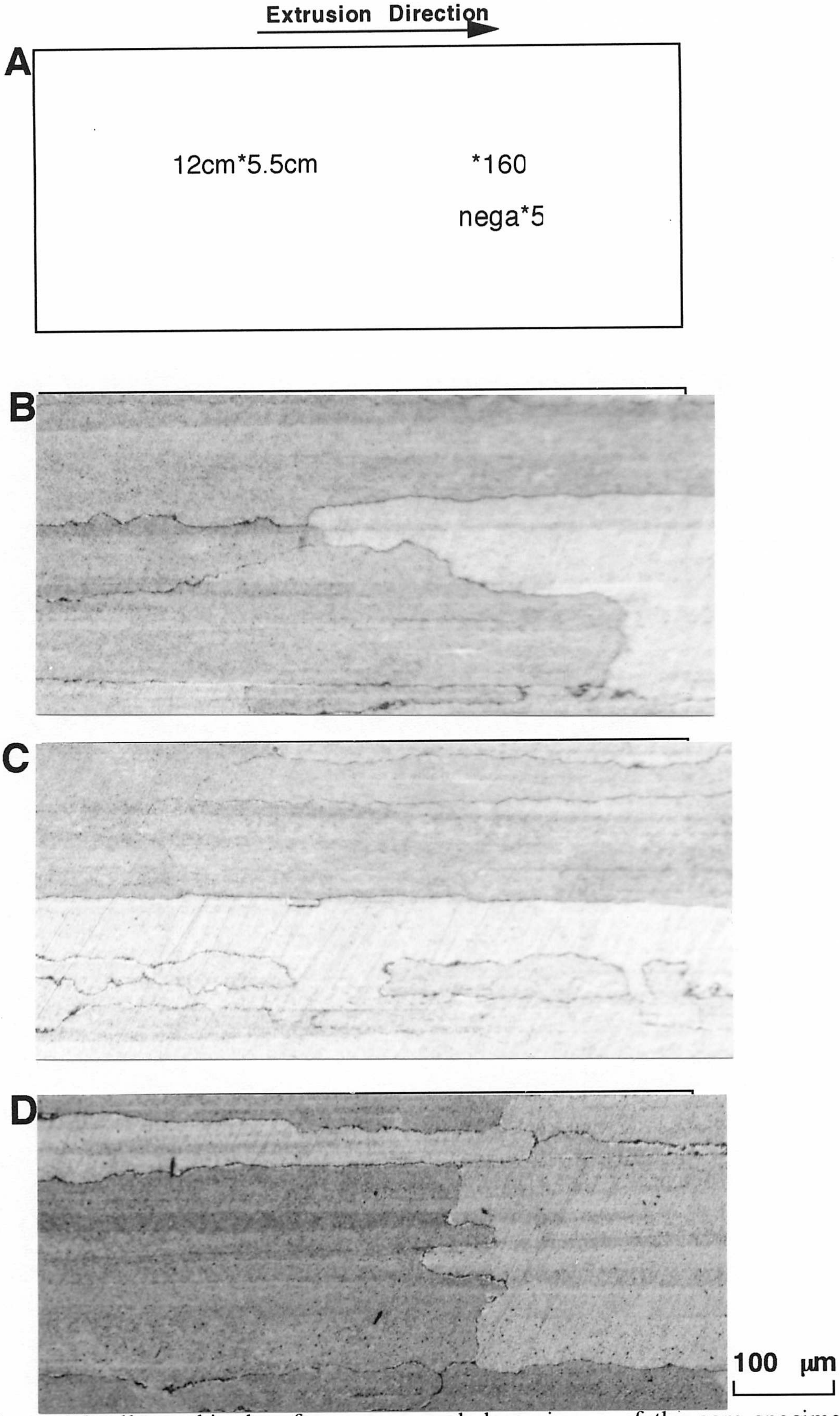

Fig. 5.11 Metallographic data from pre-annealed specimens of the core specimens which were then fully recrystallised. Pre-annealed at;
A: Without pre-annealing B: 1000 °C C: 1050 °C D:1100 °C
for a time period of 60 min.

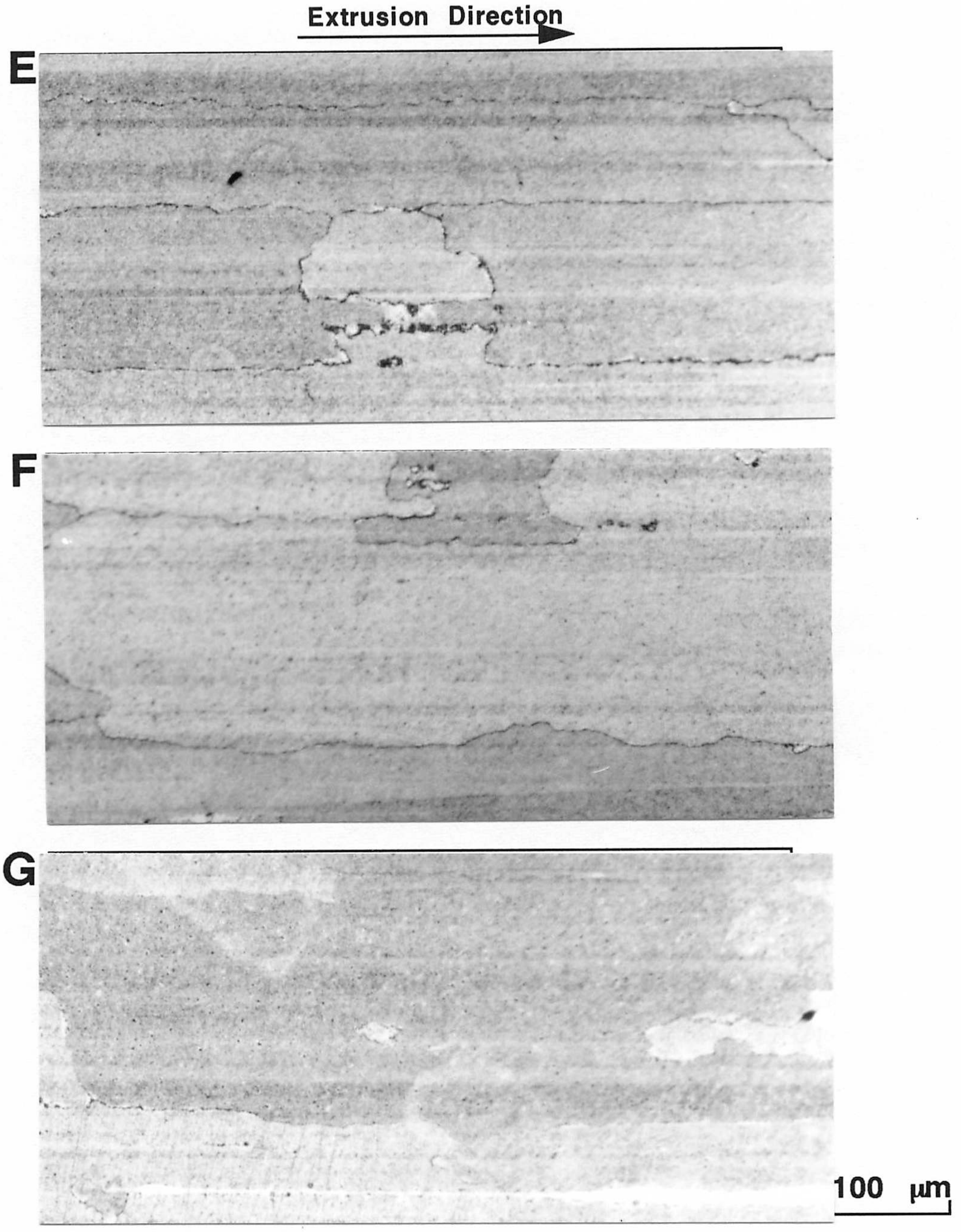

Fig. 5.11 Metallographic data from pre-annealed specimens of the core specimens which were then fully recrystallised. Pre-annealed at;
A: Without pre-annealing B: 1140 °C C: 1160 °C D:1180 °C
for a time period of 60 min.

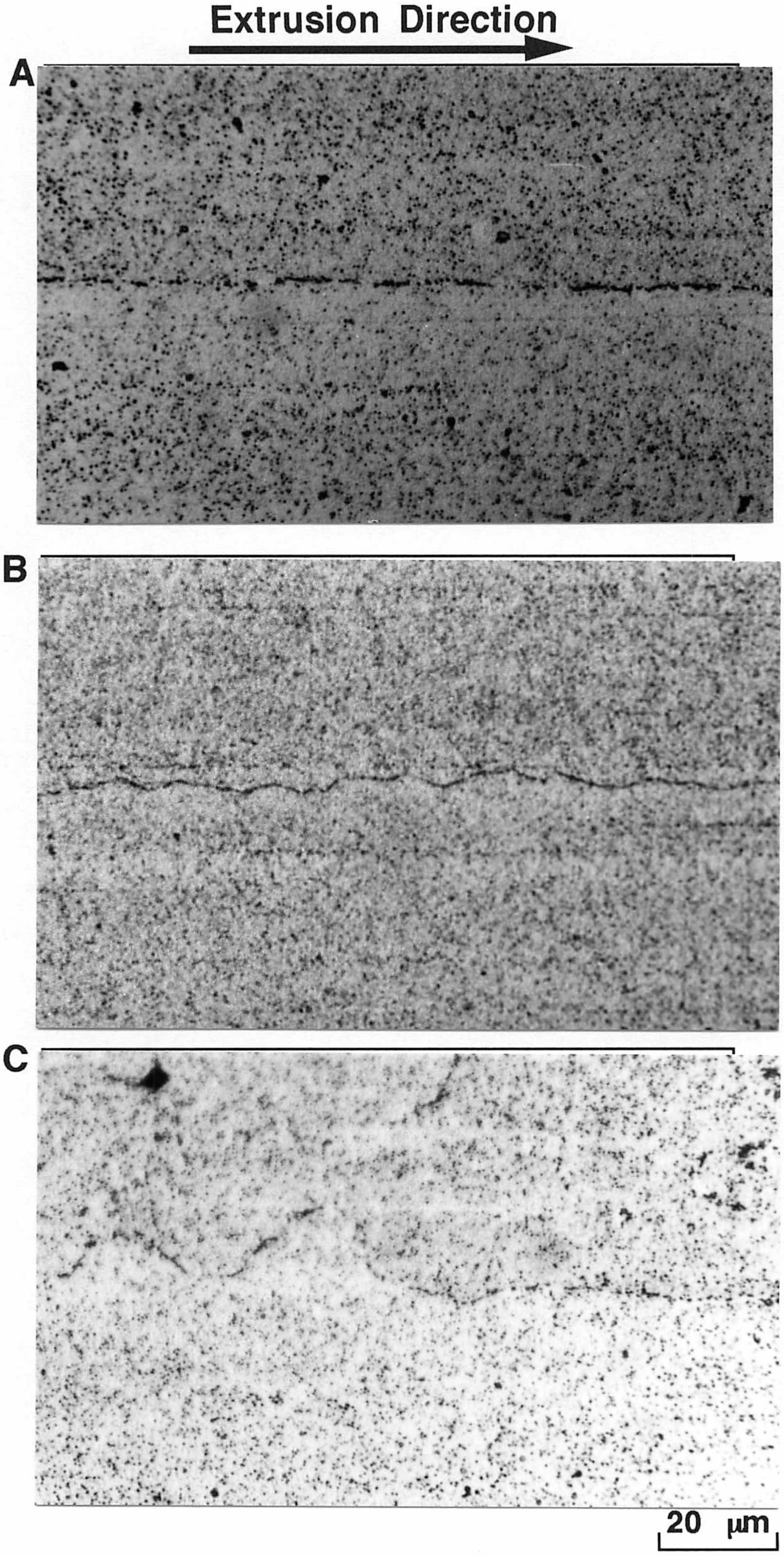

Fig. 5.12 Grain boundary topology of the intermediate specimens, pre-annealed and recrystallised. Pre-annealed at;
A: Without pre-annealing B: 1100 °C C: 1180 °C
for a time period of 60 min.

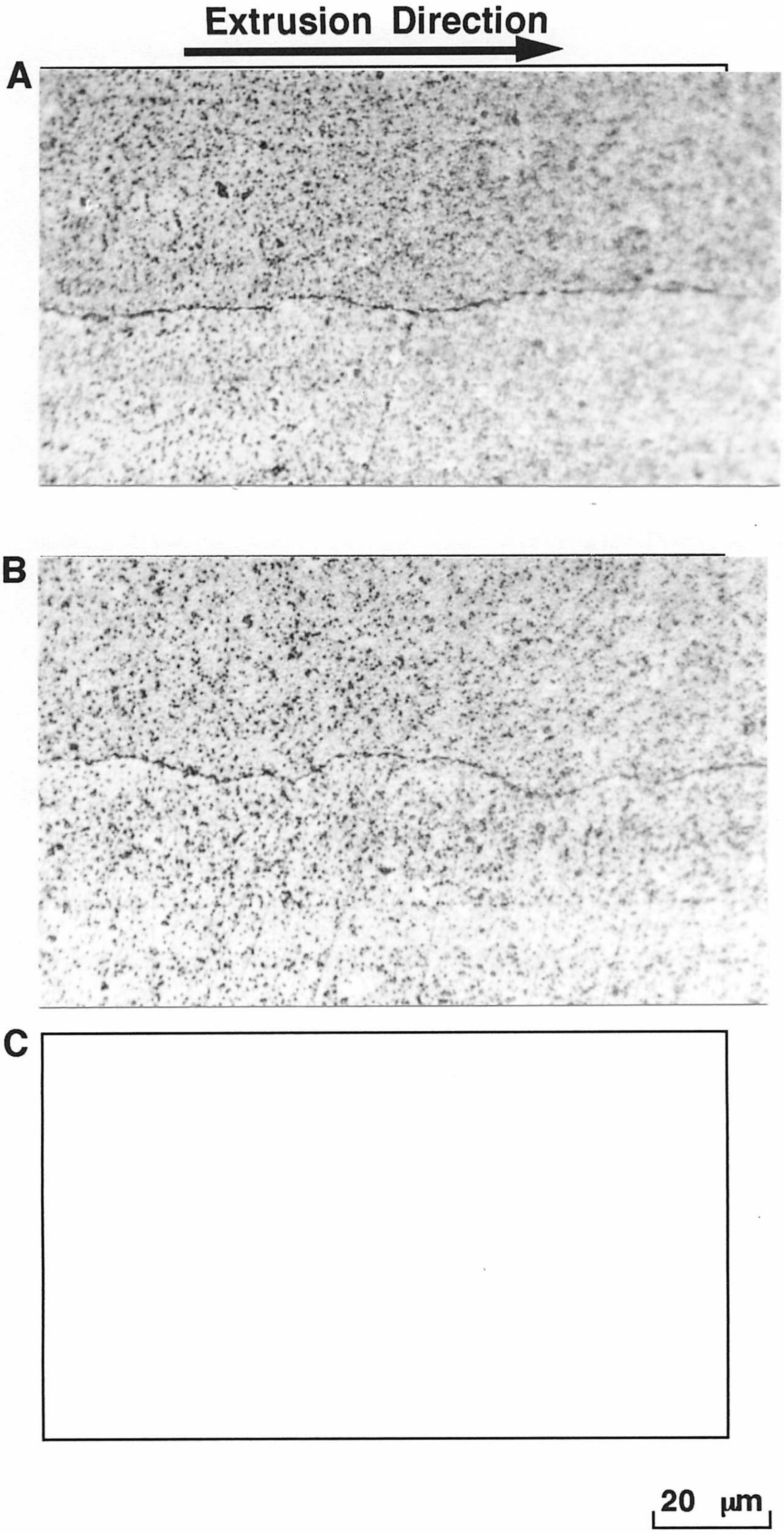

Fig. 5.13 Grain boundary topology of the core specimens, pre-annealed and recrystallised. Pre-annealed at;
A: Without pre-annealing B: 1100 °C C: 1180 °C
for a time period of 60 min.

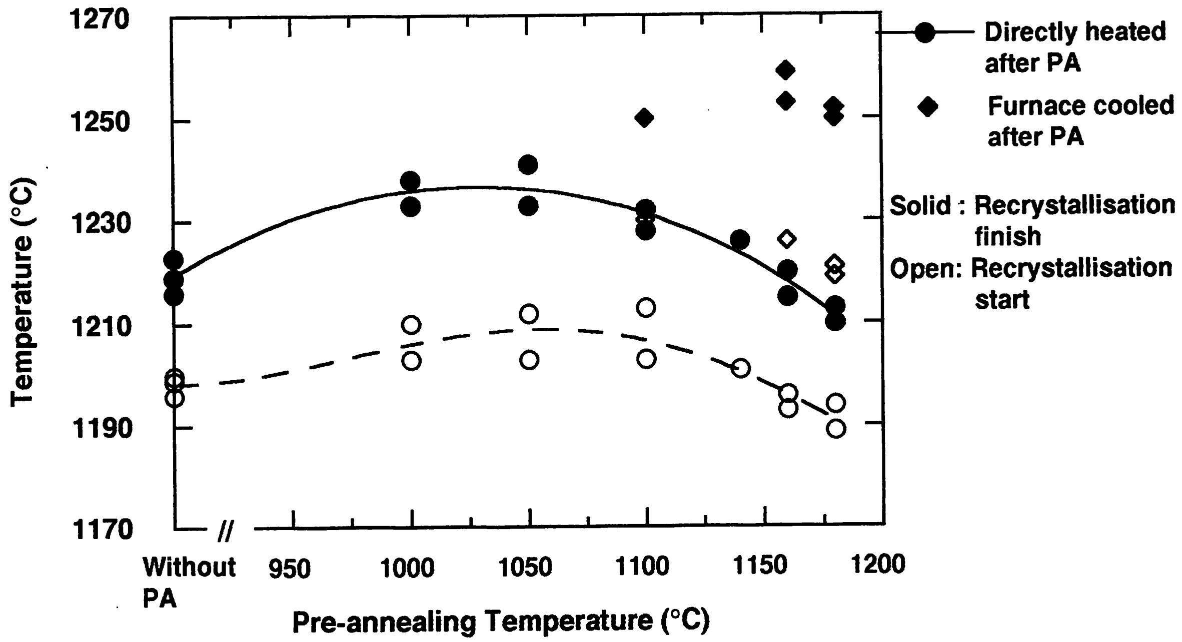

Fig. 5.14 Recrystallisation start and finish temperatures on the intermediate specimens as a function of pre-annealing temperature, for a time period of 60 min. PA stands for pre-annealing.

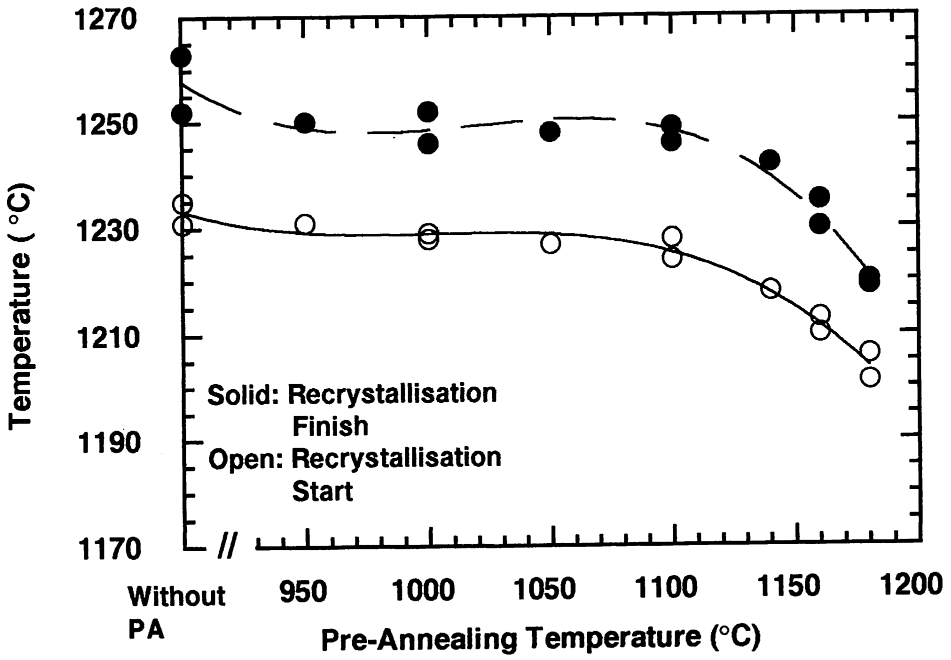

Fig. 5.15 Recrystallisation start and finish temperatures on the core specimens as a function of pre-annealing temperature, for a time period of 60 min. PA stands for pre-annealing.

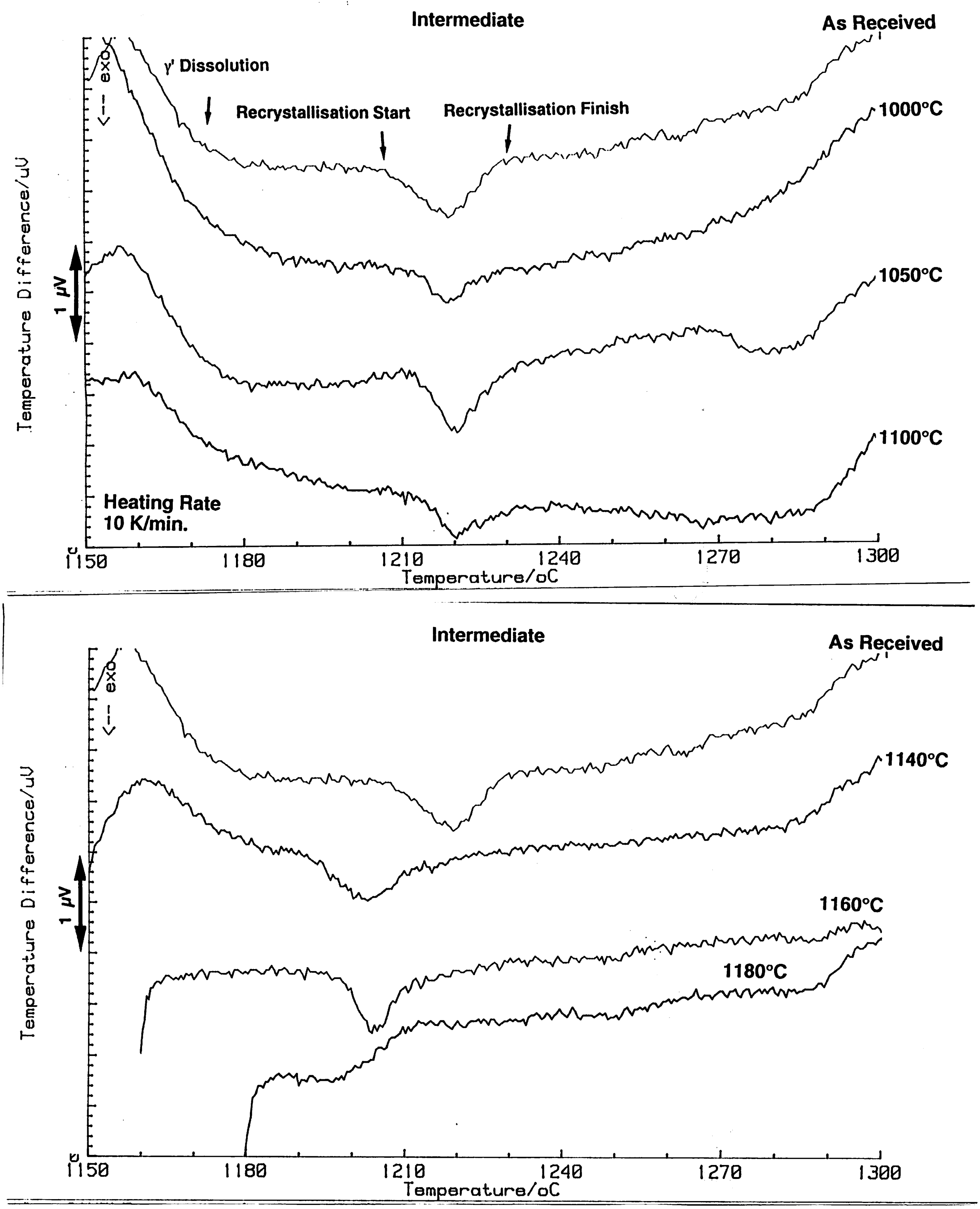

Fig. 5.16 DSC peaks of the intermediate specimens due to recrystallisation after pre-annealing and then continuously heated up to 1300 °C at the heating rate 10 K min^{-1}.

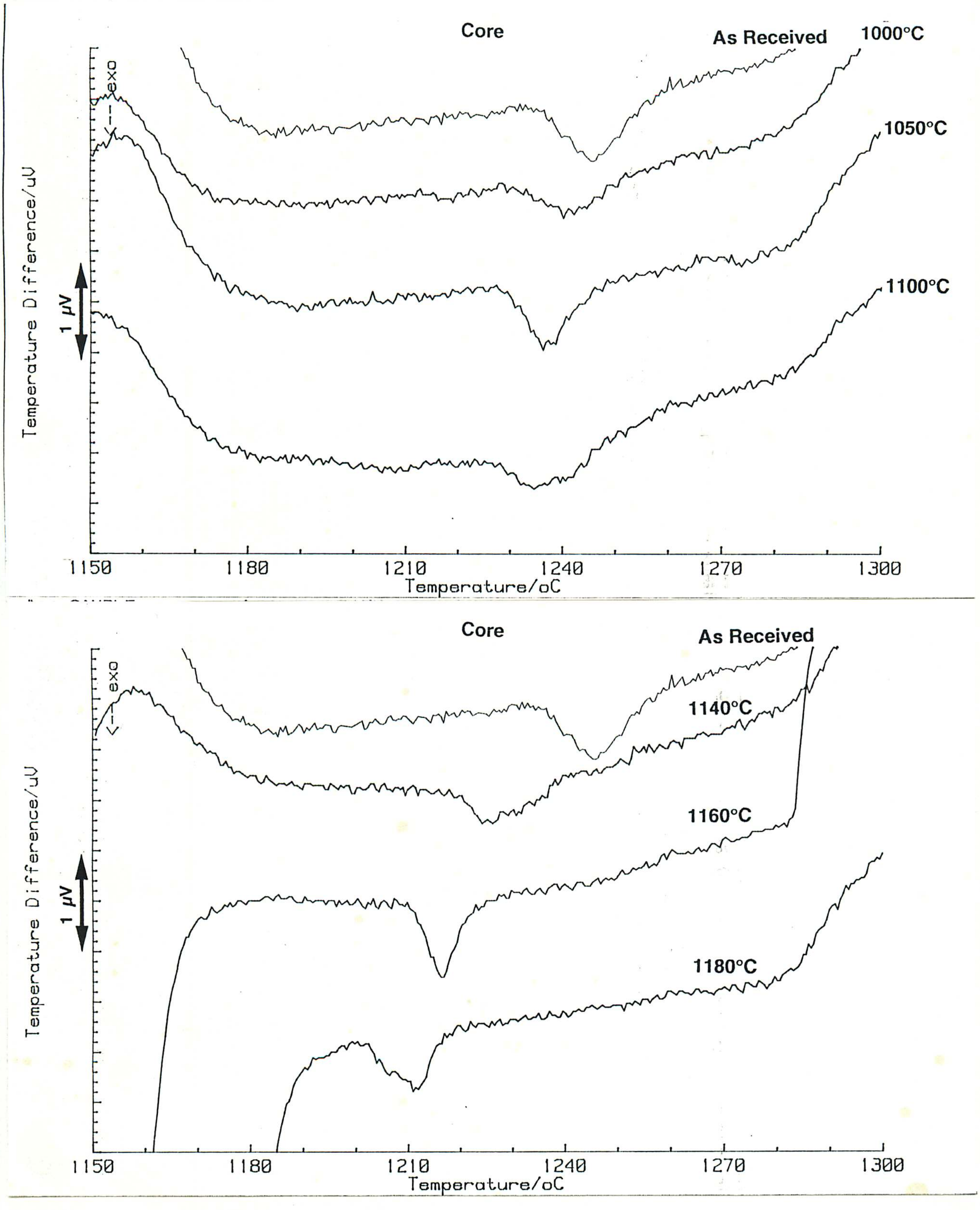

Fig. 5.17 DSC peaks of the core specimens due to recrystallisation after pre-annealing and then continuously heated up to 1300 °C at the heating rate 10 K min^{-1}.

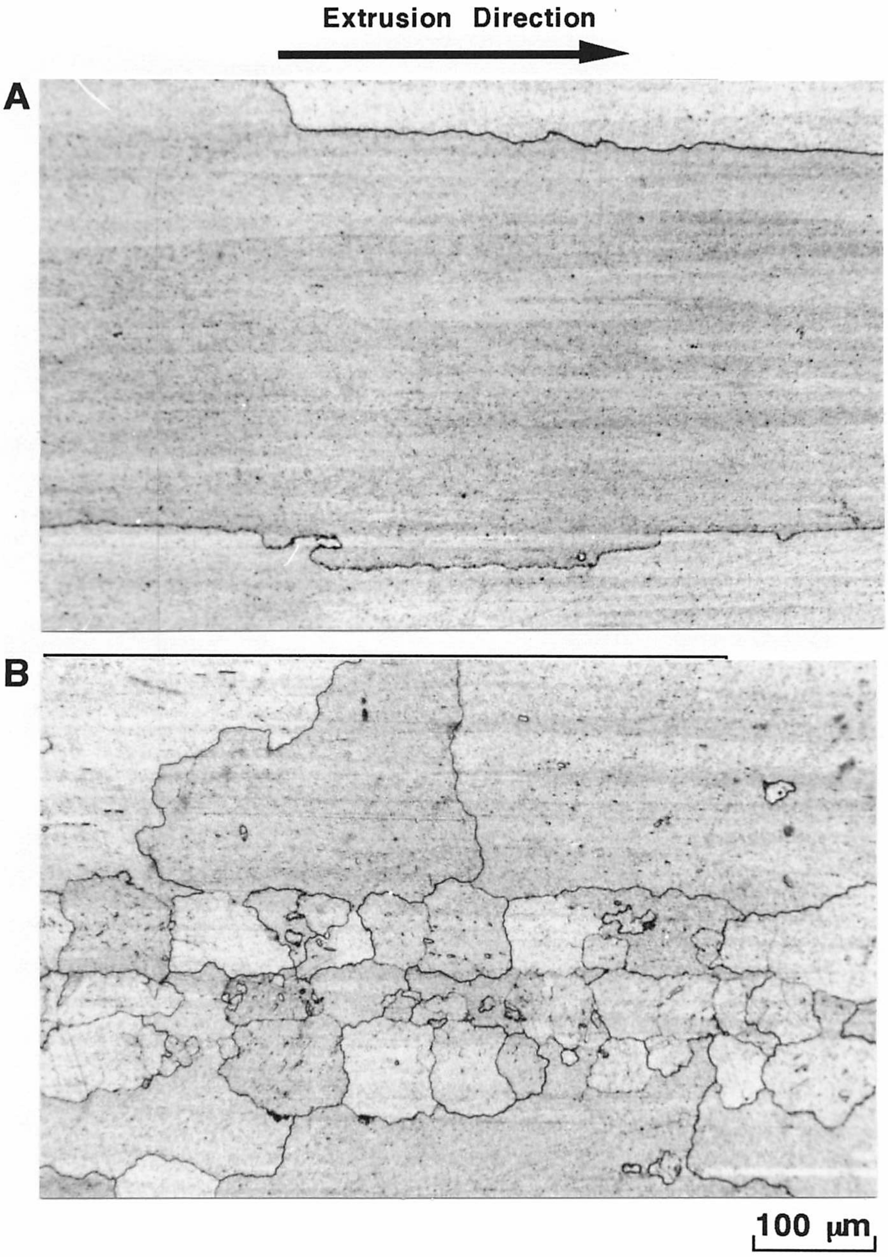

Fig. 5.18 Metallographic data from pre-annealing experiments on the intermediate specimens. Furnace cooled to room temperature and then heated to complete recrystallisation. Pre-annealed at;

A: 1160 °C B: 1180 °C

for a time period of 60 min.

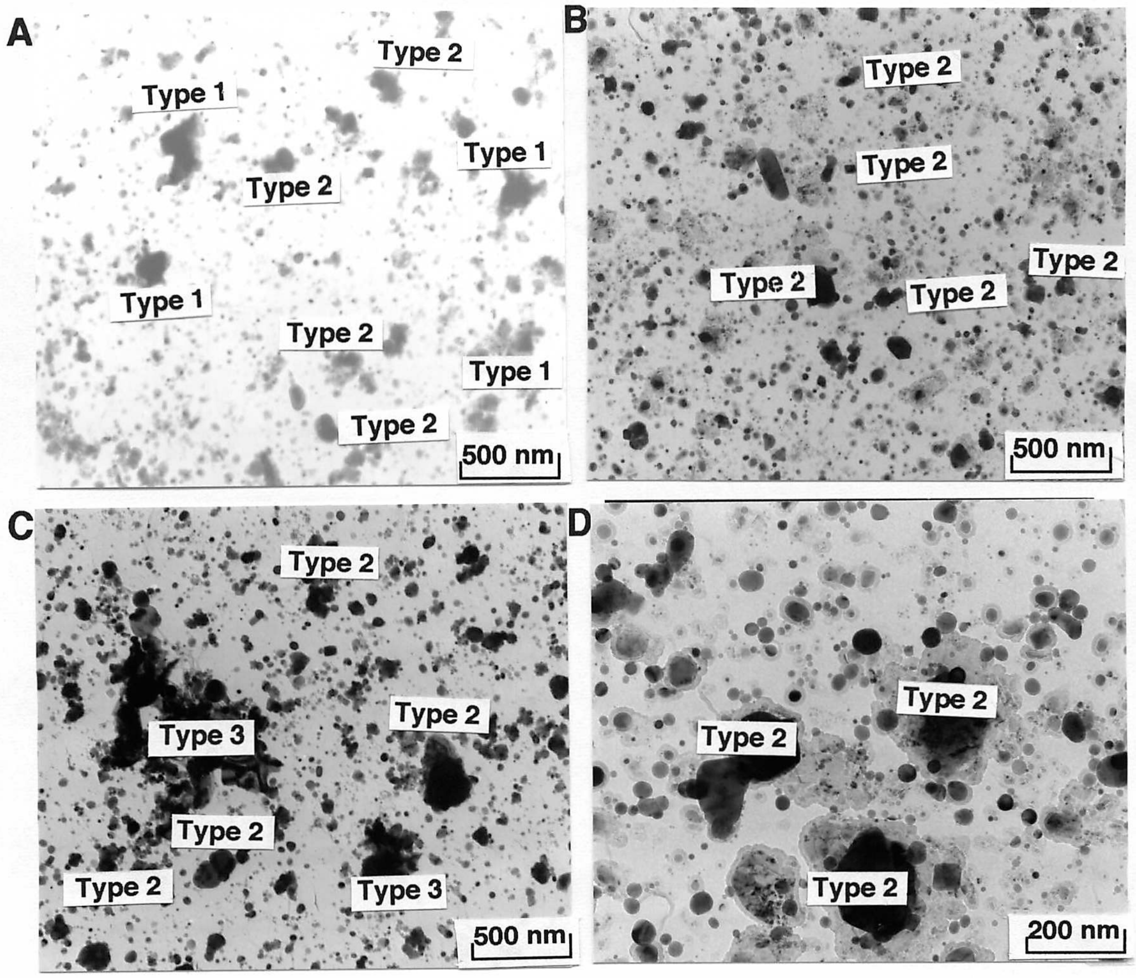

Fig. 5.19 Large particles in extraction carbon replicas of the intermediate specimens.

A: As-received

B: Isothermally annealed at 1160 °C and water quenched, unrecrystallised.

C: Isothermally annealed at 1160 °C and furnace cooled, unrecrystallised.

D: As A but then heated up to 1210 °C and water quenched, unrecrystallised.

Relative atomic percent ratio for the metallic elements in particles are;

Type 1: $Cr_{80 - 90}$-$Mo_{5 - 10}$-$Ni_{5 - 10}$-$W_{5 - 10}$

Type 2: $Ti_{90 - 95}$-$Cr_{0 - 5}$-$Ta_{0 - 10}$

Type 3: $Ti_{50 - 70}$-$Cr_{30 - 50}$-(Ni, Ta, Mo, W)$_{10}$

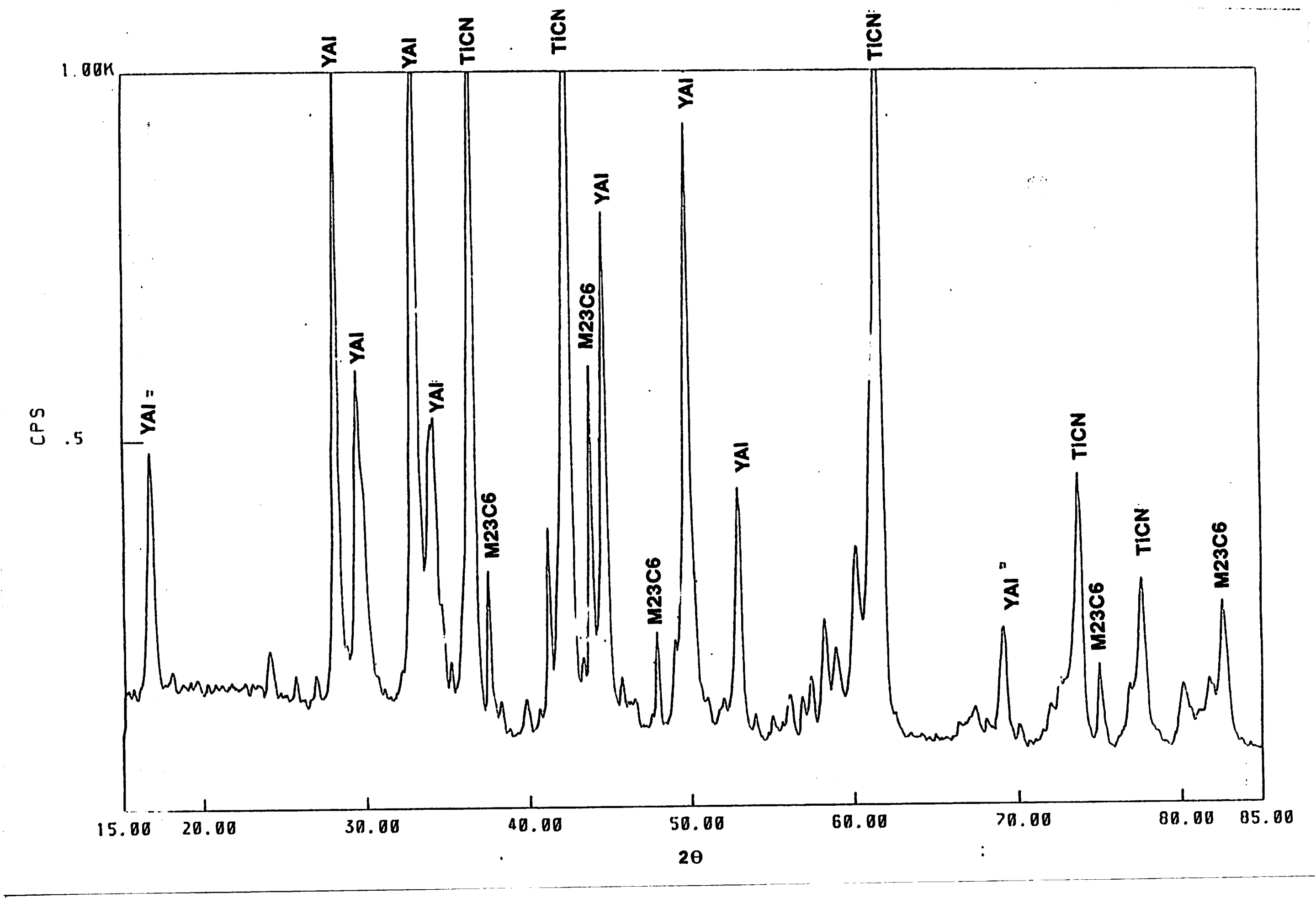

Fig. 5.20 The X-ray diffraction analysis of extractions in the continuously heated to 1160 °C and furnace cooled intermediate specimen.

The abbreviations are as follows:

M23C6: $M_{23}C_6$

YAl: Y_2O_3-Al_2O_3 mixed oxide

TiCN: Ti(C,N)

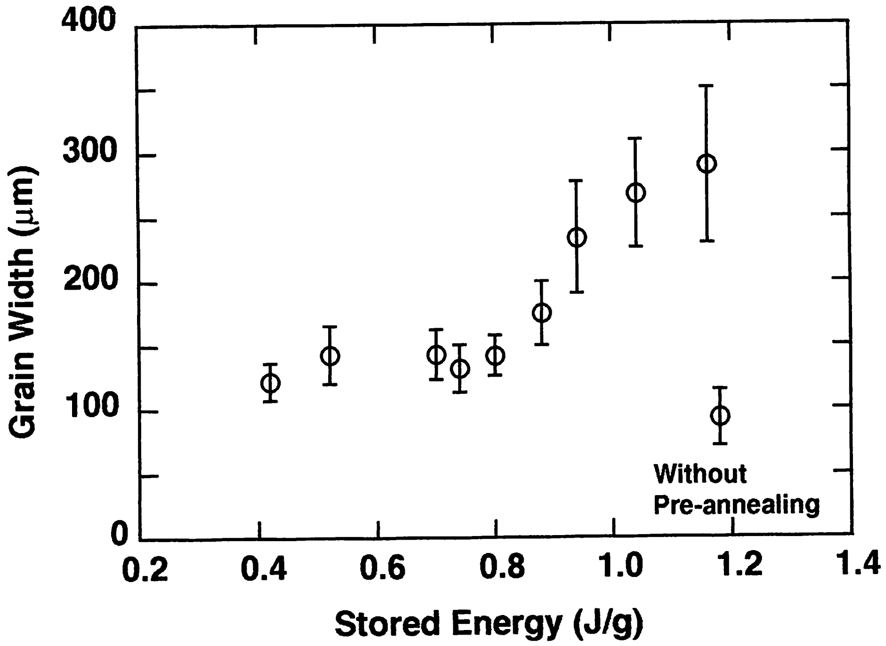

Fig. 5.21 Comparison of particle distributions between two heat treatments.

Heat treatment 1: Annealed at 1160 °C for a time period of 60 min and furnace cooled, and then heated up to 1180 °C again and water quenched.

Heat treatment 2: Annealed at 1160 °C for a time period of 60 min and water quenched.

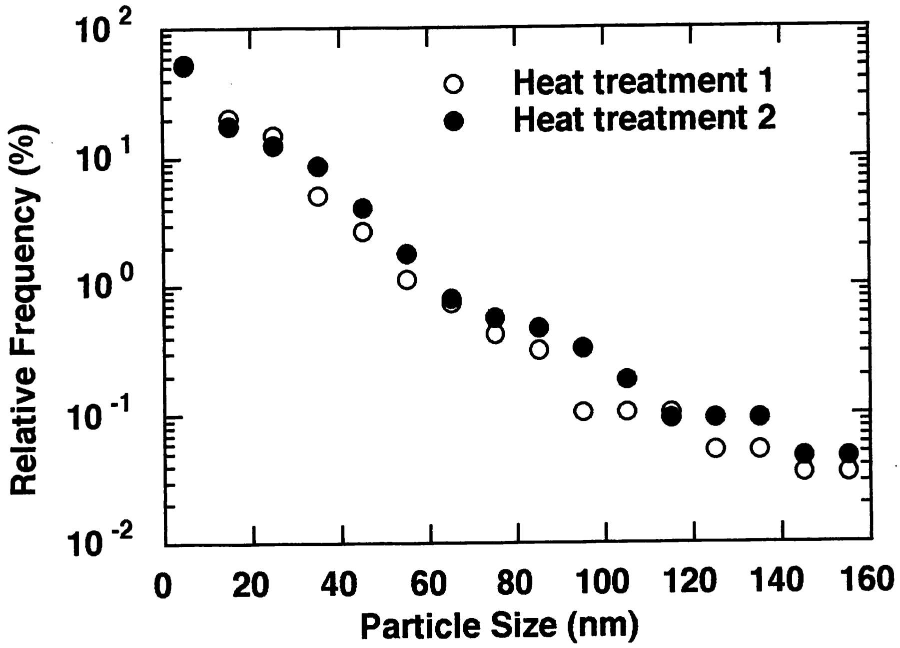

Fig. 5.22 Plot of the recrystallisation grain width as a function of stored energy for the intermediate specimens. The maximum and the minimum values are shown as the error bars.

References

1. Tanaka M., Iizuka and Ashihara H.: *Trans. Iron Steel Inst. Japan.*, **28**, (1988), p. 129
2. Suresh S.: *Metall. Trans. A*, **14**, (1983), p. 2375
3. Tanaka M., Iizuka and Ashihara H.: *J. Mater. Sci.*, **23**, (1988), p. 3827
4. Murakami K., Mino K., Harada H., and Bhadeshia H.K.D.H.: *Metall.Trans. A*, **24**, (1993), p. 1049

CHAPTER 6

CHANGES IN PRECIPITATES AND DISPERSED PARTICLES DURING HEAT TREATMENT

6.1 Introduction

The purpose here is to investigate any changes in the size, the distribution and chemical composition of precipitates and dispersed particles as a function of the heat treatment, in order to clarify their effects on recrystallisation behaviour. Hence, the investigation focuses on detailed comparisons of the microstructure before and after recrystallisation. Continuous heating and isothermal annealing experiments were carried out, using two kinds of specimens which were extracted from the same bar, but from different locations. This is because recrystallisation in *MA6000* has been found very sensitive to the location of the sample in the cross section of the extruded bar (Chapter 4) [1].

Fine yttria particles are introduced into *MA6000* during mechanical alloying in order to enhance the mechanical properties at elevated temperatures. The alloy also contains many carbide or nitride forming elements (Ti, Ta, Cr, Mo, W) and oxide forming elements (Ti, Al, Si). In addition, the mechanical alloying production method introduces contamination which is difficult to avoid. All of these particles need to be considered in the context of the recrystallisation process.

It is reported that yttrium oxide in nickel base superalloys is not as stable as had originally been anticipated [2, 3, 4, 5]. For example, it reacts with Al in the matrix to form a variety of mixed Y-Al oxides [3, 4]. The size distributions also change during heat treatment and coarsening has been reported [3, 4, 5]. It has also been reported that carbides (MC, $M_{23}C_6$) occur together with yttrium oxide in the as-received condition of *MA6000*, and that several volume percent of Ti(C,N) persists even after recrystallisation [2].

6.2 Experimental Method

Two kinds of specimens were machined from the as-extruded and hot-rolled bar; from the 'intermediate region' and the 'core region' within the cross-section of the bar (Fig. 6.1). As noted in Chapter 4, the recrystallisation temperatures of the core specimens tend to be higher than those of the intermediate specimens, and the grain structures tend to be more equiaxed [1].

The heat treatments are illustrated in Fig. 6.2. Reactions at high temperatures were measured using a differential scanning calorimetry (DSC: NETZSCH 404/301/11). The specimens for metallographic examination and analysis were heat treated using a computer controlled resistance furnace. The heat treatment atmosphere was flowing He at 50 ml min^{-1} in the DSC and Ar in the silica tubes in which the samples were sealed prior to furnace heat treatment.

An etching mixture of 2 g $CuCl_2$ in 40 ml HCl and 80 ml ethanol at 25 °C was used for optical microscopy and during the preparation of carbon extraction replicas. A reproducible etch for both metallography and for carbon extraction replicas was obtained by controlling the etching time at 30 seconds. Carbon extraction replicas were taken from the etched surfaces. The long edges of the carbon films were taken to be parallel to the extrusion direction, this makes it convenient to identify the extrusion direction in TEM micrographs.

Transmission electron microscopy (Phillips 400 T, 120 kV) was carried out on carbon extraction replicas and thin foils. An energy dispersive X-ray analyser (EDX: LINK system) with the TEM was used to identify the chemical compositions of the heavy elements present in the particles. An electron probe microanalyser (EPMA: JEOL 6400) was also used for composition analysis.

X-ray diffraction analysis of extracted phases was carried out using a Rigaku GFX-RAD3C machine.

Particle size distributions and volume fractions were measured using 5 randomly selected areas each at a magnification of 100,000 times for those particles in the size range 10 - 1000 nm, and 500000 times for the 2 - 30 nm size range. Particle sizes were determined using the following methods; Circular particles: diameter, Oval shapes: average of long diameter and short diameter, Irregular shape: average of the largest and the shortest projected dimensions. A total of 10000 particles was typically analysed for each specimen.

The apparent (stereologically uncorrected) volume fractions of particles were measured by a point counting method using the same photographs as far the particle size measurements. Projected points onto each photograph were counted, with a total of 400 points per field.

6.3. Results

6.3.1 Reactions at High Temperatures

Typical DSC curves for the intermediate and the core specimens are illustrated in Fig. 6.3 for continuous heating at 10 K min^{-1}. Three reactions are apparent: an endothermic peak around 1100 °C, an endothermic reaction between 1100 °C and 1160 °C corresponding to γ' dissolution, and an exothermic peak beyond 1200 °C due to recrystallisation [1,6]. The γ' dissolves gradually from about 1000 °C, the gradual decline in the curve corresponding to the changes in specific heat capacity as γ' dissolves [7,8,9]. As explained later, the endothermic peak near 1100 °C is due to $M_{23}C_6$ carbide dissolution, which is almost completed at 1120 °C.

6.3.2 Recrystallisation Temperatures

Metallographic data from continuously heated specimens have been found to compare well with DSC experiments. Recrystallisation was not observed in either the intermediate or core specimens up to 1190 °C at the heating rate 10 K min^{-1}. By 1230 °C , the intermediate specimens fully recrystallised but not the core specimens, which had to be heated to 1270 °C to complete recrystallisation (Figs. 6.4 and 6.5).

Isothermal annealing experiments were also carried out, at 1160 °C and 1180 °C where the γ' is in solution. Holding at these temperatures for less than 60 min caused no significant recrystallisation (Fig. 6.6). Annealing at 1160 °C causes no recrystallisation even after 3000 min (Fig. 6.6 B).

Table 6.1 Summary of metallographic experiments

		1120 °C	1160 °C	1190 °C	1230 °C	1270 °C
Continuous heating.	Intermediate	$M_{23}C_6$ dissolution	γ' dissolution	Just before recrystallisation	Recrystallisation completed	Recrystallisation completed
	Core	$M_{23}C_6$ dissolution	γ' dissolution	No recrystallisation	Just before recrystallisation	Recrystallisation completed
Isothermal heating. (Intermediate samples)		1160 °C			1180 °C	
	60 min	No recrystallisation			Partial recrystallisation	
	3000 min	No recrystallisation			(no experiment)	

The intermediate specimens recrystallised when annealed for longer than 60 min and for correspondingly shorter times when annealed at higher temperatures [1]. Partial recrystallisation was seen in several cases of specimens annealed for 60 min at 1180 °C. The core specimens never recrystallised at 1180 °C even when held at the temperature for 1440 min (1 day) [1]. The metallographic data are summarised in Table 6.1.

6.3.3 Particles in the As-received Alloy

Various sizes and shapes of particles are found in both the intermediate and the core specimens (Figs. 6.7, 6.8). The regions illustrated contain a uniform dispersion of particles but Fig. 6.9 shows another region where the distribution is not homogeneous.

The black dots aligned along the extrusion direction in the metallographic data (Figs. 6.4 and 6.5) correspond to the particles which have white contrast in the SEM secondary electron image (Fig. 6.10) with sizes of the order of several μm. These very large particles do not contain oxygen, their main metallic elements being Cr, Mo, Ni and W (Fig. 6.11). They are identified as $M_{23}C_6$ type carbides from their compositions and X-rays diffraction analysis of extractions.

Examples of the EDX results from finer particles (< 1 μm) are shown in Figs. 6.12. There are essentially four kinds of particles which can be distinguished by their chemistry. They are;

Type A: Cr-rich, Cr-Mo-Ni-W

Type B: Ti-rich, Ti-Cr-Ta

Type C: Y-Al

Type D: Y-Zr-Al.

The particle identifications were also confirmed using the X-ray diffraction analysis of extracted phases (Fig 6. 13). Type A particles are $M_{23}C_6$ carbides, and type B are TiC, TiN and probably TaN from their compositions [2]. Types C and D are mixed oxides Y_2O_3-Al_2O_3, in which the dominant phase appeares to be $YAlO_3$ (hexagonal), the remainder being $Y_4Al_2O_9$. It is reported that four kinds of mixed Y_2O_3-Al_2O_3 oxides ($Y_3Al_5O_{12}$, $YAlO_3$ perovskite, $Y_4Al_2O_9$, and $YAlO_3$ hexagonal) are found in *MA6000*, and that every oxide can contain up to 13 at. % zirconium [3,4]. Therefore it is difficult to identify the kind of oxide from the chemistry alone.

Type A particles are typically several hundred nm in diameter, although finer $M_{23}C_6$ (< 50 nm) particles could also be found, but the fraction was not found to be high, at less than 0.10. More than half of particles within the size range 50 - 200 nm were of type B. Approximately a quarter of the small particles (< 30 nm) are of type B, the rest being type C and D at sizes range than 200 nm. Some pure Al_2O_3 particles were also observed as shown in Fig. 6.14. There were no pure Y_2O_3 particles in the size range 20 - 200 nm. Some of the small particles less than 20 nm in size may be pure Y_2O_3, but the data are imprecise, because of the lack of characteristic X-ray emissions from such small particles.

More than 90 % of the particles are found to be very small, less than 30 nm size in all of the as-received specimens. There were no differences apparent in the kinds of particles nor in the relationship between sizes and chemistry, between the intermediate and the core specimens. The particle size distributions were also found to be very similar between the core and intermediate regions (Fig. 6.15).

6.3.4 Continuous Heating Experiments

Representative particle microstructures from continuous annealing experiments, just before and after recrystallisation, are shown in Figs. 6.16 - 6.19. Type A particles were found in the specimens heated up to 1090 °C but not in specimens heated to higher temperatures (Figs. 6.20, 6.21). The endothermic peak between 1090 °C and 1190 °C in the DSC curve is therefore identified to be due to the dissolution of the type A ($M_{23}C_6$) particles. Types B, C and D particles were observed in all heat treated intermediate or core specimens (Figs. 6.20 - 22). Particles were identified by composition and the X-ray diffraction. The type A, B and C/D are found to be $M_{23}C_6$, Ti(C,N), and mixed oxides Y_2O_3-Al_2O_3 respectively. An example of an X-ray diffraction pattern from the specimen heated up to 1230 °C and water quenched, is illustrated in Fig. 6.23. The particle size distributions are shown in Figs. 6.24. and 6.25. The number density of particles decreases with increasing temperature, in both the intermediate and the core specimens. However, the relative frequencies of the particles were found to remain constant at each heating stage. At temperatures greater than 1120 °C, $M_{23}C_6$ dissolves causing a decrease in the number of particles. TiC and TiN decreased during heating as they changed to Ti(C,N). The garnets also changed giving the dominant yttrium containing phases as $YAlO_3$ (hexagonal) and $YAlO_3$ (perovskite) which could not be found in the as-received material, with lesser quantities of $Y_3Al_5O_{12}$, $Y_4Al_2O_9$ and (Figs. 6.13 and 6.23).

The two main kinds of particles which remain at high temperatures, Ti(C,N) and Y_2O_3-Al_2O_3 oxides are very difficult to distinguish on micrographs but can be identified using TEM observations combined with EDX analysis. Fig. 6.26 illustrates the fraction of Ti-rich particles within a particular size range (approximately 20 - 40 nm) as a function of temperature. Approximately 200 particles in a randomly selected field were used for counting. The fraction of Ti-rich particles gradually decreases with increasing temperature. Further data (Fig. 6.27) for small particles (less than 30 nm) revealed what appears to be coarsening. From these results, it is concluded that another contribution forwards that drop in the number density of particles comes from the dissolution of small Ti-rich particles.

A comparison of the size distributions before and after recrystallisation revealed that the number of the small particles (less than 15 nm) decreased, but other size ranges were not significantly altered. It may the case that the small particles are reacting to form garnets, rather than coarsening.

The particle size distributions in the as-received specimens include at least three different kinds of particle distributions, and the ones from heated specimens also include at least two different kinds of particles. It is, therefore, impossible to compare these data simply, and it may be only a coincidence that there are no significant differences in relative frequency. Nevertheless, if the grain boundary pinning force is assumed to be independent of particle type, then these data are sufficient to estimate the pinning force.

Comparison of particle size distributions of identically heat treated the intermediate and the core specimens are shown in Fig. 6.28. The particles from the core seem coarser, but this can not explain why the recrystallisation temperature for the former region is found to be much higher than for the intermediate specimens.

The volume fractions of the particles as a function of heat-treatment temperature are shown in Fig. 6.29, where the data were normalised with respect to the as-received intermediate specimen. The error bars in the diagram show the maximum and minimum values for measurements on the same microstructural data. The volume fractions rapidly decrease with increasing temperatures up to 1230 °C, but then are nearly constant. The volume fractions observed for the intermediate and the core specimens were found to be almost the same. Inhomogeneous distributions of particles are shown in Fig. 6.30 where the boundary between the high and low particle density regions is parallel to the extrusion direction. Many of the fine particles, 50 - 100 nm in diameter, are aligned along the extrusion direction. Almost all of them were identified as the type B Ti(C,N) particles (Fig. 6.31). Pure Al_2O_3 could not be found in any of the heat treated specimens, these alumina particles react with yttria or yttrium-garnet oxides during heat treatment.

6.3.5 Isothermal Annealing

Representative particle microstructures from the intermediate specimens are shown in Figs. 6.32 - 6.34, with corresponding EDX analysis results in Figs. 6.35 - 37, and size distributions in Fig. 6.38. The annealing temperatures are greater than the $M_{23}C_6$ dissolution temperature, so that type A particles are absent. Types B, C and D particles are found at all stages of the heat treatments. The particle size distributions in the isothermally annealed specimens are very different from the data for the continuously heated specimens, with clear evidence for particle coarsening (Figs. 6.38, 39). The number of type B Ti(C,N) particles in the fine size range is significantly decreased with increasing annealing time (Fig. 6.40), but the normalised volume fraction (normalised as the intermediate specimen value is unity) remains constant after 60 min at 1160 °C and 1180 °C (Fig. 6.41). Almost all particles less than about 20 nm disappear after

3000 min at 1160 °C. The median value of the particle size shifts from 12.5 nm in the as-received state to 35 nm after 3000 min annealing at 1160 °C. A number of facetted type C particles are found after prolonged annealing (Fig. 6.42), but very few type D particles (Y_2O_3-Al_2O_3 including Zr), were found. As shown in Figs. 6.38, 6.39, there are no significant differences in particle size distributions between specimens annealed at 1160 °C or 1180 °C. None of the heat-treatments produced even partial recrystallisation. No abnormal grain growth could be found in specimens annealed for as long as 3000 min at 1160 °C, but the grain structures did coarsen (grain size is 1-2 μm). This is in spite of large changes in the particle size distributions.

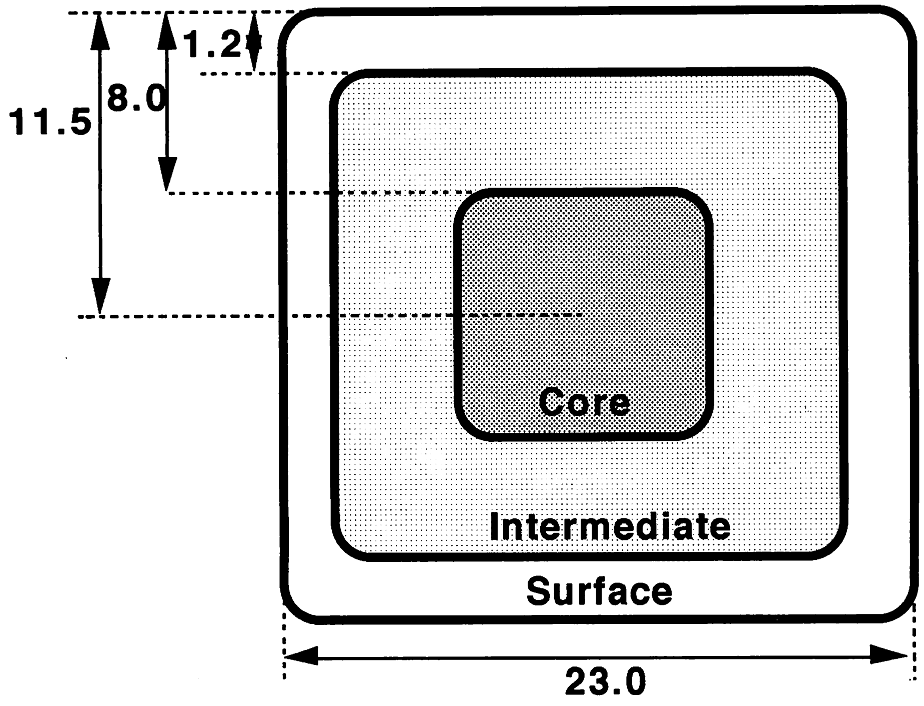

Fig. 6.1 Illustration of the surface, intermediate and core samples extracted from as received *MA6000* bar. The extraction direction is normal to the plane of the diagram.

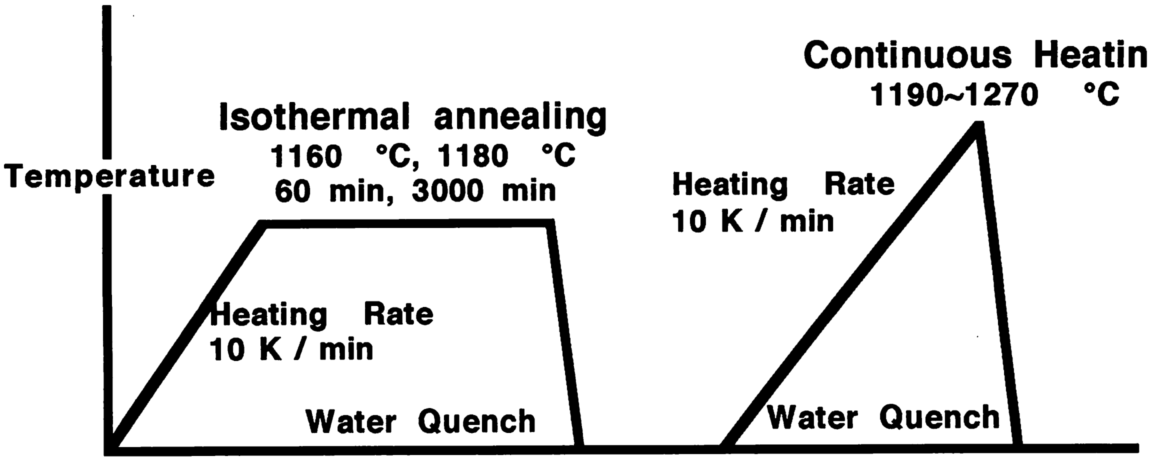

Fig. 6.2 Schematic illustration of the heat treatments used.

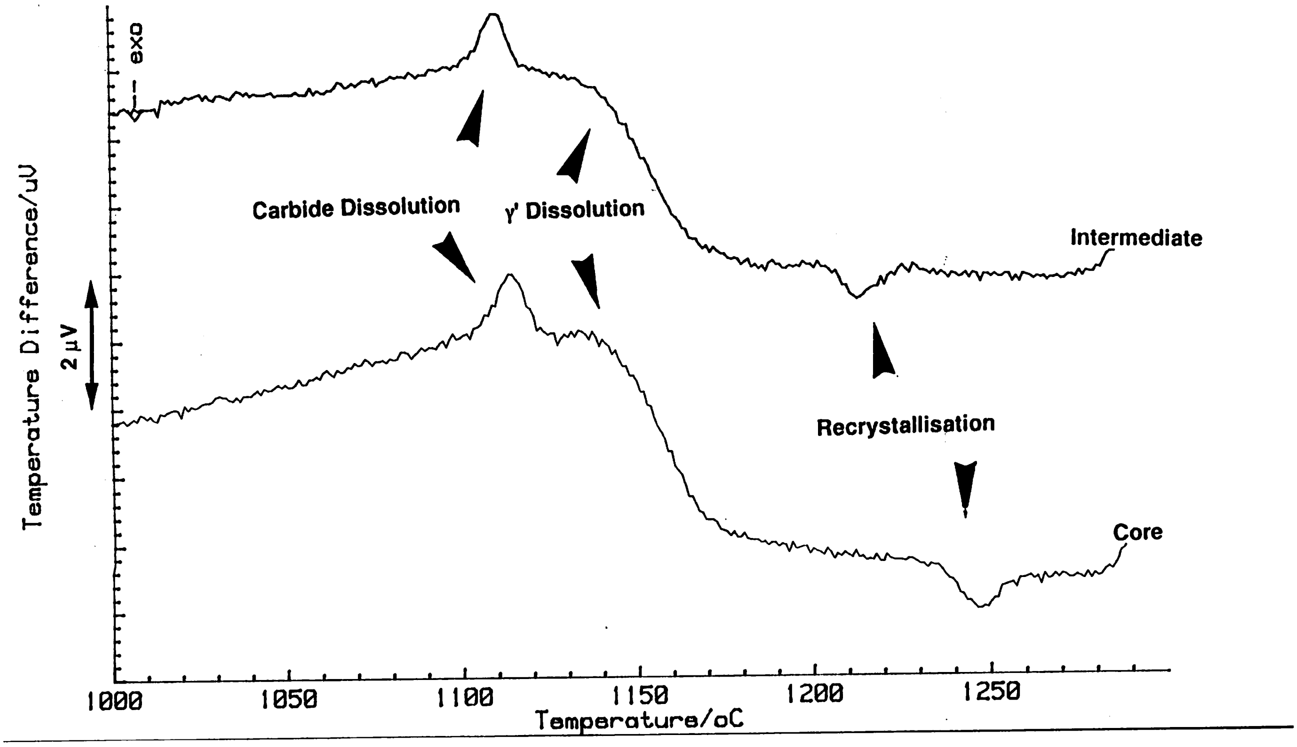

Fig. 6.3 Differential scanning calorimetry data showing the $M_{23}C_6$ dissolution peak, γ' dissolution peak and recrystallisation peak from the intermediate and core specimens. The heating rate was 10 K min^{-1}.

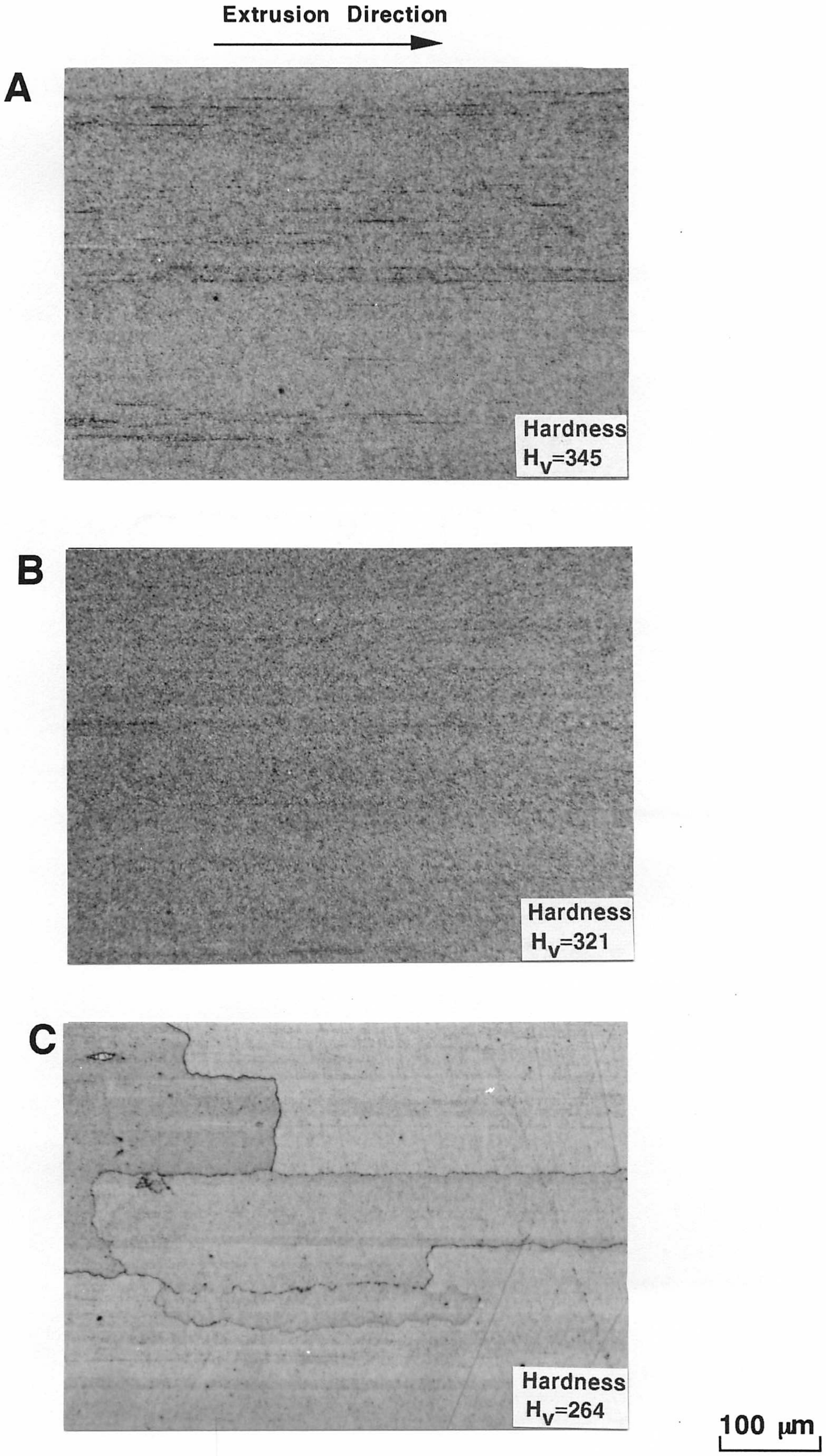

Fig. 6.4 Metallographic data from continuously heated intermediate specimens. A: As-received B: heated to 1190 °C C: heated to 1230 °C, and water quenched. The heating rate was 10 K min^{-1}.

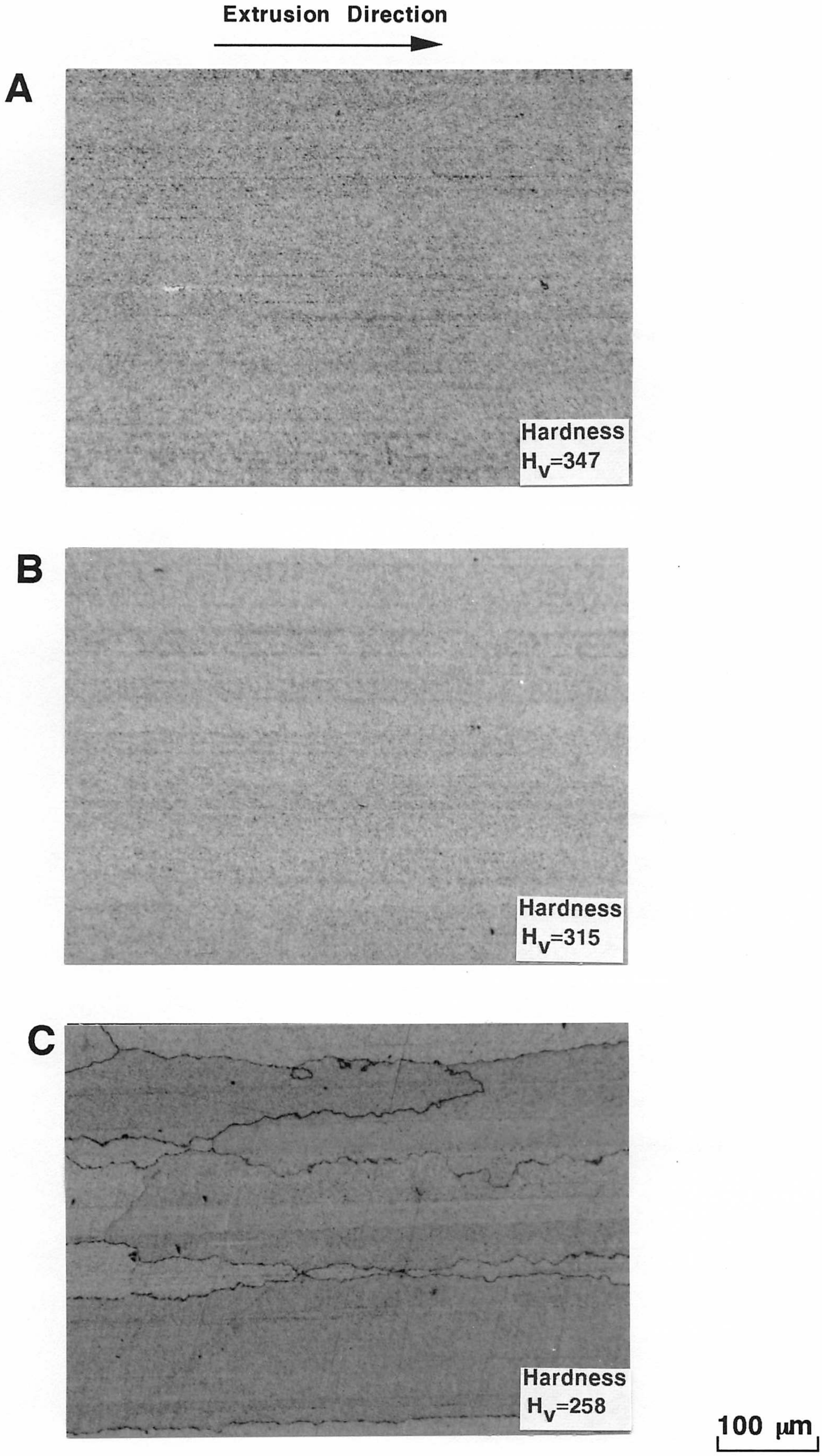

Fig. 6.5 Metallographic data from continuously heated core specimens. A: As-received B: heated to 1230 °C C: heated to 1270 °C, and water quenched. The heating rate was 10 K min^{-1}.

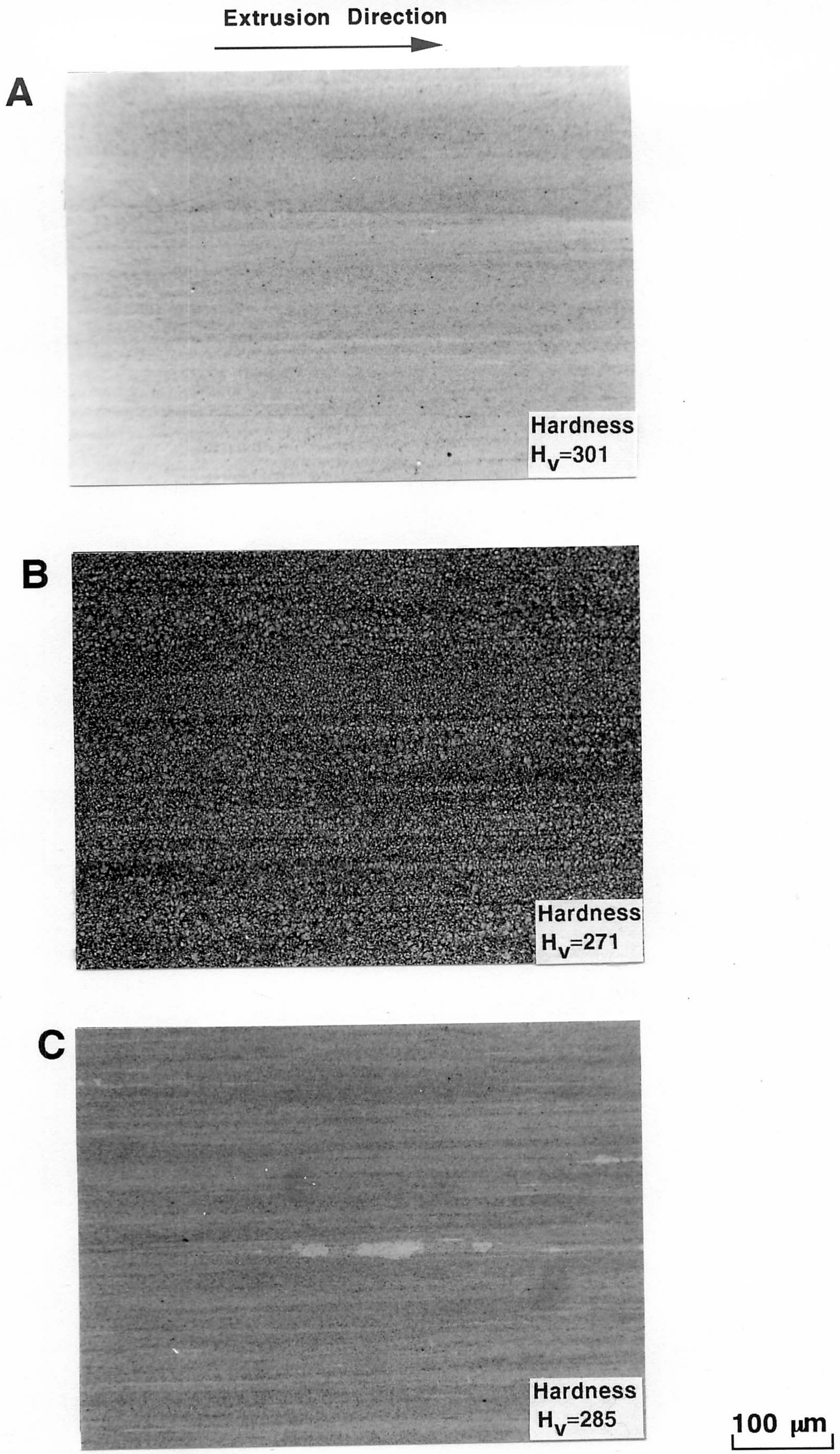

Fig. 6.6 Metallographic data from isothermally annealed specimens.
Annealed at; A: 1160 °C for 60 min B: 1160 °C for 3000 min C: 1180 °C for 60 min, and water quenched.

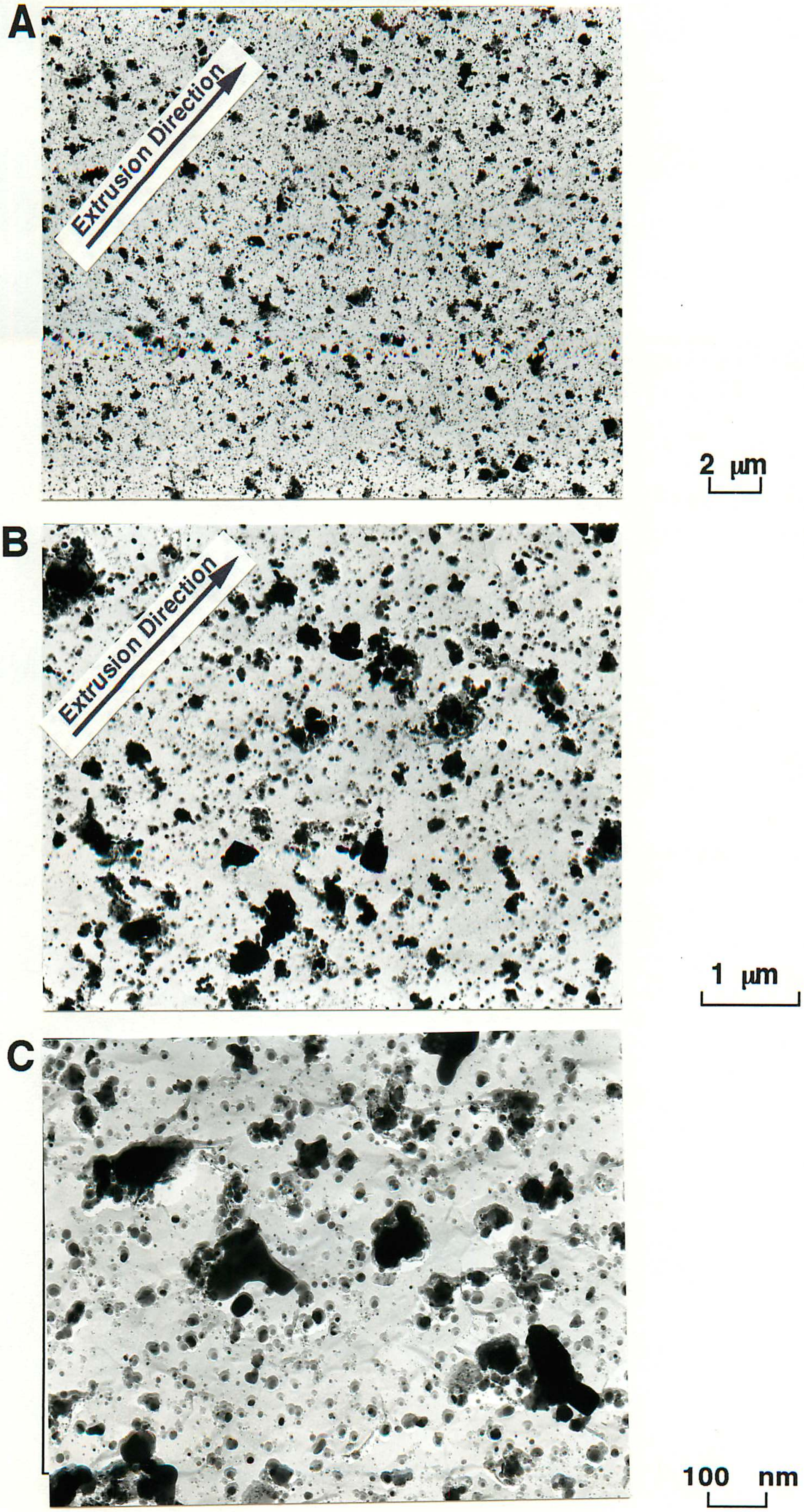

Fig. 6.7 TEM carbon extraction replica micrographs from the intermediate region of the extruded bar, as received.

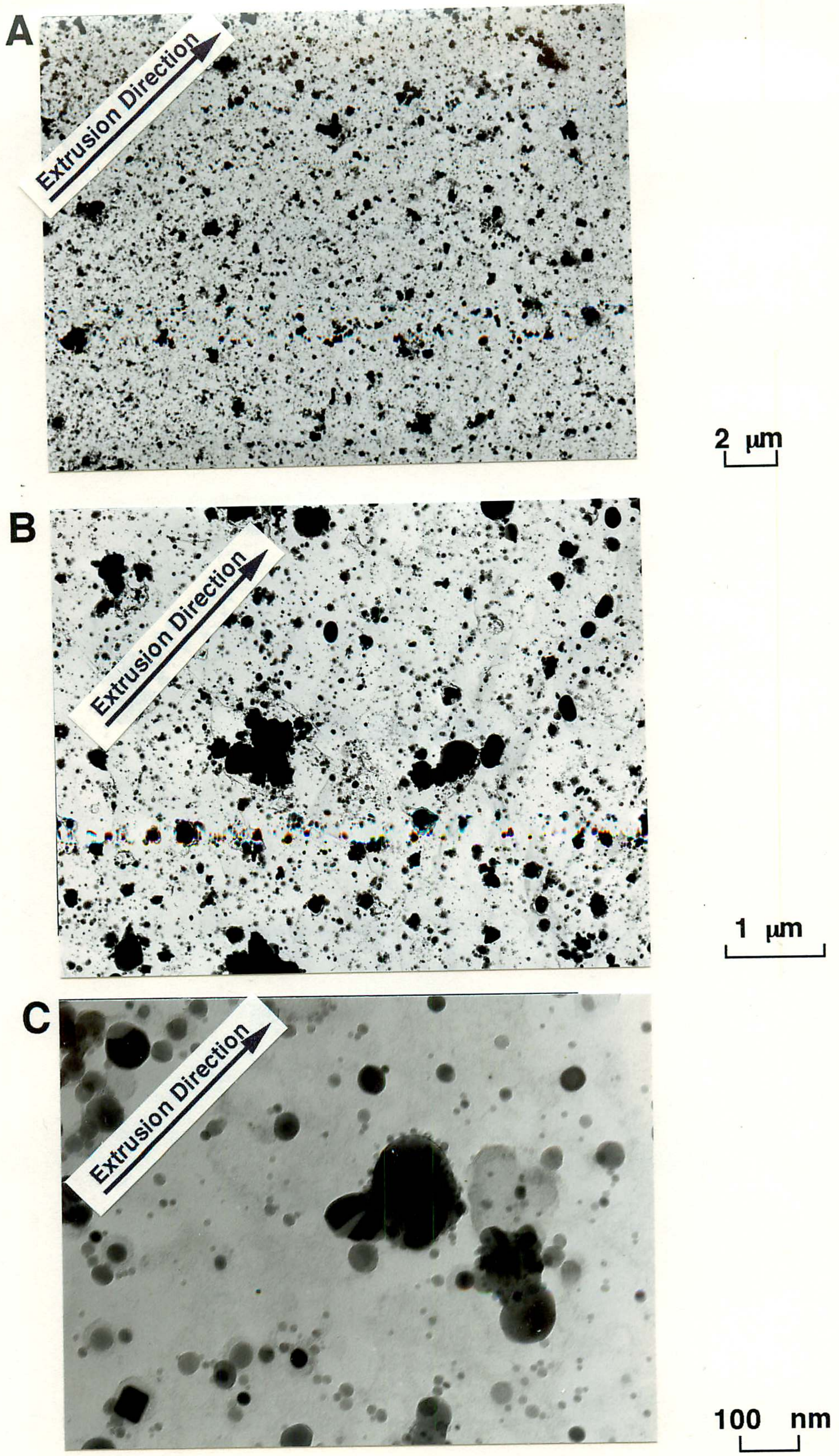

Fig. 6.8 TEM carbon extraction replica micrographs from the core region of the extruded bar, as received.

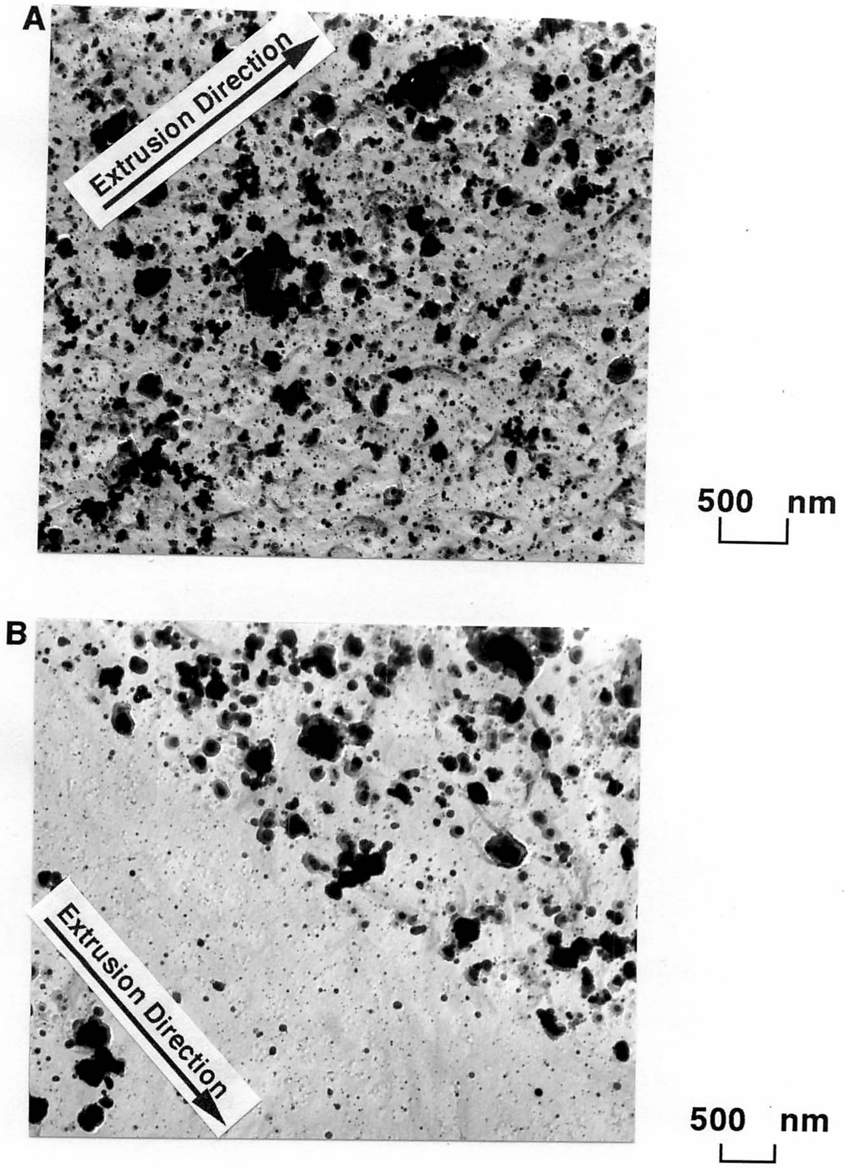

Fig. 6.9 Carbon extraction replicas of the intermediate specimens illustrating inhomogeneous particle distributions.
A, B: As-received.

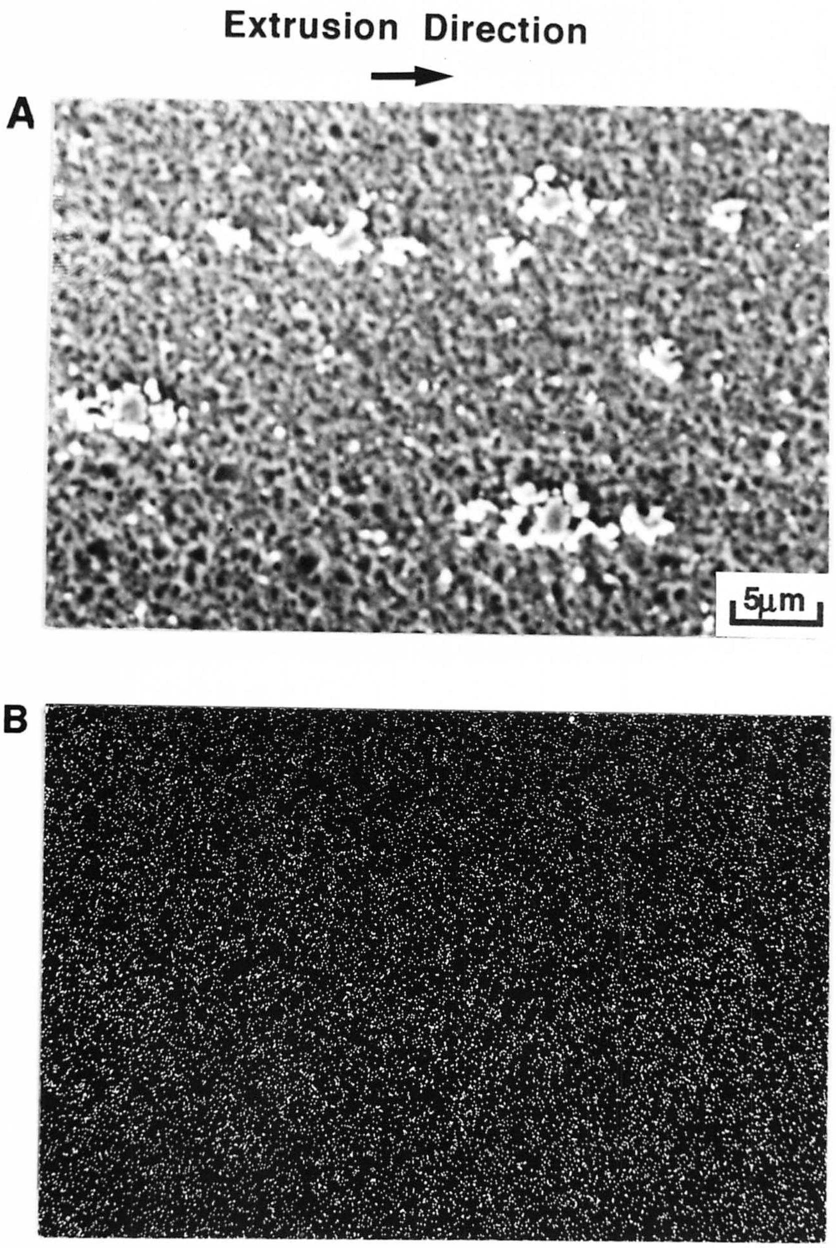

Fig. 6.10 EPMA analysis of the as-received specimen illustrating the absence of oxygen in the large particles.

A: Secondary electron image

B: Characteristic X-ray spectrum image of oxygen

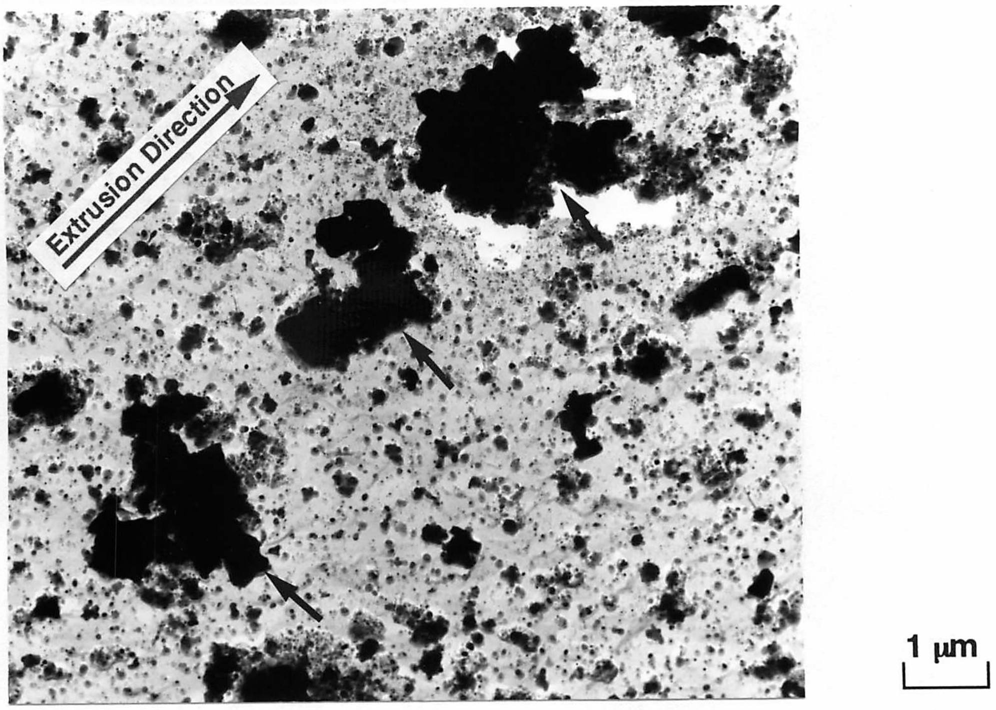

Fig. 6.11 Large particles in the as-received intermediate specimen in a carbon extraction replica. Relative atomic percent ratio for the metallic elements in the marked particle is:

Cr_{80-90}-Mo_{5-10}-Ni_{5-10}-W_{5-10}

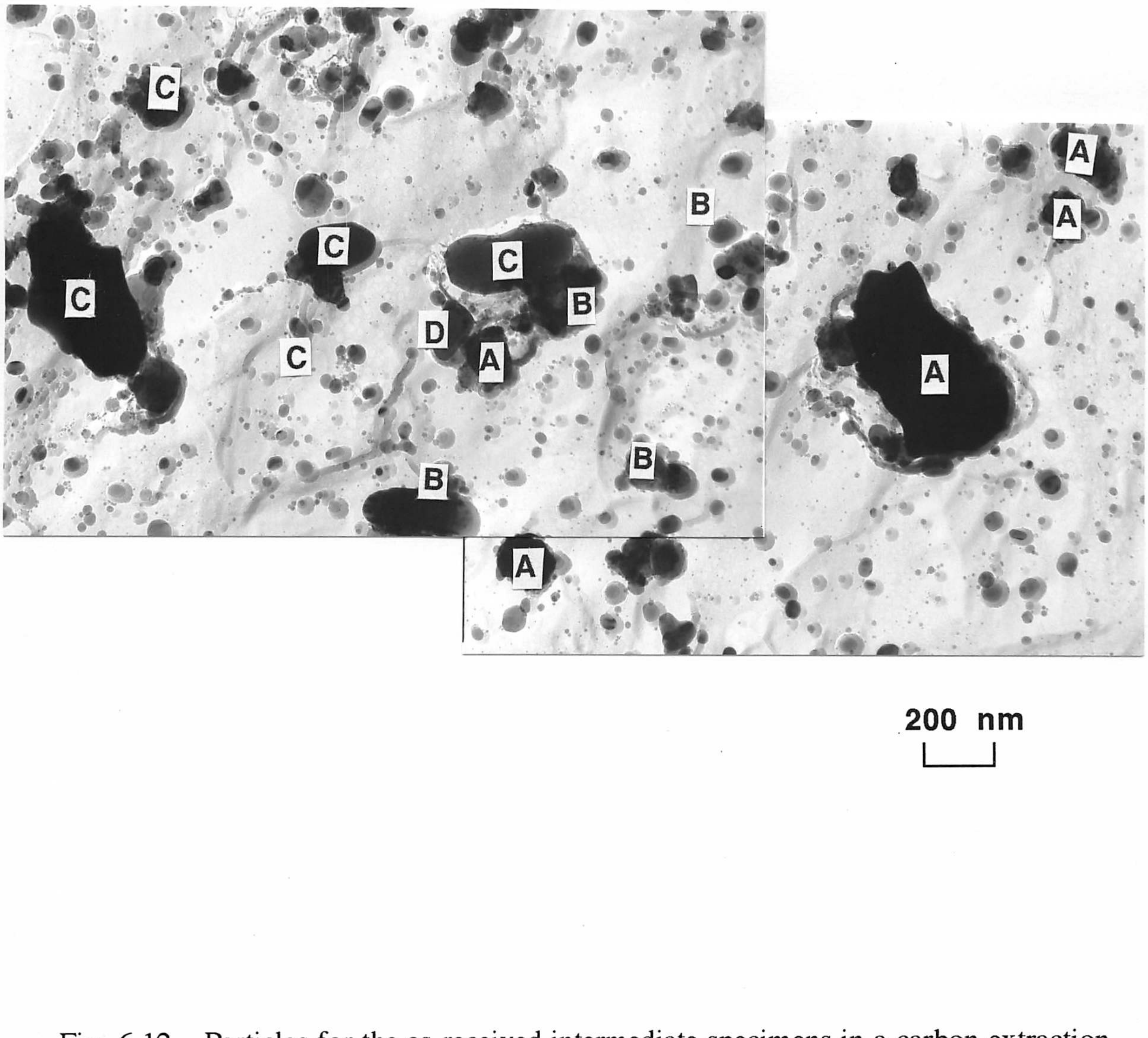

Fig. 6.12 Particles for the as-received intermediate specimens in a carbon extraction replica. Relative atomic percent ratio for the metallic elements in the marked particles are:

A: Cr_{80-90}-Mo_{5-10}-Ni_{5-10}-W_{5-10}

B: Ti_{90-95}-Cr_{0-5}-Ta_{0-10}

C: Y_{40-60}-Al_{40-60}

D: $(Y\text{-}Zr)_{40-60}$-Al_{40-60}

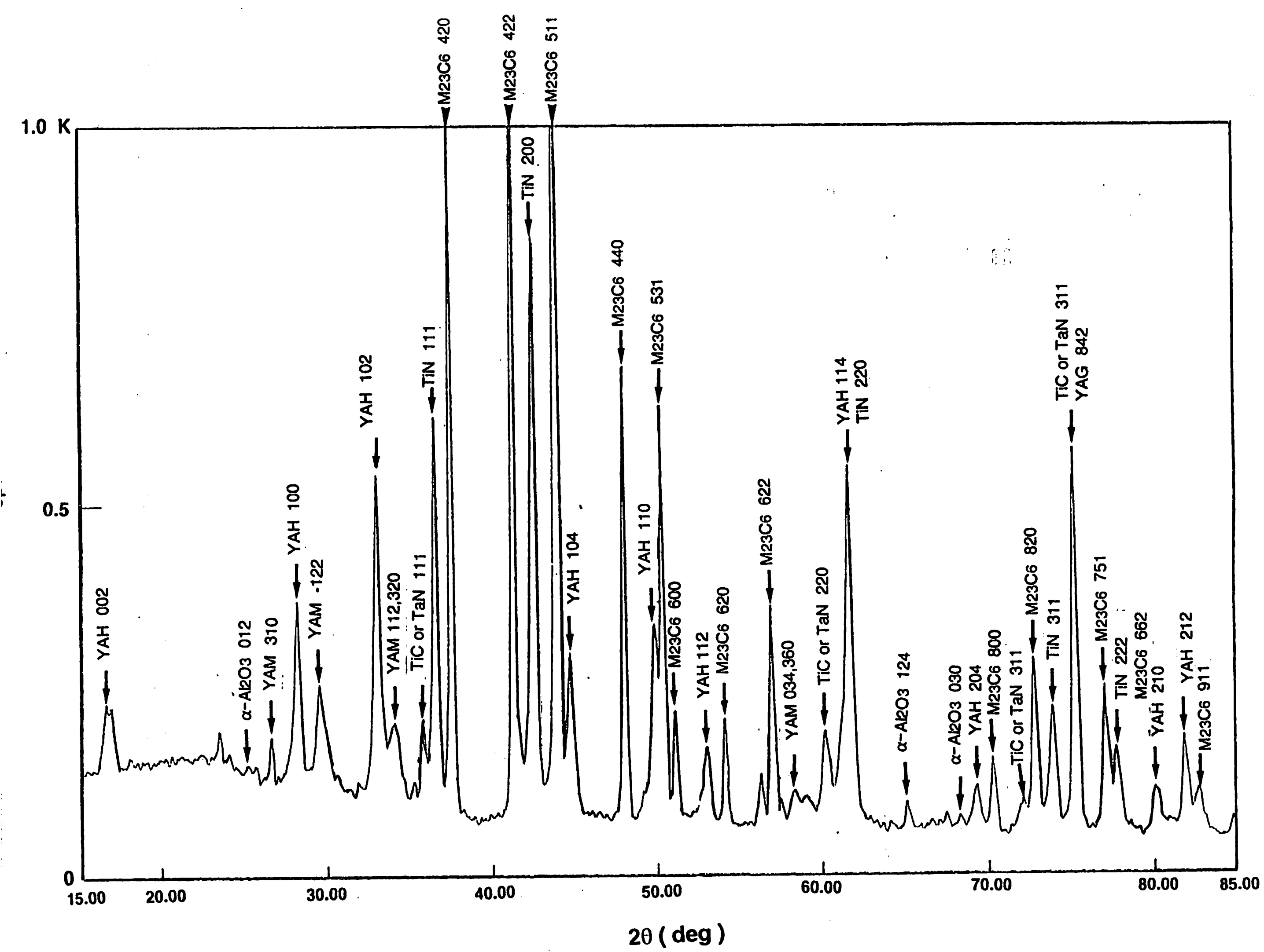

Fig. 6.13 The X-ray diffraction analysis of extractions in the as-received intermediate specimen.

TiC and TaN cannot be identified separately because they belong to the same crystal system and have very similar lattice parameters.

Numbers in the diagram stand for the plane indices, and the abbreviations are as follows:

M23C6: $M_{23}C_6$

YAH: $YAlO_3$ (hexagonal)

YAM: $Y_4Al_2O_9$

YAG: $Y_3Al_5O_{12}$

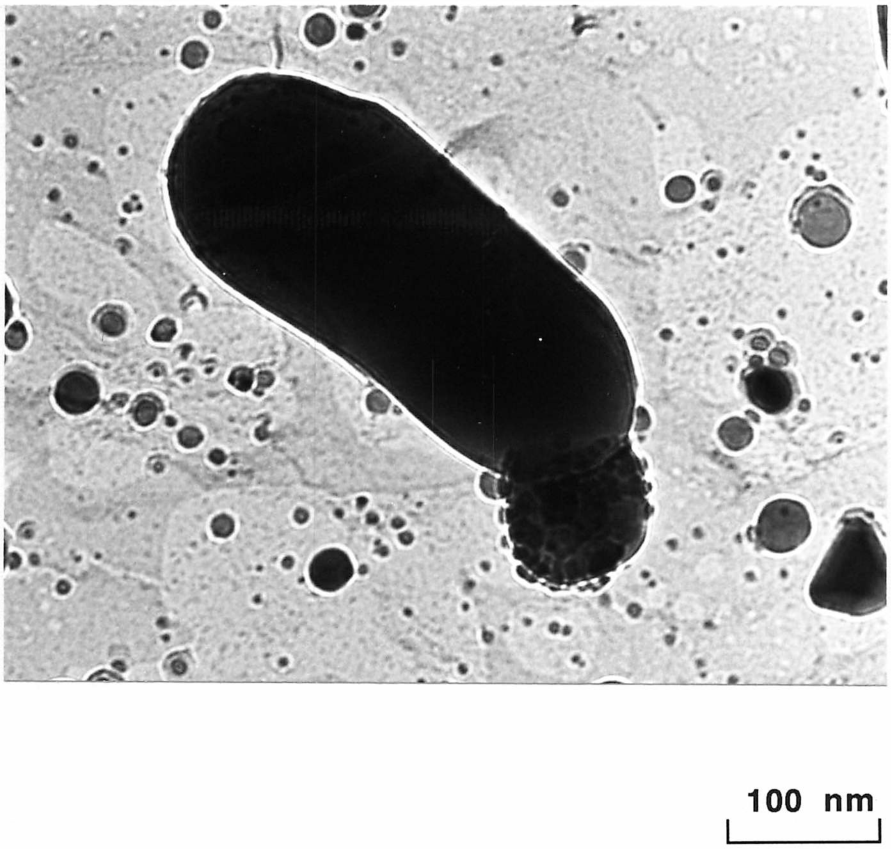

Fig. 6.14 A carbon extraction replica from the as-received intermediate specimen illustrating an Al_2O_3 particle containing no yttrium.

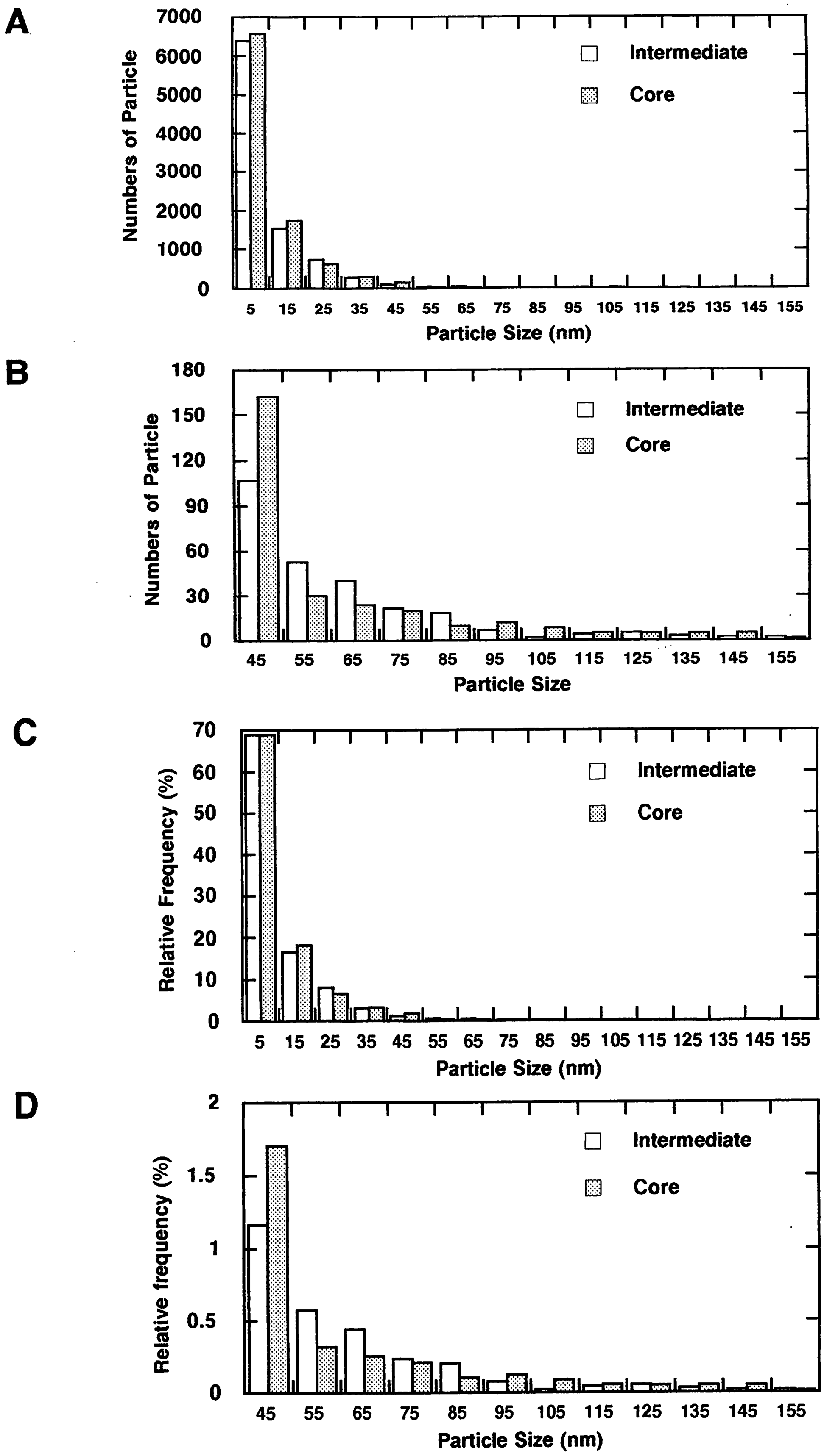

Fig. 6.15 Comparison of particle distributions for the as-received, the intermediate, and the core specimens.
A: Numbers of particles as a function of particle size
B: Same as A, but detail of large particle size area
C: Relative frequencies of particle sizes
D: Same as C, but detail of large particle size area

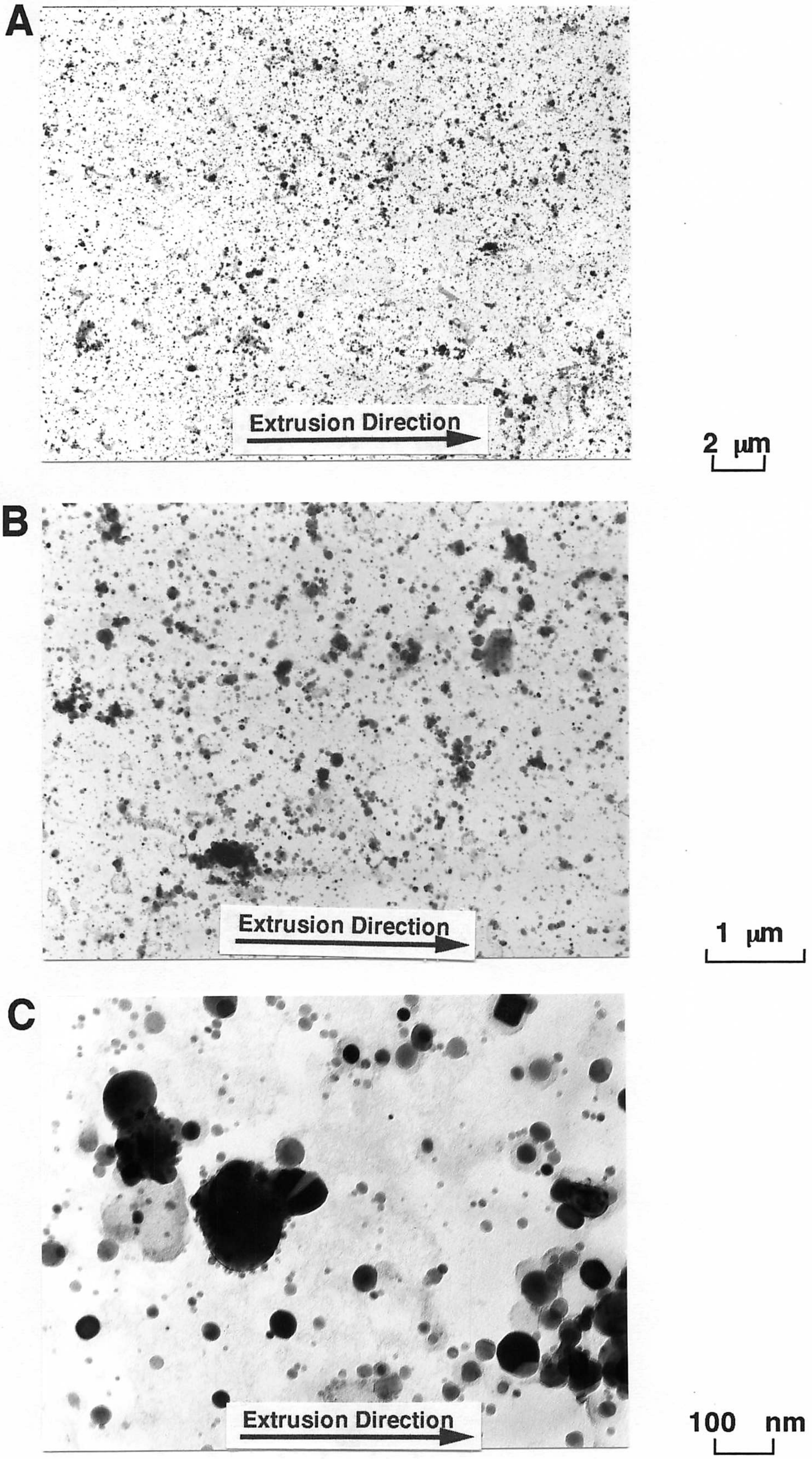

Fig. 6.16 TEM carbon extraction replica micrographs from the intermediate region of the extruded bar. Continuously heated up to 1190 °C and water quenched.

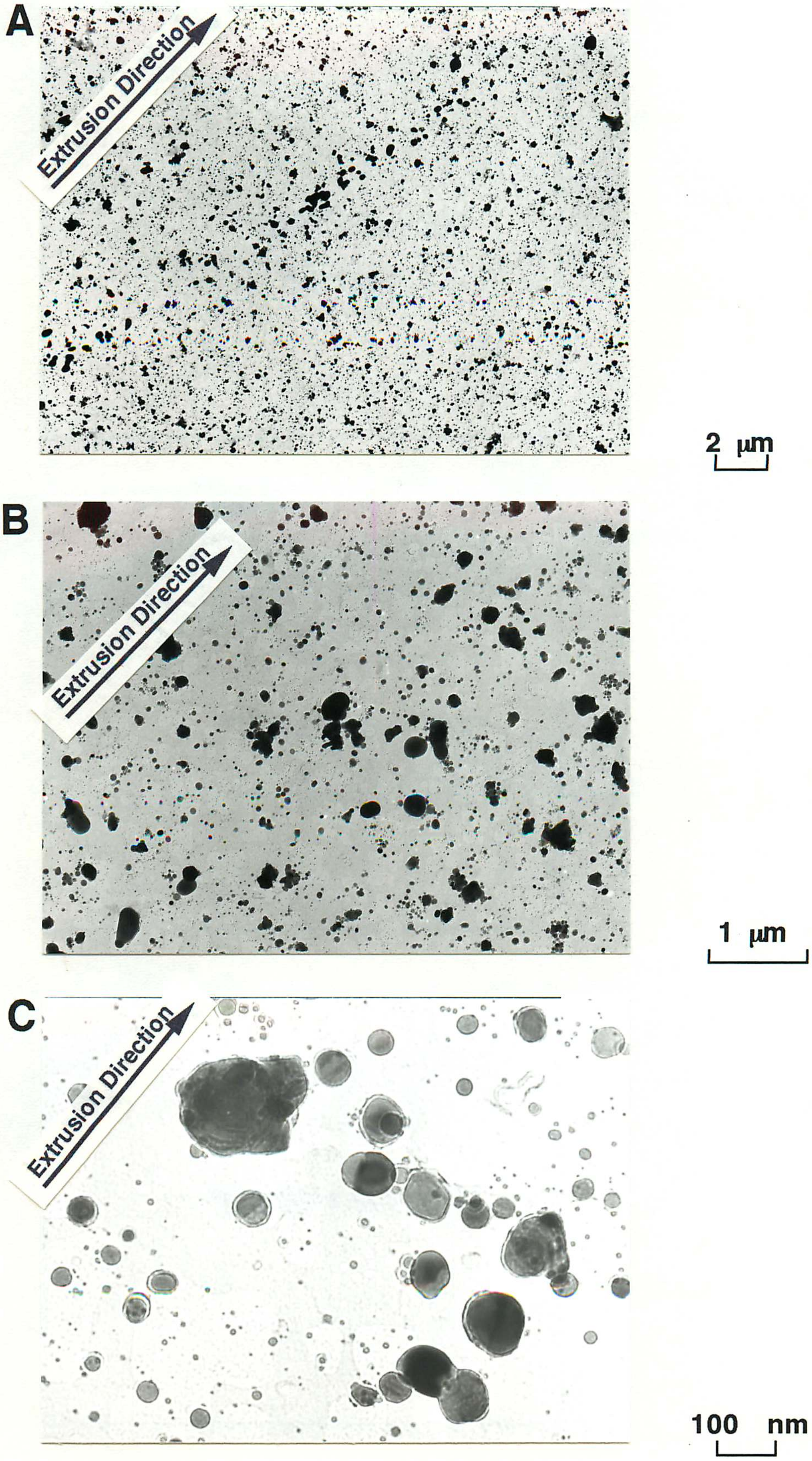

Fig. 6.17 TEM carbon extraction replica micrographs from the intermediate region of the extruded bar. Continuously heated up to 1230 °C and water quenched.

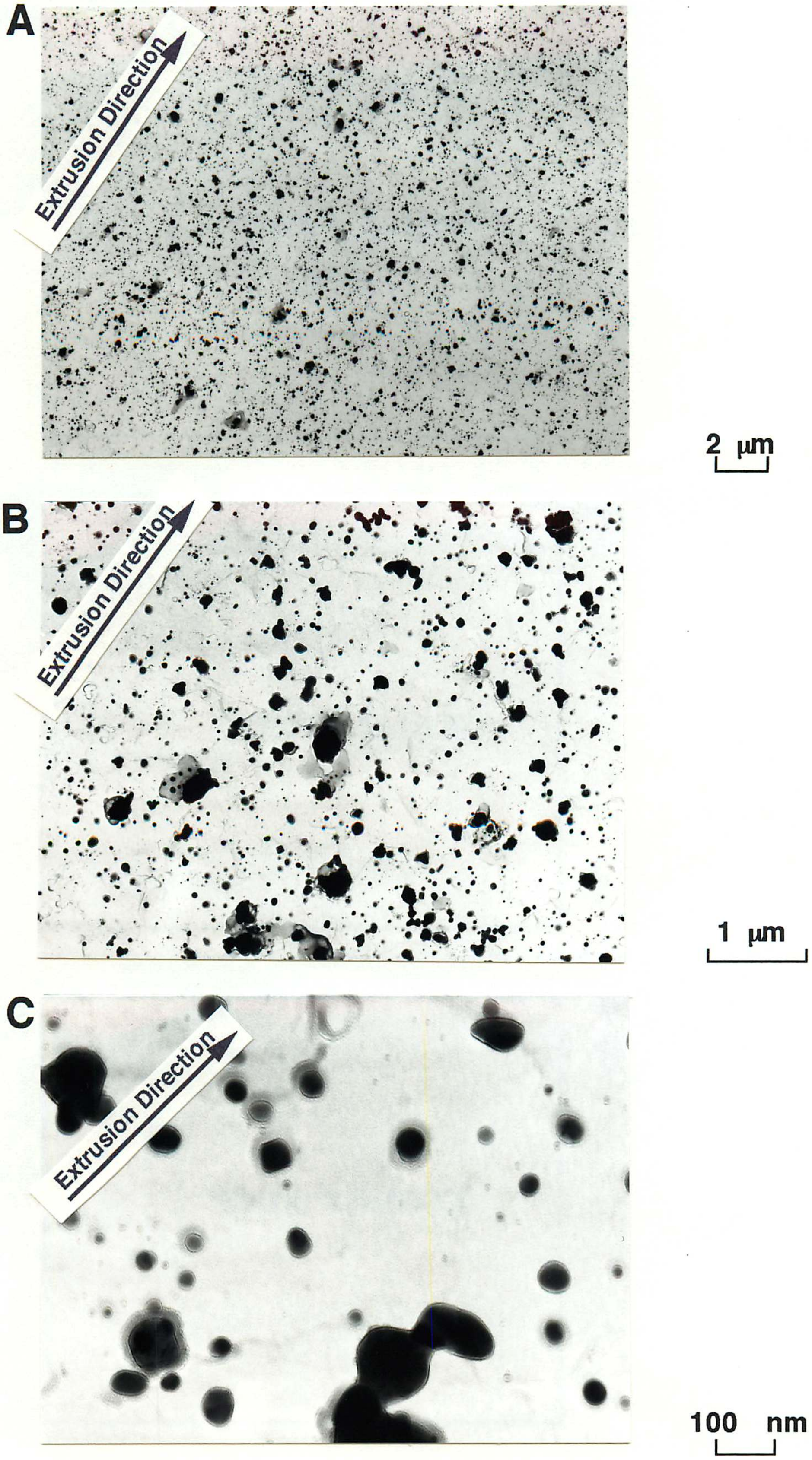

Fig. 6.18 TEM carbon extraction replica micrographs from the core region of the extruded bar. Continuously heated up to 1230 °C and water quenched.

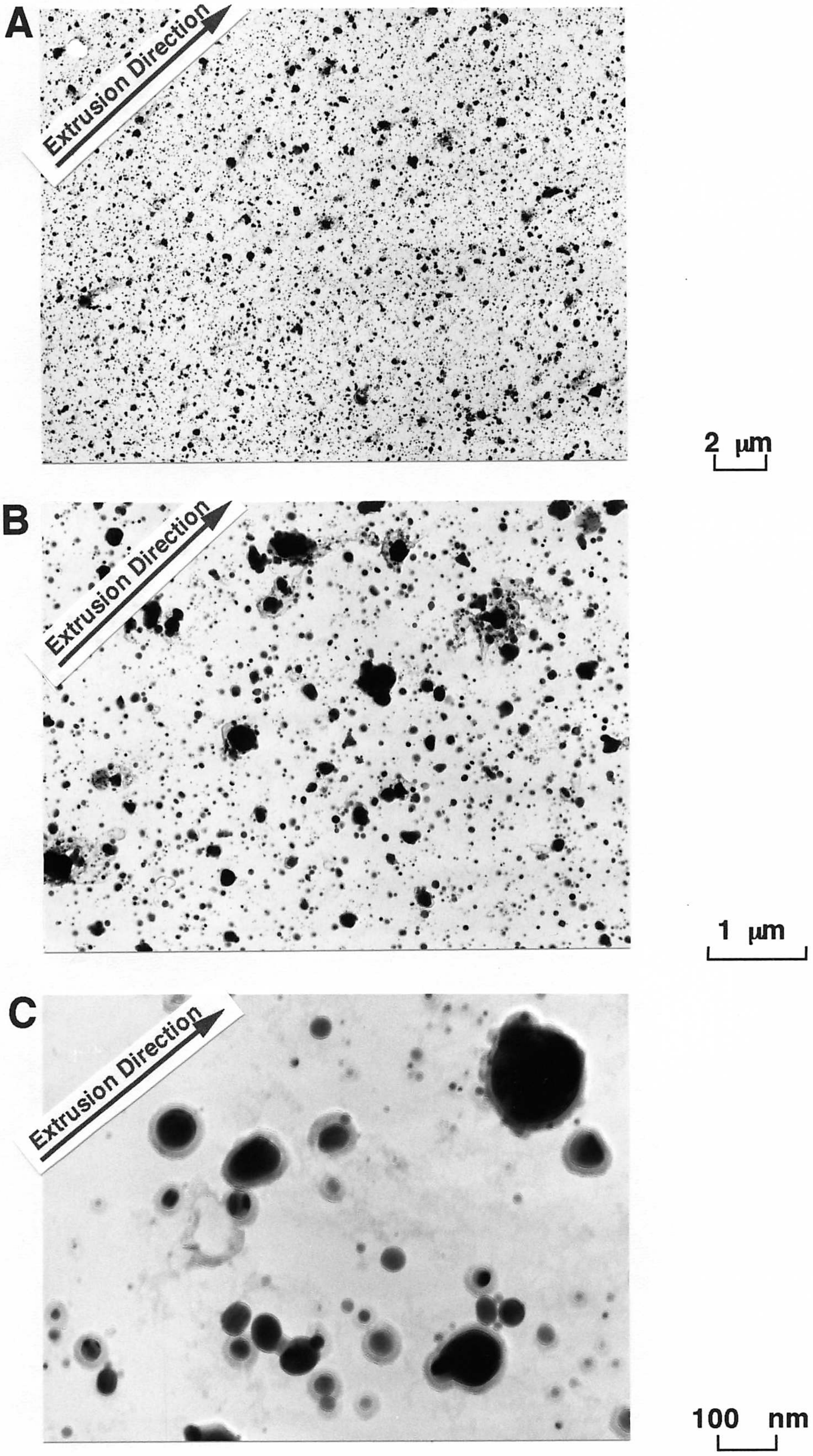

Fig. 6.19 TEM carbon extraction replica micrographs from the intermediate region of the extruded bar. Continuously heated up to 1270 °C and water quenched.

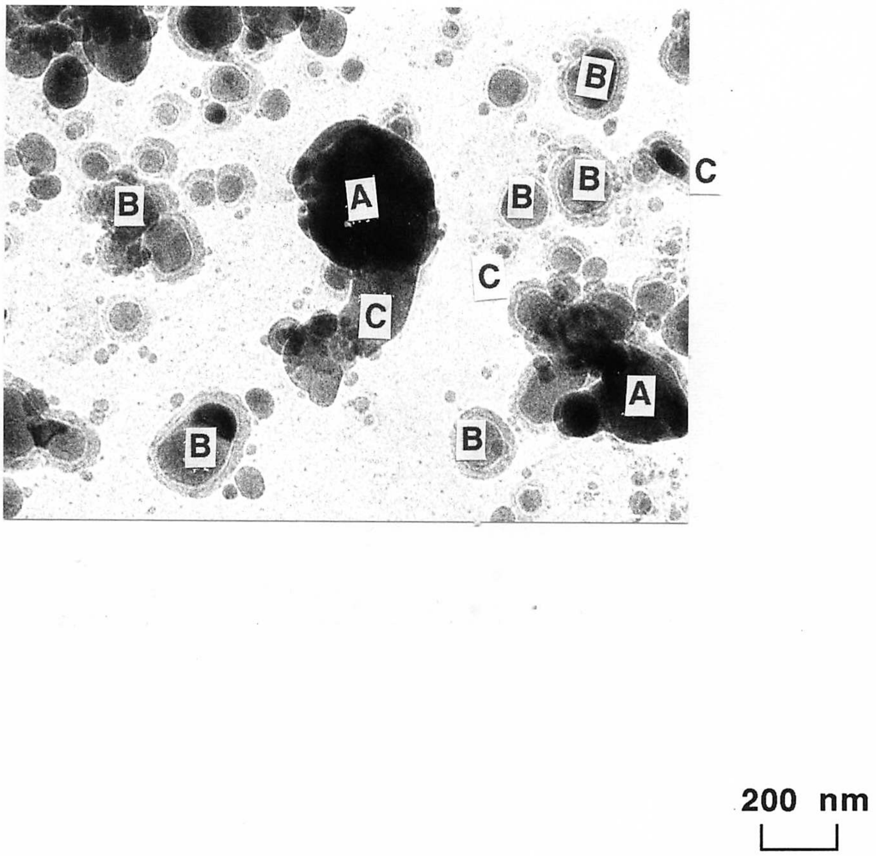

Fig. 6.20 Particles in a carbon extraction replica from the continuous heating experiment, at 1090 °C unrecrystallised, and water quenched, for the intermediate specimen. Relative atomic percent ratio for the metallic elements in the marked particles are:

A: Cr_{80-90}-Mo_{5-10}-Ni_{5-10}-W_{5-10}

B: Ti_{90-95}-Cr_{0-5}-Ta_{0-10}

C: Y_{40-60}-Al_{40-60}

D: $(Y\text{-}Zr)_{40-60}$-Al_{40-60}

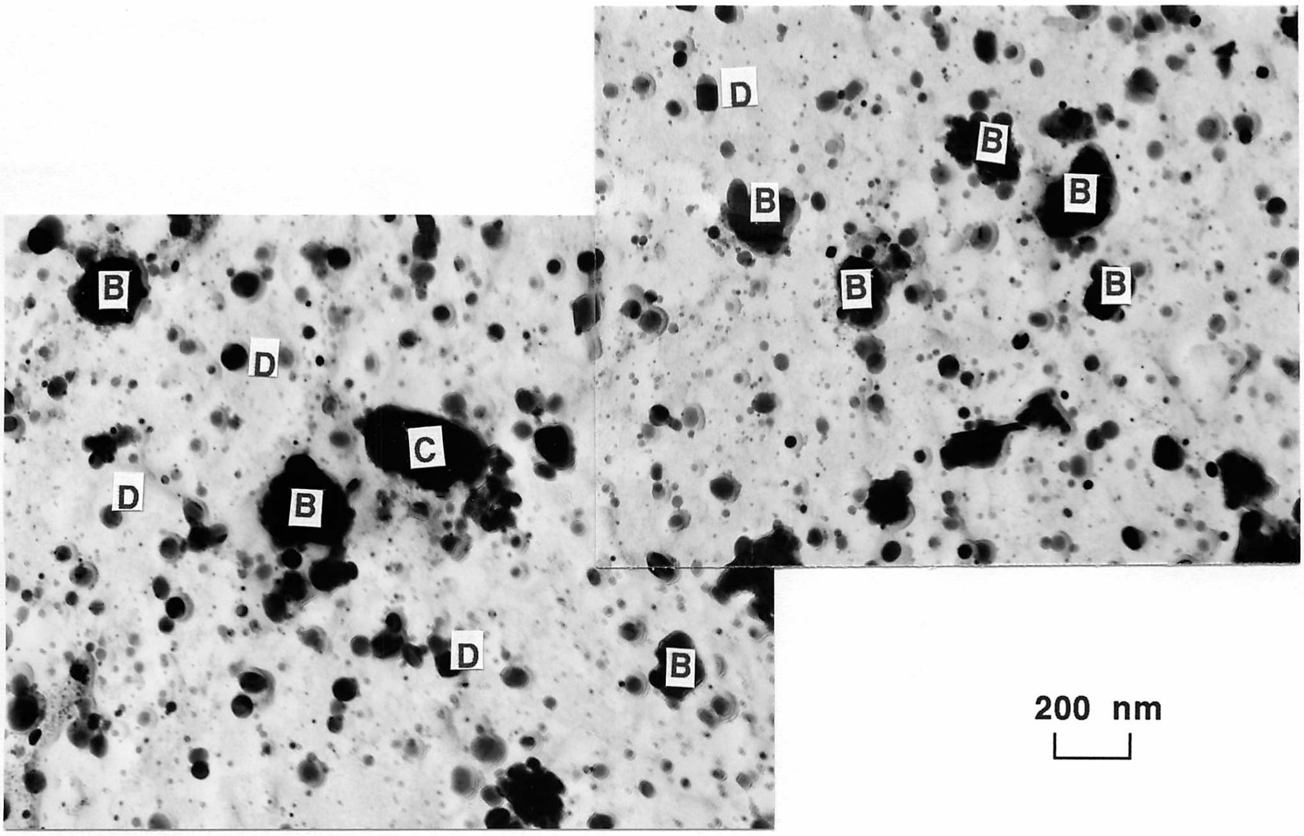

Fig. 6.21 Particles in a carbon extraction replica from the continuous heating experiment, at 1190 °C unrecrystallised, and water quenched, for the intermediate specimen. Relative atomic percent ratio for the metallic elements in the marked particles are:

B: Ti_{90-95}-Cr_{0-5}-Ta_{0-10}

C: Y_{40-60}-Al_{40-60}

D: $(Y\text{-}Zr)_{40-60}$-Al_{40-60}

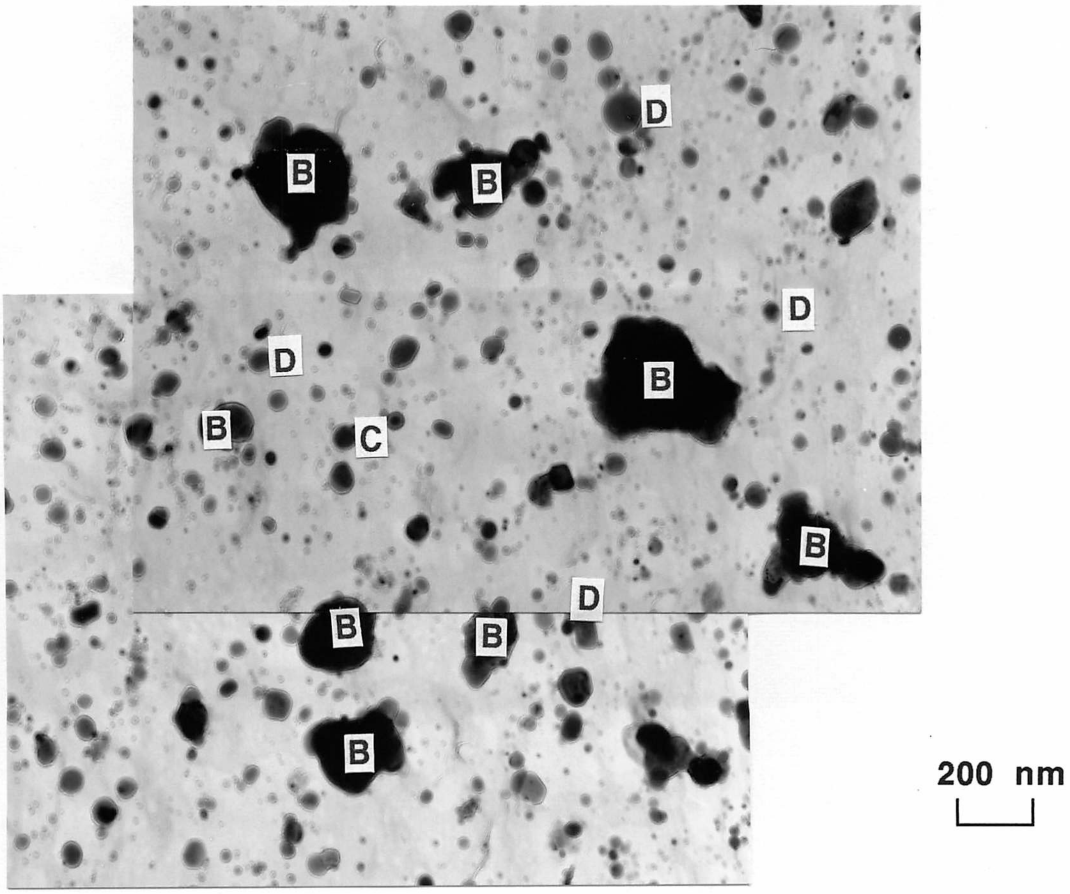

Fig. 6.22 Particles in a carbon extraction replica from the continuous heating experiment, at 1230 °C recrystallised, and water quenched, for the intermediate specimen. Relative atomic percent ratio for the metallic elements in the marked particles are:

B: Ti_{90-95}-Cr_{0-5}-Ta_{0-10}

C: Y_{40-60}-Al_{40-60}

D: $(Y\text{-}Zr)_{40-60}$-Al_{40-60}

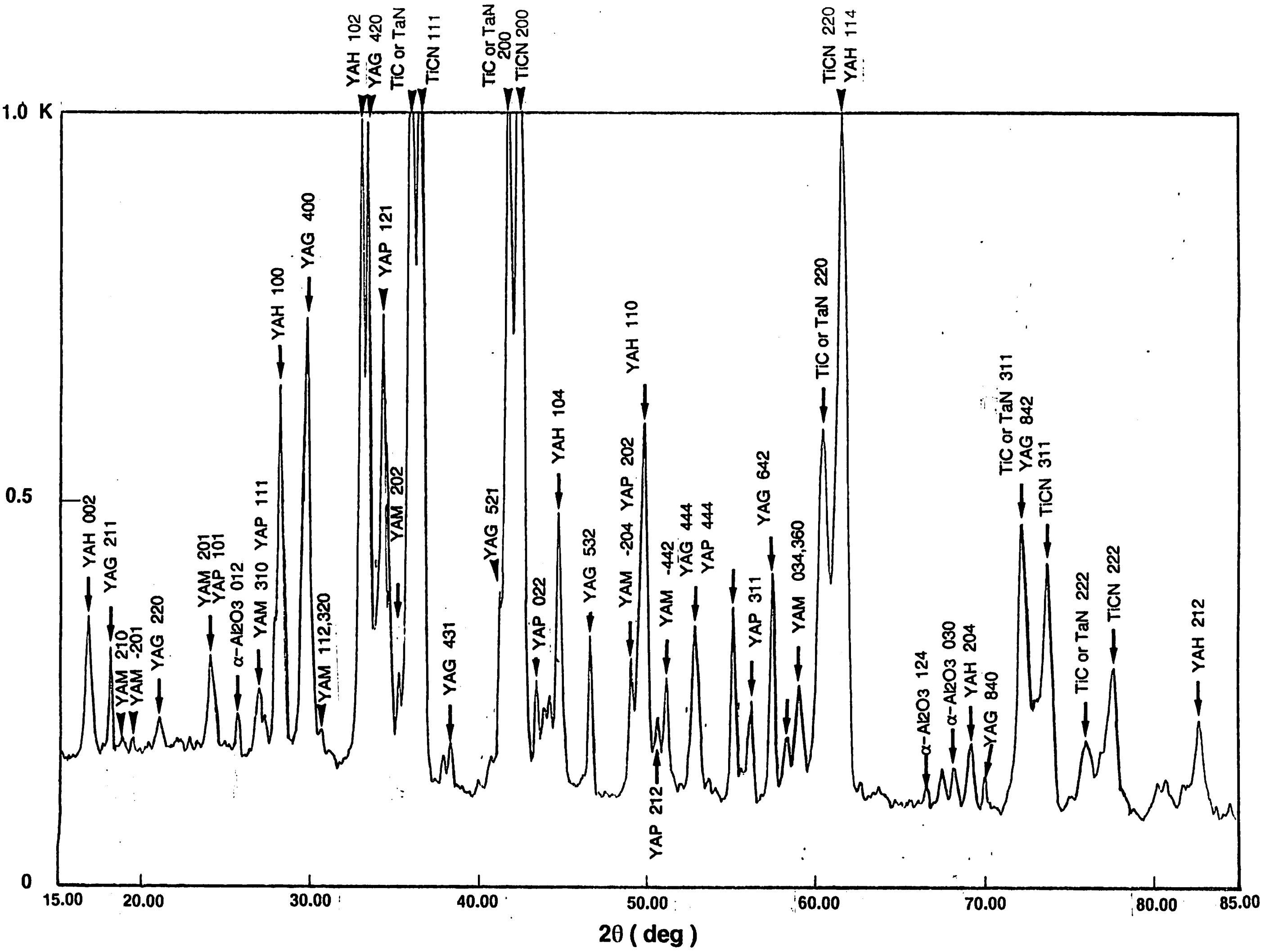

Fig. 6.23 The X-ray diffraction analysis of extractions in the continuously heated to 1230 °C and water quenched intermediate specimen.

TiC and TaN cannot be identified separately because they belong to the same crystal system and have very similar lattice parameters.

Numbers in the diagram stand for the plane indices, and the abbreviations are as follows:

M23C6: $M_{23}C_6$

YAH: $YAlO_3$ (hexagonal)

YAM: $Y_4Al_2O_9$

YAG: $Y_3Al_5O_{12}$

YAP: $YAlO_3$ (perovskite)

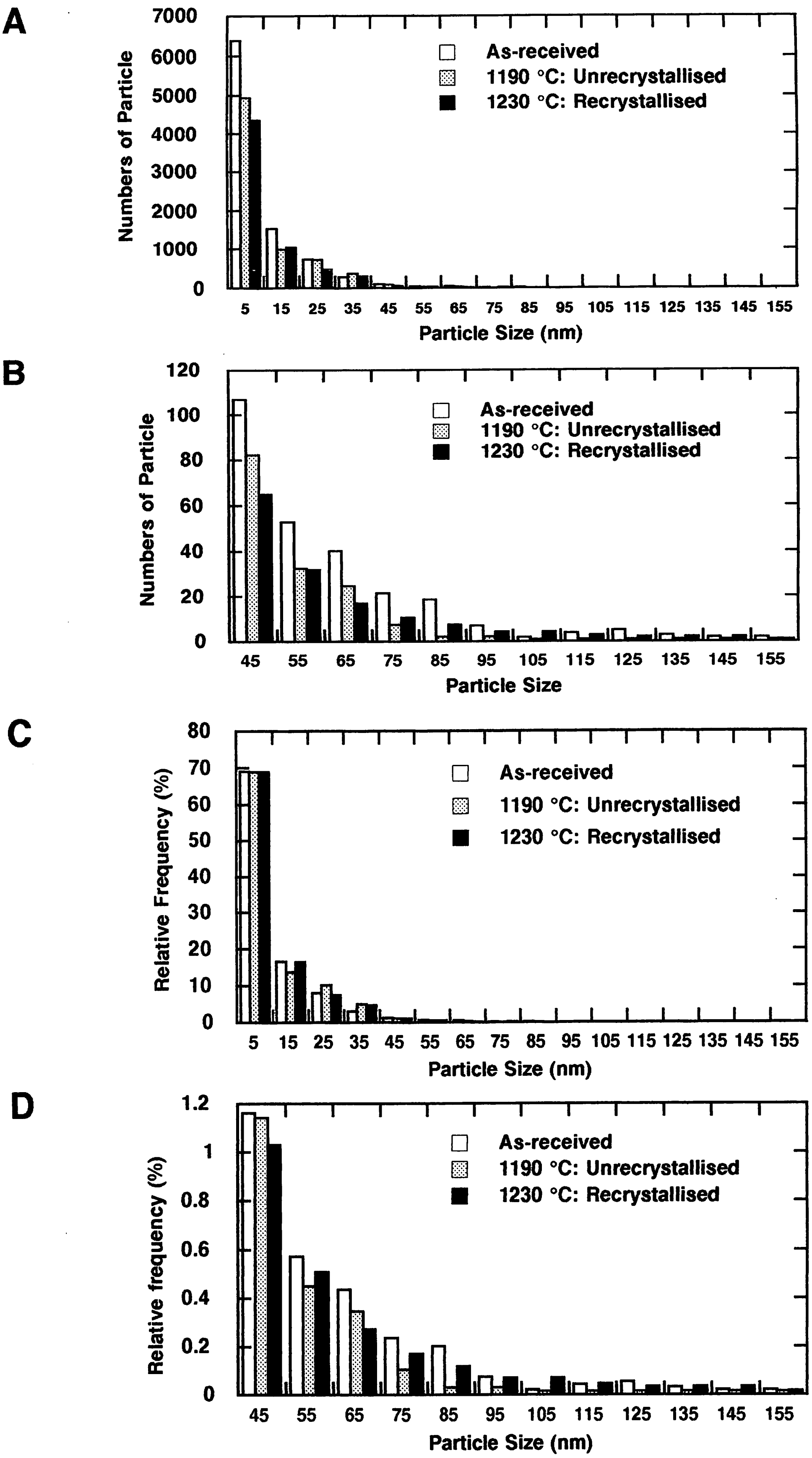

Fig. 6.24 Comparison of particle distributions for the continuously heated the intermediate specimens.

A: Numbers of particles as a function of particle size
B: Same as A, but detail of large particle size area
C: Relative frequencies of particle sizes
D: Same as C, but detail of large particle size area

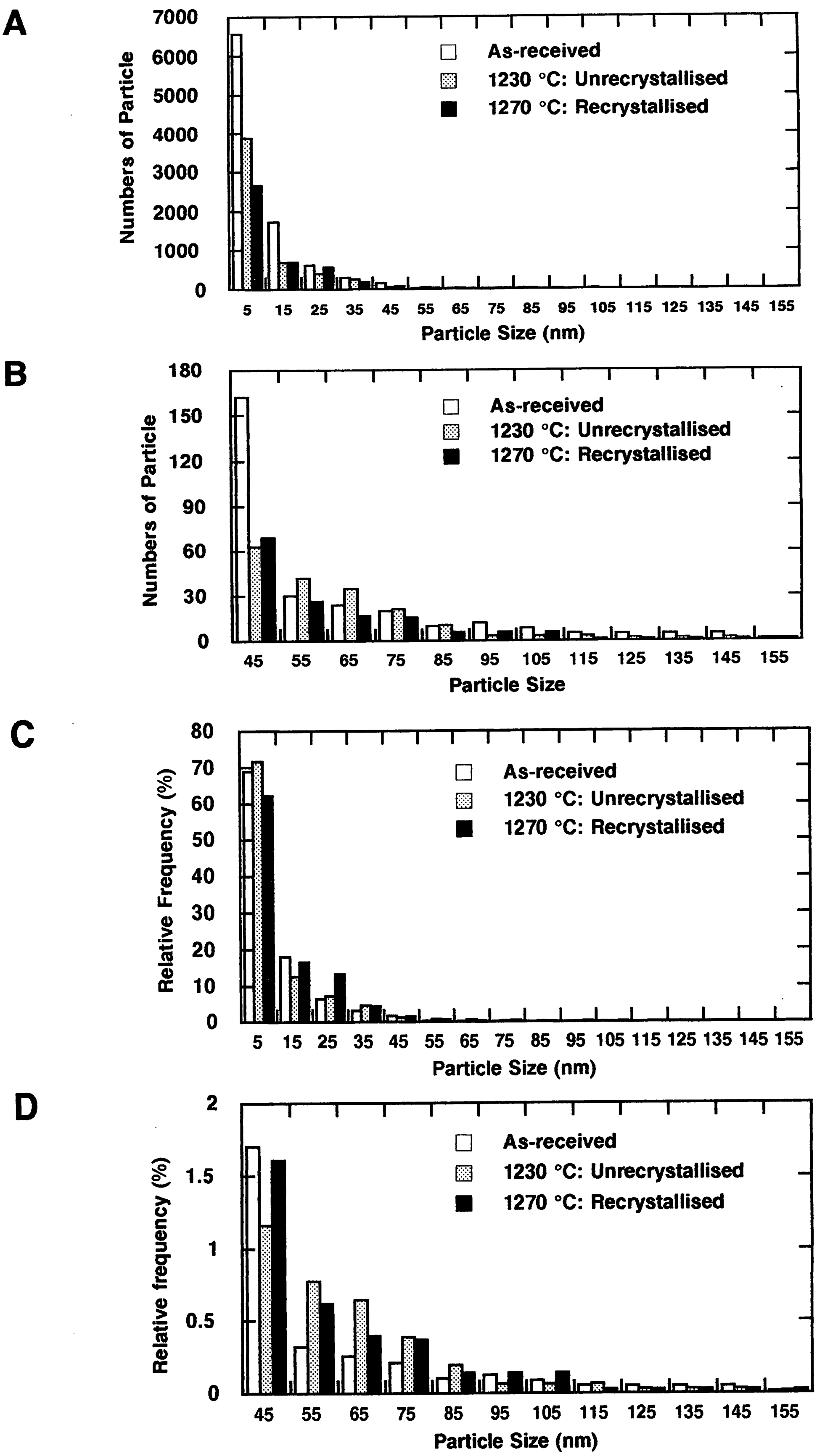

Fig. 6.25 Comparison of particle distributions for the continuously heated the core specimens.
A: Numbers of particles as a function of particle size
B: Same as A, but detail of large particle size area
C: Relative frequencies of particle sizes
D: Same as C, but detail of large particle size area

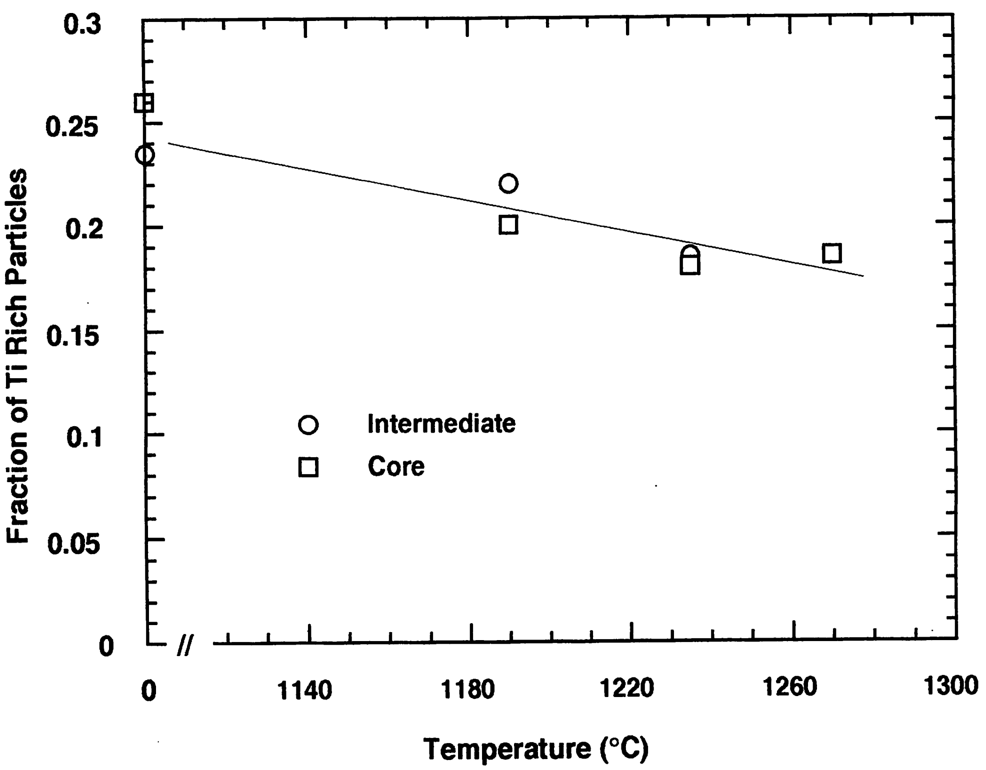

Fig. 6.26 Fraction of Ti-rich particles within a particular size range (20 - 40 nm) as a function of temperature, during continuous heating experiments.

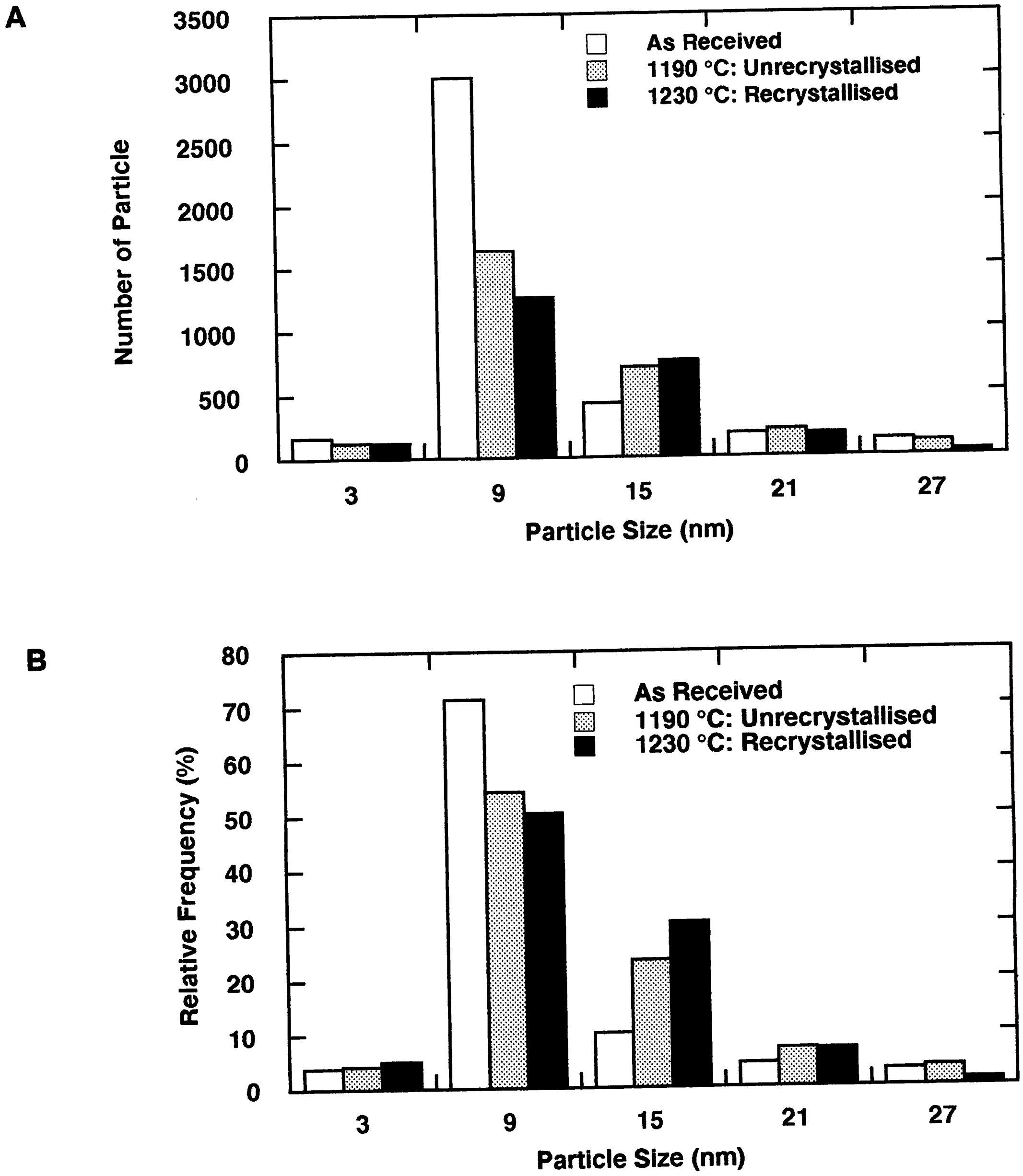

Fig. 6.27 Comparison of small particle (< 30 nm) distributions from continuous heating experiments.

A: Number of particle as a function of particle size

B: Relative frequency

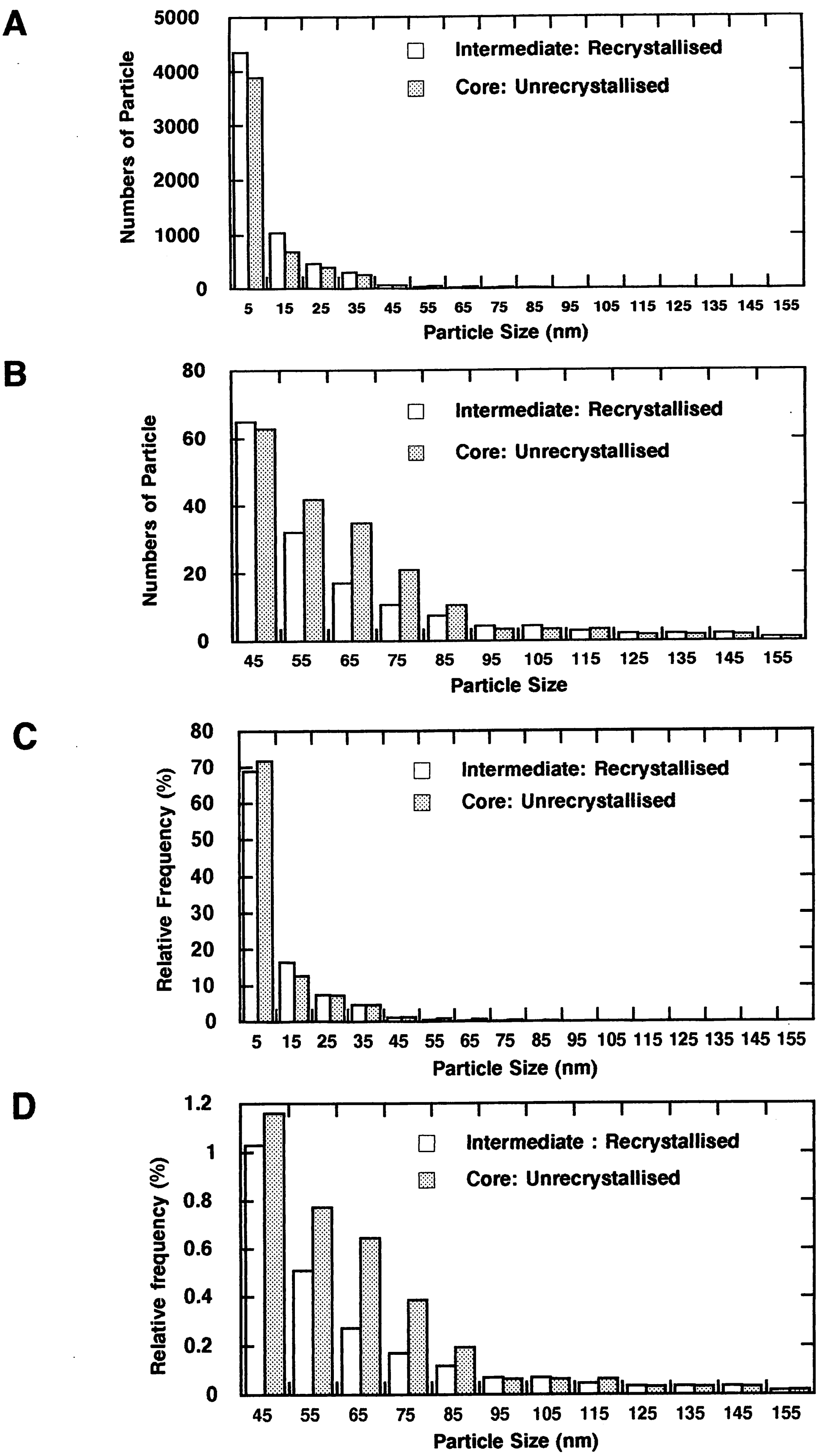

Fig. 6.28 Comparison of particle distributions between the intermediate and the core specimens continuously heated to 1230 °C.
A: Numbers of particles as a function of particle size
B: Same as A, but detail of large particle size area
C: Relative frequencies of particle sizes
D: Same as C, but detail of large particle size area

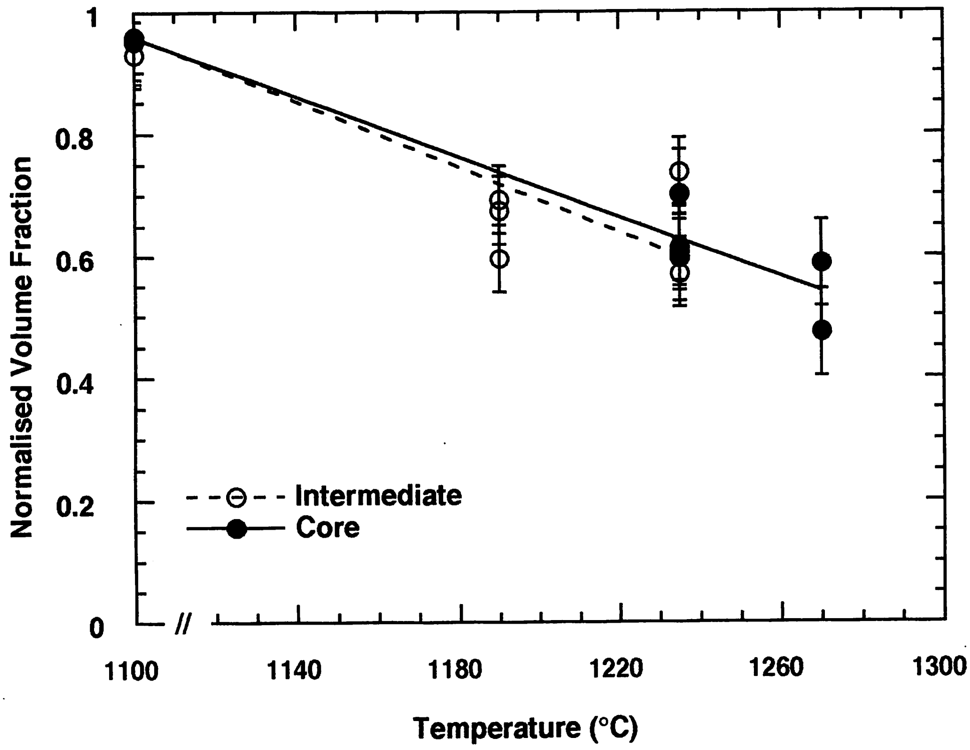

Fig. 6.29 Normalised volume fraction of particles as a function of temperature and specimen location, from continuous heating experiments. The normalised volume fraction of particles in the as received intermediate specimen is taken to be unity. The error bars in the diagram show the maximum and minimum values for measurements on the same microstructural data.

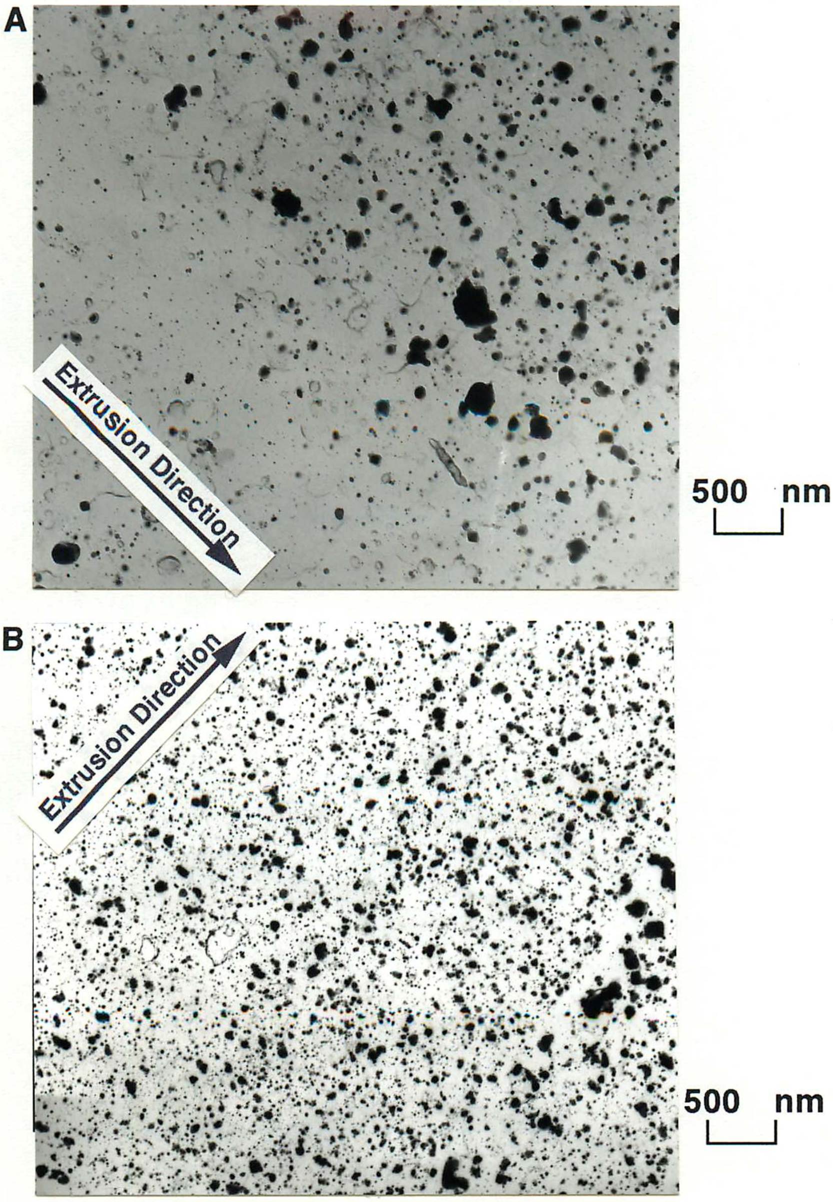

Fig. 6.30 Carbon extraction replicas of the intermediate specimens illustrating inhomogeneous particle distributions.
A, B: Continuously heated to 1190 °C and water quenched.

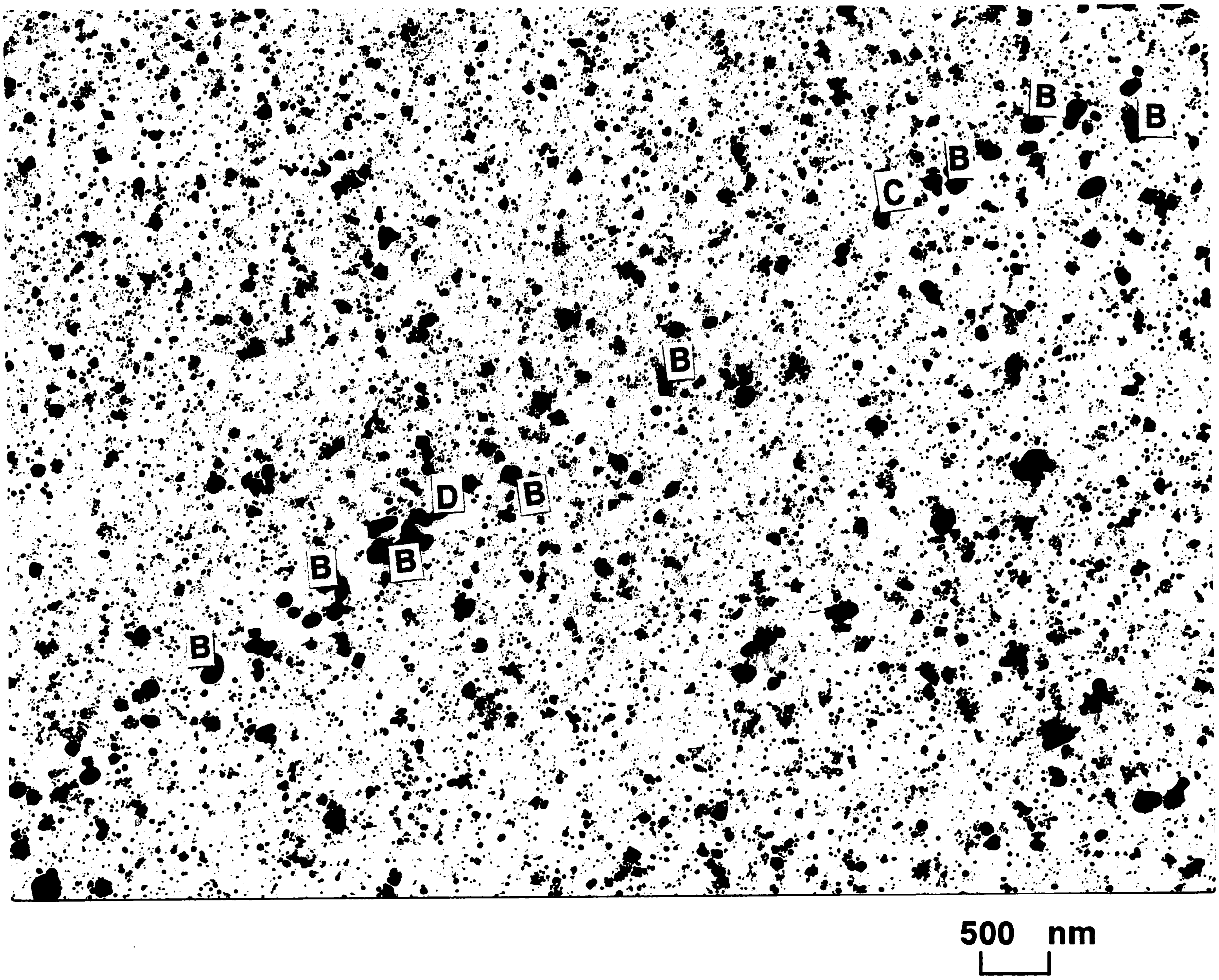

Fig. 6.31 Particles in a carbon extraction replica from the continuous heating experiment, at 1230 °C recrystallised, and water quenched, for the intermediate specimen, illustrating that most of the aligned particles are Ti-rich. Relative atomic percent ratio for the metallic elements in the marked particles are:

B: Ti_{90-95}-Cr_{0-5}-Ta_{0-10}

C: Y_{40-60}-Al_{40-60}

D: $(Y\text{-}Zr)_{40-60}$-Al_{40-60}

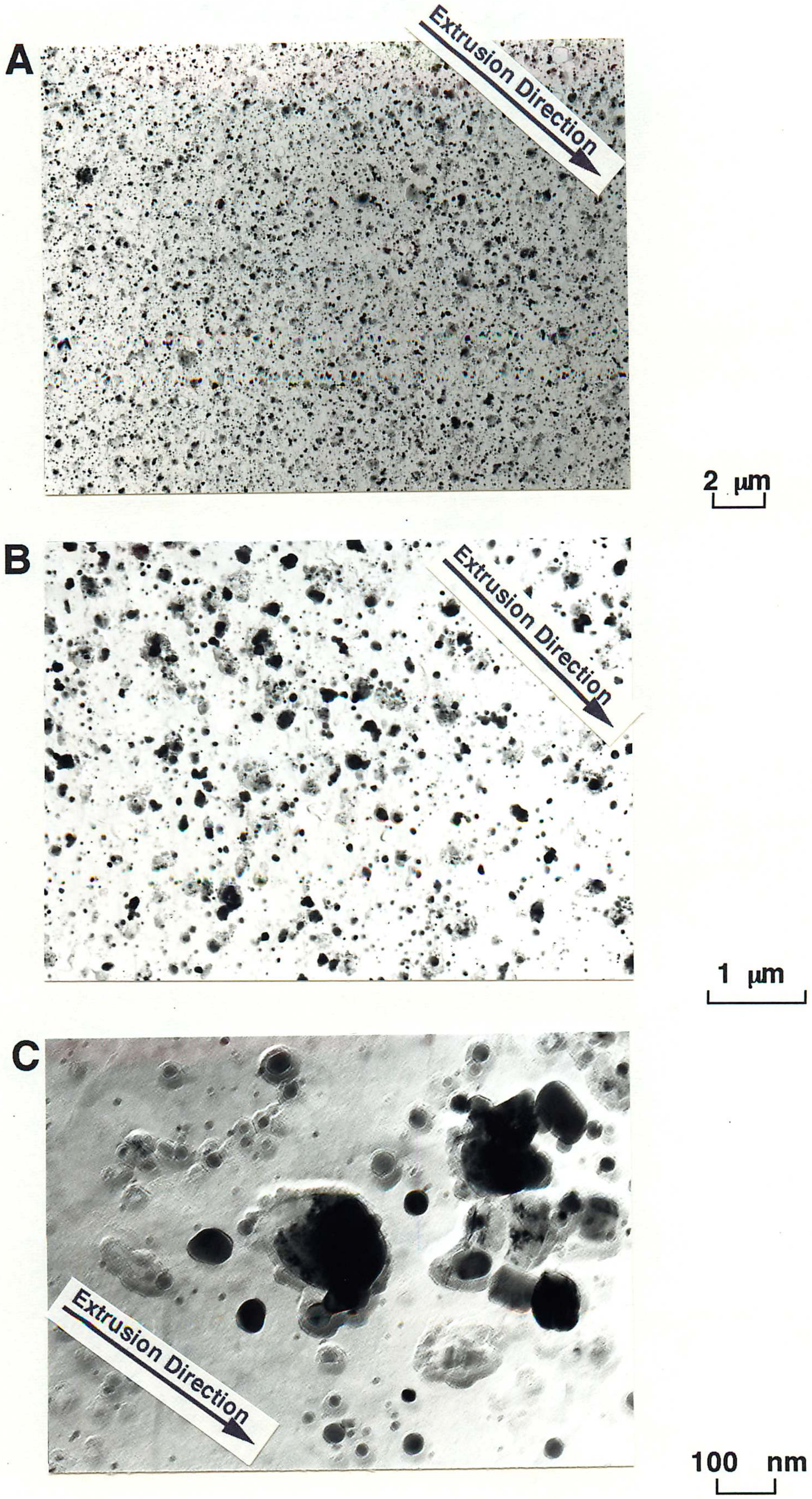

Fig. 6.32 TEM carbon extraction replica micrographs from the intermediate region of the extruded bar, isothermally annealed at 1160 °C for a time period of 60 min and water quenched.

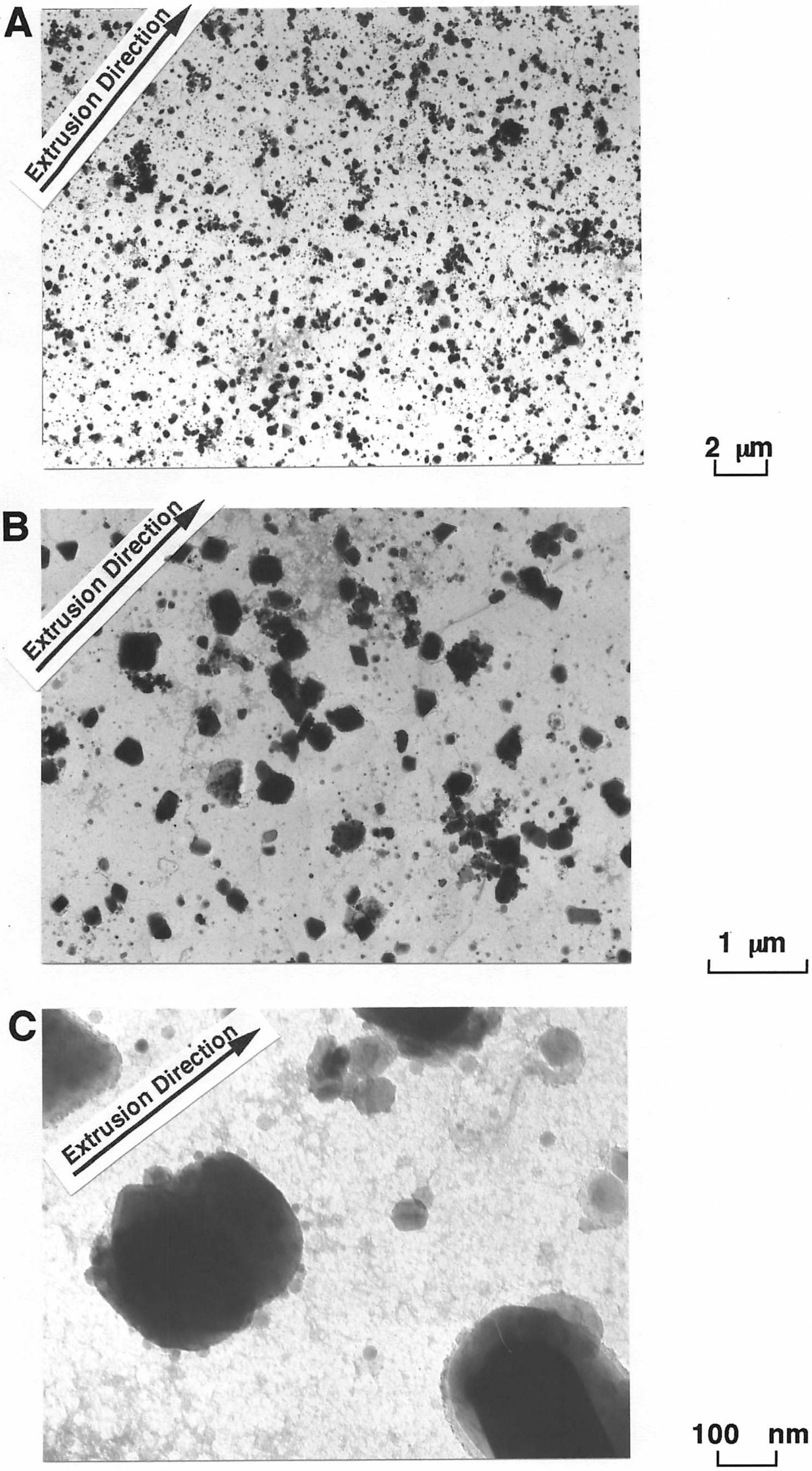

Fig. 6.33 TEM carbon extraction replica micrographs from the intermediate region of the extruded bar, isothermally annealed at 1160 °C for a time period of 3000 min and water quenched.

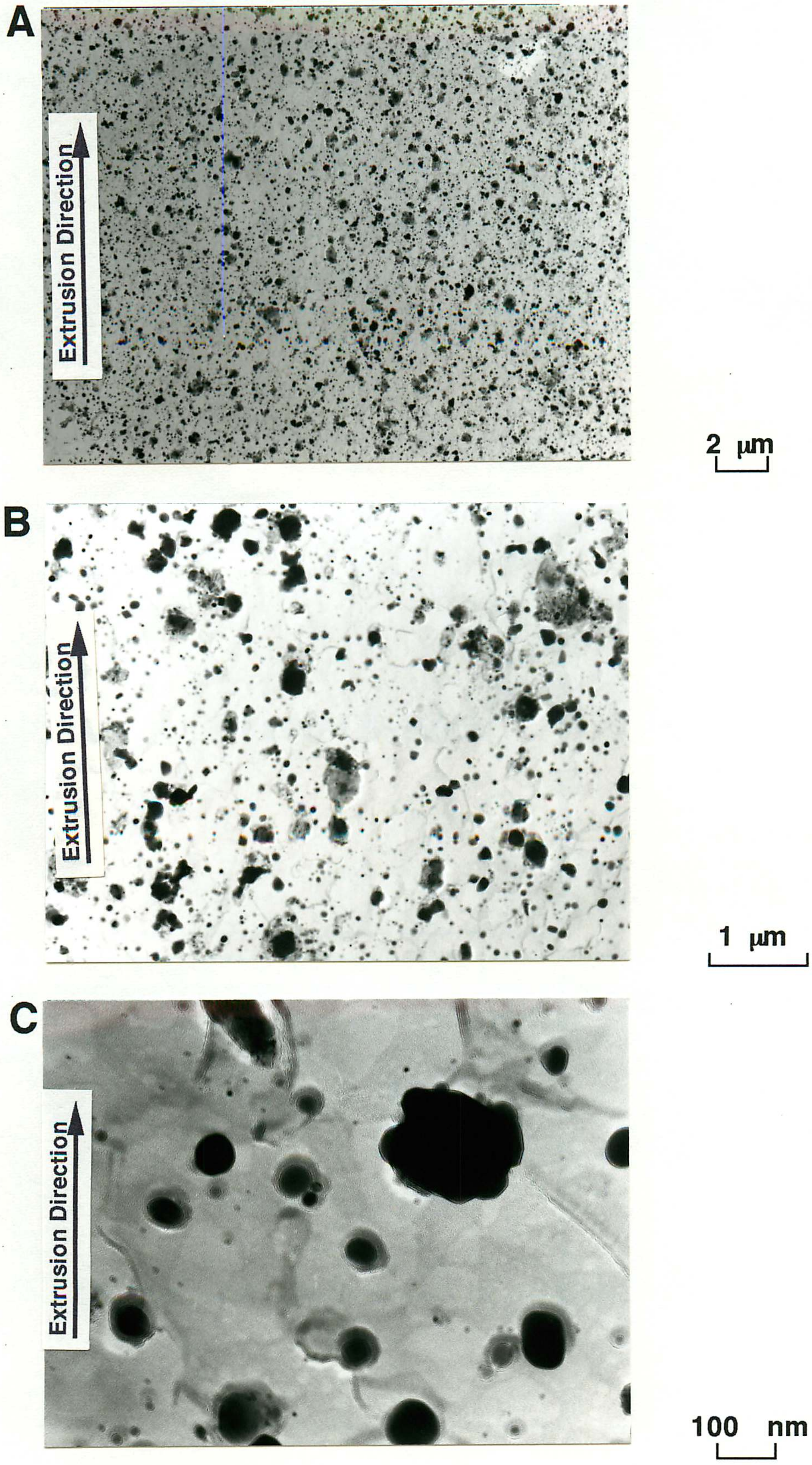

Fig. 6.34 TEM carbon extraction replica micrographs from the intermediate region of the extruded bar, isothermally annealed at 1180 °C for a time period of 60 min and water quenched.

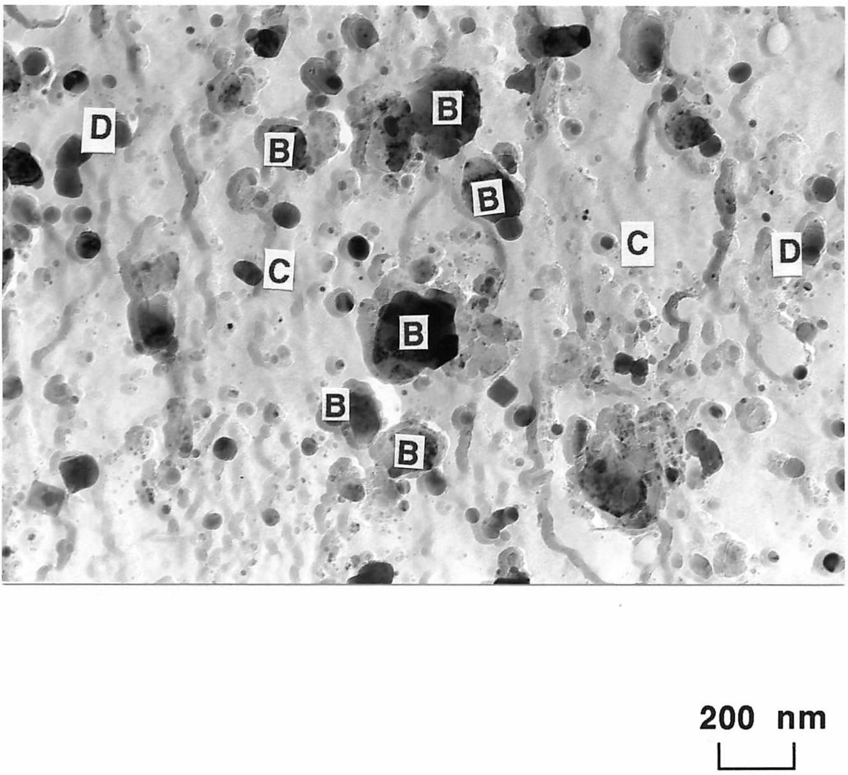

Fig. 6.35 Particles in a carbon extraction replica from the isothermal annealing experiment, at 1160 °C for a time period of 60 min, unrecrystallised, and water quenched, for the intermediate specimen. Relative atomic percent ratio for the metallic elements in the marked particles are:

B: Ti_{90-95}-Cr_{0-5}-Ta_{0-10}

C: Y_{40-60}-Al_{40-60}

D: $(Y\text{-}Zr)_{40-60}$-Al_{40-60}

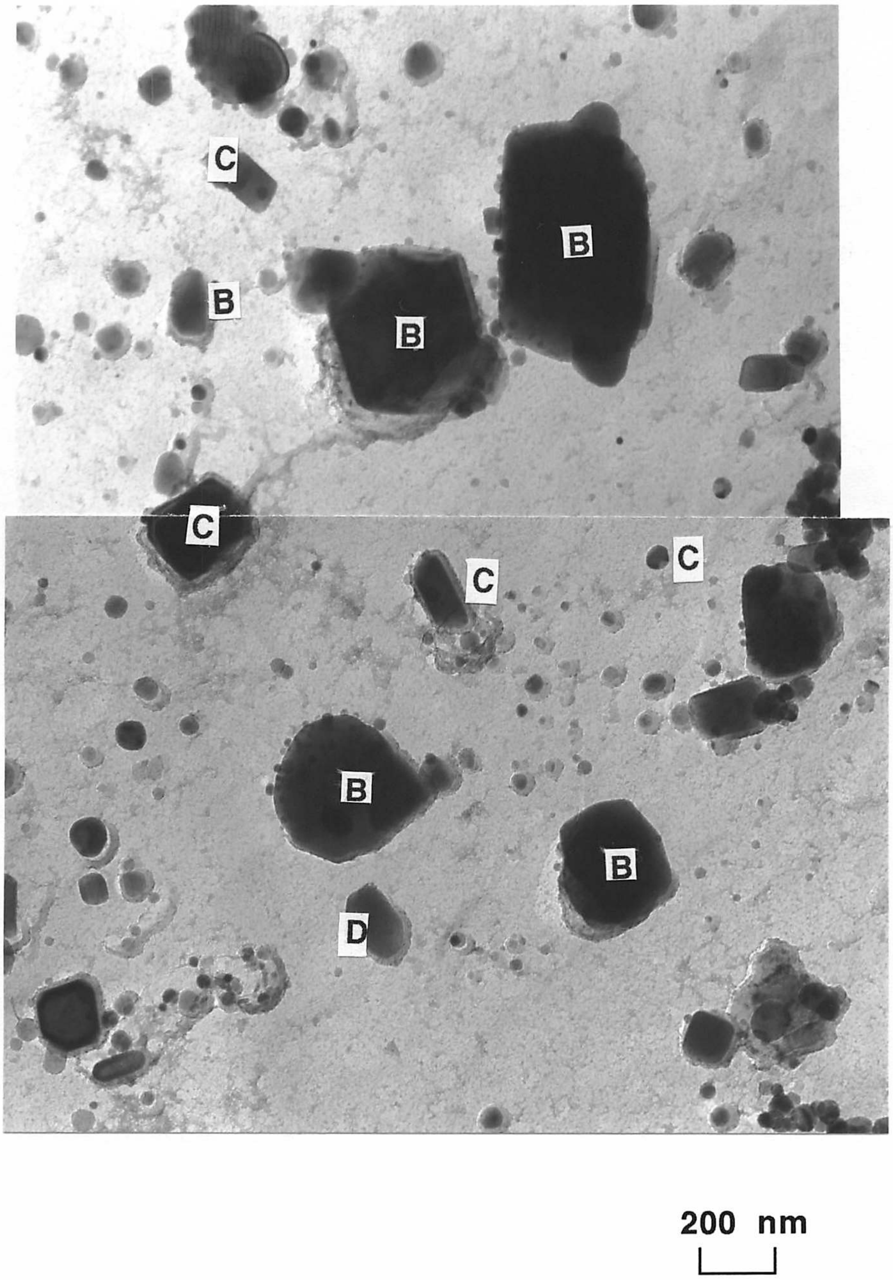

Fig. 6.36 Particles in a carbon extraction replica from the isothermal annealing experiment, at 1160 °C for a time period of 3000 min, unrecrystallised, and water quenched, for the intermediate specimen. Relative atomic percent ratio for the metallic elements in the marked particles are:

B: Ti_{90-95}-Cr_{0-5}-Ta_{0-10}

C: Y_{40-60}-Al_{40-60}

D: $(Y\text{-}Zr)_{40-60}$-Al_{40-60}

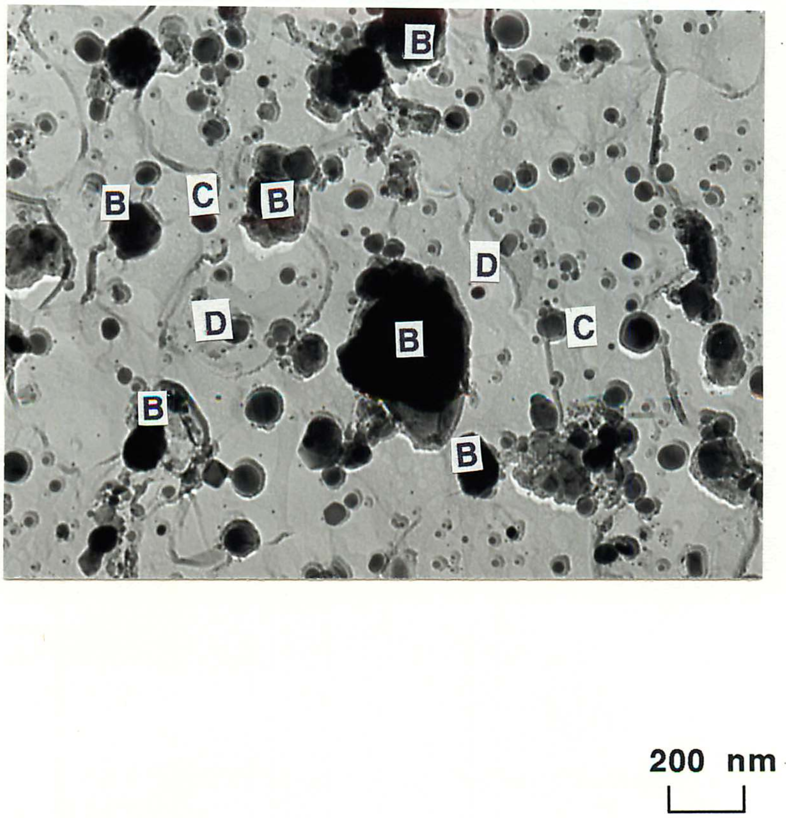

Fig. 6.37 Particles in a carbon extraction replica from the isothermal annealing experiment, at 1180 °C for a time period of 60 min, unrecrystallised, and water quenched, for the intermediate specimen. Relative atomic percent ratio for the metallic elements in the marked particles are:

B: Ti_{90-95}-Cr_{0-5}-Ta_{0-10}

C: Y_{40-60}-Al_{40-60}

D: $(Y\text{-}Zr)_{40-60}$-Al_{40-60}

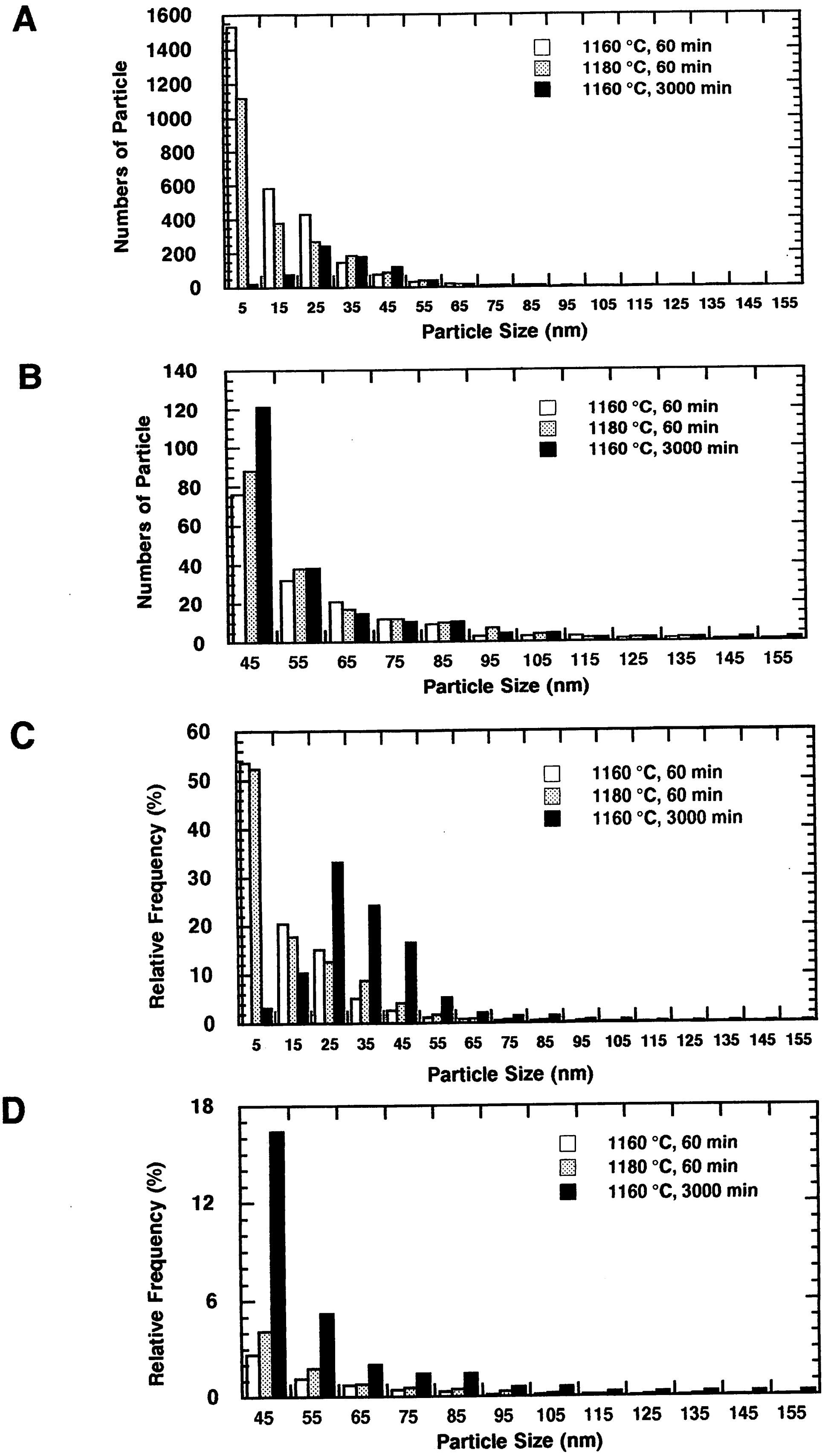

Fig. 6.38 Comparison of particle distributions for the isothermally annealed the intermediate specimens.
A: Numbers of particles as a function of particle size
B: Same as A, but detail of large particle size area
C: Relative frequencies of particle sizes
D: Same as C, but detail of large particle size area

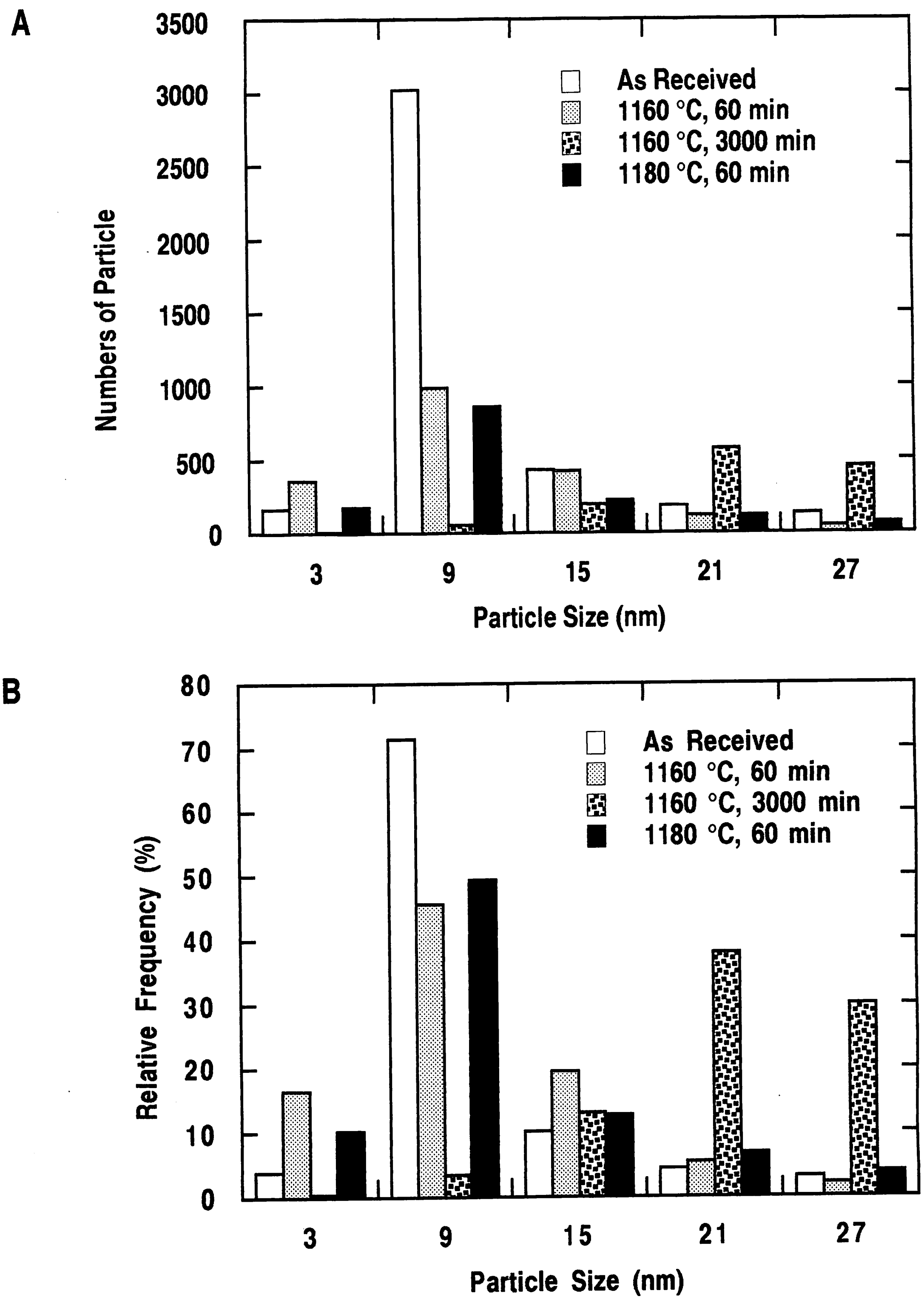

Fig. 6.39 Comparison of small particle (< 30 nm) distributions from the isothermally annealed intermediate specimens.
A: Number of particles
B: Relative frequency

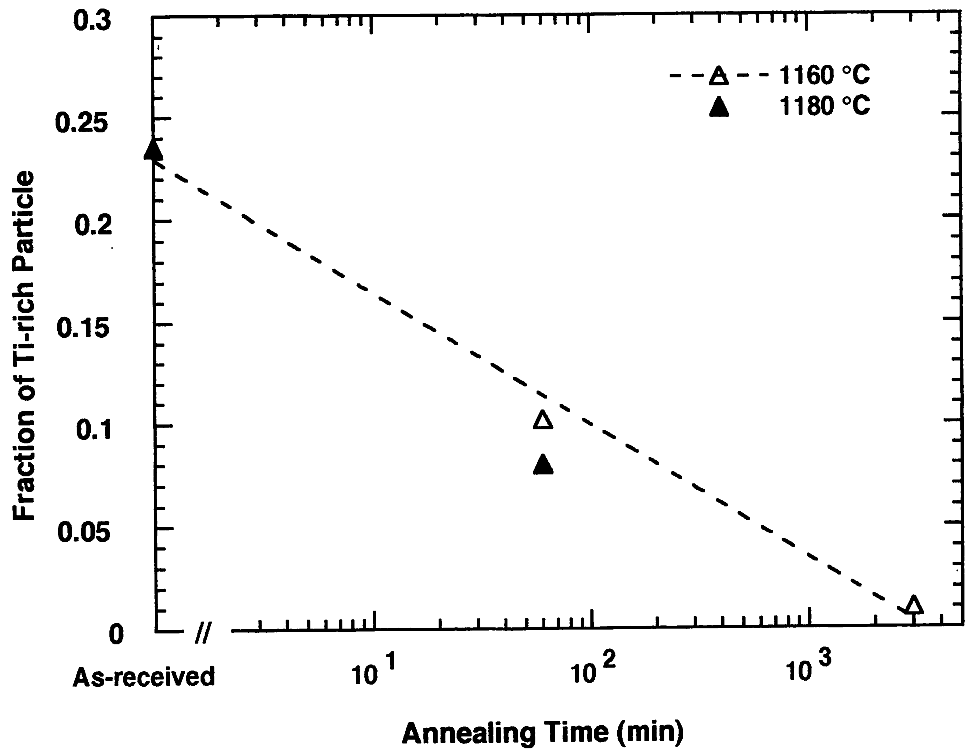

Fig. 6.40 Fraction of Ti-rich particle within a particular size range (20 - 40 nm) as a function of temperature, during continuous heating experiments.

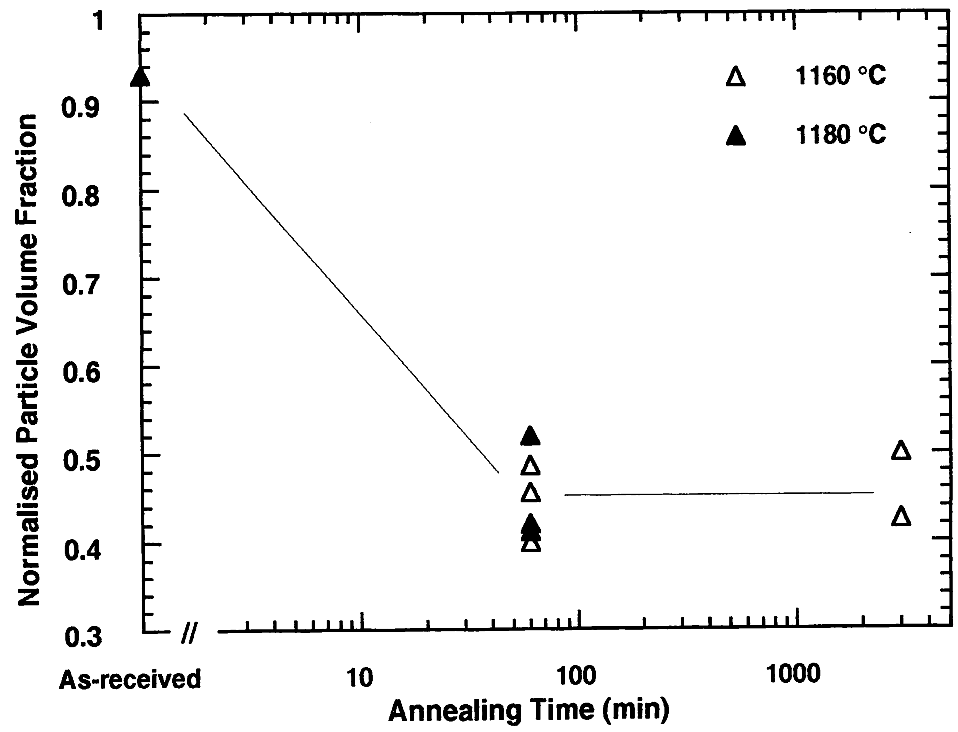

Fig. 6.41 Normalised volume fraction of particles as a function of annealing time and temperature, during isothermal annealing experiments on the intermediate specimens. The normalised volume fraction of the as-received specimen is taken to be unity. The error bars in the diagram show the maximum and minimum values for measurements on the same microstructural data.

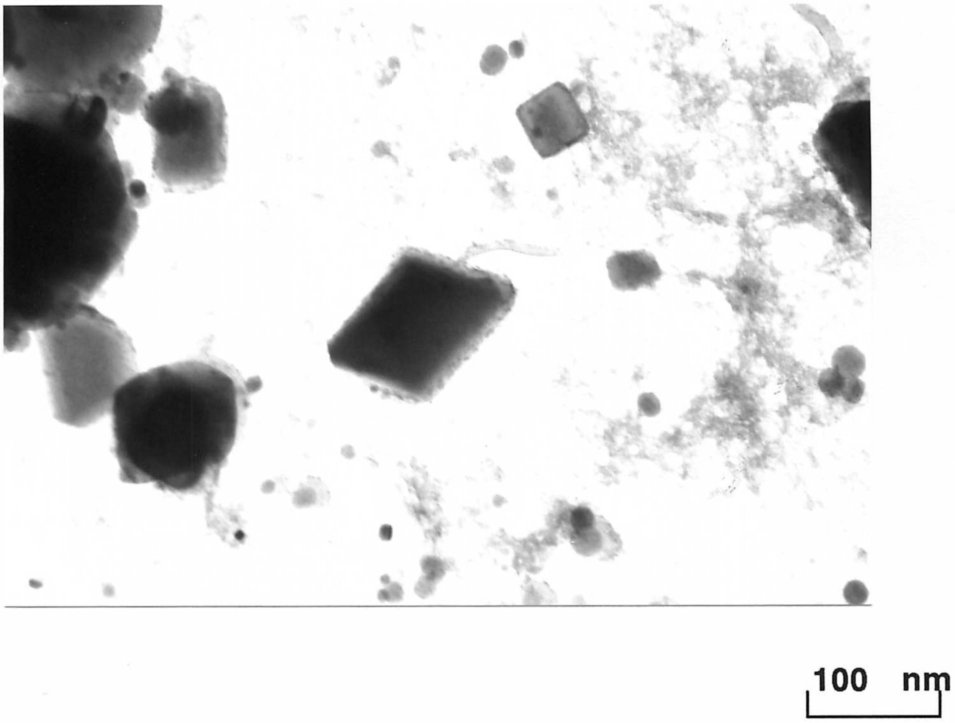

Fig. 6.42 A carbon extraction replica illustrating the facetted shape Y_2O_3-Al_2O_3 Particle.

6.4 Discussion

A summary of the observed changes in particle characteristics is presented in Tables 6.2.-6.4. The $M_{23}C_6$ carbides dissolve quickly before recrystallisation-start, even at large heating rates. This does not affect recrystallisation because the temperatures are more than a hundred degrees lower than the recrystallisation temperatures. It has been reported that the aligned $M_{23}C_6$ type carbides play an important role in inhomogeneous recrystallisation [7], but here they do not appear to do so. $M_{23}C_6$ type carbides can be found at the recrystallised grain boundaries only after slow cooling from the recrystallisation temperatures, but never in water quenched specimens (Fig. 6.43).

Type B particles, TiC, TiN found in as-received specimen change into Ti(C,N) after heat treatment, and are found to be more thermally stable at high temperatures. Very small Ti-rich particles may dissolve at temperatures in excess of 1100 °C. After reaching equilibrium, they start to coarsen. However, the effect of coarsening on the particle distribution is much smaller than the solution of smaller particles. This is because about 60 % the Ti-rich are less than 30 nm size.

Of the type C and D particles, mixed Y_2O_3-Al_2O_3 oxides are the most thermally stable but they do change in size, kind, morphology and composition. Therefore it is appropriate to consider the effect on particle changes on recrystallisation in a quantitative data.

Coarsening and dissolution take place during continuous heating, so that grain boundary pinning forces must decrease due to the heat treatment. The Zener pinning force P_r for particles of radius r is [11]:

$$P_r = C_1 V_M \sigma r N_r \qquad (6.1)$$

where C_1 is a constant whose magnitude depends on the details of the pinning process, r is the particle radius, V_M is the molar volume ($\approx 7.1 \times 10^{-6}$ m^3 mol^{-1}), and σ is the boundary energy per unit area. N_r is the number of particles per unit area (Chapter 4) [1].

$$P_p = C_1 V_M \sigma r \sum N_r \qquad (6.2)$$

The driving force for secondary recrystallisation ΔG_s is given by

$$\Delta G_s \approx V_M \sigma / R \qquad (6.3)$$

where R is the average grain size of the recrystallised microstructure [12].

Calculations of P_p and ΔG_s were carried out using reasonable values of $C_1 = \pi$ and $\sigma = 0.6$ J m^{-2}, and using measured values of R and r.

Measured N_r values are much greater than in reality because the extraction process exaggerates the number density. Therefore, only a comparison of trends can be done. Figs. 6.44 and 6.45 show the results. The pinning force decreases rapidly but the driving force does not, for both the intermediate and the core specimens. Differences in pinning force cannot therefore explain the 30 K variation in recrystallisation temperature between the two locations. The pining force significantly decreases during isothermal annealing, but this does not stimulate recrystallisation. For example, in the intermediate specimens, after annealing at 1160 °C for 60 min, the pinning force becomes much smaller but the sample nevertheless does not recrystallise (Fig. 6.45). In the recrystallisation model presented in Chapter 4, aligned particles lead to a lower recrystallisation temperature than is the case when the particles are more randomly dispersed, when even the particle volume fraction is fixed (Chapter 4) [1]. The measured mean interparticle spacing values parallel and normal to the extrusion direction do not show large anisotropy (Table 6.5). The measurements are from approximately 10 μm square of the continuously heated intermediate and core specimens. The anisotropy is therefore not very pronounced, at least over a range less than 10 μm. However, large differences can be found in the number density of particles as a function of location. It is tempting to suggest that the columnar grain size correlates with the scale of these inhomogeneities (Fig. 6.46)

The short range (less than 10 μm) anisotropy is found not to be remarkable, but there are also longer range variations in the alloy in the form of differences in particle number density (Figs. 6.9, 6.30). The recrystallised grain boundaries tend to coincide with boundary between the high and low particle density zones (Fig. 6.47).

Table 6.2 Summary of EDX analysis results from continuous heating experiments for the intermediate specimens

Size	As-received	Before Recrystallisation 1190 °C +W.Q.	After Recrystallisation 1230 °C+ W.Q.
Very Large <300 nm	$M_{23}C_6$	-	-
Large 300-100 nm	$M_{23}C_6$ TiC, TiN, TaN Y_2O_3-Al_2O_3 Y_2O_3-Al_2O_3+Zr Al_2O_3	Ti(C,N) Y_2O_3-Al_2O_3 Y_2O_3-Al_2O_3+Zr	Ti(C,N) Y_2O_3-Al_2O_3 Y_2O_3-Al_2O_3+Zr
Medium 100-50 nm	$M_{23}C_6$ TiC, TiN, TaN Y_2O_3-Al_2O_3 Y_2O_3-Al_2O_3+Zr Al_2O_3	Ti(C,N) Y_2O_3-Al_2O_3 Y_2O_3-Al_2O_3+Zr	Ti(C,N) Y_2O_3-Al_2O_3 Y_2O_3-Al_2O_3+Zr
Small 10-50 nm	$M_{23}C_6$ TiC, TiN, TaN Y_2O_3-Al_2O_3 Y_2O_3-Al_2O_3+Zr Y_2O_3(?)	Ti(C,N) Y_2O_3-Al_2O_3 Y_2O_3-Al_2O_3+Zr	Ti(C,N) Y_2O_3-Al_2O_3 Y_2O_3-Al_2O_3+Zr

Table 6.3 Summary of EDX analysis results from continuous heating experiments for the core specimen

Size	As-received	Before Recrystallisation 1230 °C +W.Q.	After Recrystallisation 1270 °C+ W.Q.
Very Large <300 nm	$M_{23}C_6$	-	-
Large 300-100 nm	$M_{23}C_6$ TiC, TiN, TaN Y_2O_3-Al_2O_3 Y_2O_3-Al_2O_3+Zr Al_2O_3	Ti(C,N) Y_2O_3-Al_2O_3 Y_2O_3-Al_2O_3+Zr	Ti(C,N) Y_2O_3-Al_2O_3 Y_2O_3-Al_2O_3+Zr
Medium 100-50 nm	$M_{23}C_6$ TiC, TiN, TaN Y_2O_3-Al_2O_3 Y_2O_3-Al_2O_3+Zr Al_2O_3	Ti(C,N) Y_2O_3-Al_2O_3 Y-Al-Zr	Ti(C,N) Y_2O_3-Al_2O_3 Y_2O_3-Al_2O_3+Zr
Small 10-50 nm	$M_{23}C_6$ TiC, TiN, TaN Y_2O_3-Al_2O_3 Y_2O_3-Al_2O_3+Zr Y_2O_3(?)	Ti(C,N) Y_2O_3-Al_2O_3 Y_2O_3-Al_2O_3+Zr	Ti(C,N) Y_2O_3-Al_2O_3 Y_2O_3-Al_2O_3+Zr

Table 6.4 Summary of EDX analysis results from isothermal annealing experiments for the Intermediate specimen

Diameter	1160 °C 60 min+W.Q	1160 °C 3000 min+W.Q.	1160 °C 60 min+W.Q.
Extra Large <300 nm	-	Ti(C,N)	-
Large 300-100 nm	Ti(C,N) Y_2O_3-Al_2O_3 Y_2O_3-Al_2O_3+Zr	Ti(C,N) Y_2O_3-Al_2O_3 Y_2O_3-Al_2O_3+Zr	Ti(C,N) Y_2O_3-Al_2O_3 Y_2O_3-Al_2O_3+Zr
Medium 100-30 nm	Ti(C,N) Y_2O_3-Al_2O_3 Y_2O_3-Al_2O_3+Zr	Ti(C,N) Y_2O_3-Al_2O_3 Y_2O_3-Al_2O_3+Zr	Ti(C,N) Y_2O_3-Al_2O_3 Y_2O_3-Al_2O_3+Zr
Small 10-30 nm	Ti(C,N) Y_2O_3-Al_2O_3 Y_2O_3-Al_2O_3+Zr	Y_2O_3-Al_2O_3 Y_2O_3-Al_2O_3+Zr	Ti(C,N) Y_2O_3-Al_2O_3 Y_2O_3-Al_2O_3+Zr

Table 6.5 Interparticle spacing

	Parallel to the extrusion direction	Normal to the extrusion direction
Intermediate	70 nm	71 nm
Core	72 nm	69 nm

The inhomogeneous particle dispersion therefore strongly affects the progress of recrystallisation.

Further metallographic data illustrate the early stages of recrystallisation, with anisotropic growth proceeding more rapidly along the high and low particle density interfaces (Fig. 6.48). Particles of size greater than 50 nm are more prevalent in some regions. Most of these larger particles are Ti-rich, indicating inhomogeneous of chemical composition.

The layered distribution of particles can be easily found at the optical microscopic scale, the high particle density zones being about 10 μm wide in the intermediate specimens, and 18 μm in the core regions (Fig. 6.49). The zones must originate during the mechanical alloying. If there are different compositions of particles at even the final stages of the mechanical alloying, these differences generate the layered structure on extrusion (Fig. 6.50). The individual powder diameter at the final stage of mechanical alloying is about 100 μm [9,10]. Since the extrusion ratio is about 10, the layer width of 10 - 18 μm is consistent with the existence of inadequately mechanically alloyed powder. It is likely that the extrusion ratio of the core area of the bar is smaller than the that of intermediate area.

Heat treatment can in principle reduce the inhomogeneities in particle distributions. It is believed that the scatter in particle fraction data is larger in continuously heated samples relative to those which are isothermally annealed. Because the latter tends to homogenise the microstructure prior to recrystallisation, thereby also leading to a more equiaxed recrystallisation structure.

Particle changes have not been found to correlate with the onset of recrystallisation. It is believed that recrystallisation in ultra fine grained materials is abnormally difficult because grain boundary bowing has to occur between closely spaced grain boundary junctions (Appendix 2)

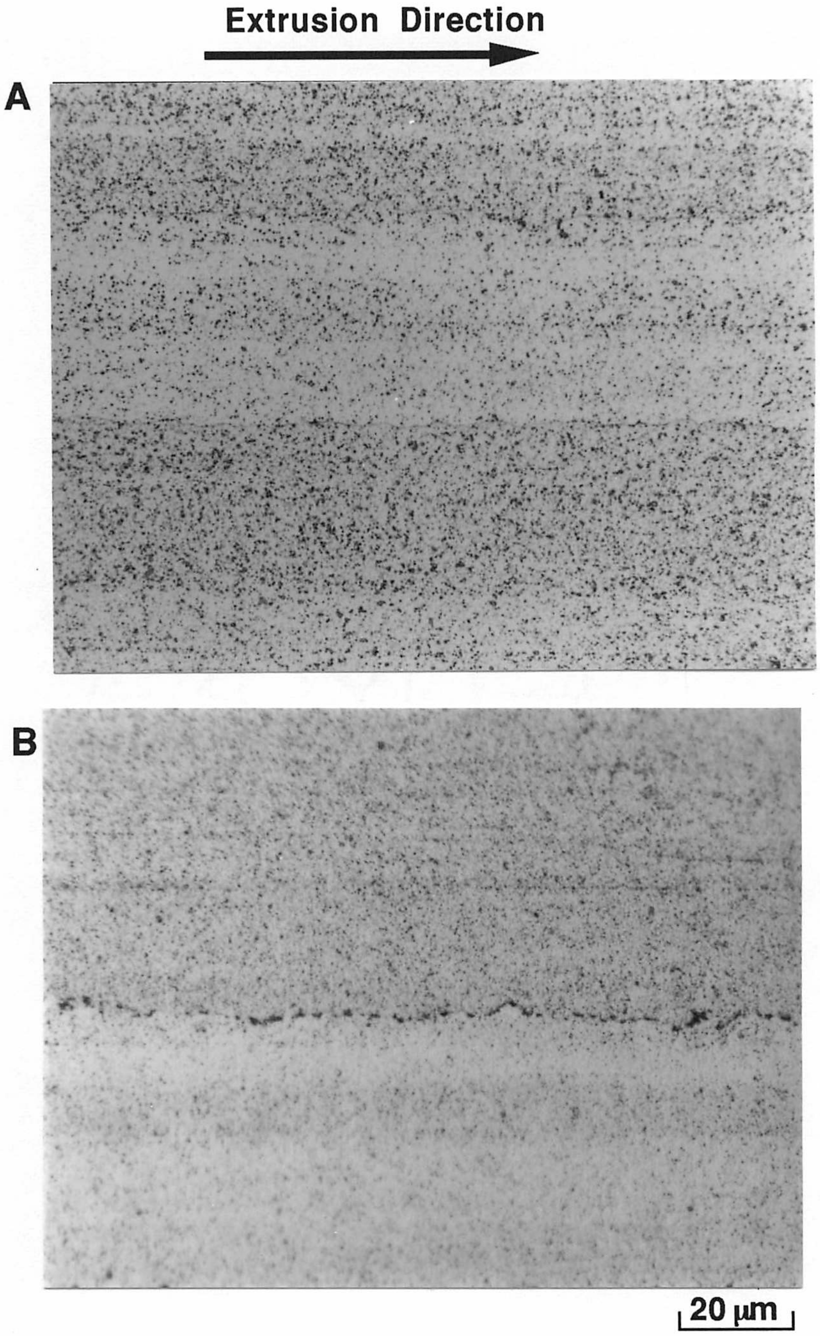

Fig. 6.43 Metallographic data for continuous heated intermediate specimens up to 1230 °C, illustrating high and low particle density layers.

A: Water quenched after heating

B: Furnace cooled after heating

Carbides precipitate at recrystallised grain boundaries in the furnace cooled specimen.

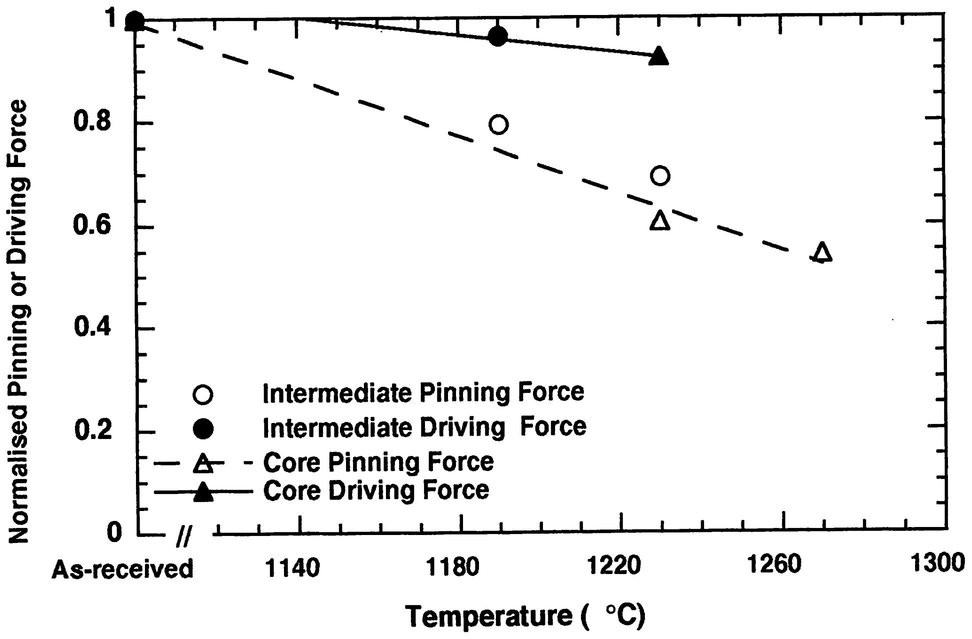

Fig. 6.44 Pinning force and driving force for recrystallisation calculated using measured particle distributions and sizes. The pinning force and driving force of the as-received intermediate specimen are taken to be unity. Continuous heating experiments.

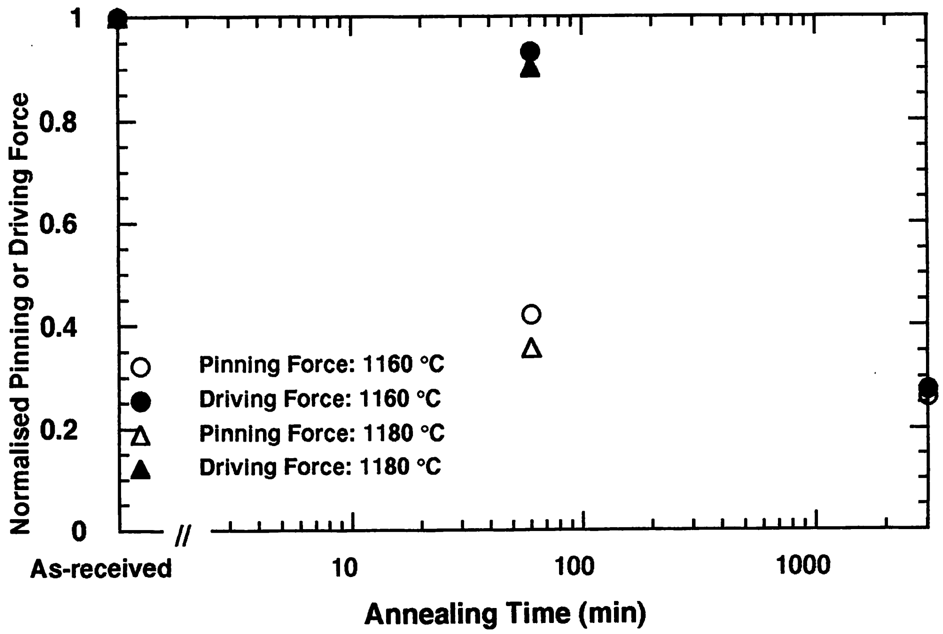

Fig. 6.45 Pinning force and driving force for recrystallisation calculated using measured particle distributions and sizes. The pinning force and driving force of the as-received intermediate specimen are taken to be unity. Isothermal annealing experiments.

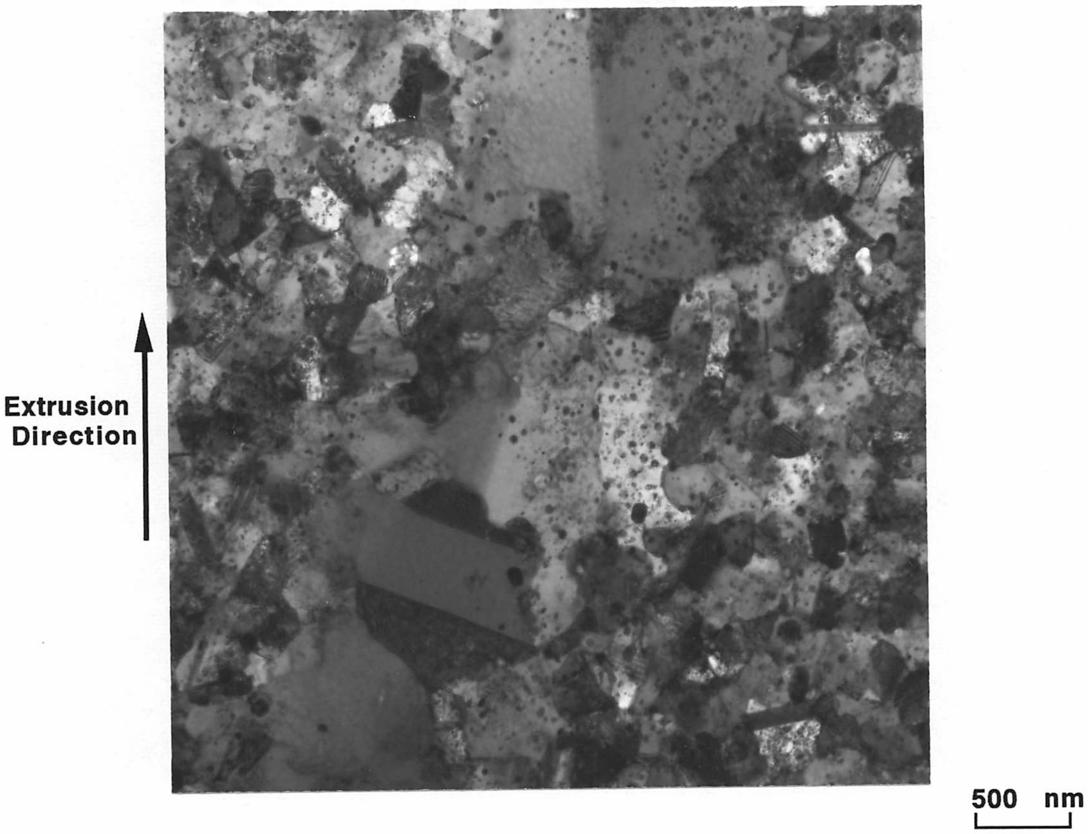

Fig. 6.46 TEM micrograph illustrating an early stage of recrystallisation. The large grains are along a particle depleted zone

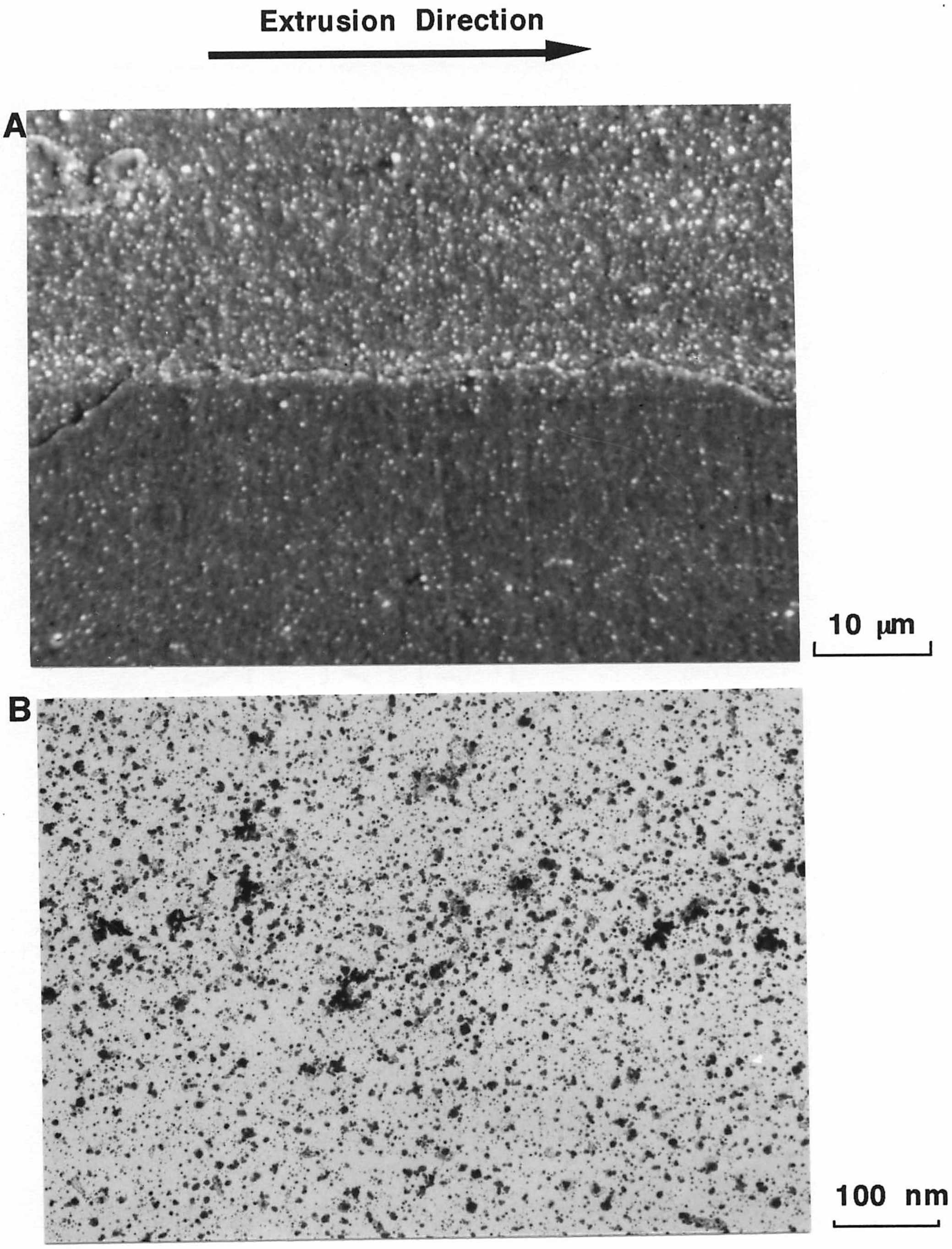

Fig. 6.47 SEM and TEM carbon extraction replica structures illustrating high and low particle density regions. A recrystallised grain boundary aligns with the interface between high and low particle density regions in the SEM structure. Intermediate region, continuously heated up to 1230 °C and water quenched, fully recrystallised. Relative volume fractions of particle V_f (V_f in the low density area = 1) are shown in the above figure B.

A: SEM B: TEM

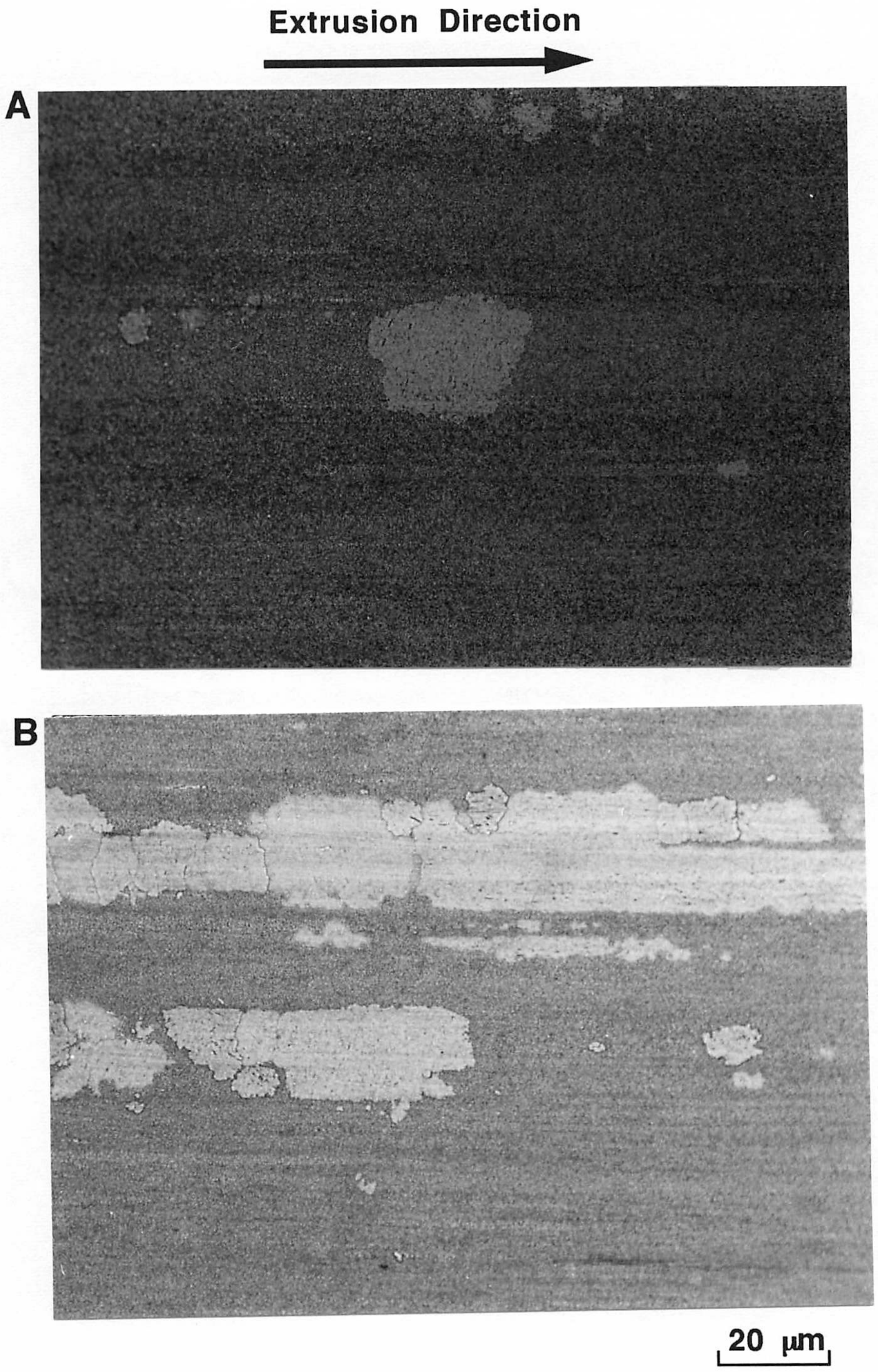

Fig. 6.48 Metallographic data from an isothermal annealing experiment, at 1180 °C for a time period of 60 min and water quenched, illustrating early stages of recrystallisation.

A: The isotropic growth of grains is disturbed by the interfaces between the high and low particle density layers.

B: Recrystallisation taking place in particular layers.

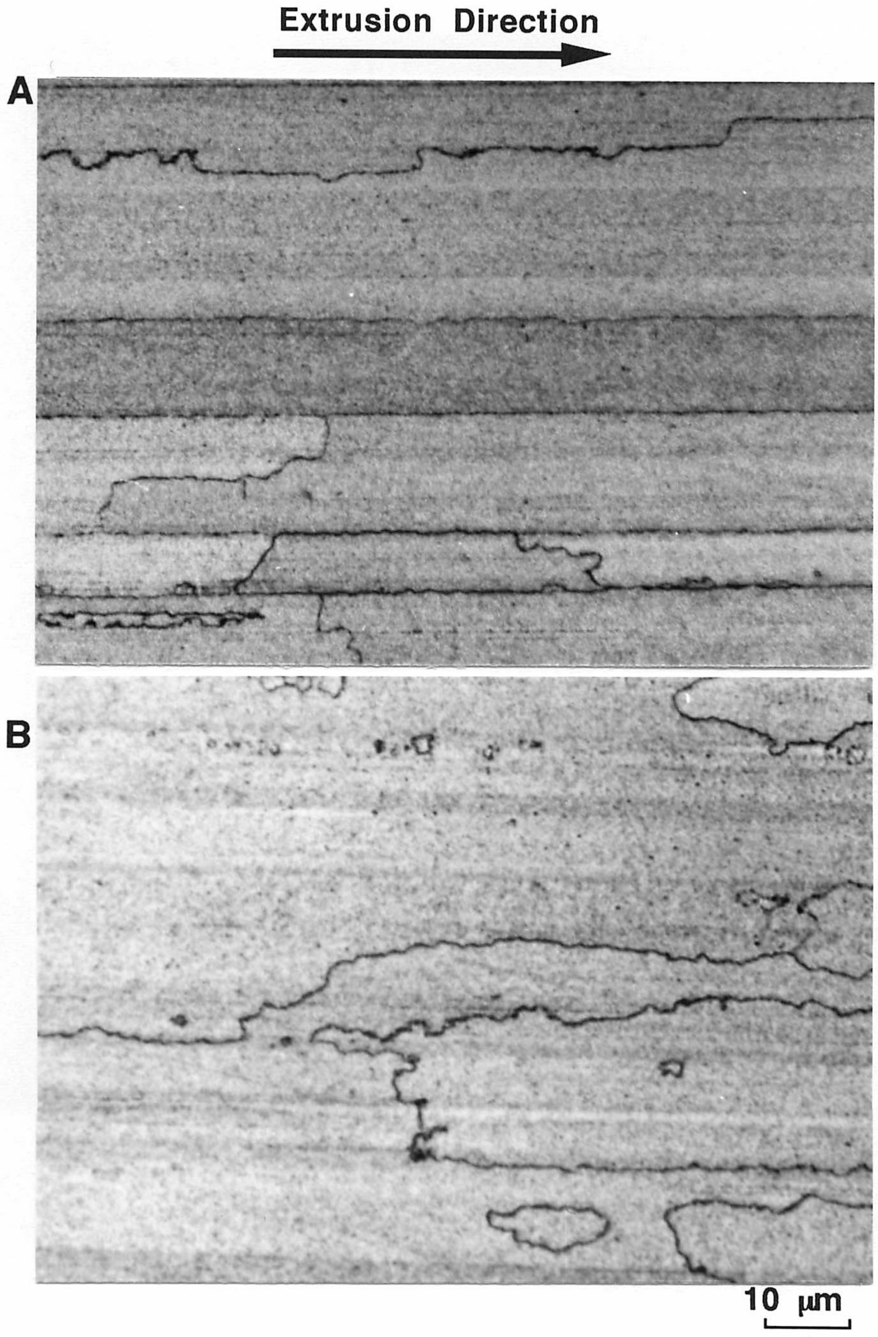

Fig. 6.49 Metallographic data from continuous heating experiments for the recrystallised intermediate and core specimens, illustrating grain boundaries and high and low particle density layers.

A: Intermediate

B: Core

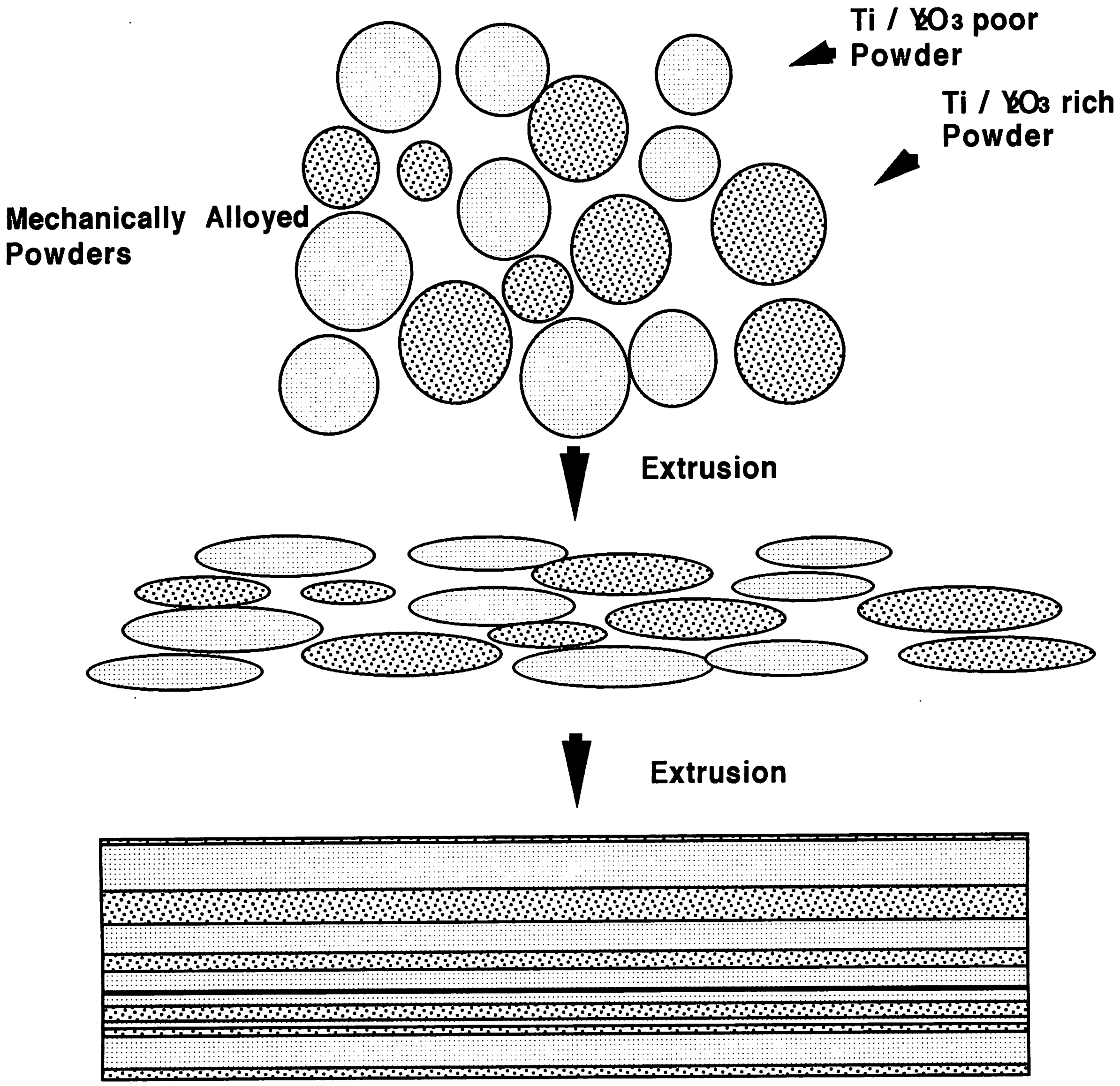

Fig. 6.50 The origin of inhomogeneties in particle distributions, illustrating how variations in powder chemistries become layers after consolidation.

6.7. Conclusions

There are at least four kinds of particles in as-received *MA6000*. $M_{23}C_6$ type carbides dissolve well before the onset of recrystallisation temperatures. The other more stable particles are Ti-rich particles, Y-Al and Y-Al-Zr particles. The Ti-rich particles are probably Ti(C,N) or mixed Ti(C,N) and Ta(C,N). Y-Al and Y-Al-Zr particles are in fact are of a variety of possible garnets.

Ignoring $M_{23}C_6$, the rather larger (50-150 nm) particles are mainly Ti-rich and the smaller particles (< 50 nm) are mainly Y-Al or Y-Al-Zr. Ti-rich particles can exist temperatures in excess of 1160 °C, but coarsening takes place relatively rapidly. The Y-Al and Y-Al-Zr particles are more thermally stable. Although they slightly increase in size during annealing, it is not clear whether this represents coarsening or reaction to form garnets.

There is no direct evidence that the coarsening of particles significant with regard to the onset of recrystallisation. However, inhomogeneities in the distribution of particles influence both the anisotropy and scale of the directionally recrystallised microstructure. The origin of the inhomogenity is probably the imperfection of the mechanical alloying process.

References

1. Murakami K., Mino K., Harada H., and Bhadeshia H.K.D.H.: *Metall. Trans.*, (1993), **24A**, p. 1049.
2. Hotzler R. K. and Glasgow T. K.: *Metall. Trans.*, (1982), **13A**, p 1665.
3. Schaffer G. B., Loretto M. H., Smallman R. E. and Brooks J. W.: *Acta Metall.*, (1989), **37**, p. 2551.
4. Lawn R. E., Wilson F. G., and Desforges C. D. : *Powder Metall.*, (1976), **19**, p. 196.
5. Kang K., Benn R.C. : *Metall. Trans.*, (1985), **16A**, p. 1285.
6. K., Mino K., Harada H., Bhadeshia H.K.D.H. and Yamazaki M. : *Mater Sci. Forum.*, (1992), **88-90**, p. 213.
7. Kim S. S. and Hanada S. : to be submitted to *Trans. JIM.*
8. Murakami K., Harada H. and Bhadeshia H.K.D.H.: *Proceedings of Heat & Surface* '92, (1992), ed. by Tamura I., Japan Technical Information Service, Tokyo, p. 269
9. Benjamin J. S. : *Metall. Trans.* (1970), **1**, p. 2943.
10. Kang S. K.and Benn R. C.: *Metall. Trans.* (1986), **18A**, p. 747.
11. *Recrystallization of Metallic Materials,* edited by Haessner F., K. Hasselkus, Stuttgart, Germany, (1978), p. 12.

CHAPTER 7

CONCLUSIONS AND FUTURE WORK

The major aim of this research was to obtain a metallurgical understanding for the process of directional recrystallisation in mechanically alloyed oxide dispersion strengthened (ODS) nickel base superalloys. A number of experiments were carried out to complement the aim and essential results are summarised here.

The effect of a pre-annealing heat treatments below the temperature at which significant recrystallisation begins, is to reduce the stored energy. On a microscopic scale, pre-annealing initiates the recrystallisation process, so that subsequent gross recrystallisation is accelerated. There are two other consequences of the reduced stored energy. Firstly, the recrystallised grain boundary topology becomes relatively rough as the driving force for grain boundary motion is reduced relative to the pinning force due to the oxide particles. Secondly, due to the associated reduced grain boundary velocity, recrystallisation is able to develop from many different sites during subsequent continuous heating, giving a more refined ultimate microstructure. By contrast, at large stored energies the grain growth velocity is so large that the few grains which begin their growth first are able to swamp all others, giving a coarse grain structure.

Extruded bars of *MA6000* have been found to exhibit significant variations in microstructure following secondary recrystallisation anneals. The surface regions tend to recrystallise at a more rapid rate relative to the core regions. Furthermore, the recrystallised grains at the surface are more anisotropic relative to the core regions. These results can be understood if it is assumed that inhomogeneous deformation during extrusion causes a more pronounced alignment of particles at the surface regions. This interpretation has to some extent been verified using a theoretical model for recrystallisation in the presence of anisotropic dispersion of pinning particles. The nonuniform dispersion of particles certainly influences the recrystallisation behaviour in ODS alloys. The particles in *MA6000* have been found to consist of oxides and carbides/nitrides, and are not as thermally stable as they had been originally considered.

There are at least two kinds of particles which persist at the recrystallisation temperature. There are Ti(C,N) and mixed oxides of Y_2O_3-Al_2O_3. Ti(C,N) survives at high temperatures greater than 1160 °C, but coarsening takes place relatively rapidly. Mixed oxides of Y_2O_3-Al_2O_3 are more thermally stable but slow coarsening occurs also; there is some doubt as to whether this is true coarsening or growth due to the reaction between yttria and alumina. The important observation is that there is no direct evidence that the coarsening of particles is responsible for triggering recrystallisation. Although short range ($\approx$ 10 μm) inhomogenities are found in the distribution of particles, there are in addition long range nonuniformities. These long range inhomogenities determine the growth direction of the recrystallising grains, and the final metallography. The origin of the inhomogenity is probably a degree of imperfect mechanical alloying.

The work presented in this dissertation suggests numerous new experiments. The most exciting of these is to pursue the idea that an ultrafine grained microstructure has difficulty in undergoing secondary recrystallisation. The idea is that the grain boundary junctions are so closely spaced that they make grain boundary bowing a very difficult process. This concept needs to be developed rigorously. There are many qualitative predictions. Nonuniformities in the grain size should lead to drastic reductions in the recrystallisation temperatures. Single phase nanocrystaline materials should find it impossible to recrystallise.

Appendix 1

Computer Program for the Calcuration of the Recrystallisation Temperaures

A computer program for the calcuration of the recrystallisation temperature here is according to the model in CHAPTER 4: using a modified Johnson-Mehl-Avrami equation assuming anisotropy of boundary (recrystallised-unrecrystallised interface) velocities due to the alignment of small particles. The theory of Johnson-Mehl-Avrami approach deals with static annealing, however, the experiments were involved continuous heating. This anisothermal heat-treatment can be taken into account by representing the continuous heating curve as a series of small isothermal steps. This program involves calucurations for continuous heating at constant heating rates or for any heat pattern. Parameters to be input are shown in Tables 4.2. The output is the volume fraction at each temperature or time after annealing.

The program also involves the calculation of kinetic strength. The principle of kinetic strength is explained in Chapter 2.

```
Copyright Bhadeshia, Harada, Mino, and Murakami K., University of Cambridge, 1993
C Directional Recrystallisation
C Last line used 7
      IMPLICIT REAL*8(A-H,K-Z),INTEGER(I,J)
      DOUBLE PRECISION TIME(500),KTEMP(500)
      AVER=1.3D+00
      KTEMPH=1500.0D+00+273.15D+00
      R=8.3143D+00
      QKIN=410000.0D+00
      QINT=284512.0D+00
      DKIN=0.374D-13
C
      C1=1.5D+10
C
      DKIN2=3.1283*DKIN
C STORE=SIGMA*VM*2/lbar
      STORE=30.0D+00
      FRAC=0.01D+00
      ANFRAC=15.0D+00
      RAD=0.01D-06
      SIGMA=0.6D+00
      JP=21
      CALL LOGO(1.0D+00)
      WRITE(*,6)
6     FORMAT(//////////////////
     &10X,' Please choose method:'//
     &15X,' Kinetic strength analysis          = 1'/
     &15X,' Directional recrystallisation theory = 2'//)
      CALL REEDI(JCHOS)
      IF(JCHOS .LT. 1 .OR. JCHOS .GT. 2)CALL BOUNDI(JCHOS,1,2)
5     CALL DEFAUL(DKIN,DKIN2,QKIN,STORE,RAD,FRAC,SIGMA,JP,KTEMPH
     &,QINT,C1,ANFRAC)
      CALL RCOMP(TIME,KTEMP,IH,KTEMPL,KTEMPH,HRATE,
     &JID,JCON,JYES)
C
C Heating Curve: constant heating rate as in DSC
      IF(JCON .EQ. 0) GOTO 2
      DTIME=((KTEMPH-KTEMPL)/HRATE)/500.0D+00
      KTEMP(1)=KTEMPL
      TIME(1)=0.0D+00
            DO 1 I=2,500
            TIME(I)=(I-1)*DTIME
            KTEMP(I)=KTEMPL + HRATE*TIME(I)
1           IF(KTEMP(I) .GT. KTEMPH)GOTO 3
3           IH=I-1
C Finish constant heating rate input
C
2     IF(JCHOS .EQ. 1) CALL  AKIN(TIME,KTEMP,IH,
     &QKIN,R,DKIN,DKIN2,JP)
```

```
C
      IF(JCHOS .EQ. 2) CALL DXX(IH,STORE,FRAC,RAD,
     &R,KTEMP,TIME,SIGMA,C1,QINT,JP,ANFRAC)
      WRITE(*,4)
4     FORMAT(///30X,' Kinetic strength analysis  = 1'/
     &       30X,' Directional Rex. analysis  = 2'/
     &       30X,' Exit                       = 0'///)
      CALL REEDI(JCHOS)
      IF(JCHOS .LT. 0 .OR. JCHOS .GT. 2)CALL BOUNDI(JCHOS,0,2)
      IF(JCHOS .EQ. 0)GOTO 7
      GOTO 5
7     STOP
      END
C
C HRATE is the heating rate during heating at a constant rate
C IH is the number of time-temperature pairs during arbitrary heating
C JID is an arbitrary identification number
C JCON allows either a constant HRATE (JCON=1) or an input of
C    time-temperature pairs (JCON=0)
C KTEMP Kelvin
C QKIN is the activation energy for kinetic strength calculation
C self diffusion in alpha iron (57 data book) 252295 Joules per mole
C QINT is the activation energy for atom transfer across boundary
C R is the gas constant
C TIME  minutes
C*********************************************************************
      SUBROUTINE  AKIN(TIME,KTEMP,IH,QKIN,R,DKIN,DKIN2,JP)
      IMPLICIT REAL*8(A-H,K-Z),INTEGER(I,J)
      DOUBLE PRECISION TIME(500),KTEMP(500),AKTEMP(500)
      KIN=0
C
          WRITE(*,3)
3         FORMAT(40X,'  KTEMP',3X,'CTEMP',5X,'KIN,  min'/)
          JDUM=0
          JDUM2=0
        DO 1 I=1,IH
        AKTEMP(I)=DEXP(-QKIN/(R*KTEMP(I)))
        IF(I .GT. 1)CALL TRAPE(TIME,AKTEMP,KIN,I)
        IF(I. GT. 1 .AND. KIN .GT. 0.01*DKIN .AND. JP*DINT(I/JP)
     &    .EQ. I)WRITE(*,2)KTEMP(I),(KTEMP(I)-273.15),KIN
        IF(KIN .GE. DKIN .AND. JDUM .EQ. 0)THEN
          WRITE(*,2)KTEMP(I),(KTEMP(I)-273.15),KIN
          WRITE(*,5)
          PAUSE ' Press RETURN to continue'
          WRITE(*,3)
          JDUM=1
        ENDIF
        IF(KIN .GE. DKIN2 .AND. JDUM2 .EQ. 0)THEN
          WRITE(*,2)KTEMP(I),(KTEMP(I)-273.15),KIN
          WRITE(*,7)
```

```
          JDUM2=1
          CALL REEDI(JYES)
          IF(JYES .EQ. 0) GOTO 6
       ENDIF
2           FORMAT(38X,F8.0,F8.0,2X,D12.3)
1           CONTINUE
C
6    IF(IH .GT. 1)CALL TRAPE(TIME,AKTEMP,KIN,IH)
     EXCKIN=KIN-DKIN2
     DELT=TIME(IH)-TIME(1)
     KTEFF=KIN/(DELT)
     KTEFF= -QKIN/(R*DLOG(KTEFF))
     WRITE(*,4)KTEFF,(KTEFF-273.15),DELT,EXCKIN
4    FORMAT(////
    &10X,' Effective isothermal annealing temperature, K ',F8.0/
    &10X,' Effective isothermal annealing temperature, C ',F8.0/
    &10X,' Annealed over a time interval, mins          ',F8.0/
    &10X,'  Wasted kinetic strength, mins               ',D12.4//)
5    FORMAT(//10X,' Directional Recrystallisation INITIATED'/)
7    FORMAT(//10X,' Directional Recrystallisation COMPLETED'//
    &      10X,' Continue to higher temperatures ?      '/
    &      10X,' Yes = 1        No = 0'/)
     RETURN
     END
C
C JP controls printing
C KIN is the kinetic strength of the heat treatment,  1/min
C DKIN2 is the KIN needed to cause equiaxed 100% recrystallisation
C EXCKIN kinetic strength available beyond that needed For 100% directional
recrystalliation
C DKIN is the KIN needed to cause 100 % directional recrystallisation
C KTEMP an array containing temperature values, Kelvin
C KTEFF effective absolute temperature for anisothermal heat treatment
C QKIN the activation energy appropriate for kinetic strength calculation,  J/mol
C TIME an array containing time values, s
C-------------------------------------------------------------------
     SUBROUTINE BOUND(A,B,C)
     DOUBLE PRECISION A,B,C,D
2     WRITE(*,1)B,C
1    FORMAT(12X,' Input value out of bounds'/
    &14X,' The limits are ',D12.4,' to ', D12.4///
    &14X,' Input new value, or 999 to continue with'/
    &14X,' original risky input                  ')
     CALL REED(D)
     IF(D .EQ. 999.0)GOTO 3
     A=D
     IF(A .LT. B .OR. A .GT. C)GOTO 2
3    RETURN
     END
C*****************************************************************************
```

```
      SUBROUTINE BOUNDI(I,J1,J2)
      IMPLICIT INTEGER(I,J)
2      WRITE(*,1)J1,J2
1     FORMAT(12X,' Input value out of bounds'/
     &14X,' The limits are ',I5   ,' to ', I5  ///)
      CALL REEDI(I)
      IF(I .LT. J1 .OR. I .GT. J2)GOTO 2
      RETURN
      END
C-----------------------------------------------------------------
      SUBROUTINE LOGO(AVER)
      DOUBLE PRECISION AVER
      WRITE(*,432)
432   FORMAT(//////////)
      WRITE(*,1)
1     FORMAT(
     &10X,' ************************************************',
     &'***********')
      WRITE(*,2)
2     FORMAT(10X,'  **',55X,'**')
      WRITE(*,2)
      WRITE(*,6)AVER
6     FORMAT(10X,' **',
     &5X,' DIRECTIONAL RECRYSTALLISATION (Version ',F3.1,') '
     &,5X,'**')
      WRITE(*,2)
      WRITE(*,2)
300   WRITE(*,2)
      WRITE(*,8)
8     FORMAT(10X,' **',8X,'               by              ',
     &9X,'**')
      WRITE(*,2)
      WRITE(*,9)
9     FORMAT(10X,' **',8X,'     Bhadeshia, Harada and Mino      ',
     &9X,'**')
      WRITE(*,2)
      WRITE(*,10)
10    FORMAT(10X,' **',8X,'     University of Cambridge/JRDC    ',
     &9X,'**')
      WRITE(*,11)
11    FORMAT(10X,' **',8X,'                                  ',
     &9X,'**')
      WRITE(*,12)
12    FORMAT(10X,' **',8X,'            AADC Project           ',
     &9X,'**')
      WRITE(*,2)
      WRITE(*,2)
      WRITE(*,1)
      WRITE(*,433)
433   FORMAT(////)
```

```
      PAUSE 'Press RETURN to continue'
      RETURN
      END
C------------------------------------------------------------------
      SUBROUTINE RCOMP(TIME,KTEMP,IH,KTEMPL,KTEMPH,HRATE,
     &JID,JCON,JYES)
      IMPLICIT REAL*8(A-H, K-Z),INTEGER(I,J)
      DOUBLE PRECISION TIME(500),KTEMP(500)
      IF(JYES .EQ. 1)GOTO 1
      WRITE(*,21)
21    FORMAT(////19X,' Identification Number ?')
      CALL REEDI(JID)
C
1     WRITE(*,30)
30    FORMAT(19X,' Constant heating rate ?'/
     &       19X,' 1 = Yes      0 = No    '/)
      CALL REEDI(JCON)
      IF(JCON .GT. 1 .OR. JCON .LT. 0)CALL BOUNDI(JCON,0,1)
      IF(JCON .EQ. 0)GOTO 2
      WRITE(*,22)
22    FORMAT(19X,' Heating rate, K/min ?')
      CALL REED(HRATE)
      IF(HRATE .LT. 0.1D-03 .OR. HRATE .GT. 40.0D+00)
     &CALL BOUND(HRATE,0.1D-03,40.0D+00)
      WRITE(*,27)
27    FORMAT(19X,' Start temperature, K ?')
      CALL REED(KTEMPL)
      GOTO 29
2     WRITE(*,23)
23    FORMAT(///////
     &       29X,' *** Nonlinear heating rate option  *** '//
     &       29X,' Input Time (min) Temperature (K) pairs'/
     &       29X,' in ASCENDING order of time.          '//
     &       29X,' To terminate input, set time=999, ktemp=999'/
     &       29X,' Maximum of 500 pairs of data permitted'//)
      DO 24 II=1,500
      CALL REED2(TIME(II),KTEMP(II))
      IF(TIME(II) .EQ. 999.0D+00) GOTO 25
24    TIME(II)=TIME(II)-TIME(1)
25    IH=II-1
      KTEMPL=KTEMP(1)
      KTEMPH=KTEMP(IH)
29    IF(JYES .NE. 0) GOTO 8
8     JYES=0
      RETURN
      END
C HRATE is the heating rate during heating at a constant rate
C I is the number of time-temperature pairs during arbitrary heating
C JID is an arbitrary identification number
C JCON allows either a constant HRATE (JCON=1) or an input of
```

```
C     time-temperature pairs (JCON=0)
C-------------------------------------------------------------------
      SUBROUTINE REED2(A,B)
      DOUBLE PRECISION A,B
996    READ(*,*,ERR=999)A,B
        GOTO 998
999       WRITE(*,997)
997       FORMAT(19X,' Incorrect Input. Try again'/)
        GOTO 996
998    RETURN
      END
C-------------------------------------------------------------------
C-------------------------------------------------------------------
      SUBROUTINE REED(A)
      DOUBLE PRECISION A
996    READ(*,*,ERR=999)A
        GOTO 998
999       WRITE(*,997)
997       FORMAT(19X,' Incorrect Input. Try again'/)
        GOTO 996
998    RETURN
      END
C-------------------------------------------------------------------
      SUBROUTINE REEDI(I)
      INTEGER I
996    READ(*,*,ERR=999)I
        GOTO 998
999       WRITE(*,997)
997       FORMAT(19X,' Incorrect Input. Try again'/)
        GOTO 996
998    RETURN
      END
C
C*********************************************************************


      SUBROUTINE TRAPE(X,Y,ANS,NDIM)
      DOUBLE PRECISION X(1000),Y(1000),AZ(1000)
      DOUBLE PRECISION SUM1,SUM2,ANS
C
      SUM2=0.D+00
      IF(NDIM-1)4,3,1
C
C     INTEGRATION LOOP
    1 DO 2 I=2,NDIM
      SUM1=SUM2
      SUM2=SUM2+.5D+00*(X(I)-X(I-1))*(Y(I)+Y(I-1))
    2 AZ(I-1)=SUM1
    3 AZ(NDIM)=SUM2
      ANS=SUM2
```

```
  4 RETURN
    END
C
C
C     PURPOSE
C       TO COMPUTE THE VECTOR OF INTEGRAL VALUES FOR A GIVEN
C       GENERAL TABLE OF ARGUMENT AND FUNCTION VALUES.
C
C     USAGE
C        CALL TRAPE (X,Y,Z,NDIM)
C
C     DESCRIPTION OF PARAMETERS
C       X    - DOUBLE PRECISION INPUT VECTOR OF ARGUMENT VALUES.
C       Y    - DOUBLE PRECISION INPUT VECTOR OF FUNCTION VALUES.
C       Z    - THE RESULTING DP. VECTOR OF INTEGRAL VALUES. Z MAY BE
C              IDENTICAL WITH X OR Y.
C       NDIM  - THE DIMENSION OF VECTORS X,Y,Z. NDIM MAX. 1000
C
C     REMARKS
C       NO ACTION IN CASE NDIM LESS THAN 1.
C
C     SUBROUTINES AND FUNCTION SUBPROGRAMS REQUIRED
C       NONE
C
C     METHOD
C       BEGINNING WITH Z(1)=0, EVALUATION OF VECTOR Z IS DONE BY
C       MEANS OF TRAPEZOIDAL RULE (SECOND ORDER FORMULA).
C       FOR REFERENCE, SEE
C       F.B.HILDEBRAND, INTRODUCTION TO NUMERICAL ANALYSIS,
C       MCGRAW-HILL, NEW YORK/TORONTO/LONDON, 1956, PP.75.
C
C**************************************************************************
C Need a heat flow model to generate the time-temperature curves
C Need something about the effect of temperature gradient
C ------------------------------------------------------------
     SUBROUTINE DEFAUL(DKIN,DKIN2,QKIN,STORE,RAD,
    &FRAC,SIGMA,JP,KTEMPH,QINT,C1,ANFRAC)
     IMPLICIT REAL*8(A-H,K-Z), INTEGER(I,J)
     DOUBLE PRECISION AC(8),C(8)
 22  WRITE(*,23)DKIN,DKIN2,QKIN,JP,STORE,RAD,FRAC,SIGMA,KTEMPH
    &,QINT,C1,ANFRAC
 23  FORMAT(//////' ************************************'
    &,'**********************************************'/
    &10X,' Current  values, kinetic strength analysis'//
    &10X,' 1. DKIN   min  ',D12.4,'     2. DKIN2   min ',D12.4/
    &10X,' 3. QKIN   J/mol',D12.4,'     4. JP (print)  ',I5  //
    &10X,' Current  values, directional recrystallisation analysis'//
    &10X,' 5. STORE J/mol ',D12.4,'     6. RAD   m     ',D12.4/
    &10X,' 7. FRAC        ',D12.4,'     8. SIGMA J/m**2',D12.4/
    &10X,' 9. KTEMPH K    ',F12.0,'    10. QINT J/mole ',D12.4/
```

```
    &10X,'11. C1 m/min    ',D12.4,'     12. ANFRAC       ',D12.4//
    &//10X,' ANY ALTERATIONS ?'//20X,
    & ' (Choose item number,   or Continue = 0) '//
    &' **********************************'
    &,'**********************************************'//)
     CALL REEDI(JYES)
     IF(JYES .GT. 12 .OR. JYES .LT. 0)CALL BOUNDI(JYES,0,12)
     IF(JYES .EQ. 0) GOTO 24
     IF(JYES .EQ. 1) GOTO 1
     IF(JYES .EQ. 2) GOTO 2
     IF(JYES .EQ. 3) GOTO 3
     IF(JYES .EQ. 4) GOTO 4
     IF(JYES .EQ. 5) GOTO 5
     IF(JYES .EQ. 6) GOTO 6
     IF(JYES .EQ. 7) GOTO 7
     IF(JYES .EQ. 8) GOTO 8
     IF(JYES .EQ. 9) GOTO 9
     IF(JYES .EQ. 10) GOTO 10
     IF(JYES .EQ. 11) GOTO 11
     IF(JYES .EQ. 12) GOTO 12
1    WRITE(*,*)'                    DKIN,  mins  ?'
     CALL REED(DKIN)
     WRITE(*,25)
25   FORMAT(10X,' Remember to modify DKIN2 if necessary'/
    &        ' DKIN2 should be lager than DKIN      '/)
     PAUSE 'Press RETURN to continue'
     GOTO 22
2    WRITE(*,*)'                    DKIN2, mins   ?'
     CALL REED(DKIN2)
     GOTO 22
3    WRITE(*,*)'                    QKIN, J/mol   ?'
     CALL REED(QKIN)
     GOTO 22
4    WRITE(*,*)'                    JP (print)    ?'
     CALL REEDI(JP)
     GOTO 22
5    WRITE(*,*)'                    STORE J/mol   ?'
     CALL REED(STORE)
     GOTO 22
6    WRITE(*,*)'                    RAD    m      ?'
     CALL REED(RAD)
     GOTO 22
7    WRITE(*,*)'                    FRAC          ?'
     CALL REED(FRAC)
     GOTO 22
8    WRITE(*,*)'                    SIGMA, J/m**2 ?'
     CALL REED(SIGMA)
     GOTO 22
9    WRITE(*,*)'                    KTEMPH K      ?'
     CALL REED(KTEMPH)
```

```
   GOTO 22
10  WRITE(*,*)'                QINT  J/mole  ?'
   CALL REED(QINT)
   GOTO 22
11  WRITE(*,*)'                C1 m/min     ?'
   CALL REED(C1)
   GOTO 22
12  WRITE(*,*)'                ANFRAC       ?'
   CALL REED(ANFRAC)
   GOTO 22
24  RETURN
   END
C-------------------------------------------------------------------
   SUBROUTINE DXX(IH,STORE,FRAC,RAD,R,KTEMP,
  &TIME,SIGMA,C1,QINT,JP,ANFRAC)
   IMPLICIT REAL*8(A-H,K-Z),INTEGER(I,J)
   DOUBLE PRECISION KTEMP(500),TIME(500),PSI(500)
   JDUM=0
   WRITE(*,3)
   DO 1 I=1,IH-1
C
   IF(I .EQ. 1)THEN
    DTIME=(TIME(I+1)-TIME(I))/2.0D+00
    CALL VOL(PSI(I),STORE,FRAC,RAD,R,KTEMP(I),SIGMA,DTIME,
  & ANISOT,ANFRAC,0,C1,QINT)
   ELSE
    CALL VOL(PSII,STORE,FRAC,RAD,R,KTEMP(I),SIGMA,DTIME0,
  & ANISOT,ANFRAC,1,C1,QINT)
    DTIME=((TIME(I+1)-TIME(I-1))/2.0D+00) + DTIME0
    CALL VOL(PSI(I),STORE,FRAC,RAD,R,KTEMP(I),SIGMA,DTIME,
  & ANISOT,ANFRAC,0,C1,QINT)
   ENDIF
C
   PSII=PSI(I)
   IF(JP*DINT(I/JP) .EQ. I .AND. PSI(I) .GT. 0.01)
  &WRITE(*,2)KTEMP(I),KTEMP(I)-273.15, TIME(I),PSI(I),
  &DTIME,DTIME0,ANISOT
C
7     IF(PSI(I) .GT. 0.05D+00 .AND. JDUM .EQ. 0)THEN
      WRITE(*,2)KTEMP(I),KTEMP(I)-273.15, TIME(I),PSI(I),
  &    DTIME,DTIME0,ANISOT
      WRITE(*,6)
      JDUM=1
      PAUSE 'Press RETURN to continue'
      WRITE(*,3)
     ENDIF
C
   IF(PSI(I) .GT. 0.9899D+00) THEN
     WRITE(*,2)KTEMP(I),KTEMP(I)-273.15, TIME(I),PSI(I),
  &  DTIME,DTIME0,ANISOT
```

```
      WRITE(*,5)
      GOTO 10
    ENDIF
1      CONTINUE
10      WRITE(*,9)PSI(I-1)
C
C
2   FORMAT(10X,2F8.0,F8.2,F8.3,2D9.2,F10.1)
3   FORMAT(/////10X,' KTEMP  CTEMP   TIME    PSI  DTIME',
   &'  DTIME0  ANISOT'/)
5   FORMAT(/' Directional recrystallisation COMPLETED'/)
6   FORMAT(/' Directional recrystallisation INITIATED'/)
9   FORMAT(/' Fraction Recrystallised =  ',F8.2/)
    RETURN
    END
C-----------------------------------------------------------------
    SUBROUTINE VOL(PSI,STORE,FRAC,RAD,R,KTEMP,SIGMA,TIME,
   &ANISOT,ANFRAC,J,C1,QINT)
    IMPLICIT REAL*8(A-H,K-Z),INTEGER(I,J)
C ANFRAC ratio of particle spacing in x direction to y or z direction
C DX spacing in x direction, METERS
C x is the extrusion direction
C NOV nuclei per unit volume
C NV number of particles per unit volume m**-3
C sample of unit length along z direction
C
    NV=3.0D+00*FRAC/(4.0D+00*3.14159D+00*RAD*RAD*RAD)
    DX=(ANFRAC*ANFRAC/NV)**(1.0/3.0)
    DY=DX/ANFRAC
    DZ=DY
    NOV=1.0D+09
C NX,NY,NZ number of particles per unit area normal to x, y, z axes
    NX=1.0D+00/(DY*DZ)
    NY=1.0D+00/(DZ*DX)
    NZ=NY
    IF(PSI .GE. 1.0D+00) PSI=0.99D+00
    CALL VELOC(VELX,STORE,NX,RAD,R,KTEMP,SIGMA,QINT,C1)
    CALL VELOC(VELY,STORE,NY,RAD,R,KTEMP,SIGMA,QINT,C1)
    VELZ=VELY
C
            ANISOT=VELX*TIME/DY
C
C     WRITE(*,222)DX,DY,NX,NY,VELX,VELY
C 222  FORMAT(6D12.2)
C    PAUSE
    IF(J .EQ. 0) THEN
    PSI = 1.0D+00 - DEXP(-NOV*VELX*TIME*DY*DZ)
    ELSE
    TIME=-DLOG(1.0D+00-PSI)/(NOV*VELX*DY*DZ)
    ENDIF
```

```
      RETURN
      END
C
C Based on modified form of equation 4.10, p.19, Christian (1975)
C volume fraction of isothermal recrystallisation when the
C number of available nucleation sites quickly becomes zero.
C Grains assumed to be rectangular parallelopipeds after recrystallisation
C
C PSI is the volume fraction recrystallised
C STORE stored energy responsible for recrystallisation J/mol
C KTEMP Kelvin
C FRAC volume fraction of oxide particles
C NOV number of initial nucleation sites per unit volume 1/m**3
C RAD oxide particle size
C VEL velocity of grain boundary
C-------------------------------------------------------------------
      SUBROUTINE VELOC(VEL,STORE,NX,RAD,R,KTEMP,SIGMA,Q,C1)
      IMPLICIT REAL*8(A-H,K-Z),INTEGER(I,J)
      R=8.3143D+00
      VM=7.1D-06
C G reduced due to pinning by particles
      G=STORE-(3.14159D+00*RAD*SIGMA*NX)*VM
      IF(G .LE. 0.0) THEN
         VEL=0.0D+00
         GOTO 1
      ELSE
         VEL=C1*DEXP(-Q/(R*KTEMP))*
     &    (1.0D0 - DEXP(-G/(R*KTEMP)))
      ENDIF
1     RETURN
      END
C  C1 has units of m/min
C  FRAC is the volume fraction of pinning particles
C  G net driving force for interfacial motion, J/mol
C  KTEMP Kelvin C  Q activation energy, J/mol for atom transfer across the interface
C  R universal gas constant, J/mol/K
C  STORE is the stored energy, J/mol
C  RAD is the mean particle RADIUS, m
C  VEL is the interfacial velocity, m/s
C  VM is the molar volume
C  SIGMA grain boundary energy per unit area, J/m**2
C*********************************************************************
```

Appendix 2

An Approach to the Nucleation of Recrystallisation in Mechanically Alloyed Materials

Introduction

In the present work we propose a new approach for the onset of recrystallisation in mechanically alloyed materials. Recrystallisation requires the bowing of grain boundaries. If the initial grain size becomes fine enough, then the grain boundary junctions may themselves become significant pinning points. The sparing of the pinning points may become so small as to 'prevent' recrystallisation (*i.e.* greatly raise the activation energy for recrystallisation.)

In general, the recrystallisation temperatures of mechanically alloyed materials are very high, more than 0.8 T_m (T_m= melting temperature); indeed, they sometimes approach the melting temperatures [1,2]. The trigger mechanism for recrystallisation in mechanically alloyed materials has been discussed for a long time and several mechanisms have been proposed. The dissolution or coarsening of small particles [3], and solute drag effects [4] are representative, but they cannot explain many of the experimental observations. We have shown the coarsening or dissolution of particles does not correlate with the onset of recrystallisation (Chapter 6); others have shown that solute atoms are unlikely to drag recrystallisation fronts in superalloys which contain many solutes [5]. Everything about mechanically alloyed materials suggests that the activation energy for recrystallisation is very high. For example, the high recrystallisation temperatures, the rapid completion of recrystallisation once initiated and the generality of these observations for both nickel base and iron base alloys.

Nucleation of Recrystallisation

In secondary recrystallisation, the word 'nucleation' may not be an accurate description because some of the already existing grains grow to form the recrystallised microstructure. Nevertheless, the kinetics of the actual process involve an operational recrystallisation stage. The free energy change ΔG accompanying the formation of an embryo whose volume is V and the surface area is A, is given by:

$$\Delta G = -\Delta G_V V + \sigma A + \Delta G_s V \qquad (1)$$

where ΔG_V is the chemical free energy change per unit volume, σ is the effective interfacial energy per unit area of embryo / matrix interface and ΔG_s is the coherency strain energy accompanying nucleation. Nucleation of recrystallisation is assumed to involve grain boundary bulging toward unrecrystallised area (Fig. 7.1). To simplify the shape of the grain boundary before bulging, it is assumed to be a disc whose diameter is R. The bulged part (hatched in Fig. 1) is a part of large sphere whose diameter is R. Equation (1) is therefore modified to:

$$\Delta G = -\Delta G_V\ V + \sigma\,(A - A_0) \quad (2)$$

V is the recrystallised volume due to the bulging of a grain boundary, A is the boundary area before bulging and A_0 is the boundary area after bulging.

If the bulge height is h, A_0, A and V are respectively;

$$A_0 = \pi D^2 / 4 \qquad (3)$$

$$A = 2\pi r h = \frac{\pi D^2}{4} + \pi h^2 \qquad (4)$$

$$V = \pi R h^2 - \pi h^3 / 3 = \frac{4\pi h D^2}{8} + \frac{\pi h^3}{6} \qquad (5)$$

therefore equation (1) is given by

$$\Delta G = -\frac{\Delta G_V \pi h D^2}{8V_M} + \frac{\pi h^3}{6} + \sigma \pi h^2 \qquad (6)$$

where $V_M \approx 7.1 \times 10^{-6}$ m^{3}mol^{-1} is the molar volume.

Fig. 2 illustrates ΔG (per mol) as a function of D and grain size h. It follows that ΔG goes through a maximum to form a barrier whose height is the activation energy for recrystallisation. The value of h for the maximum height is the critical bulging height, if the height becomes in excess of the value, the grain can rapidly grow. ΔG_V is a function of average grain size, here we used the experimentally measured value (5.0 X 10^6 J m^{-3}). D represents a growing grain diameter. Fig. 2 also illustrates that a smaller grain needs higher activation energy to grow and critical bulging height h is almost independent on D. The activation energies are quite high, several ten thousands times of the activation energy for self diffusion. This leads the observed difficulty of nucleation. The predicted large activation energy is entirely consistent with all the unusual aspects of recrystallisation in the mechanically alloyed materials. Furthermore, it is predicted that the recrystallised grain size will be very coarse since once an effective nucleus is formed, its growth rate is expected to be massive.

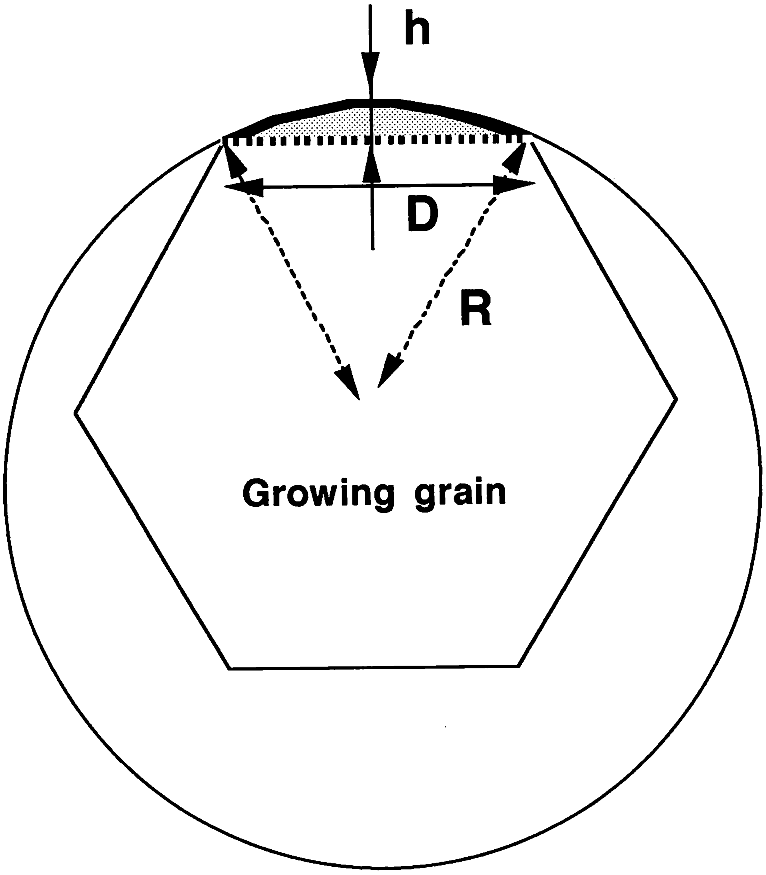

Fig. 1 Schematic drawing of bulging of a grain boundary.

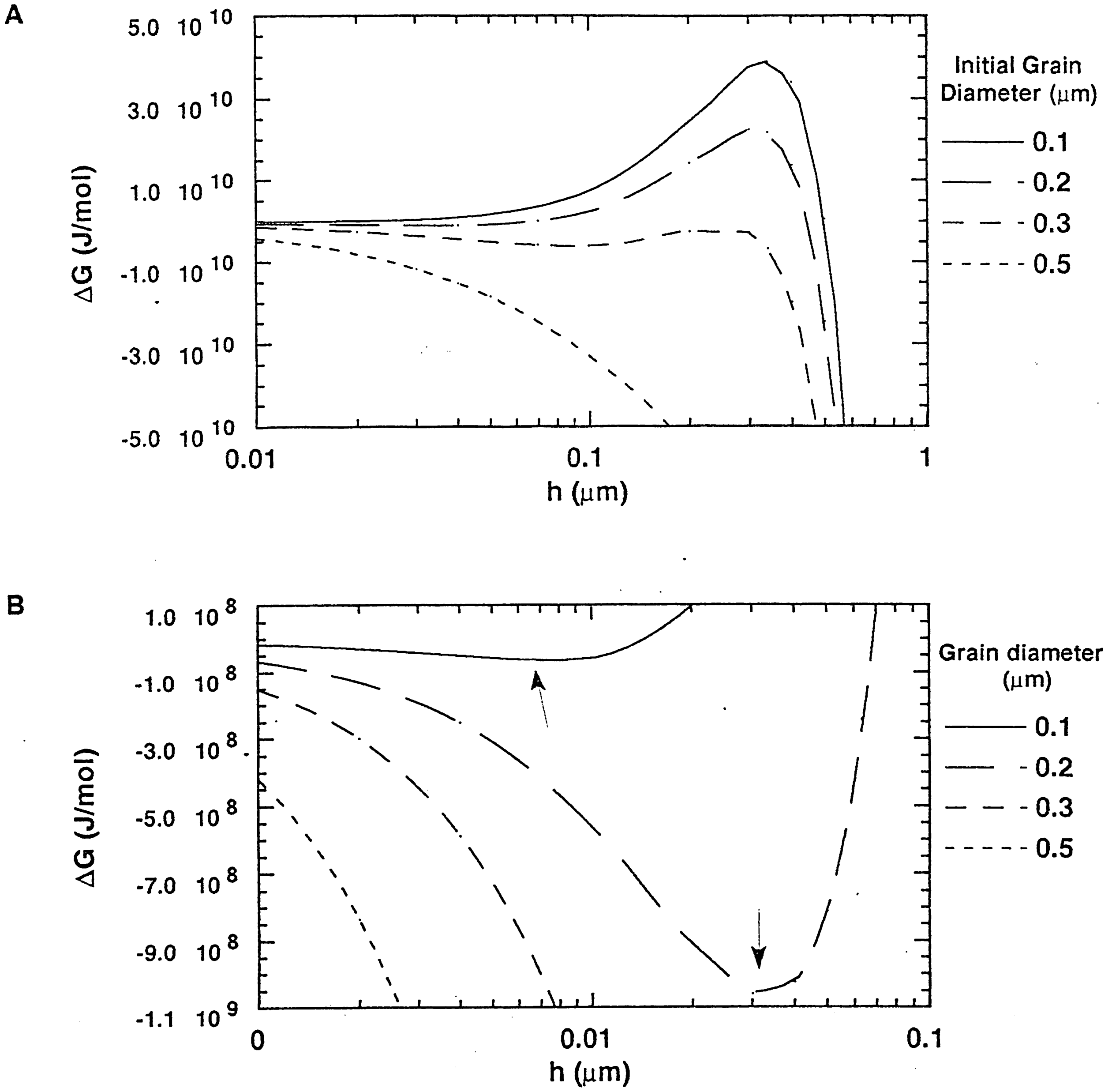

Fig. 2 ΔG as a function of h and D. Diagram B is a detail of around the one of the inflection points.

References

1. Mino K., Harada K., Bhadeshia H.K.D.H., and Yamazaki M.: *Mater. Sci. Forum,* (1992), **88-90**, p213
2. Benjamin J. S.: *Metall. Trans.* (1970), **1**, p.2943.
3. Schaffer G. B., Loretto M. H., Smallman R. E., and Brooks J. W.,: *Acta Metall.*, (1989) 379, p. 2551.
4. Jongenburger C. P., and Singer R. F. : *Advanced Materials and Processing Techniques for Structural Applications*, ed. by Khan T. and Lasaimoniet A., (1988), p. 339
5. Nakagawa Y. G., Terashima H. and Mino K.: Proceeding of *The 6th International Symposium on Superalloys,* (1988), ed. by Duhl D. N., p. 81
6. Christian J. W.: *Theory of Transformation in Metals and Alloys*, Part 1, 2nd edn., Pergamon Press, Oxford, (1975)